REPUBLIC OF TURKEY
YILDIZ TECHNICAL UNIVERSITY
GRADUATE SCHOOL OF SCIENCE AND ENGINEERING

SCATTERING ANALYSIS OF THREE DIMENSIONAL OBJECTS ABOVE ARBITRARILY ROUGH SURFACES BY CURRENT DECOMPOSITION METHOD

Yunus Emre YAMAÇ

DOCTOR OF PHILOSOPHY THESIS
Department of Electronics & Communications Engineering
Program of Telecommunications

Supervisor
Prof. Dr. Ahmet KIZILAY

February, 2023

REPUBLIC OF TURKEY
YILDIZ TECHNICAL UNIVERSITY
GRADUATE SCHOOL OF SCIENCE AND ENGINEERING

SCATTERING ANALYSIS OF THREE DIMENSIONAL OBJECTS ABOVE ARBITRARILY ROUGH SURFACES BY CURRENT DECOMPOSITION METHOD

A thesis submitted by Yunus Emre YAMAÇ in partial fulfillment of the requirements for the degree of **DOCTOR OF PHILOSOPHY** is approved by the committee on 01.02.2023 in Department of Electronics & Communications Engineering, Program of Telecommunications.

Prof. Dr. Ahmet KIZILAY
Yildiz Technical University
Supervisor

Approved By the Examining Committee

Prof. Dr. Ahmet KIZILAY, Supervisor
Yildiz Technical University _____

Assoc. Prof. Dr. Hamid TORPİ, Member
Yıldız Technical University _____

Prof. Dr. Mustafa Emre AYDEMİR, Member
Esenyurt University _____

Assoc. Prof. Dr. Peyman MAHOUTİ, Member
Yıldız Technical University _____

Prof. Dr. Mehmet ÇAYÖREN, Member
İstanbul Technical University _____

I hereby declare that I have obtained the required legal permissions during data collection and exploitation procedures, that I have made the in-text citations and cited the references properly, that I haven't falsified and/or fabricated research data and results of the study and that I have abided by the principles of the scientific research and ethics during my Thesis Study under the title of Scattering Analysis of Three Dimensional Objects above Arbitrarily Rough Surfaces by Current Decomposition Method supervised by my supervisor, Prof. Dr. Ahmet KIZILAY. In the case of a discovery of false statement, I am to acknowledge any legal consequence.

Yunus Emre YAMAÇ

Signature

This study was supported by the Scientific and Technological Research Council of Turkey (TUBITAK) Grant No: 119N196

Dedicated to my family
and my cat Cirilla

ACKNOWLEDGEMENTS

To begin with, my advisor, Prof. Dr. Ahmet KIZILAY, has my sincere gratitude for all of his time, help, suggestions, patience, and mentoring throughout the years. I especially want to express my gratitude to him for giving me fatherly guidance.

I will always be grateful to my parents for their love and support as I pursue my education. I want to express my gratitude to my sister Merve and brother Mehmet for their care, support, and direction.

I would like to express my gratitude to my former colleagues and professors at Yıldız Technical University. I would like to thank my dear friends Dr. Ramazan DAŞBAŞI and Melek DAŞBAŞI for their help and guidance.

I would like to thank my professors Assoc. Prof. Dr. Hamid TORPİ and Prof. Dr. Mustafa Emre AYDEMİR in my thesis committee for their time and advice. I would like to thank my professor Prof. Dr. Ahmet Serdar TüRK for the experiences he provided me. I would also like to thank my former roommates at Yıldız Technical University, Dr. Mehmet ÜNAL and Dr. Alper ÇALIŞKAN for their help.

Finally, I also want to express my sincere gratitude to my colleagues at the Antenna Test and Research Laboratory at TÜBİTAK for their support and good wishes.

Yunus Emre YAMAÇ

TABLE OF CONTENTS

LIST OF SYMBOLS

ω	Angular Frequency
σ	Conductivity of Medium
∇	Del Operator
∇_s	Del Operator on Surface
∇_t	Del Operator in x-and y-directions
$\overline{\overline{\mathbf{G}}}_e$	Dyadic form of Green's Function for L operator
$\vec{\mathbf{E}}$	Electric Field Vector
G_0	Free-Space scalar Green's Function
f	Frequency
$\mathscr{F}$	Fourier Transform
$\vec{\mathbf{k}}_i$	Incident Wave Vector
η	Intrinsic Impedance of Medium
η_0	Intrinsic Impedance of Free-Space
$\mathfrak{K}$	K operator of Integral Equations in Operator Notation
$\mathfrak{L}$	L operator of Integral Equations in Operator Notation
$\vec{\mathbf{H}}$	Magnetic Field Vector
G_p	Periodic Green's Function
μ	Permeability of Medium
ϵ	Permittivity of Medium
β	Phase Constant
β_x	Phase Constant in x-direction
β_y	Phase Constant in y-direction
β_z	Phase Constant in z-direction

q	Phase Constant in z-direction for Periodic Surface Cases
β_m	Phase Constant in x-direction for Floquet Modes
β_n	Phase Constant in y-direction for Floquet Modes
q_{mn}	Phase Constant in z-direction for Floquet Modes
$\vec{\mathbf{r}}$	Position Vector for Observation Point
$\vec{\mathbf{r}}'$	Position Vector for Source Point
ε	Relative Error
$\vec{\mathbf{k}}_s$	Scattered Wave Vector
$\vec{\mathbf{J}}$	Surface Electric Current Density Vector
$\vec{\mathbf{M}}$	Surface Magnetic Current Density Vector
$\mathfrak{s}$	Surface Function
$\hat{\mathbf{n}}$	Unit Normal Vector of Surface
$\hat{\mathbf{t}}$	Unit Tangent Vector of Surface
λ	Wavelength
λ_d	Wavelength of Dielectric Medium
λ_0	Wavelength of Free-Space
k	Wavenumber

LIST OF ABBREVIATIONS

1-D	One-Dimensional
2-D	Two-Dimensional
3-D	Three-Dimensional
ACA	Adaptive Cross Approximation
EFIE	Electric Field Integral Equation
EFIE-MoM	Electric Field Integral Equation-Method of Moments
EM	Electromagnetic
FMMM	Floquet Mode-Matching Method
FS-PGF	Free Space-Periodic Green's Function
GF	Green's Function
GPR	Ground Penetrating Radar
HOBF	Higher-Order Basis Function
IE	Integral Equation
KA	Kirchhoff Approximation
MFIE	Magnetic Field Integral Equation
MLFMA	Multi-Level Fast Multipole Algorithm
MoM	Method of Moments
PEC	Perfect Electric Conductor
PGF	Periodic Green's Function
PMCHWT	Poggio–Miller–Chang–Harrington–Wu-Tsai
PO	Physical Optics
RCS	Radar Cross Section
RWG	Rao-Wilton-Glisson

SIE	Surface Integral Equation
SPM	Small Perturbation Method
TE	Transverse Electric
TM	Transverse Magnetic

LIST OF FIGURES

LIST OF TABLES

ABSTRACT

Scattering Analysis of Three Dimensional Objects above Arbitrarily Rough Surfaces by Current Decomposition Method

Yunus Emre YAMAÇ

Department of Electronics & Communications Engineering
Doctor of Philosophy Thesis

Supervisor: Prof. Dr. Ahmet KIZILAY

A practical approach called the perturbation or current decomposition method, based on a decomposition of currents on infinitely long surfaces, is introduced to treat 3-D scattering problems of targets located above or below any half-space for the first time. The scattering problem of a PEC object located above or below a flat dielectric or rough surface is addressed by modifying the surface integral equations (SIEs). The rough surfaces are modeled as periodic and perfectly conductive, and the periodic Green's functions are used to obtain the induced currents for any degree of surface roughness. A flat dielectric ground is also employed in the implementations of the proposed approach. The method of moments (MoM) is used to solve the resulting SIEs, while well-known RWG (Rao-Wilton-Glisson) basis functions are exploited for discretization.

In this thesis, the perturbation approach is based on the fact that the surface current densities on the infinitely long interfaces can be decomposed as the induced current without the object and the perturbation current on a finite partition of the infinite surface. Moreover, this method assumes that perturbation currents' amplitude is negligible while far away from the object. Besides, to compare and prove the achievements of the proposed approach, the image theory, commercial electromagnetic (EM) solvers, and studies from the literature are utilized. Hence, the proposed approach and formulations establish considerable accuracy while providing an undemanding computation without involving a tapered wave illumination or deriving a half-space Green's function. Additionally, this method yields a significantly

superior solution even when using a plane wave rather than a tapered wave approach for illumination at low-grazing angles.

Keywords: Current decomposition, RCS (Radar Cross Section), scattering, periodic surface, perturbation method

ÖZET

Keyfi Engebeye Sahip Yüzeyler Üzerinde Bulunan Üç Boyutlu Nesnelerin Akım Ayrıştırma Yöntemiyle Saçılma Analizi

Yunus Emre YAMAÇ

Elektronik & Haberleşme Mühendisliği Anabilim Dalı
Doktora Tezi

Danışman: Prof. Dr. Ahmet KIZILAY

Sonsuz uzun yüzeylerde akımların ayrıştırılmasına dayanan pertürbasyon veya akım ayrıştırma yöntemi adı verilen pratik bir yaklaşım, ilk kez herhangi bir yarı uzayın üstünde veya altında bulunan hedeflerin 3 boyutlu saçılma problemlerini çözmek için tanıtılmaktadır. Düz dielektrik veya pürüzlü bir yüzeyin üstünde veya altında bulunan bir PEC cisminin saçılma sorunu, yüzey integral denklemleri (YİD) değiştirilerek ele alınır. Pürüzlü yüzeyler, periyodik ve mükemmel iletken olarak modellenmiştir ve periyodik Green fonksiyonları, herhangi bir yüzey pürüzlülüğü derecesi için indüklenen akımları elde etmek için kullanılmaktadır. Önerilen yaklaşımın uygulamalarında düz bir dielektrik zemin de faydanılmaktadır. Elde edilen YİD'leri çözmek için momentler yöntemi kullanılırken, ayrıklaştırma için iyi bilinen RWG (Rao-Wilton-Glisson) temel fonksiyonlarından yararlanılır.

Bu tezde pertürbasyon yaklaşımı, sonsuz uzunluktaki arayüzlerdeki yüzey akım yoğunluklarının cisim yokken indüklenen akım ve sonsuz yüzeyin sonlu bir bölümündeki pertürbasyon akımı olarak ayrıştırılabileceğine dayanmaktadır. Ayrıca, bu yöntem pertürbasyon akımlarının genliğinin nesneden uzaktayken ihmal edilebilir olduğunu varsaymaktadır. Ayrıca, önerilen yaklaşımın başarılarını karşılaştırmak ve kanıtlamak için görüntü teorisi, ticari elektromanyetik çözücüler ve literatürdeki çalışmalardan yararlanılmıştır. Bu nedenle, önerilen yaklaşım ve formülasyonlar, bir konik dalga aydınlatması gerektirmeden veya bir yarı-uzay Green fonksiyonu türetmeden iddiasız bir hesaplama sağlarken önemli ölçüde doğruluk vermektedir.

Ek olarak, bu yöntem, düşük gelme açılarında aydınlatma için konik bir dalga yaklaşımı yerine bir düzlem dalga kullanıldığında bile önemli ölçüde üstün bir çözüm sağlamaktadır.

Anahtar Kelimeler: Akım ayrıştırma, RKA (Radar Kesit Alanı), saçılma, periyodik yüzeyler, pertürbasyon yöntemi

1
INTRODUCTION

1.1 Literature Review

For optics and remote sensing applications, modeling a surface of a medium such as a sea and ground and calculating electromagnetic scattering from these surfaces has been an essential subject for researchers from the past to present. However, most analytic and numerical solutions for this forward bi-static scattering problem have focused on random or arbitrary rough conductive or dielectric surfaces with single-or multi-layer to model artificial and natural rough surfaces [1–15]. One of the well-known classical solutions of this rough surface scattering is the Small Perturbation Method (SPM), initially derived by Rice in the 1950s [1]. Rice reported that the sinusoidal and random slightly rough surfaces could be solved analytically with the first-and second-order SPM. Besides, when the order of the solution increases, the scattering coefficients become highly complicated in the SPM [9]. This is because an iterative method should be employed to determine higher-order coefficients in the SPM. Therefore, increasing the convergence of the related series leads to complexity, especially in the solution for multi-layer dielectric interfaces [7, 10, 11].

An alternative solution approach called Rayleigh-Fourier or Floquet Mode-Matching Method (FMMM) based on the Rayleigh hypothesis without using perturbation theory is also studied in [12, 16]. In this method, the scattering from 1-D sinusoidal surfaces can be easily calculated with Bessel functions as reported in [12]. However, these analytical or semi-analytical solutions are based on Lord Rayleigh's assumption that the scattered fields consist of the sum of up-and-down-going plane waves. Nevertheless, it is proved that the roughness of surfaces has restrictions in the Rayleigh hypothesis [8].

On the order hand, integral equations (IEs) are among the most commonly used methods to solve any roughness degree of the surface, and several IE approaches deal with these types of problems. The physical constraints are considered in determining the approaches, and the solution domain is bounded due to limited

computer resources and natural antenna radiation patterns. A tapered beam is thereby exercised as the first approach to avoid edge singularity from a bounded solution region [14]. This approach's main drawback is increasing the solution domain and losing accuracy at large incidence angles concerning the surface normal. Since the wavefront of the wave radiating from the antenna is assumed to turn into a plane wave, a far-reaching illumination effect on the rough surface arises at shallow grazing angles. As a result, unwanted radiations can still occur by the solution domain edges that have to be physically truncated for near-grazing angle problems in the tapered beam approach. The solution domain is bounded with a cancellation method of edge effects as the second approach. In this method, the resistive strips can be added to boundaries to overcome this problem [15]. As reported in [2], the rough surfaces can also be modeled as a bounded perturbation with a new formulation. The scattered fields are conceded as perturbations from local roughness. The incident wave can be assumed as a plane wave rather than a tapered beam in this near-grazing illumination approach.

The third IE approach for handling surface roughness is the periodic-surface moment method [3] or named EFIE-MoM (Electric Field Integral Equation-Method of Moments) method as given in [13]. The periodic surface EFIE-MoM method is an alternative solution to obtain the scattering from rough surfaces. Compared to artificial illumination with a tapered beam as the solution domain grows at small grazing angles, the periodic surface moment method reduces the computational burden for these types of problems and avoids singularity at the surface edges [3]. Moreover, this approach selects a surface partition randomly, and the remaining part is considered periodic with this selected partition [4]. Besides, there are also different approaches in the literature in order to solve IEs. For example, a closed-form of classical PGF via using a complex image technique has been obtained for arbitrary rough surfaces [5], as well as a numerical method based on the calculation of the Green's function (GF) of a locally rough interface with and without any periodicity as perturbation series of internal and external roughness is also reported for direct and inverse scattering problems [6].

In addition to periodic rough surface scattering, the scattering analyses from an object above an infinite or finite length rough surfaces and solution methods of these problems are also one of the principal challenges focused on by researchers for predicting the electromagnetic characteristic and shape of the scattering object. Therefore, many studies have been performed for the electromagnetic modeling of these scattering problems investigating the effect of a rough surface and interactions between the scattering between the object and the surface. For this purpose, more accurate and faster solution methods have been continued to study in recent years.

These methods are generally based on iterative or MoM solutions of IEs. In brief, they can be divided into five headings: obtaining an approximate or exact GF [17–20], acquiring an approximate hybrid solution with a numerical solution and analytical approaches [21–24], operating a tapered wave approach in a general MoM solution [25–28], employing matrix and domain decomposition and fast solution methods [29–36], and lastly finding a hybrid solution by combining different and same type numerical computational methods [37–40]. Moreover, several studies combine some of these headings [41–46].

We know that obtaining the exact GF for rough surfaces is only sometimes possible. Thereby, some approximations must be applied, such as by assuming that the rough interface is locally present to implement a buried object approach [18] or having a large radius of curvature relative to the wavelength to be valid for the Kirchhoff approximation (KA) [19] or having a small surface height to apply the SPM [20]. In addition, analytical approximations such as the small slope approximation, the SPM, and the KA are also used with numerical solutions without obtaining GF [22, 23]. However, these approximations depend on surface roughness, meaning they only work correctly for some situations. Besides, as mentioned before, the infinite solution domain of a half-space scattering problem can be bounded by a tapered wave approach in a fully MoM solution to neglect edge effects [25–27]. The main weakness of this approach is the massive increment of the solution domain for low-grazing angle illuminations [28]. The fourth solution method has handled large solution domains using decomposition and fast solution methods to increase solution speed by decreasing computational burden. For this purpose, generalized forward-backward [30], Adaptive Cross Approximation (ACA) [32], and Multi-Level Fast Multipole Algorithm (MLFMA) [36] methods are studied by researchers. Some other numerical techniques in combination with MoM are also employed in recent years. A disadvantage of these last two approaches is that one must rigorously truncate and decide practical interaction domain on a rough surface to achieve a precise solution.

Lastly, researchers have extensively studied the scattering analyses caused by an arbitrarily shaped object above and below a flat dielectric for a dielectric and flat half-space case. Wherein analytical and numerical approaches, the IE formulations for dielectric-dielectric interfaces are also exploited for this purpose in [43, 47–55]. A perfectly conducting plate is inserted into a dielectric half-space in a general numerical solution, except for a sphere. This problem is solved by employing EFIE in the spectral domain [50]. In this thesis, our proposed method for buried objects is validated by comparing with [50]. However, the other studies mentioned above can also be employed for comparison.

1.2 Objective of the Thesis

In this thesis, an EFIE-based periodic MoM solution is obtained after a detailed review process of available formulations. First of all, the periodic-MoM code is generated for perfectly conducting surfaces simulated a sea or wet soil. Then the resulting EFIE is solved to calculate scattering from the surfaces with arbitrary roughness. The infinite surface is considered periodic to prevent edge effects, and free space-periodic Green's function (FS-PGF) is chosen to be the IE's kernel. Subsequently, the convergence problem of the FS-PGF is addressed by the acceleration techniques suggested in [56–63], and the acceleration techniques are compared for frequency, dimensions of the unit cell, and surface height. Additionally, the modified RWG (Rao-Wilton-Glisson) basis and testing functions can model the current's non-zero component on the boundaries as in [64, 65]. Consequently, the methods employed in the periodic-MoM formulations consist of the discretization of the periodic surface currents by special basis and testing functions for inner and boundary edges to provide the continuity of surface current and the acceleration of the PGF's double series sum by Kummer's and Ewald's transformations. Finally, in detail, these two primary acceleration techniques are compared within an MoM code to handle realistic 3-D scattering problems. Besides, singularities that will arise in these methods are discussed, and the extraction of near-and far-field equations is also given in this thesis.

Also, the verification and accuracy of the EFIE-MoM solution are benchmarked with Rayleigh-based solutions and commercial software. For this purpose, a commercial software package (FEKO) is employed for comparison, validation, and accuracy achievements. The MoM solution is analytically compared to Rayleigh-based methods for slightly rough 2-D surfaces. Therefore, the proposed full-wave solution agrees well with Rayleigh-based methods and achieves higher accuracy than FEKO. Besides, the EFIE-MoM has no restrictions on the surface's roughness, and even highly rough surfaces can be solved by this method, unlike the analytical solutions. Besides, the formulation of the FMMM can produce a more comfortable solution than SPM. In this thesis, as a small contribution to the literature, the 2-D periodicity of the surface is also solved and formulated by the FMMM for any slightly rough surfaces.

This thesis proposes a current decomposition approach in the spatial domain for the scattering problems of a 3-D object above a 2-D rough surface with an MoM solution. Unlike the other studies in the literature, this approach allows one to precisely truncate the solution domain with the desired accuracy by decomposing the perturbed and induced currents on the rough surface and also has no significant constraint on the roughness degree due to not comprising any approximation methods as KA, SPM, and PO. Furthermore, the rough surface is designated to be periodic in order to be able

to evaluate the induced current on the rough surface without an object present and avoid edge effects. The scattering problem in low grazing angles can be treated easier without requiring a tapered wave so that a plane wave can carry out the illumination through the periodic rough surface and the current decomposition method. Although a periodic rough surface appears to be a constraint, periodicity length can be increased with the object's size.

Moreover, the perturbation method is applied to the scattering problems that insert an object above or below a flat and infinite dielectric interface. The proposed method presents an alternative solution to the literature and can also produce high-accuracy solutions for any scattering scenario in which the object shape can be chosen arbitrarily. Besides, the infinite ground can be lossless or lossy. The target object is chosen as PEC for simplification in this scattering scenario. Despite the earlier calculations, a new perturbed surface current exists on the dielectric ground surface. The EFIE and MFIE are thereby exploited with the Poggio–Miller–Chang–Harrington–Wu-Tsai (PMCHWT) formulation [43] to calculate the equivalent surface currents for the dielectric interface. The induced electric current on the target is attained by solving the EFIE on the surface. The validations of the proposed method are realized by comparing commercial software (CST Microwave Studio) and the literature.

As a result, the proposed solution approach in this thesis offers an alternative to the literature through all these mentioned features. However, this approach has been validated for 2-D scattering problems in previous studies that address the scattering problems from the object above a sinusoidal surface [66–68], from a buried object below a flat [69, 70] and a periodic surface [71], as well as from the objects partially buried [72–74]. In this thesis, unlike previous studies, a more realistic solution is considered for the first time. RWG basis function fulfills the discretization of the surface currents, and RWG-based special basis and testing functions are employed for the periodic rough surface to discretize the induced current on the infinity surface without the object present [75].

In the thesis's organization, the formulations of the EFIE-MoM solution are given in detail in Chapter 2. The validations and performance tests of the periodic-MoM formulations for several cases are carried out with the FMMM, conventional arbitrary-order SPM, and FEKO software. Furthermore, a helpful general semi-analytical and a specific analytical solution of the FMMM for arbitrary and sinusoidal periodic surfaces are also derived. These 2-D FMMM formulations are derived for the first time through this thesis. The proposed approach is formulated in Chapter 3, and numerical results are verified and discussed. The image theory is

used for the validations, in which the MoM solves the obtained EFIE. In Chapter 4, the effects of various surface roughnesses, size or height of the object, incident angles, and truncated rough surfaces are assessed in detail by utilizing the findings in Chapter 2. In Chapter 5, the perturbation method is applied to a scattering problem caused by a PEC target above a flat, infinite dielectric surface. The PMCHWT formulation is employed for the dielectric surface, and on the surface of the PEC object, the EFIE is solved with the MoM. The validations are performed by commercial software. Lastly, in Chapter 6, the scattering problem from a buried PEC object inside a dielectric ground plane is addressed by the perturbation method.

1.3 Hypothesis

In this thesis, 3-D scattering problems from a PEC object above or below infinite rough or flat surfaces are treated using a current decomposition method (or named perturbation method) based on the separation of equivalent current density on the infinite interface as induced without the object present and perturbed current with the object present densities in the spatial domain. The total current on the infinite surface is the sum of these induced and perturbed currents. Our assumption in this thesis is that the perturbed current density caused by the object is firmly dominant only in a limited area on the periodic surface. Therefore, the infinite solution domain is forcibly bounded, and the perturbed current caused by the object on the infinite surface is zero except for the perturbation surface. This assumption gives us considerable accuracy while providing an effortless computation without obtaining a half-space GF or exploiting a tapered wave illumination. Also, the proposed method can apply any scattering scenario, and we have derived the sample formulations of some of them. Moreover, considering illumination at low-grazing angles, our proposed approach may yield a superior solution than a tapered wave so that the current rapidly converges to zero on the edges of the truncated perturbation surface, even using a plane wave illumination in our method.

2
SCATTERING ANALYSES OF ARBITRARILY ROUGH PERIODIC SURFACES BY ANALYTICAL APPROACHES AND MOMENTS METHOD

In this chapter, a periodic-MoM-based code with high accuracy performance is developed to calculate electromagnetic scattering from a periodic conductive surface in two dimensions with any degree of roughness. First, the existing separate methods in the literature are reviewed step by step to composing a periodic EFIE-MoM solution for 2-D periodic surfaces. Then, the dynamic selection of optimal formulation of the periodic-MoM solutions created using these existing methods is evaluated to reduce solution time and obtain high accuracy. In Section 2.2, the performance parameters of the existing methods are investigated in solving a real 3-D scattering problem by a periodic MoM for the first time in the literature. Eventually, a commercial EM solver with a similar numerical approach is employed for comparison, validation, and accuracy achievements of these different periodic-MoM formulations.

Furthermore, an analytical solution named FMMM (Floquet Mode-Matching Method) is developed based on the Rayleigh hypothesis for slightly rough surfaces, and the accuracy of the code is tested using this analytical solution. This study is entirely compatible with analytical solutions and gives better results than this commercial EM solver in terms of accuracy. Also, in Section 2.1, the FMMM formulation derived for comparison provides a more straightforward solution than the SPM (Small Perturbation Method), a classical solution method, and it is adapted to two-dimensional surface roughness for the first time in this thesis. However, unlike the analytical solutions, this full-wave solution has no restriction on surface roughness.

2.1 Formulations

This section focuses on a numerical solution of a scattering problem from two-dimensional periodic conductive rough surfaces. For this purpose, we first have

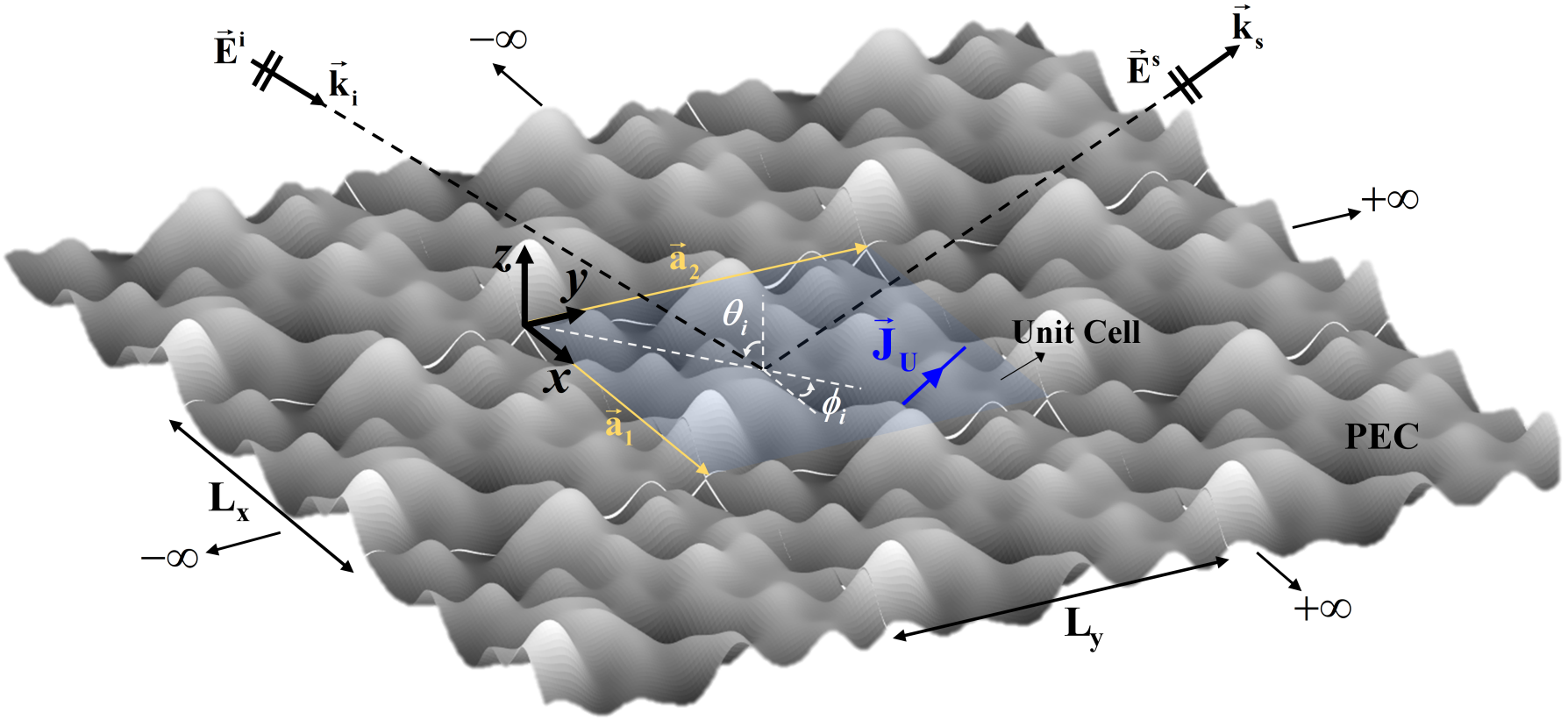

Figure 2.1 Configuration of a scattering problem from a unit cell of a periodic conducting surface

derived the free-space periodic Green's function (FS-PGF) for two-dimensional unit impulse sources as presented in Appendix A. Later, Kummer's and Ewald's transform have also been employed to accelerate the doubly periodic series sum of the FS-PGF. Additionally, although this section focuses on a numerical solution by moments method, analytical solutions based on the Rayleigh hypothesis for the scattering problem from a periodic surface, named SPM and FMMM, have also been introduced to verify the numerical solution. The proposed full-wave numerical solution agrees well with the SPM and the FMMM. Also, in our numerical solution, there is no restriction on the surface roughness compared to the Rayleigh-based methods. As a result, herein, we initially start by deriving analytical formulations for this section.

Firstly, assume that a plane wave is an incident on a periodic conductive rough surface $\{z = \mathfrak{s}(x,y)\}$ with the incidence angles of θ_i and ϕ_i as depicted in Figure 2.1. As shown in Figure 2.1, the PEC surface is located on the $x-y$ plane, and the upper region of this surface is the vacuum. $\vec{\mathbf{a}}_1$ and $\vec{\mathbf{a}}_2$ are the primitive lattice vectors, and L_x and L_y are the dimensions of the unit cell. The rough surface is periodic with L_x and L_y, and the surface function satisfies the condition of the periodicity $\{z = \mathfrak{s}(x,y) = \mathfrak{s}(x+L_x, y+L_y)\}$. The polarization of the incident plane wave is determined depending on whether it is parallel or perpendicular to the plane of incidence. Under the assumption of $e^{j\omega t}$ time dependence, the incident electric field is expressed as follows

$$\vec{\mathbf{E}}_i = \hat{\mathbf{e}}_i E_0 e^{-j\vec{\mathbf{k}}_i\cdot\vec{\mathbf{r}}} = (\hat{\boldsymbol{\theta}}\cos\alpha + \hat{\boldsymbol{\phi}}\sin\alpha)E_0 e^{-j\beta_0\hat{\mathbf{k}}_i\cdot\vec{\mathbf{r}}} = (\hat{\mathbf{v}}_i + \hat{\mathbf{h}}_i)E_0 e^{-j\beta_0\hat{\mathbf{k}}_i\cdot\vec{\mathbf{r}}} \tag{2.1}$$

where α is the polarization angle and $\vec{\mathbf{k}}_i = \beta_0\hat{\mathbf{k}}_i$ is the incident vector of the wave. $\alpha = 0°$ and $\alpha = 90°$ are θ-polarization (vertical $\hat{\mathbf{v}}_i$ or TM polarization) and ϕ-polarization (horizontal $\hat{\mathbf{h}}_i$ or TE polarization), respectively. The polarization unit vectors $\hat{\boldsymbol{\phi}}_i = \hat{\mathbf{x}}\sin\phi_i - \hat{\mathbf{y}}\cos\phi_i$ and $\hat{\boldsymbol{\theta}}_i = \hat{\mathbf{x}}\cos\phi_i\cos\theta_i + \hat{\mathbf{y}}\sin\phi_i\cos\theta_i + \hat{\mathbf{z}}\sin\theta_i$ are defined according to Figure 2.1. Besides, in (2.1), the incident wave vector is $\vec{\mathbf{k}}_i = \beta_x\hat{\mathbf{x}} + \beta_y\hat{\mathbf{y}} - q\hat{\mathbf{z}}$ and the wave number is $\beta_0 = \omega\sqrt{\mu_0\epsilon_0}$, where $\beta_x = \beta_0\cos\phi_i\sin\theta_i$, $\beta_y = \beta_0\sin\phi_i\sin\theta_i$, and $q = \beta_0\cos\theta_i$.

Moreover, combining with Floquet's theorem, the general expression of the scattering field from a periodic surface seen in Figure 2.1 can be written as

$$\vec{\mathbf{E}}^s(x,y,z) = \hat{\mathbf{e}}_s \sum_{m=-\infty}^{\infty}\sum_{n=-\infty}^{\infty} e^{-j\beta_m x}e^{-j\beta_n y} f_{mn}(z) \tag{2.2}$$

At this point, we can talk about Rayleigh-based methods.

2.1.1 Rayleigh-Based Methods

Lord Rayleigh's assumption states that the scattering fields consist of the sum of up-and-down-going plane waves. Under the assumption of the Rayleigh hypothesis, subjecting the fields in (2.1) and (2.2) to homogeneous Helmholtz equation, $f_{mn}(z)$ and its coefficients for each Floquet mode can be found. After invoking the Rayleigh hypothesis, a general representation of the scattering field can be decomposed as vertical and horizontal fields

$$\vec{\mathbf{E}}^s(\vec{\mathbf{r}}) = \sum_{m=-\infty}^{\infty} \sum_{n=-\infty}^{\infty} \left(\hat{\mathbf{h}}_{mn} A_{mn} + \hat{\mathbf{v}}_{mn} B_{mn}\right) e^{-j\vec{\mathbf{k}}_s \cdot \vec{\mathbf{r}}} \tag{2.3}$$

where, $\hat{\mathbf{h}}_{mn}$ and $\hat{\mathbf{v}}_{mn}$ is the horizontal and vertical unit vector for each Floquet mode. On the other hand, the magnetic field intensity and the current density on the surface

$$\vec{\mathbf{H}}^s(\vec{\mathbf{r}}) = \frac{\hat{\mathbf{k}}_s \times \vec{\mathbf{E}}^s(\vec{\mathbf{r}})}{\eta_0} \tag{2.4}$$

can also be expressed as a plane wave. Thereby, the electric current density can be found on the rough surface as follows

$$\vec{\mathbf{J}}_s(\vec{\mathbf{r}}) = \hat{\mathbf{n}} \times \left[\vec{\mathbf{H}}^i(\vec{\mathbf{r}}) + \vec{\mathbf{H}}^s(\vec{\mathbf{r}})\right]\Big|_{\text{ on } S} \tag{2.5}$$

Here, the unit normal vector of the surface $\hat{\mathbf{n}}$ is

$$\begin{aligned} \hat{\mathbf{n}} = \frac{\nabla[z - \mathfrak{s}(x,y)]}{\|\nabla[z - \mathfrak{s}(x,y)]\|} &= \frac{\hat{z} - \hat{x}\frac{\partial \mathfrak{s}(x,y)}{\partial x} - \hat{y}\frac{\partial \mathfrak{s}(x,y)}{\partial y}}{\sqrt{1 + \frac{\partial^2 \mathfrak{s}(x,y)}{\partial x^2} + \frac{\partial^2 \mathfrak{s}(x,y)}{\partial y^2}}} \\ &= \frac{\hat{\mathbf{z}} - \hat{\mathbf{x}}\mathfrak{s}_x - \hat{\mathbf{y}}\mathfrak{s}_y}{\sqrt{1 + \mathfrak{s}_x^2 + \mathfrak{s}_y^2}} \end{aligned} \tag{2.6}$$

Then, the definitions of the unit vectors for scattered and incident waves are as follows

$$\hat{\mathbf{h}}_i = \frac{\vec{\mathbf{k}}_i \times \hat{\mathbf{z}}}{\left\|\vec{\mathbf{k}}_i \times \hat{\mathbf{z}}\right\|} \tag{2.7}$$

$$\hat{\mathbf{v}}_i = \vec{\mathbf{h}}_i \times \hat{\mathbf{k}}_i \tag{2.8}$$

Here, (2.7) and (2.8) are written for incident wave in (2.1), and

$$\hat{\mathbf{h}}_{mn} = \frac{\vec{\mathbf{k}}_s \times \hat{\mathbf{z}}}{\left\|\vec{\mathbf{k}}_s \times \hat{\mathbf{z}}\right\|} \tag{2.9}$$

$$\hat{\mathbf{v}}_{mn} = \vec{\mathbf{h}}_{mn} \times \hat{\mathbf{k}}_s \tag{2.10}$$

are stated for the scattered wave in (2.3). Also, the scattered wave vector

$$\hat{\mathbf{k}}_s = \hat{\mathbf{k}}_{mn} = \hat{\mathbf{x}}\beta_m + \hat{\mathbf{y}}\beta_n + \hat{\mathbf{z}}q_{mn} \tag{2.11}$$

can be defined in which through the Floquet's theorem

$$\beta_m = \beta_x + 2\pi m/L_x \tag{2.12}$$

$$\beta_n = \beta_y + 2\pi n/L_y \tag{2.13}$$

are defined, and also

$$\beta_{mn} = \sqrt{\beta_m^2 + \beta_n^2} \tag{2.14}$$

can be stated. Hence, the definition of q_{mn} is as follows

$$q_{mn} = \begin{cases} \sqrt{\beta_0^2 - \|\beta_{mn}\|^2} & \cdots \quad \beta_0 \geq \|\beta_{mn}\|^2 \\ -j\sqrt{\|\beta_{mn}\|^2 - \beta_0^2} & \cdots \quad \beta_0 < \|\beta_{mn}\|^2 \end{cases} \tag{2.15}$$

Furthermore, utilizing (2.9) and (2.10), the unit vectors are

$$\hat{\mathbf{h}}_{mn} = \frac{1}{\beta_{mn}}(\hat{x}\beta_n - \hat{y}\beta_m) \tag{2.16}$$

$$\hat{\mathbf{v}}_{mn} = -\hat{\mathbf{x}}\frac{\beta_m q_{mn}}{\beta_{mn}\beta_0} - \hat{\mathbf{y}}\frac{\beta_n q_{mn}}{\beta_{mn}\beta_0} + \hat{\mathbf{z}}\frac{\beta_{mn}}{\beta_0} \tag{2.17}$$

Now, after these basic definitions under Rayleigh hypothesis, we are ready to subject boundary conditions to (2.1) and (2.2)

$$\left(\hat{\mathbf{z}}-\hat{\mathbf{x}}\mathfrak{s}_x-\hat{\mathbf{y}}\mathfrak{s}_y\right)\times\left(\vec{\mathbf{E}}^i+\vec{\mathbf{E}}^s\right)\Big|_{z=\mathfrak{s}(x,y)}=0 \tag{2.18}$$

and substituting (2.1) and (2.2) in (2.18)

$$(\hat{\mathbf{z}}-\nabla_t\mathfrak{s})\times\left(\hat{\mathbf{e}}_i E_0 e^{-j\vec{\mathbf{k}}_i\cdot\vec{\mathbf{r}}}\right)=-(\hat{\mathbf{z}}-\nabla_t\mathfrak{s})\times\sum_{m,n=-\infty}^{\infty}\left(\hat{\mathbf{h}}_{mn}A_{mn}+\hat{\mathbf{v}}_{mn}B_{mn}\right)e^{-j\vec{\mathbf{k}}_s\cdot\vec{\mathbf{r}}}\Big|_{z=\mathfrak{s}(x,y)} \tag{2.19}$$

is obtained. Finally, employing simplifications

$$(\hat{\mathbf{z}}-\nabla_t\mathfrak{s})\times\left(\hat{\mathbf{e}}_i E_0 e^{jqf}\right)=-(\hat{\mathbf{z}}-\nabla_t\mathfrak{s})\times\sum_{m,n=-\infty}^{\infty}\left(\hat{\mathbf{h}}_{mn}A_{mn}+\hat{\mathbf{v}}_{mn}B_{mn}\right)e^{-jq_{mn}\mathfrak{s}}e^{j2\pi\left(mx/L_x+ny/L_y\right)} \tag{2.20}$$

is derived. Here, $\mathfrak{s}=\mathfrak{s}(x,y)$, and if $\mathfrak{s}$ is a periodic function

$$\mathfrak{s}(x,y)=\sum_{m=-\infty}^{\infty}\sum_{n=-\infty}^{\infty}C_{mn}e^{-j\frac{2\pi mx}{L_x}}e^{-j\frac{2\pi nx}{L_y}} \tag{2.21}$$

can be expanded with the Fourier series. Here, C_{mn} coefficients are defined as follows

$$C_{mn}=\frac{1}{L_xL_y}\int_0^{L_x}\int_0^{L_y}\mathfrak{s}(x,y)e^{j\frac{2\pi mx}{L_x}}e^{j\frac{2\pi nx}{L_y}}dxdy \tag{2.22}$$

(2.20) will be solved in two different analytical approaches in the next subsections. Expanding the Fourier series of the surface functions will be utilized.

2.1.1.1 Small Perturbation Method

A perturbation approach can be used to treat electromagnetic waves' dispersion from a slightly rough surface [1]. It is assumed that the surface fluctuations and rough surface slopes are much less than the incident wavelength. In order to convert the transmitted and reflected fields into upward- and downward-moving waves, the SPM applies the Rayleigh hypothesis. Following that, the boundary conditions are used to calculate the field amplitudes. In order to solve (2.20), A_{mn} and B_{mn} can be expanded

with perturbation theory

$$A_{mn} = \sum_{M=0}^{\infty} A_{mn}^{(M)}, \quad B_{mn} = \sum_{M=0}^{\infty} B_{mn}^{(M)} \tag{2.23}$$

and by using the Taylor series for exponential terms

$$e^{jq\mathfrak{s}} = \sum_{M=0}^{\infty} \frac{[jq\mathfrak{s}]^M}{M!}, \quad e^{-jq_{mn}\mathfrak{s}} = \sum_{M=0}^{\infty} \frac{[-jq_{mn}\mathfrak{s}]^M}{M!} \tag{2.24}$$

can be specified. The perturbation theory is comprised of expanding the exponential function whose power series assume that $q\mathfrak{s} \ll 1$. Now, if (2.20) is rearranged

$$\begin{aligned} &\nabla_t \mathfrak{s} \times \hat{\mathbf{e}}_i E_0 e^{jq\mathfrak{s}} + \sum_{m,n=-\infty}^{\infty} \left[\nabla_t \mathfrak{s} \times \hat{\mathbf{h}}_{mn} A_{mn} + \nabla_t \mathfrak{s} \times \hat{\mathbf{v}}_{mn} B_{mn}\right] e^{-jq_{mn}\mathfrak{s}} \\ &= \hat{\mathbf{z}} \times \hat{\mathbf{e}}_i E_0 e^{jq\mathfrak{s}} + \sum_{m,n=-\infty}^{\infty} \left[\hat{\mathbf{z}} \times \hat{\mathbf{h}}_{mn} A_{mn} + \hat{\mathbf{z}} \times \hat{\mathbf{v}}_{mn} B_{mn}\right] e^{-jq_{mn}\mathfrak{s}} \end{aligned} \tag{2.25}$$

We will use only x and y components to solve A_{mn} and B_{mn} coefficients, and the unit vectors products can be rewritten to simplify (2.25)

$$\nabla_t \mathfrak{s} \times \hat{\mathbf{h}}_{mn} = \cdots \hat{\mathbf{z}} \tag{2.26}$$

$$\hat{z} \times \hat{\mathbf{v}}_{mn} = \frac{q_{mn}}{\beta_0} \hat{\mathbf{h}}_{mn} \tag{2.27}$$

$$\nabla_t \mathfrak{s} \times \hat{\mathbf{v}}_{mn} = [\nabla_t \mathfrak{s} \times \hat{\mathbf{z}}] \frac{\beta_{mn}}{\beta_0} \tag{2.28}$$

using (2.26) and (2.27) in (2.25)

$$\begin{aligned} &\nabla_t \mathfrak{s} \times \hat{\mathbf{e}}_i E_0 e^{jq\mathfrak{s}} + \sum_{m,n=-\infty}^{\infty} [\nabla_t \mathfrak{s} \times \hat{\mathbf{v}}_{mn} B_{mn}] e^{-jq_{mn}\mathfrak{s}} \\ &= \hat{\mathbf{z}} \times \hat{\mathbf{e}}_i E_0 e^{jq\mathfrak{s}} + \sum_{m,n=-\infty}^{\infty} \left[\hat{\mathbf{z}} \times \hat{\mathbf{h}}_{mn} A_{mn} + \frac{q_{mn}}{\beta_0} \hat{\mathbf{h}}_{mn} B_{mn}\right] e^{-jq_{mn}\mathfrak{s}} \end{aligned} \tag{2.29}$$

and it is simplified again by using (2.28)

$$\sum_{m,n=-\infty}^{\infty} e^{-j\frac{2\pi mx}{L_x}} e^{-j\frac{2\pi nx}{L_y}} e^{-jq_{mn}\mathfrak{s}} \left[\hat{\mathbf{z}} \times \hat{\mathbf{h}}_{mn} A_{mn} + \frac{q_{mn}}{\beta_0} \hat{\mathbf{h}}_{mn} B_{mn} \right] = -\hat{\mathbf{z}} \times \hat{\mathbf{e}}_i E_0 e^{jq\mathfrak{s}}$$
$$+ [\nabla_t \mathfrak{s} \times \hat{\mathbf{e}}_i] E_0 e^{jq\mathfrak{s}} + \sum_{m,n=-\infty}^{\infty} e^{-j\frac{2\pi mx}{L_x}} e^{-j\frac{2\pi nx}{L_y}} e^{-jq_{mn}\mathfrak{s}} [\nabla_t \mathfrak{s} \times \hat{\mathbf{z}}] \frac{\beta_{mn}}{\beta_0} B_{mn} \tag{2.30}$$

and lastly applying (2.23) and (2.24), an iterative solution is obtained for arbitrary-order SPM [7]

$$\sum_{m,n=-\infty}^{\infty} e^{-j\frac{2\pi mx}{L_x}} e^{-j\frac{2\pi nx}{L_y}} \left[\hat{\mathbf{z}} \times \hat{\mathbf{h}}_{mn} A_{mn}^{(M)} + \hat{\mathbf{h}}_{mn} \frac{q_{mn}}{\beta_0} B_{mn}^{(M)} \right] = S^{(M)}(x,y)$$
$$= -(\hat{\mathbf{z}} \times \hat{\mathbf{e}}_i) E_0 \frac{(jq\mathfrak{s})^{(M)}}{M!} + [\nabla_t \mathfrak{s} \times \hat{\mathbf{e}}_i] E_0 \frac{(jq\mathfrak{s})^{(M-1)}}{(M-1)!}$$
$$- \sum_{l=0}^{M-1} \frac{(-j\mathfrak{s})^{M-l}}{(M-l)!} \left[\sum_{m,n=-\infty}^{\infty} e^{-j\frac{2\pi mx}{L_x}} e^{-j\frac{2\pi nx}{L_y}} \left[\hat{\mathbf{z}} \times \hat{\mathbf{h}}_{mn} A_{mn}^{(l)} q_{mn}^{M-l} + \frac{q_{mn}}{\beta_0} \hat{\mathbf{h}}_{mn} B_{mn}^{(l)} q_{mn}^{M-l} \right] \right] \tag{2.31}$$
$$+ \sum_{l=0}^{M-1} \frac{(-j\mathfrak{s})^{M-l-1}}{(M-l-1)!} \left[\sum_{m,n=-\infty}^{\infty} e^{-j\frac{2\pi mx}{L_x}} e^{-j\frac{2\pi nx}{L_y}} \left[\nabla_t \mathfrak{s} \times \hat{\mathbf{z}} \frac{\beta_{mn}}{\beta_0} B_{mn}^{(l)} q_{mn}^{M-l-1} \right] \right]$$

Eventually, to find A_{mn} and B_{mn} for order M, an iterative solution is employed as follows

$$A_{m'n'}^{(M)} = \left(\hat{\mathbf{z}} \times \hat{\mathbf{h}}_{m'n'} \right) \cdot \mathscr{F} \left[S^{(M)}(x,y) \right]_{m'n'} \tag{2.32}$$

$$\frac{q_{mn}}{\beta_0} B_{m'n'}^{(M)} = \hat{\mathbf{h}}_{m'n'} \cdot \mathscr{F} \left[S^{(M)}(x,y) \right]_{m'n'} \tag{2.33}$$

where, $\mathscr{F}$ specifies the Fourier transform. The surface function $\mathfrak{s}$ should be expanded to the Fourier series. These coefficients are solved in MATLAB software with Symbolic Math Toolbox.

2.1.1.2 Floquet Mode-Matching Method

Another analytical approach is the FMMM. Assume that the polarization vector of the incident wave

$$\hat{\mathbf{e}}_i = \hat{\mathbf{x}} e_x + \hat{\mathbf{y}} e_y + \hat{\mathbf{z}} e_z \tag{2.34}$$

Before applying FMMM to (2.20), some unit vector products should be carried out for simplification

$$(\hat{\mathbf{z}}-\nabla_t \mathfrak{s})\times\hat{\mathbf{e}}_i=-\hat{\mathbf{x}}\left(\mathfrak{s}_y e_z+e_y\right)+\hat{\mathbf{y}}\left(e_x+\mathfrak{s}_x e_z\right)+\hat{\mathbf{z}}\left(\mathfrak{s}_y e_x-\mathfrak{s}_x e_y\right) \tag{2.35}$$

$$(\hat{\mathbf{z}}-\nabla_t \mathfrak{s})\times\hat{\mathbf{h}}_{mn}=\hat{\mathbf{x}}\frac{\beta_m}{\beta_{mn}}+\hat{\mathbf{y}}\frac{\beta_n}{\beta_{mn}}+\hat{\mathbf{z}}\left(\mathfrak{s}_x\frac{\beta_m}{\beta_{mn}}+\mathfrak{s}_y\frac{\beta_n}{\beta_{mn}}\right) \tag{2.36}$$

$$\begin{aligned}(\hat{\mathbf{z}}-\nabla_t \mathfrak{s})\times\hat{\mathbf{v}}_{mn}=&-\hat{\mathbf{x}}\left(\mathfrak{s}_y\frac{\beta_{mn}}{\beta_0}-\frac{\beta_n q_{mn}}{\beta_{mn}\beta_0}\right)-\hat{\mathbf{y}}\left(\frac{\beta_m q_{mn}}{\beta_{mn}\beta_0}-\mathfrak{s}_x\frac{\beta_{mn}}{\beta_0}\right)\\&+\hat{\mathbf{z}}\left(\mathfrak{s}_x\frac{\beta_n q_{mn}}{\beta_{mn}\beta_0}-\mathfrak{s}_y\frac{\beta_m q_{mn}}{\beta_{mn}\beta_0}\right)\end{aligned} \tag{2.37}$$

Using (2.20) with (2.35), (2.36), and (2.37), the solution of this linear equation system can be obtained with only two vector components with Galerkin method, so the x-component of the system

$$\begin{aligned}\left[A_{mn}\frac{\beta_m}{\beta_{mn}}+B_{mn}\left(\frac{\beta_n q_{mn}}{\beta_{mn}\beta_0}-\mathfrak{s}_y\frac{\beta_{mn}}{\beta_0}\right)\right]e^{-jq_{mn}\mathfrak{s}}e^{j2\pi\left[(u-m)x/L_x+(v-n)y/L_y\right]}&\\=\left(\mathfrak{s}_y e_z+e_y\right)e^{jq\mathfrak{s}}e^{j2\pi\left[ux/L_x+vy/L_y\right]}&\end{aligned} \tag{2.38}$$

and y-component of the system

$$\begin{aligned}\left[A_{mn}\frac{\beta_n}{\beta_{mn}}+B_{mn}\left(\mathfrak{s}_x\frac{\beta_{mn}}{\beta_0}-\frac{\beta_m q_{mn}}{\beta_{mn}\beta_0}\right)\right]e^{-jq_{mn}\mathfrak{s}}e^{j2\pi\left[(u-m)x/L_x+(v-n)y/L_y\right]}&\\=-\left(\mathfrak{s}_x e_z+e_x\right)e^{jq\mathfrak{s}}e^{j2\pi\left[ux/L_x+vy/L_y\right]}&\end{aligned} \tag{2.39}$$

Here, $K\in\mathbb{C}^{u\times v\times m\times n\times 2\times 2}$, $X\in\mathbb{C}^{m\times n\times 2\times 1}$, and $L\in\mathbb{C}^{u\times v\times 2\times 1}$ are tensors, and they can be turned a matrix form. Thus, the solution of (2.38) and (2.39) in the form of

$$KX=L \tag{2.40}$$

where $\overline{\overline{\mathbf{K}}}$ matrices

$$\overline{\overline{\mathbf{K}}}_{11}=\frac{1}{L_x L_y}\int_0^{L_x}\int_0^{L_y}\frac{\beta_m}{\beta_{mn}}e^{-jq_{mn}\mathfrak{s}}e^{j2\pi\left[(u-m)x/L_x+(v-n)y/L_y\right]}dxdy \tag{2.41}$$

$$\bar{\bar{\mathbf{K}}}_{12} = \frac{1}{L_x L_y}\int_0^{L_x}\int_0^{L_y}\left(\frac{\beta_n q_{mn}}{\beta_{mn}\beta_0} - \mathfrak{s}_y\frac{\beta_{mn}}{\beta_0}\right)e^{-jq_{mn}\mathfrak{s}}e^{j2\pi\left[(u-m)x/L_x+(v-n)y/L_y\right]}dxdy \quad (2.42)$$

$$\bar{\bar{\mathbf{K}}}_{21} = \frac{1}{L_x L_y}\int_0^{L_x}\int_0^{L_y}\frac{\beta_n}{\beta_{mn}}e^{-jq_{mn}\mathfrak{s}}e^{j2\pi\left[(u-m)x/L_x+(v-n)y/L_y\right]}dxdy \quad (2.43)$$

$$\bar{\bar{\mathbf{K}}}_{22} = \frac{1}{L_x L_y}\int_0^{L_x}\int_0^{L_y}\left(\mathfrak{s}_x\frac{\beta_{mn}}{\beta_0} - \frac{\beta_m q_{mn}}{\beta_{mn}\beta_0}\right)e^{-jq_{mn}\mathfrak{s}}e^{j2\pi\left[(u-m)x/L_x+(v-n)y/L_y\right]}dxdy \quad (2.44)$$

and $\bar{\bar{\mathbf{L}}}$ matrices

$$\bar{\bar{\mathbf{L}}}_{11} = \frac{1}{L_x L_y}\int_0^{L_x}\int_0^{L_y}\left(\mathfrak{s}_y e_z + e_y\right)e^{jq\mathfrak{s}}e^{j2\pi\left[ux/L_x+vy/L_y\right]}dxdy \quad (2.45)$$

$$\bar{\bar{\mathbf{L}}}_{21} = -\frac{1}{L_x L_y}\int_0^{L_x}\int_0^{L_y}\left(e_x + \mathfrak{s}_x e_z\right)e^{jq\mathfrak{s}}e^{j2\pi\left[ux/L_x+vy/L_y\right]}dxdy \quad (2.46)$$

are derived. Consequently, these matrices are written in the form below, and the solution is obtained

$$\begin{bmatrix}\bar{\bar{\mathbf{K}}}_{11} & \bar{\bar{\mathbf{K}}}_{12}\\ \bar{\bar{\mathbf{K}}}_{21} & \bar{\bar{\mathbf{K}}}_{22}\end{bmatrix}\begin{bmatrix}\bar{\bar{\mathbf{A}}}^{(mn)}\\ \bar{\bar{\mathbf{B}}}^{(mn)}\end{bmatrix} = \begin{bmatrix}\bar{\bar{\mathbf{L}}}_{11}\\ \bar{\bar{\mathbf{L}}}_{21}\end{bmatrix} \quad (2.47)$$

Here, each integrand can be solved numerically. Thus, this linear equation system presents a semi-analytical solution. However, if the rough surface is chosen as a sinusoidal function, as follows

$$z = \mathfrak{s}(x,y) = -h\left[cos\left(\frac{2\pi x}{L_x}\right) + cos\left(\frac{2\pi y}{L_y}\right)\right] \quad (2.48)$$

The solution of the FMMM can be obtained by utilizing Bessel functions for sinusoidal surfaces. Here, Bessel identities are employed for this purpose

$$J_n(x) = \frac{1}{2\pi}\int_0^{2\pi}e^{-jn\theta}e^{jxsin\theta}d\theta \quad (2.49)$$

$$J_{-n}(x) = (-1)^n J_n(x) \quad (2.50)$$

Using Bessel's identities $\bar{\bar{\mathbf{K}}}$ matrices can be formed as follows

$$\bar{\bar{\mathbf{K}}}_{11} = \frac{\beta_m}{\beta_{mn}} (j)^{|u-m|} (j)^{|v-n|} J_{|u-m|}(q_{mn}h) J_{|v-n|}(q_{mn}h) \tag{2.51}$$

$$\begin{aligned}\bar{\bar{\mathbf{K}}}_{12} = -\frac{\beta_{mn}}{\beta_0}\frac{h\pi}{L_y} (j)^{|u-m|} J_{|u-m|}(q_{mn}h)\left[(j)^{|v-n|} J_{|v-n+1|}(q_{mn}h) + (j)^{|v-n|} J_{|v-n-1|}(q_{mn}h)\right] \\ + \frac{\beta_n q_{mn}}{\beta_{mn}\beta_0} (j)^{|u-m|} (j)^{|v-n|} J_{|u-m|}(q_{mn}h) J_{|v-n|}(q_{mn}h)\end{aligned} \tag{2.52}$$

$$\bar{\bar{\mathbf{K}}}_{21} = \frac{\beta_n}{\beta_{mn}} (j)^{|u-m|} (j)^{|v-n|} J_{|u-m|}(q_{mn}h) J_{|v-n|}(q_{mn}h) \tag{2.53}$$

$$\begin{aligned}\bar{\bar{\mathbf{K}}}_{22} = \frac{\beta_{mn}}{\beta_0}\frac{h\pi}{L_X} (j)^{|v-n|} J_{|v-n|}(q_{mn}h)\left[(j)^{|u-m|} J_{|u-m+1|}(q_{mn}h) + (j)^{|u-m|} J_{|u-m-1|}(q_{mn}h)\right] \\ - \frac{\beta_m q_{mn}}{\beta_{mn}\beta_0} (j)^{|u-m|} (j)^{|v-n|} J_{|u-m|}(q_{mn}h) J_{|v-n|}(q_{mn}h)\end{aligned} \tag{2.54}$$

and $\bar{\bar{\mathbf{L}}}$ matrices

$$\begin{aligned}\bar{\bar{\mathbf{L}}}_{11} = \frac{e_z h}{L_y} (-j)^{|u|} J_{|u|}(qh)\left[(-j)^{|v|} J_{|v+1|}(qh) + (-j)^{|v|} J_{|v-1|}(qh)\right] \\ + e_y (-j)^{|u|} (-j)^{|v|} J_{|u|}(qh) J_{|v|}(qh)\end{aligned} \tag{2.55}$$

$$\begin{aligned}\bar{\bar{\mathbf{L}}}_{21} = \frac{e_z h}{L_x} (-j)^{|v|} J_{|v|}(qh)\left[(-j)^{|u|} J_{|u+1|}(qh) + (-j)^{|u|} J_{|u-1|}(qh)\right] \\ - e_x (-j)^{|u|} (-j)^{|v|} J_{|u|}(qh) J_{|v|}(qh)\end{aligned} \tag{2.56}$$

are derived. Thus, these matrices are written in the form in (2.47), and the solution is obtained analytically.

2.1.2 EFIE-MoM Solution

The Rayleigh assumption, as mentioned in earlier studies, will not be valid on the boundary of the surface as the result of the singularity [76]. Hence, the surface gradient should be smaller than 0.448, and the assumption is only valid for a slightly rough shallow surface [8]. It should be noted that the field expression given in (2.2) is not a regular function in all domains, i.e., it cannot differentiate in a classical sense on the boundary. The solution can be obtained with boundary integrals on the surface, therefore, using boundary condition on the periodic PEC surface in Figure 2.1

$$\hat{\mathbf{n}} \times \left[\vec{\mathbf{E}}^{i} + \vec{\mathbf{E}}^{s}\left(\vec{\mathbf{J}}_{U}\right)\right]\Big|_{\text{on } S_U} = 0 \tag{2.57}$$

is obtained. Here, $\hat{\mathbf{n}}$ is the unit normal vector of the surface, and the IE of the scattered electric field $\vec{\mathbf{E}}^{s}\left(\vec{\mathbf{J}}_{U}\right)$ can be written in dyadic representation

$$\vec{\mathbf{E}}^{s}\left(\vec{\mathbf{J}}_{U}\right) = -j\omega\mu_0 \int_{S'_U} \left[\bar{\bar{\mathbf{I}}} + \frac{1}{\beta_0^2}\nabla\nabla\right] G_p\left(\vec{\mathbf{r}}|\vec{\mathbf{r}}'\right) \cdot \vec{\mathbf{J}}_{U}\left(\vec{\mathbf{r}}'\right) dS'_U \tag{2.58}$$

Here, $\vec{\mathbf{J}}_U$ denotes the current density on the unit cell of the periodic surface, G_p is doubly periodic free-space Green's function, and S'_U implies the surface domain in the unit cell. $\bar{\bar{\mathbf{I}}} = \hat{\mathbf{x}}\hat{\mathbf{x}} + \hat{\mathbf{y}}\hat{\mathbf{y}} + \hat{\mathbf{z}}\hat{\mathbf{z}}$ is the unit dyad. The currents on the periodic surface in the other unit cells may be written in terms of the current on the center unit cell as follows

$$\vec{\mathbf{J}}_1\left(x' + mL_x, y' + nL_y, z'\right) = e^{-j\beta_x mL_x} e^{-j\beta_y nL_y} \vec{\mathbf{J}}_U\left(x', y', z'\right) \tag{2.59}$$

According to (2.59), the currents outside the center unit cell can be found by adding a phase difference to the current in a unit cell, and the added phase is in proportion to the size of the lattice, the number m and n represented the (m, n)-th cell and phase constants in x and y coordinates. Using this current source approach combined with Floquet's theorem, the PGF is derived from periodically spreading point charges in the $x - y$ plane in a lattice. However, the PGF can alternatively be obtained from free-space Green's function (spatial form) [60]

$$G_p^{spatial}\left(\vec{\mathbf{r}}|\vec{\mathbf{r}}'\right) = \frac{1}{4\pi} \sum_{m=-\infty}^{\infty} \sum_{n=-\infty}^{\infty} e^{-j\beta_x mL_x} e^{-j\beta_y nL_y} \frac{e^{-j\beta_0 R_{mn}}}{R_{mn}} \tag{2.60}$$

and Poisson's transform is applied to find the spectral form of (2.60) as reported in [59]

$$G_p^{spectral}\left(\vec{\mathbf{r}}|\vec{\mathbf{r}}'\right) = -\frac{j}{2L_x L_y} \sum_{m=-\infty}^{\infty} \sum_{n=-\infty}^{\infty} \frac{e^{-j\beta_m\left(x-x'\right)} e^{-j\beta_n\left(y-y'\right)} e^{-jq_{mn}\left|z-z'\right|}}{q_{mn}} \tag{2.61}$$

where R_{mn}

$$R_{mn} = \left\|\vec{\mathbf{r}} - \vec{\mathbf{r}}'_{mn}\right\| = \sqrt{\left(x - x' - mL_x\right)^2 + \left(y - y' - nL_y\right)^2 + \left(z - z'\right)^2} \tag{2.62}$$

Here, $\vec{\mathbf{r}}$ is the observation point, $\vec{\mathbf{r}}'_{mn}$ is the source point in the (m,n)-th cell. The total field consists of the reflected field (coherent field) as a specular reflection on a smooth surface in case of $m=0$, $n=0$, and the scattering field as an incoherent field from the surface roughness in case of any other m and n. The coherent field will decrease due to the roughness leading to the distribution of the scattering field in all directions.

The IE method, in combination with the MoM, is a rigorous and effective treatment for the scattering problems from rough surfaces. Before applying the MoM, equations (2.58) and (2.1) are substituted in (2.57), and the EFIE is obtained by using boundary condition on the tangential electric field as follows

$$\left[\hat{\mathbf{e}}_i E_0 e^{-j\vec{\mathbf{k}}_i.\vec{\mathbf{r}}}\right]_{\tan} = \left[j\omega\mu_0 \int_{S'_U} \left[\bar{\bar{\mathbf{I}}} + \frac{1}{\beta_0^2}\nabla\nabla\right] G_p\left(\vec{\mathbf{r}}|\vec{\mathbf{r}}'\right)\cdot\vec{\mathbf{J}}_U\left(\vec{\mathbf{r}}'\right) dS'_U \right]_{\tan} \tag{2.63}$$

Now, the equation (2.63) can be converted into a linear system by employing the MoM

$$\bar{\bar{\mathbf{Z}}}_{(\zeta\psi)}\bar{\mathbf{I}}_{(\psi)} = \bar{\mathbf{V}}_{(\zeta)} \tag{2.64}$$

where

$$Z_{(\zeta\psi)} = j\beta_0\eta_0 \left[\int_{T_\zeta^\pm}\int_{T_\psi^\pm} \vec{\mathbf{f}}_\zeta(\vec{\mathbf{r}})\cdot\vec{\mathbf{f}}_\psi\left(\vec{\mathbf{r}}'\right) G_p\left(\vec{\mathbf{r}}|\vec{\mathbf{r}}'\right) dS_{T_\psi^\pm} dS_{T_\zeta^\pm} - \frac{1}{\beta_0^2}\int_{T_\zeta^\pm}\int_{T_\psi^\pm} \left[\nabla_s\cdot\vec{\mathbf{f}}_\zeta(\vec{\mathbf{r}})\right]\left[\nabla'_s\cdot\vec{\mathbf{f}}_\psi\left(\vec{\mathbf{r}}'\right)\right] G_p\left(\vec{\mathbf{r}}|\vec{\mathbf{r}}'\right) dS_{T_\psi^\pm} dS_{T_\zeta^\pm} \right] \tag{2.65}$$

and

$$V_{(\zeta)} = \int_{T_\zeta^\pm} \vec{\mathbf{f}}_\zeta(\vec{\mathbf{r}})\cdot\vec{\mathbf{E}}^i dS_{T_\zeta^\pm} \tag{2.66}$$

where $\vec{\mathbf{f}}_\zeta(\vec{\mathbf{r}})$ and $\vec{\mathbf{f}}_\psi(\vec{\mathbf{r}}')$ are testing and basis functions, respectively. The induced current density $\vec{\mathbf{J}}_U = \sum_{\psi=1}^{N} I_\psi \vec{\mathbf{f}}_\psi(\vec{\mathbf{r}}')$ has expanded a set of basis functions, and triangular elements are used to discretize the PEC surface. The basis and testing functions are applied to the edges of triangles on the surface. Considering the unit

cell of a periodic surface, well-known RWG basis functions are employed [77] and demonstrated in Figure 2.2 for inner edges. Here, l_ψ indicates the edge length on the discretized surface. T_ψ^+ and T_ψ^- are the plus and minus triangles intersecting this common edge. A_ψ^+ and A_ψ^- imply the areas of these triangles, respectively. $\vec{\mathbf{v}}_\psi^+$ and $\vec{\mathbf{v}}_\psi^-$ are the free vertices vectors of these triangles and will be used to define the surface current. As seen in Figure 2.2, the surface current is defined with red-colored arrow lines. The current direction is $\vec{\mathbf{r}}'-\vec{\mathbf{v}}_\psi^-$ for the T_ψ^- triangle and $\vec{\mathbf{v}}_\psi^+-\vec{\mathbf{r}}'$ for the T_ψ^+ triangle. It should also be noted that the RWG basis function is a first-order or linear basis function, and divergence conforming [78].

Additionally, in order to ensure continuity of the current between the boundaries of unit cells, a special basis and testing functions will be utilized. For this purpose, RWG basis and testing functions will be modified to be added phase shifts with the lengths of the lattice for each boundary edge. As a result, three different basis and testing functions are needed to calculate the surface current accurately. The basis and testing functions can be given in more detail at this point.

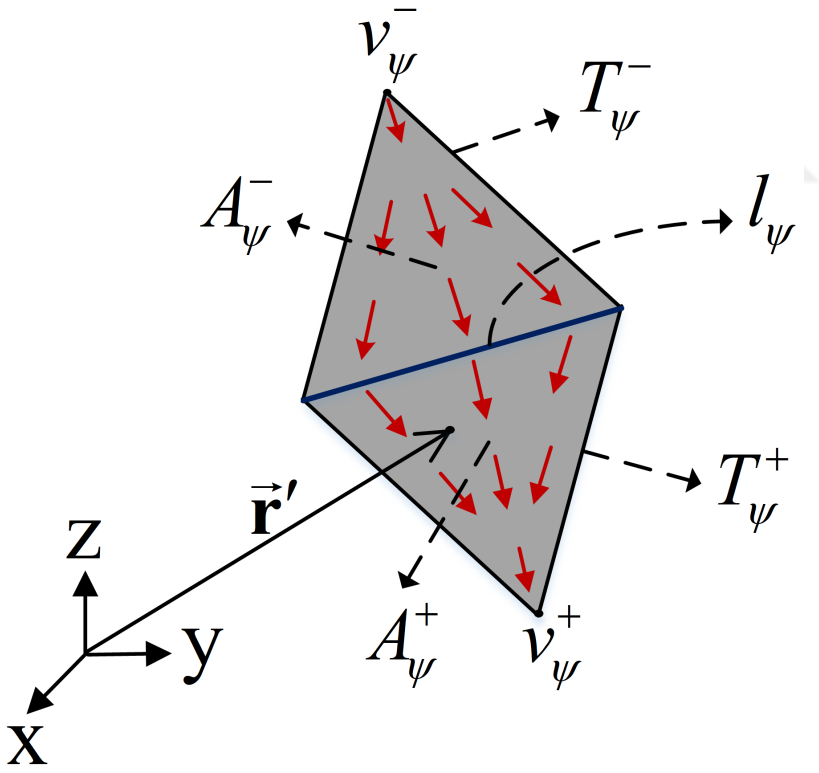

Figure 2.2 Representation of RWG basis function

2.1.2.1 Basis and Testing Functions for a Periodic Unit Cell

The infinite periodic surface can be modeled to be restricted to a unit cell by means of the PGF so that all calculations are performed within the unit cell, as seen in the

highlighted area of Figure 2.1. The top view of a sample of the periodic surface's mesh structure is given in Figure 2.3 to determine proper edges and triangular element pairs. The first type of basis and testing functions are based on a conventional RWG basis for the inner edges [77]

$$\vec{\mathbf{f}}_{\psi}^{(1)}(\vec{\mathbf{r}}') = \begin{cases} \vec{\boldsymbol{\rho}}_{\psi}^{+}(\vec{\mathbf{r}}')\frac{l_{\psi}}{2A_{\psi}^{1+}}, & \vec{\mathbf{r}}' \in T_1^+ \\ \vec{\boldsymbol{\rho}}_{\psi}^{-}(\vec{\mathbf{r}}')\frac{l_{\psi}}{2A_{\psi}^{1-}}, & \vec{\mathbf{r}}' \in T_1^- \\ 0, & \text{otherwise.} \end{cases} \tag{2.67}$$

$$\vec{\mathbf{f}}_{\zeta}^{(1)}(\vec{\mathbf{r}}) = \begin{cases} \vec{\boldsymbol{\rho}}_{\zeta}^{+}(\vec{\mathbf{r}})\frac{l_{\zeta}}{2A_{\zeta}^{1+}}, & \vec{\mathbf{r}} \in T_1^+ \\ \vec{\boldsymbol{\rho}}_{\zeta}^{-}(\vec{\mathbf{r}})\frac{l_{\zeta}}{2A_{\zeta}^{1-}}, & \vec{\mathbf{r}} \in T_1^- \\ 0, & \text{otherwise.} \end{cases} \tag{2.68}$$

The second type basis and testing functions are defined for the horizontal boundary edges [64, 75]

$$\vec{\mathbf{f}}_{\psi}^{(2)}(\vec{r}') = \begin{cases} \vec{\boldsymbol{\rho}}_{\psi}^{+}(\vec{\mathbf{r}}')\frac{l_{\psi}}{2A_{\psi}^{2+}}e^{-j\vec{\mathbf{k}}\cdot\vec{\mathbf{a}}_1}, & \vec{\mathbf{r}}' \in T_2^+ \\ \vec{\boldsymbol{\rho}}_{\psi}^{-}(\vec{\mathbf{r}}')\frac{l_{\psi}}{2A_{\psi}^{2-}}, & \vec{\mathbf{r}}' \in T_2^- \\ 0, & \text{otherwise.} \end{cases} \tag{2.69}$$

$$\vec{\mathbf{f}}_{\zeta}^{(2)}(\vec{\mathbf{r}}) = \begin{cases} \vec{\boldsymbol{\rho}}_{\zeta}^{+}(\vec{\mathbf{r}})\frac{l_{\zeta}}{2A_{\zeta}^{2+}}e^{j\vec{\mathbf{k}}\cdot\vec{\mathbf{a}}_1}, & \vec{\mathbf{r}} \in T_2^+ \\ \vec{\boldsymbol{\rho}}_{\zeta}^{-}(\vec{\mathbf{r}})\frac{l_{\zeta}}{2A_{\zeta}^{2-}}, & \vec{\mathbf{r}} \in T_2^- \\ 0, & \text{otherwise.} \end{cases} \tag{2.70}$$

Also, the third type basis and testing functions are defined for the vertical boundary edges [64, 75]

$$\vec{\mathbf{f}}_{\psi}^{(3)}(\vec{\mathbf{r}}') = \begin{cases} \vec{\boldsymbol{\rho}}_{\psi}^{+}(\vec{\mathbf{r}}')\frac{l_{\psi}}{2A_{\psi}^{3+}}e^{-j\vec{\mathbf{k}}\cdot\vec{\mathbf{a}}_2}, & \vec{\mathbf{r}}' \in T_3^+ \\ \vec{\boldsymbol{\rho}}_{\psi}^{-}(\vec{\mathbf{r}}')\frac{l_{\psi}}{2A_{\psi}^{3-}}, & \vec{\mathbf{r}}' \in T_3^- \\ 0, & \text{otherwise.} \end{cases} \tag{2.71}$$

$$\vec{\mathbf{f}}_{\zeta}^{(3)}(\vec{\mathbf{r}}) = \begin{cases} \vec{\boldsymbol{\rho}}_{\zeta}^{+}(\vec{\mathbf{r}})\frac{l_{\zeta}}{2A_{\zeta}^{3+}}e^{j\vec{\mathbf{k}}\cdot\vec{\mathbf{a}}_2}, & \vec{\mathbf{r}} \in T_3^+ \\ \vec{\boldsymbol{\rho}}_{\zeta}^{-}(\vec{\mathbf{r}})\frac{l_{\zeta}}{2A_{\zeta}^{3-}}, & \vec{\mathbf{r}} \in T_3^- \\ 0, & \text{otherwise.} \end{cases} \tag{2.72}$$

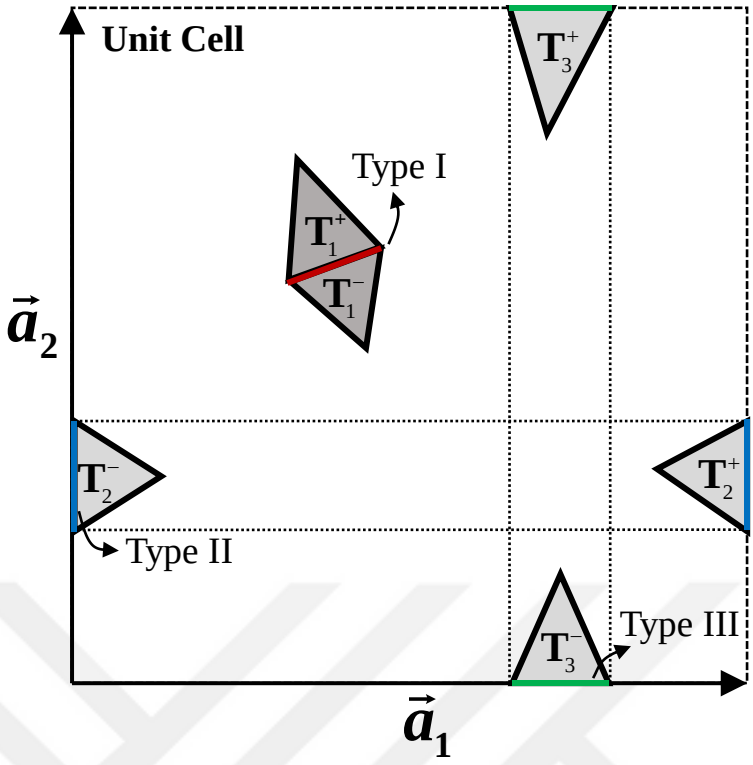

Figure 2.3 Inner and boundary edges forming three different basis and testing functions

where $\vec{\mathbf{a}}_{(1,2)}$ are the lattice's translation vectors for the second and third type basis and testing functions, respectively. The basis and testing functions are defined separately on the plus and minus triangles of the shared edge. Thus, l_ψ is the length of the ψ-th edge, and

$$\vec{\boldsymbol{\rho}}_\psi^+ = \vec{\mathbf{v}}_\psi^+ - \vec{\mathbf{r}}' \tag{2.73}$$

$$\vec{\boldsymbol{\rho}}_\psi^- = \vec{\mathbf{r}}' - \vec{\mathbf{v}}_\psi^- \tag{2.74}$$

are stated. As in Figure 2.2, T_ψ^+ and T_ψ^- are the triangles of this common edge. Also, $\vec{\mathbf{v}}_\psi^\pm$ are the vectors that indicate free-vertices of the triangles. These expressions can be written similarly for the testing function. By substituting the findings above in (2.65), the resulting integrals can be solved by numerical quadrature [78–80]. The unknown current constants are found for each edge. The edges of boundaries are also periodic; hence it is sufficient to find the related unknowns on only one side of the boundaries. Furthermore, ∇_s is the surface del operator, and

$$\nabla_s \cdot \vec{\boldsymbol{\rho}}_\zeta^+(\vec{\mathbf{r}}) = -\frac{l_\zeta}{A_\zeta^+} \tag{2.75}$$

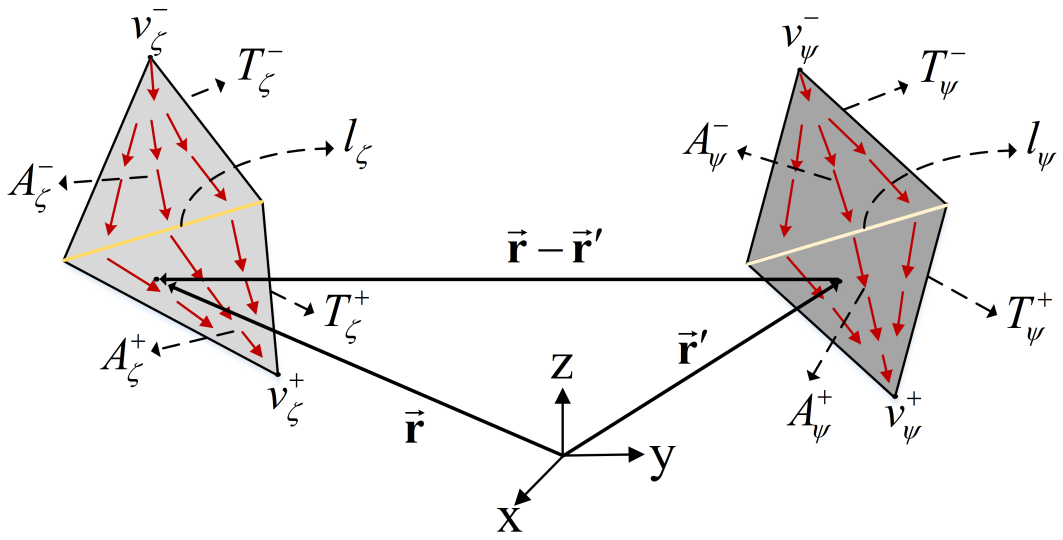

Figure 2.4 Demonstration of RWG basis and testing function for testing and basis edges

$$\nabla_s \cdot \vec{\boldsymbol{\rho}}_\zeta^-(\vec{\mathbf{r}}) = \frac{l_\zeta}{A_\zeta^-} \tag{2.76}$$

also,

$$\nabla_s' \cdot \vec{\boldsymbol{\rho}}_\psi^+(\vec{\mathbf{r}}) = -\frac{l_\psi}{A_\psi^+} \tag{2.77}$$

$$\nabla_s' \cdot \vec{\boldsymbol{\rho}}_\psi^-(\vec{\mathbf{r}}') = \frac{l_\psi}{A_\psi^-} \tag{2.78}$$

are found. Moreover, the derivation of (2.65) will not give in this thesis, so it has been discussed in detail in [78, 80]. However, it would be helpful for a reader to share a short representation for the calculation of a general $Z_{(\zeta\psi)}$ as given in (2.65). As seen in Figure 2.4, the total $Z_{(\zeta\psi)}$ should be the sum of the calculation of the integrals on the minus and plus triangles for the testing and basis edges

$$Z_{\zeta\psi} = Z_{\zeta\psi}^{--} + Z_{\zeta\psi}^{+-} + Z_{\zeta\psi}^{-+} + Z_{\zeta\psi}^{++} \tag{2.79}$$

The superscripts $(+)$ and $(-)$ indicate the plus and minus triangles, respectively. These terms can be written on the plus and minus triangles in 2.79. Now, substituting (2.67), (2.68), (2.76), and (2.78) in (2.80) for the inner edges, $Z_{\zeta\psi}^{--}$ term can be stated as follows

$$Z_{\zeta\psi}^{--} = j\beta_0\eta_0 \left[\frac{l_\zeta l_\psi}{4A_\zeta^- A_\psi^-} \int_{T_\zeta^-} \int_{T_\psi^-} \vec{\boldsymbol{\rho}}_\zeta^{\,-}(\vec{\mathbf{r}}) \cdot \vec{\boldsymbol{\rho}}_\psi^{\,-}(\vec{\mathbf{r}}') G_p(\vec{\mathbf{r}}|\vec{\mathbf{r}}') dS_{T_\psi^-} dS_{T_\zeta^-} \right.$$
$$\left. - \frac{1}{\beta_0^2} \frac{l_\zeta l_\psi}{A_\zeta^- A_\psi^-} \int_{T_\zeta^-} \int_{T_\psi^-} G_p(\vec{\mathbf{r}}|\vec{\mathbf{r}}') dS_{T_\psi^-} dS_{T_\zeta^-} \right] \quad (2.80)$$

with a similar way

$$Z_{\zeta\psi}^{+-} = j\beta_0\eta_0 \left[\frac{l_\zeta l_\psi}{4A_\zeta^+ A_\psi^-} \int_{T_\zeta^+} \int_{T_\psi^-} \vec{\boldsymbol{\rho}}_\zeta^{\,+}(\vec{\mathbf{r}}) \cdot \vec{\boldsymbol{\rho}}_\psi^{\,-}(\vec{\mathbf{r}}') G_p(\vec{\mathbf{r}}|\vec{\mathbf{r}}') dS_{T_\psi^-} dS_{T_\zeta^+} \right.$$
$$\left. + \frac{1}{\beta_0^2} \frac{l_\zeta l_\psi}{A_\zeta^+ A_\psi^-} \int_{T_\zeta^+} \int_{T_\psi^-} G_p(\vec{\mathbf{r}}|\vec{\mathbf{r}}') dS_{T_\psi^-} dS_{T_\zeta^+} \right] \quad (2.81)$$

$$Z_{\zeta\psi}^{-+} = j\beta_0\eta_0 \left[\frac{l_\zeta l_\psi}{4A_\zeta^- A_\psi^+} \int_{T_\zeta^-} \int_{T_\psi^+} \vec{\boldsymbol{\rho}}_\zeta^{\,-}(\vec{\mathbf{r}}) \cdot \vec{\boldsymbol{\rho}}_\psi^{\,+}(\vec{\mathbf{r}}') G_p(\vec{\mathbf{r}}|\vec{\mathbf{r}}') dS_{T_\psi^+} dS_{T_\zeta^-} \right.$$
$$\left. + \frac{1}{\beta_0^2} \frac{l_\zeta l_\psi}{A_\zeta^- A_\psi^+} \int_{T_\zeta^-} \int_{T_\psi^+} G_p(\vec{\mathbf{r}}|\vec{\mathbf{r}}') dS_{T_\psi^+} dS_{T_\zeta^-} \right] \quad (2.82)$$

$$Z_{\zeta\psi}^{++} = j\beta_0\eta_0 \left[\frac{l_\zeta l_\psi}{4A_\zeta^+ A_\psi^+} \int_{T_\zeta^+} \int_{T_\psi^+} \vec{\boldsymbol{\rho}}_\zeta^{\,+}(\vec{\mathbf{r}}) \cdot \vec{\boldsymbol{\rho}}_\psi^{\,+}(\vec{\mathbf{r}}') G_p(\vec{\mathbf{r}}|\vec{\mathbf{r}}') dS_{T_\psi^+} dS_{T_\zeta^+} \right.$$
$$\left. - \frac{1}{\beta_0^2} \frac{l_\zeta l_\psi}{A_\zeta^+ A_\psi^+} \int_{T_\zeta^+} \int_{T_\psi^+} G_p(\vec{\mathbf{r}}|\vec{\mathbf{r}}') dS_{T_\psi^+} dS_{T_\zeta^+} \right] \quad (2.83)$$

are found. Additionally, for a vertical boundary testing edge with an inner basis edge

$$Z_{\zeta\psi}^{--} = j\beta_0\eta_0 \left[\frac{l_\zeta l_\psi}{4A_\zeta^- A_\psi^-} \int_{T_\zeta^-} \int_{T_\psi^-} \vec{\boldsymbol{\rho}}_\zeta^{\,-}(\vec{\mathbf{r}}) \cdot \vec{\boldsymbol{\rho}}_\psi^{\,-}(\vec{\mathbf{r}}') G_p(\vec{\mathbf{r}}|\vec{\mathbf{r}}') dS_{T_\psi^-} dS_{T_\zeta^-} \right.$$
$$\left. - \frac{1}{\beta_0^2} \frac{l_\zeta l_\psi}{A_\zeta^- A_\psi^-} \int_{T_\zeta^-} \int_{T_\psi^-} G_p(\vec{\mathbf{r}}|\vec{\mathbf{r}}') dS_{T_\psi^-} dS_{T_\zeta^-} \right] \quad (2.84)$$

$$Z_{\zeta\psi}^{+-} = j\beta_0\eta_0 \left[e^{j\vec{\mathbf{k}}\cdot\vec{\mathbf{a}}_2} \right] \left[\frac{l_\zeta l_\psi}{4A_\zeta^+ A_\psi^-} \int_{T_\zeta^+} \int_{T_\psi^-} \vec{\boldsymbol{\rho}}_\zeta^{\,+}(\vec{\mathbf{r}}) \cdot \vec{\boldsymbol{\rho}}_\psi^{\,-}(\vec{\mathbf{r}}') G_p(\vec{\mathbf{r}}|\vec{\mathbf{r}}') dS_{T_\psi^-} dS_{T_\zeta^+} \right.$$
$$\left. + \frac{1}{\beta_0^2} \frac{l_\zeta l_\psi}{A_\zeta^+ A_\psi^-} \int_{T_\zeta^+} \int_{T_\psi^-} G_p(\vec{\mathbf{r}}|\vec{\mathbf{r}}') dS_{T_\psi^-} dS_{T_\zeta^+} \right] \quad (2.85)$$

$$Z_{\zeta\psi}^{-+} = j\beta_0\eta_0 \left[\frac{l_\zeta l_\psi}{4A_\zeta^- A_\psi^+} \int_{T_\zeta^-} \int_{T_\psi^+} \vec{\boldsymbol{\rho}}_\zeta^{\,-}(\vec{\mathbf{r}}) \cdot \vec{\boldsymbol{\rho}}_\psi^{\,+}(\vec{\mathbf{r}}') G_p(\vec{\mathbf{r}}|\vec{\mathbf{r}}') dS_{T_\psi^+} dS_{T_\zeta^-} \right.$$
$$\left. + \frac{1}{\beta_0^2} \frac{l_\zeta l_\psi}{A_\zeta^- A_\psi^+} \int_{T_\zeta^-} \int_{T_\psi^+} G_p(\vec{\mathbf{r}}|\vec{\mathbf{r}}') dS_{T_\psi^+} dS_{T_\zeta^-} \right] \quad (2.86)$$

$$Z_{\zeta\psi}^{++} = j\beta_0\eta_0 \left[e^{j\vec{\mathbf{k}}\cdot\vec{\mathbf{a}}_2} \right] \left[\frac{l_\zeta l_\psi}{4A_\zeta^+ A_\psi^+} \int_{T_\zeta^+} \int_{T_\psi^+} \vec{\boldsymbol{\rho}}_\zeta^{\,+}(\vec{\mathbf{r}}) \cdot \vec{\boldsymbol{\rho}}_\psi^{\,+}(\vec{\mathbf{r}}') G_p(\vec{\mathbf{r}}|\vec{\mathbf{r}}') dS_{T_\psi^+} dS_{T_\zeta^+} \right.$$
$$\left. - \frac{1}{\beta_0^2} \frac{l_\zeta l_\psi}{A_\zeta^+ A_\psi^+} \int_{T_\zeta^+} \int_{T_\psi^+} G_p(\vec{\mathbf{r}}|\vec{\mathbf{r}}') dS_{T_\psi^+} dS_{T_\zeta^+} \right] \quad (2.87)$$

and for a vertical boundary basis edge with an inner testing edge

$$Z_{\zeta\psi}^{--} = j\beta_0\eta_0 \left[\frac{l_\zeta l_\psi}{4A_\zeta^- A_\psi^-} \int_{T_\zeta^-} \int_{T_\psi^-} \vec{\boldsymbol{\rho}}_\zeta^{\,-}(\vec{\mathbf{r}}) \cdot \vec{\boldsymbol{\rho}}_\psi^{\,-}(\vec{\mathbf{r}}') G_p(\vec{\mathbf{r}}|\vec{\mathbf{r}}') dS_{T_\psi^-} dS_{T_\zeta^-} \right.$$
$$\left. - \frac{1}{\beta_0^2} \frac{l_\zeta l_\psi}{A_\zeta^- A_\psi^-} \int_{T_\zeta^-} \int_{T_\psi^-} G_p(\vec{\mathbf{r}}|\vec{\mathbf{r}}') dS_{T_\psi^-} dS_{T_\zeta^-} \right] \quad (2.88)$$

$$Z_{\zeta\psi}^{+-} = j\beta_0\eta_0 \left[\frac{l_\zeta l_\psi}{4A_\zeta^+ A_\psi^-} \int_{T_\zeta^+} \int_{T_\psi^-} \vec{\boldsymbol{\rho}}_\zeta^{\,+}(\vec{\mathbf{r}}) \cdot \vec{\boldsymbol{\rho}}_\psi^{\,-}(\vec{\mathbf{r}}') G_p(\vec{\mathbf{r}}|\vec{\mathbf{r}}') dS_{T_\psi^-} dS_{T_\zeta^+} \right.$$
$$\left. + \frac{1}{\beta_0^2} \frac{l_\zeta l_\psi}{A_\zeta^+ A_\psi^-} \int_{T_\zeta^+} \int_{T_\psi^-} G_p(\vec{\mathbf{r}}|\vec{\mathbf{r}}') dS_{T_\psi^-} dS_{T_\zeta^+} \right] \quad (2.89)$$

$$Z_{\zeta\psi}^{-+} = j\beta_0\eta_0 \left[e^{-j\vec{\mathbf{k}}\cdot\vec{\mathbf{a}}_2} \right] \left[\frac{l_\zeta l_\psi}{4A_\zeta^- A_\psi^+} \int_{T_\zeta^-} \int_{T_\psi^+} \vec{\boldsymbol{\rho}}_\zeta^{\,-}(\vec{\mathbf{r}}) \cdot \vec{\boldsymbol{\rho}}_\psi^{\,+}(\vec{\mathbf{r}}') G_p(\vec{\mathbf{r}}|\vec{\mathbf{r}}') dS_{T_\psi^+} dS_{T_\zeta^-} \right.$$
$$\left. + \frac{1}{\beta_0^2} \frac{l_\zeta l_\psi}{A_\zeta^- A_\psi^+} \int_{T_\zeta^-} \int_{T_\psi^+} G_p(\vec{\mathbf{r}}|\vec{\mathbf{r}}') dS_{T_\psi^+} dS_{T_\zeta^-} \right] \quad (2.90)$$

$$Z_{\zeta\psi}^{++} = j\beta_0\eta_0 \left[e^{-j\vec{\mathbf{k}}\cdot\vec{\mathbf{a}}_2} \right] \left[\frac{l_\zeta l_\psi}{4A_\zeta^+ A_\psi^+} \int_{T_\zeta^+} \int_{T_\psi^+} \vec{\boldsymbol{\rho}}_\zeta^{\,+}(\vec{\mathbf{r}}) \cdot \vec{\boldsymbol{\rho}}_\psi^{\,+}(\vec{\mathbf{r}}') G_p(\vec{\mathbf{r}}|\vec{\mathbf{r}}') dS_{T_\psi^+} dS_{T_\zeta^+} \right.$$
$$\left. - \frac{1}{\beta_0^2} \frac{l_\zeta l_\psi}{A_\zeta^+ A_\psi^+} \int_{T_\zeta^+} \int_{T_\psi^+} G_p(\vec{\mathbf{r}}|\vec{\mathbf{r}}') dS_{T_\psi^+} dS_{T_\zeta^+} \right] \quad (2.91)$$

and for a horizontal boundary testing edge with an inner basis edge

$$Z_{\zeta\psi}^{--} = j\beta_0\eta_0 \left[\frac{l_\zeta l_\psi}{4A_\zeta^- A_\psi^-} \int_{T_\zeta^-} \int_{T_\psi^-} \vec{\boldsymbol{\rho}}_\zeta^-(\vec{\mathbf{r}}) \cdot \vec{\boldsymbol{\rho}}_\psi^-(\vec{\mathbf{r}}') G_p(\vec{\mathbf{r}}|\vec{\mathbf{r}}') dS_{T_\psi^-} dS_{T_\zeta^-} \right.$$
$$\left. - \frac{1}{\beta_0^2} \frac{l_\zeta l_\psi}{A_\zeta^- A_\psi^-} \int_{T_\zeta^-} \int_{T_\psi^-} G_p(\vec{\mathbf{r}}|\vec{\mathbf{r}}') dS_{T_\psi^-} dS_{T_\zeta^-} \right] \quad (2.92)$$

$$Z_{\zeta\psi}^{+-} = j\beta_0\eta_0 \left[e^{j\vec{\mathbf{k}}\cdot\vec{\mathbf{a}}_1} \right] \left[\frac{l_\zeta l_\psi}{4A_\zeta^+ A_\psi^-} \int_{T_\zeta^+} \int_{T_\psi^-} \vec{\boldsymbol{\rho}}_\zeta^+(\vec{\mathbf{r}}) \cdot \vec{\boldsymbol{\rho}}_\psi^-(\vec{\mathbf{r}}') G_p(\vec{\mathbf{r}}|\vec{\mathbf{r}}') dS_{T_\psi^-} dS_{T_\zeta^+} \right.$$
$$\left. + \frac{1}{\beta_0^2} \frac{l_\zeta l_\psi}{A_\zeta^+ A_\psi^-} \int_{T_\zeta^+} \int_{T_\psi^-} G_p(\vec{\mathbf{r}}|\vec{\mathbf{r}}') dS_{T_\psi^-} dS_{T_\zeta^+} \right] \quad (2.93)$$

$$Z_{\zeta\psi}^{-+} = j\beta_0\eta_0 \left[\frac{l_\zeta l_\psi}{4A_\zeta^- A_\psi^+} \int_{T_\zeta^-} \int_{T_\psi^+} \vec{\boldsymbol{\rho}}_\zeta^-(\vec{\mathbf{r}}) \cdot \vec{\boldsymbol{\rho}}_\psi^+(\vec{\mathbf{r}}') G_p(\vec{\mathbf{r}}|\vec{\mathbf{r}}') dS_{T_\psi^+} dS_{T_\zeta^-} \right.$$
$$\left. + \frac{1}{\beta_0^2} \frac{l_\zeta l_\psi}{A_\zeta^- A_\psi^+} \int_{T_\zeta^-} \int_{T_\psi^+} G_p(\vec{\mathbf{r}}|\vec{\mathbf{r}}') dS_{T_\psi^+} dS_{T_\zeta^-} \right] \quad (2.94)$$

$$Z_{\zeta\psi}^{++} = j\beta_0\eta_0 \left[e^{j\vec{\mathbf{k}}\cdot\vec{\mathbf{a}}_1} \right] \left[\frac{l_\zeta l_\psi}{4A_\zeta^+ A_\psi^+} \int_{T_\zeta^+} \int_{T_\psi^+} \vec{\boldsymbol{\rho}}_\zeta^+(\vec{\mathbf{r}}) \cdot \vec{\boldsymbol{\rho}}_\psi^+(\vec{\mathbf{r}}') G_p(\vec{\mathbf{r}}|\vec{\mathbf{r}}') dS_{T_\psi^+} dS_{T_\zeta^+} \right.$$
$$\left. - \frac{1}{\beta_0^2} \frac{l_\zeta l_\psi}{A_\zeta^+ A_\psi^+} \int_{T_\zeta^+} \int_{T_\psi^+} G_p(\vec{\mathbf{r}}|\vec{\mathbf{r}}') dS_{T_\psi^+} dS_{T_\zeta^+} \right] \quad (2.95)$$

and for a horizontal boundary basis edge with an inner testing edge

$$Z_{\zeta\psi}^{--} = j\beta_0\eta_0 \left[\frac{l_\zeta l_\psi}{4A_\zeta^- A_\psi^-} \int_{T_\zeta^-} \int_{T_\psi^-} \vec{\boldsymbol{\rho}}_\zeta^{\,-}(\vec{\mathbf{r}}) \cdot \vec{\boldsymbol{\rho}}_\psi^{\,-}(\vec{\mathbf{r}}') G_p(\vec{\mathbf{r}}|\vec{\mathbf{r}}') dS_{T_\psi^-} dS_{T_\zeta^-} \right.$$
$$\left. - \frac{1}{\beta_0^2} \frac{l_\zeta l_\psi}{A_\zeta^- A_\psi^-} \int_{T_\zeta^-} \int_{T_\psi^-} G_p(\vec{\mathbf{r}}|\vec{\mathbf{r}}') dS_{T_\psi^-} dS_{T_\zeta^-} \right] \quad (2.96)$$

$$Z_{\zeta\psi}^{+-} = j\beta_0\eta_0 \left[\frac{l_\zeta l_\psi}{4A_\zeta^+ A_\psi^-} \int_{T_\zeta^+} \int_{T_\psi^-} \vec{\boldsymbol{\rho}}_\zeta^{\,+}(\vec{\mathbf{r}}) \cdot \vec{\boldsymbol{\rho}}_\psi^{\,-}(\vec{\mathbf{r}}') G_p(\vec{\mathbf{r}}|\vec{\mathbf{r}}') dS_{T_\psi^-} dS_{T_\zeta^+} \right.$$
$$\left. + \frac{1}{\beta_0^2} \frac{l_\zeta l_\psi}{A_\zeta^+ A_\psi^-} \int_{T_\zeta^+} \int_{T_\psi^-} G_p(\vec{\mathbf{r}}|\vec{\mathbf{r}}') dS_{T_\psi^-} dS_{T_\zeta^+} \right] \quad (2.97)$$

$$Z_{\zeta\psi}^{-+} = j\beta_0\eta_0 \left[e^{-j\vec{\mathbf{k}}\cdot\vec{\mathbf{a}}_1} \right] \left[\frac{l_\zeta l_\psi}{4A_\zeta^- A_\psi^+} \int_{T_\zeta^-} \int_{T_\psi^+} \vec{\boldsymbol{\rho}}_\zeta^{\,-}(\vec{\mathbf{r}}) \cdot \vec{\boldsymbol{\rho}}_\psi^{\,+}(\vec{\mathbf{r}}') G_p(\vec{\mathbf{r}}|\vec{\mathbf{r}}') dS_{T_\psi^+} dS_{T_\zeta^-} \right.$$
$$\left. + \frac{1}{\beta_0^2} \frac{l_\zeta l_\psi}{A_\zeta^- A_\psi^+} \int_{T_\zeta^-} \int_{T_\psi^+} G_p(\vec{\mathbf{r}}|\vec{\mathbf{r}}') dS_{T_\psi^+} dS_{T_\zeta^-} \right] \quad (2.98)$$

$$Z_{\zeta\psi}^{++} = j\beta_0\eta_0 \left[e^{-j\vec{\mathbf{k}}\cdot\vec{\mathbf{a}}_1} \right] \left[\frac{l_\zeta l_\psi}{4A_\zeta^+ A_\psi^+} \int_{T_\zeta^+} \int_{T_\psi^+} \vec{\boldsymbol{\rho}}_\zeta^{\,+}(\vec{\mathbf{r}}) \cdot \vec{\boldsymbol{\rho}}_\psi^{\,+}(\vec{\mathbf{r}}') G_p(\vec{\mathbf{r}}|\vec{\mathbf{r}}') dS_{T_\psi^+} dS_{T_\zeta^+} \right.$$
$$\left. - \frac{1}{\beta_0^2} \frac{l_\zeta l_\psi}{A_\zeta^+ A_\psi^+} \int_{T_\zeta^+} \int_{T_\psi^+} G_p(\vec{\mathbf{r}}|\vec{\mathbf{r}}') dS_{T_\psi^+} dS_{T_\zeta^+} \right] \quad (2.99)$$

are found. On the other hand, for a vertical basis edge and a horizontal testing edge on the boundaries

$$Z_{\zeta\psi}^{--} = j\beta_0\eta_0 \left[\frac{l_\zeta l_\psi}{4A_\zeta^- A_\psi^-} \int_{T_\zeta^-} \int_{T_\psi^-} \vec{\boldsymbol{\rho}}_\zeta^{\,-}(\vec{\mathbf{r}}) \cdot \vec{\boldsymbol{\rho}}_\psi^{\,-}(\vec{\mathbf{r}}') \, G_p(\vec{\mathbf{r}}|\vec{\mathbf{r}}') \, dS_{T_\psi^-} dS_{T_\zeta^-} \right.$$
$$\left. - \frac{1}{\beta_0^2} \frac{l_\zeta l_\psi}{A_\zeta^- A_\psi^-} \int_{T_\zeta^-} \int_{T_\psi^-} G_p(\vec{\mathbf{r}}|\vec{\mathbf{r}}') \, dS_{T_\psi^-} dS_{T_\zeta^-} \right] \quad (2.100)$$

$$Z_{\zeta\psi}^{+-} = j\beta_0\eta_0 \left[e^{j\vec{\mathbf{k}}\cdot\vec{\mathbf{a}}_1} \right] \left[\frac{l_\zeta l_\psi}{4A_\zeta^+ A_\psi^-} \int_{T_\zeta^+} \int_{T_\psi^-} \vec{\boldsymbol{\rho}}_\zeta^{\,+}(\vec{\mathbf{r}}) \cdot \vec{\boldsymbol{\rho}}_\psi^{\,-}(\vec{\mathbf{r}}') \, G_p(\vec{\mathbf{r}}|\vec{\mathbf{r}}') \, dS_{T_\psi^-} dS_{T_\zeta^+} \right.$$
$$\left. + \frac{1}{\beta_0^2} \frac{l_\zeta l_\psi}{A_\zeta^+ A_\psi^-} \int_{T_\zeta^+} \int_{T_\psi^-} G_p(\vec{\mathbf{r}}|\vec{\mathbf{r}}') \, dS_{T_\psi^-} dS_{T_\zeta^+} \right] \quad (2.101)$$

$$Z_{\zeta\psi}^{-+} = j\beta_0\eta_0 \left[e^{-j\vec{\mathbf{k}}\cdot\vec{\mathbf{a}}_2} \right] \left[\frac{l_\zeta l_\psi}{4A_\zeta^- A_\psi^+} \int_{T_\zeta^-} \int_{T_\psi^+} \vec{\boldsymbol{\rho}}_\zeta^{\,-}(\vec{\mathbf{r}}) \cdot \vec{\boldsymbol{\rho}}_\psi^{\,+}(\vec{\mathbf{r}}') \, G_p(\vec{\mathbf{r}}|\vec{\mathbf{r}}') \, dS_{T_\psi^+} dS_{T_\zeta^-} \right.$$
$$\left. + \frac{1}{\beta_0^2} \frac{l_\zeta l_\psi}{A_\zeta^- A_\psi^+} \int_{T_\zeta^-} \int_{T_\psi^+} G_p(\vec{\mathbf{r}}|\vec{\mathbf{r}}') \, dS_{T_\psi^+} dS_{T_\zeta^-} \right] \quad (2.102)$$

$$Z_{\zeta\psi}^{++} = j\beta_0\eta_0 \left[e^{-j\vec{\mathbf{k}}\cdot\vec{\mathbf{a}}_2} \right] \left[e^{j\vec{\mathbf{k}}\cdot\vec{\mathbf{a}}_1} \right] \left[\frac{l_\zeta l_\psi}{4A_\zeta^+ A_\psi^+} \int_{T_\zeta^+} \int_{T_\psi^+} \vec{\boldsymbol{\rho}}_\zeta^{\,+}(\vec{\mathbf{r}}) \cdot \vec{\boldsymbol{\rho}}_\psi^{\,+}(\vec{\mathbf{r}}') \, G_p(\vec{\mathbf{r}}|\vec{\mathbf{r}}') \, dS_{T_\psi^+} dS_{T_\zeta^+} \right.$$
$$\left. - \frac{1}{\beta_0^2} \frac{l_\zeta l_\psi}{A_\zeta^+ A_\psi^+} \int_{T_\zeta^+} \int_{T_\psi^+} G_p(\vec{\mathbf{r}}|\vec{\mathbf{r}}') \, dS_{T_\psi^+} dS_{T_\zeta^+} \right] \quad (2.103)$$

and for a vertical testing edge and a horizontal basis edge

$$Z_{\zeta\psi}^{--} = j\beta_0\eta_0 \left[\frac{l_\zeta l_\psi}{4A_\zeta^- A_\psi^-} \int_{T_\zeta^-} \int_{T_\psi^-} \vec{\boldsymbol{\rho}}_\zeta^{\,-}(\vec{\mathbf{r}}) \cdot \vec{\boldsymbol{\rho}}_\psi^{\,-}(\vec{\mathbf{r}}') G_p(\vec{\mathbf{r}}|\vec{\mathbf{r}}') dS_{T_\psi^-} dS_{T_\zeta^-} \right.$$
$$\left. - \frac{1}{\beta_0^2} \frac{l_\zeta l_\psi}{A_\zeta^- A_\psi^-} \int_{T_\zeta^-} \int_{T_\psi^-} G_p(\vec{\mathbf{r}}|\vec{\mathbf{r}}') dS_{T_\psi^-} dS_{T_\zeta^-} \right] \quad (2.104)$$

$$Z_{\zeta\psi}^{+-} = j\beta_0\eta_0 \left[e^{-j\vec{\mathbf{k}}\cdot\vec{\mathbf{a}}_1} \right] \left[\frac{l_\zeta l_\psi}{4A_\zeta^+ A_\psi^-} \int_{T_\zeta^+} \int_{T_\psi^-} \vec{\boldsymbol{\rho}}_\zeta^{\,+}(\vec{\mathbf{r}}) \cdot \vec{\boldsymbol{\rho}}_\psi^{\,-}(\vec{\mathbf{r}}') G_p(\vec{\mathbf{r}}|\vec{\mathbf{r}}') dS_{T_\psi^-} dS_{T_\zeta^+} \right.$$
$$\left. + \frac{1}{\beta_0^2} \frac{l_\zeta l_\psi}{A_\zeta^+ A_\psi^-} \int_{T_\zeta^+} \int_{T_\psi^-} G_p(\vec{\mathbf{r}}|\vec{\mathbf{r}}') dS_{T_\psi^-} dS_{T_\zeta^+} \right] \quad (2.105)$$

$$Z_{\zeta\psi}^{-+} = j\beta_0\eta_0 \left[e^{j\vec{\mathbf{k}}\cdot\vec{\mathbf{a}}_2} \right] \left[\frac{l_\zeta l_\psi}{4A_\zeta^- A_\psi^+} \int_{T_\zeta^-} \int_{T_\psi^+} \vec{\boldsymbol{\rho}}_\zeta^{\,-}(\vec{\mathbf{r}}) \cdot \vec{\boldsymbol{\rho}}_\psi^{\,+}(\vec{\mathbf{r}}') G_p(\vec{\mathbf{r}}|\vec{\mathbf{r}}') dS_{T_\psi^+} dS_{T_\zeta^-} \right.$$
$$\left. + \frac{1}{\beta_0^2} \frac{l_\zeta l_\psi}{A_\zeta^- A_\psi^+} \int_{T_\zeta^-} \int_{T_\psi^+} G_p(\vec{\mathbf{r}}|\vec{\mathbf{r}}') dS_{T_\psi^+} dS_{T_\zeta^-} \right] \quad (2.106)$$

$$Z_{\zeta\psi}^{++} = j\beta_0\eta_0 \left[e^{-j\vec{\mathbf{k}}\cdot\vec{\mathbf{a}}_1} \right] \left[e^{j\vec{\mathbf{k}}\cdot\vec{\mathbf{a}}_2} \right] \left[\frac{l_\zeta l_\psi}{4A_\zeta^+ A_\psi^+} \int_{T_\zeta^+} \int_{T_\psi^+} \vec{\boldsymbol{\rho}}_\zeta^{\,+}(\vec{\mathbf{r}}) \cdot \vec{\boldsymbol{\rho}}_\psi^{\,+}(\vec{\mathbf{r}}') G_p(\vec{\mathbf{r}}|\vec{\mathbf{r}}') dS_{T_\psi^+} dS_{T_\zeta^+} \right.$$
$$\left. - \frac{1}{\beta_0^2} \frac{l_\zeta l_\psi}{A_\zeta^+ A_\psi^+} \int_{T_\zeta^+} \int_{T_\psi^+} G_p(\vec{\mathbf{r}}|\vec{\mathbf{r}}') dS_{T_\psi^+} dS_{T_\zeta^+} \right] \quad (2.107)$$

are derived. Then, a vertical testing edge with a vertical testing edge on the vertical boundary

$$Z_{\zeta\psi}^{--} = j\beta_0\eta_0 \left[\frac{l_\zeta l_\psi}{4A_\zeta^- A_\psi^-} \int_{T_\zeta^-} \int_{T_\psi^-} \vec{\boldsymbol{\rho}}_\zeta^{\,-}(\vec{\mathbf{r}}) \cdot \vec{\boldsymbol{\rho}}_\psi^{\,-}(\vec{\mathbf{r}}') G_p(\vec{\mathbf{r}}|\vec{\mathbf{r}}') dS_{T_\psi^-} dS_{T_\zeta^-} \right.$$
$$\left. - \frac{1}{\beta_0^2} \frac{l_\zeta l_\psi}{A_\zeta^- A_\psi^-} \int_{T_\zeta^-} \int_{T_\psi^-} G_p(\vec{\mathbf{r}}|\vec{\mathbf{r}}') dS_{T_\psi^-} dS_{T_\zeta^-} \right] \quad (2.108)$$

$$Z_{\zeta\psi}^{+-} = j\beta_0\eta_0 \left[e^{-j\vec{\mathbf{k}}\cdot\vec{\mathbf{a}}_2} \right] \left[\frac{l_\zeta l_\psi}{4A_\zeta^+ A_\psi^-} \int_{T_\zeta^+} \int_{T_\psi^-} \vec{\boldsymbol{\rho}}_\zeta^{\,+}(\vec{\mathbf{r}}) \cdot \vec{\boldsymbol{\rho}}_\psi^{\,-}(\vec{\mathbf{r}}') G_p(\vec{\mathbf{r}}|\vec{\mathbf{r}}') dS_{T_\psi^-} dS_{T_\zeta^+} \right.$$
$$\left. + \frac{1}{\beta_0^2} \frac{l_\zeta l_\psi}{A_\zeta^+ A_\psi^-} \int_{T_\zeta^+} \int_{T_\psi^-} G_p(\vec{\mathbf{r}}|\vec{\mathbf{r}}') dS_{T_\psi^-} dS_{T_\zeta^+} \right] \quad (2.109)$$

$$Z_{\zeta\psi}^{-+} = j\beta_0\eta_0 \left[e^{j\vec{\mathbf{k}}\cdot\vec{\mathbf{a}}_2} \right] \left[\frac{l_\zeta l_\psi}{4A_\zeta^- A_\psi^+} \int_{T_\zeta^-} \int_{T_\psi^+} \vec{\boldsymbol{\rho}}_\zeta^{\,-}(\vec{\mathbf{r}}) \cdot \vec{\boldsymbol{\rho}}_\psi^{\,+}(\vec{\mathbf{r}}') G_p(\vec{\mathbf{r}}|\vec{\mathbf{r}}') dS_{T_\psi^+} dS_{T_\zeta^-} \right.$$
$$\left. + \frac{1}{\beta_0^2} \frac{l_\zeta l_\psi}{A_\zeta^- A_\psi^+} \int_{T_\zeta^-} \int_{T_\psi^+} G_p(\vec{\mathbf{r}}|\vec{\mathbf{r}}') dS_{T_\psi^+} dS_{T_\zeta^-} \right] \quad (2.110)$$

$$Z_{\zeta\psi}^{++} = j\beta_0\eta_0 \left[\frac{l_\zeta l_\psi}{4A_\zeta^+ A_\psi^+} \int_{T_\zeta^+} \int_{T_\psi^+} \vec{\boldsymbol{\rho}}_\zeta^{\,+}(\vec{\mathbf{r}}) \cdot \vec{\boldsymbol{\rho}}_\psi^{\,+}(\vec{\mathbf{r}}') G_p(\vec{\mathbf{r}}|\vec{\mathbf{r}}') dS_{T_\psi^+} dS_{T_\zeta^+} \right.$$
$$\left. - \frac{1}{\beta_0^2} \frac{l_\zeta l_\psi}{A_\zeta^+ A_\psi^+} \int_{T_\zeta^+} \int_{T_\psi^+} G_p(\vec{\mathbf{r}}|\vec{\mathbf{r}}') dS_{T_\psi^+} dS_{T_\zeta^+} \right] \quad (2.111)$$

and lastly, a horizontal testing edge with a horizontal testing edge on the horizontal boundary

$$Z_{\zeta\psi}^{--} = j\beta_0\eta_0 \left[\frac{l_\zeta l_\psi}{4A_\zeta^- A_\psi^-} \int_{T_\zeta^-} \int_{T_\psi^-} \vec{\boldsymbol{\rho}}_\zeta^{\,-}(\vec{\mathbf{r}}) \cdot \vec{\boldsymbol{\rho}}_\psi^{\,-}(\vec{\mathbf{r}}') \, G_p(\vec{\mathbf{r}}|\vec{\mathbf{r}}') \, dS_{T_\psi^-} dS_{T_\zeta^-} \right.$$
$$\left. - \frac{1}{\beta_0^2} \frac{l_\zeta l_\psi}{A_\zeta^- A_\psi^-} \int_{T_\zeta^-} \int_{T_\psi^-} G_p(\vec{\mathbf{r}}|\vec{\mathbf{r}}') \, dS_{T_\psi^-} dS_{T_\zeta^-} \right] \quad (2.112)$$

$$Z_{\zeta\psi}^{+-} = j\beta_0\eta_0 \left[e^{-j\vec{\mathbf{k}}\cdot\vec{\mathbf{a}}_1} \right] \left[\frac{l_\zeta l_\psi}{4A_\zeta^+ A_\psi^-} \int_{T_\zeta^+} \int_{T_\psi^-} \vec{\boldsymbol{\rho}}_\zeta^{\,+}(\vec{\mathbf{r}}) \cdot \vec{\boldsymbol{\rho}}_\psi^{\,-}(\vec{\mathbf{r}}') \, G_p(\vec{\mathbf{r}}|\vec{\mathbf{r}}') \, dS_{T_\psi^-} dS_{T_\zeta^+} \right.$$
$$\left. + \frac{1}{\beta_0^2} \frac{l_\zeta l_\psi}{A_\zeta^+ A_\psi^-} \int_{T_\zeta^+} \int_{T_\psi^-} G_p(\vec{\mathbf{r}}|\vec{\mathbf{r}}') \, dS_{T_\psi^-} dS_{T_\zeta^+} \right] \quad (2.113)$$

$$Z_{\zeta\psi}^{-+} = j\beta_0\eta_0 \left[e^{j\vec{\mathbf{k}}\cdot\vec{\mathbf{a}}_1} \right] \left[\frac{l_\zeta l_\psi}{4A_\zeta^- A_\psi^+} \int_{T_\zeta^-} \int_{T_\psi^+} \vec{\boldsymbol{\rho}}_\zeta^{\,-}(\vec{\mathbf{r}}) \cdot \vec{\boldsymbol{\rho}}_\psi^{\,+}(\vec{\mathbf{r}}') \, G_p(\vec{\mathbf{r}}|\vec{\mathbf{r}}') \, dS_{T_\psi^+} dS_{T_\zeta^-} \right.$$
$$\left. + \frac{1}{\beta_0^2} \frac{l_\zeta l_\psi}{A_\zeta^- A_\psi^+} \int_{T_\zeta^-} \int_{T_\psi^+} G_p(\vec{\mathbf{r}}|\vec{\mathbf{r}}') \, dS_{T_\psi^+} dS_{T_\zeta^-} \right] \quad (2.114)$$

$$Z_{\zeta\psi}^{++} = j\beta_0\eta_0 \left[\frac{l_\zeta l_\psi}{4A_\zeta^+ A_\psi^+} \int_{T_\zeta^+} \int_{T_\psi^+} \vec{\boldsymbol{\rho}}_\zeta^{\,+}(\vec{\mathbf{r}}) \cdot \vec{\boldsymbol{\rho}}_\psi^{\,+}(\vec{\mathbf{r}}') \, G_p(\vec{\mathbf{r}}|\vec{\mathbf{r}}') \, dS_{T_\psi^+} dS_{T_\zeta^+} \right.$$
$$\left. - \frac{1}{\beta_0^2} \frac{l_\zeta l_\psi}{A_\zeta^+ A_\psi^+} \int_{T_\zeta^+} \int_{T_\psi^+} G_p(\vec{\mathbf{r}}|\vec{\mathbf{r}}') \, dS_{T_\psi^+} dS_{T_\zeta^+} \right] \quad (2.115)$$

are obtained. Here,

$$\begin{aligned} \vec{\boldsymbol{\rho}}_\zeta^{\,-}(\vec{\mathbf{r}}) \cdot \vec{\boldsymbol{\rho}}_\psi^{\,-}(\vec{\mathbf{r}}') &= \left(\vec{\mathbf{r}} - \vec{\mathbf{v}}_\zeta^-\right) \cdot \left(\vec{\mathbf{r}}' - \vec{\mathbf{v}}_\psi^-\right) \\ &= \vec{\mathbf{v}}_\zeta^- \cdot \vec{\mathbf{v}}_\psi^- - \vec{\mathbf{r}} \cdot \vec{\mathbf{v}}_\psi^- - \vec{\mathbf{v}}_\zeta^- \cdot \vec{\mathbf{r}}' + \vec{\mathbf{r}} \cdot \vec{\mathbf{r}}' \end{aligned} \quad (2.116)$$

$$\begin{aligned} \vec{\boldsymbol{\rho}}_\zeta^{\,+}(\vec{\mathbf{r}}) \cdot \vec{\boldsymbol{\rho}}_\psi^{\,-}(\vec{\mathbf{r}}') &= \left(\vec{\mathbf{v}}_\zeta^+ - \vec{\mathbf{r}}\right) \cdot \left(\vec{\mathbf{r}}' - \vec{\mathbf{v}}_\psi^-\right) \\ &= -\vec{\mathbf{v}}_\zeta^+ \cdot \vec{\mathbf{v}}_\psi^- + \vec{\mathbf{r}} \cdot \vec{\mathbf{v}}_\psi^- + \vec{\mathbf{v}}_\zeta^+ \cdot \vec{\mathbf{r}}' - \vec{\mathbf{r}} \cdot \vec{\mathbf{r}}' \end{aligned} \quad (2.117)$$

$$\begin{aligned}\vec{\boldsymbol{\rho}}_{\zeta}^{-}(\vec{\mathbf{r}})\cdot\vec{\boldsymbol{\rho}}_{\psi}^{+}(\vec{\mathbf{r}}')&=\left(\vec{\mathbf{r}}-\vec{\mathbf{v}}_{\zeta}^{-}\right)\cdot\left(\vec{\mathbf{v}}_{\psi}^{+}-\vec{\mathbf{r}}'\right)\\&=-\vec{\mathbf{v}}_{\zeta}^{-}\cdot\vec{\mathbf{v}}_{\psi}^{+}+\vec{\mathbf{r}}\cdot\vec{\mathbf{v}}_{\psi}^{+}+\vec{\mathbf{v}}_{\zeta}^{-}\cdot\vec{\mathbf{r}}'-\vec{\mathbf{r}}\cdot\vec{\mathbf{r}}'\end{aligned}\tag{2.118}$$

$$\begin{aligned}\vec{\boldsymbol{\rho}}_{\zeta}^{+}(\vec{\mathbf{r}})\cdot\vec{\boldsymbol{\rho}}_{\psi}^{+}(\vec{\mathbf{r}}')&=\left(\vec{\mathbf{v}}_{\zeta}^{+}-\vec{\mathbf{r}}\right)\cdot\left(\vec{\mathbf{v}}_{\psi}^{+}-\vec{\mathbf{r}}'\right)\\&=\vec{\mathbf{v}}_{\zeta}^{+}\cdot\vec{\mathbf{v}}_{\psi}^{+}-\vec{\mathbf{r}}\cdot\vec{\mathbf{v}}_{\psi}^{+}-\vec{\mathbf{v}}_{\zeta}^{+}\cdot\vec{\mathbf{r}}'+\vec{\mathbf{r}}\cdot\vec{\mathbf{r}}'\end{aligned}\tag{2.119}$$

can be written.

2.1.2.2 Scattered Near-and Far-Field Equations

After finding the surface current density on the periodic conductive surface, the scattered field in a near-or-far-field region may be needed to evaluate it concerning the position of the observation point. Consequently, for upper half-space; i.e., ($z > (\mathfrak{s})_{max}$), thus, $|z-z'| \rightarrow (z-z')$ and the scattering E-field

$$\vec{\mathbf{E}}^{s}\left(\vec{\mathbf{J}}_{U}\right)=-j\beta_{0}\eta_{0}\sum_{\psi=1}^{N}I_{\psi}\int_{T_{\psi}^{\pm}}\left[\bar{\bar{\mathbf{I}}}+\frac{1}{\beta_{0}^{2}}\nabla\nabla\right]G_{p}\left(\vec{\mathbf{r}}|\vec{\mathbf{r}}'\right)\cdot\vec{\mathbf{f}}_{\psi}\left(\vec{\mathbf{r}}'\right)dS_{T_{\psi}^{\pm}}\tag{2.120}$$

One can write (2.120) as

$$\begin{aligned}\vec{\mathbf{E}}^{s}\left(\vec{\mathbf{J}}_{U}\right)=-j\beta_{0}\eta_{0}\sum_{\psi=1}^{N}I_{\psi}\Bigg[&\int_{T_{\psi}^{\pm}}\vec{\mathbf{f}}_{\psi}\left(\vec{\mathbf{r}}'\right)G_{p}\left(\vec{\mathbf{r}}|\vec{\mathbf{r}}'\right)dS_{T_{\psi}^{\pm}}+\\&\frac{1}{\beta_{0}^{2}}\int_{T_{\psi}^{\pm}}\vec{\mathbf{f}}_{\psi}\left(\vec{\mathbf{r}}'\right)\cdot\nabla\nabla G_{p}\left(\vec{\mathbf{r}}|\vec{\mathbf{r}}'\right)dS_{T_{\psi}^{\pm}}\Bigg]\end{aligned}\tag{2.121}$$

In order to calculate near-fields, the double gradient of the PGF shall be derived. If the spectral form of the PGF is employed

$$\nabla\nabla G_{p}^{spectral}\left(\vec{\mathbf{r}}|\vec{\mathbf{r}}'\right)=-G_{p}^{spectral}\left(\vec{\mathbf{r}}|\vec{\mathbf{r}}'\right)\vec{\mathbf{k}}_{mn}\vec{\mathbf{k}}_{mn}=G_{p}^{spectral}\left(\vec{\mathbf{r}}|\vec{\mathbf{r}}'\right)\vec{\mathbf{k}}_{mn}\otimes\vec{\mathbf{k}}_{mn}\tag{2.122}$$

where $\otimes$ sign denotes the tensor product. Although the spectral form PGF provides eliminates the solution's complexity, the slowing convergence will begin a small problem at points very close to the surface. However, the convergence will not be a constraint in the far-field region. On the other hand, the near-field expression

in (2.122) for observation points just above the surface ($z \leq (\mathfrak{s})_{max}$)

$$\nabla\nabla G_p\left(\vec{\mathbf{r}}|\vec{\mathbf{r}}'\right) = -G_p\left(\vec{\mathbf{r}}|\vec{\mathbf{r}}'\right)\begin{bmatrix} \beta_m^2 & \beta_m\beta_n & \beta_m q_{mn}\frac{(z-z')}{|z-z'|} \\ \beta_n\beta_m & \beta_n^2 & \beta_n q_{mn}\frac{(z-z')}{|z-z'|} \\ q_{mn}\beta_m\frac{(z-z')}{|z-z'|} & q_{mn}\beta_n\frac{(z-z')}{|z-z'|} & q_{mn}^2\left[\frac{|z-z'|^2-(z-z')^2}{(-jq_{mn})|z-z'|(z-z')^2}+\frac{(z-z')^2}{|z-z'|^2}\right] \end{bmatrix} \tag{2.123}$$

is the double gradient of (2.61).

2.1.2.3 Acceleration Techniques

The periodicity is embedded in the kernel of the EFIE in (2.58) with a linear progressive phase shift resulting from Floquet's theorem. The rough surface is modeled by dividing with periodic lattices, thus, reducing the infinite surface to a single unit cell. However, the solution of the EFIE suffers from the numerical computation of the FS-PGF owing to the relevant series converging very slowly. Accelerating the doubly periodic series is vital in obtaining numerical calculations effectively. The convergence problem arises when the surface height is low so that the observation point will be somewhat close to the surface, especially for the spectral form of PGF. The spectral PGF will converge rapidly as the observation point moves away from the surface since the spectral representation is the Fourier transform of its spatial form. In order to speed up the convergence, some decomposition techniques are fortunately reported in several studies for 1-D and 2-D periodicity of the surface [56–63].

PGF with Kummer's transformation [60] is given as

$$G_p\left(\vec{\mathbf{r}}|\vec{\mathbf{r}}'\right) = G_p^{spectral}\left(\vec{\mathbf{r}}|\vec{\mathbf{r}}'\right) - G_p^{spectral,asymptotic}\left(\vec{\mathbf{r}}|\vec{\mathbf{r}}'\right) + G_p^{spatial,asymptotic}\left(\vec{\mathbf{r}}|\vec{\mathbf{r}}'\right) \tag{2.124}$$

$$\begin{aligned} G_p\left(\vec{\mathbf{r}}|\vec{\mathbf{r}}'\right) = & \frac{1}{2L_xL_y}\sum_{m=-\infty}^{+\infty}\sum_{n=-\infty}^{+\infty}\frac{e^{-j\beta_m(x-x')}e^{-j\beta_n(y-y')}e^{-jq_{mn}|z-z'|}}{jq_{mn}} \\ & - \frac{1}{2L_xL_y}\sum_{m=-\infty}^{+\infty}\sum_{n=-\infty}^{+\infty}\frac{e^{-j\beta_m(x-x')}e^{-j\beta_n(y-y')}e^{-u_{mn}|z-z'|}}{u_{mn}} \\ & + \frac{1}{4\pi}\sum_{m=-\infty}^{+\infty}\sum_{n=-\infty}^{+\infty}e^{-j\beta_x mL_x}e^{-j\beta_y mL_y}\frac{e^{-uR_{mn}}}{R_{mn}} \end{aligned} \tag{2.125}$$

where u is the smoothing parameter, and u_{mn}

$$u_{mn}^2 = \left\|\vec{\boldsymbol{\beta}}_{mn}\right\|^2 + u^2 \tag{2.126}$$

Then, if u^2 is added and subtracted in (2.15) yields

$$\begin{aligned} q_{mn} &= -j\sqrt{\left\|\vec{\boldsymbol{\beta}}_{mn}\right\|^2 + u^2 - (k^2 + u^2)} \\ &= -j\sqrt{u_{mn}^2 - (k^2 + u^2)} \end{aligned} \tag{2.127}$$

The choice of the smoothing parameter u affects the convergence of spatial and spectral sums, so a reasonable choice of u is recommended as half the size of the maximum reciprocal lattice vector [60]. For an orthogonal 2-D lattice seen in Figure 2.1, these vectors are $\vec{\mathbf{k}}_1 = (2\pi/L_x)\hat{\mathbf{x}}$ and $\vec{\mathbf{k}}_2 = (2\pi/L_y)\hat{\mathbf{y}}$. Thus, the smoothing parameter is $u = \pi/\min(L_x, L_y)$.

Ewald's method is one of the most effective ways to accelerate the FS-PGF computation. The method is based on the identity as follows

$$\frac{e^{-j\beta_0 R}}{R} = \frac{2}{\sqrt{\pi}} \int_0^\infty e^{-jR^2 s^2 + \frac{\beta_0^2}{4s^2}} \tag{2.128}$$

The PGF is decomposed into spatial and spectral forms

$$G_p\left(\vec{\mathbf{r}}|\vec{\mathbf{r}}'\right) = G_1^{spectral}\left(\vec{\mathbf{r}}|\vec{\mathbf{r}}'\right) + G_2^{spatial}\left(\vec{\mathbf{r}}|\vec{\mathbf{r}}'\right) \tag{2.129}$$

where decomposed functions are obtained as follows

$$G_2^{spatial}\left(\vec{\mathbf{r}}|\vec{\mathbf{r}}'\right) = \frac{1}{8\pi} \sum_{m=-\infty}^{\infty} \sum_{n=-\infty}^{\infty} \frac{e^{-j\beta_x L_x} e^{-j\beta_y L_y}}{R_{mn}} \times \sum_{\pm} e^{\pm j\beta_0 R_{mn}} \operatorname{erfc}\left(R_{mn}E \pm j\frac{\beta_0}{2E}\right) \tag{2.130}$$

$$G_1^{spectral}\left(\vec{\mathbf{r}}|\vec{\mathbf{r}}'\right) = \frac{1}{4L_x L_y} \sum_{m=-\infty}^{\infty} \sum_{n=-\infty}^{\infty} \frac{e^{-j\beta_m(x-x')} e^{-j\beta_n(y-y')}}{jq_{mn}} \times \sum_{\pm} e^{\pm j(z-z')q_{mn}} \operatorname{erfc}\left(\frac{jq_{mn}}{2E} \pm (z-z')E\right) \tag{2.131}$$

In (2.130) and (2.131), $\sum_{\pm}$ denotes the sum of the related terms with + and − signs. The derivation of the equations (2.130) and (2.131) will not be given in detail in this thesis. In addition, the choice of the optimal value of E is essential to minimize the number of terms required to reach the desired error value for convergence. The optimum value of E has been discussed in [62], but, in this thesis, the optimum E parameter is chosen as follows

$$E_{opt} = \sqrt{\frac{\pi}{2L_x L_y}} \tag{2.132}$$

This choice results in better convergence time over a more comprehensive frequency range. For high frequencies or large periodic spacings, a complete condition on E must be determined to avoid loss of accuracy as in [61]

$$E = \max\left(E_{opt}, \frac{\beta_0}{2H}\right) \tag{2.133}$$

where H is the maximum number to be permitted $\exp(H^2)$ in order to avoid cancellation errors.

2.1.2.4 Extraction of Singular Terms

In the MoM matrix calculation in (2.65), the self-terms should be appropriately handled to overcome $1/R$ singularities of the spatial GFs in accelerating the evaluations of IEs. The cancellation of potential GFs' singularity is conventionally treated by singularity subtraction, and regularization approaches [81–84]. In this thesis, the singularity subtraction approach is employed as follows

$$\int_{S'} \vec{\mathbf{f}}\left(\vec{\mathbf{r}}'\right) G_p\left(\vec{\mathbf{r}}|\vec{\mathbf{r}}'\right) dS' = \underbrace{\int_{S'} \vec{\mathbf{f}}\left(\vec{\mathbf{r}}'\right)\left[G_p\left(\vec{\mathbf{r}}|\vec{\mathbf{r}}'\right) - G_p^{asymptotic}\left(\vec{\mathbf{r}} \to \vec{\mathbf{r}}'|\vec{\mathbf{r}}'\right)\right] dS'}_{\text{Integrated Numerically}} + \underbrace{\int_{S'} \vec{\mathbf{f}}\left(\vec{\mathbf{r}}'\right) G_p^{asymptotic}\left(\vec{\mathbf{r}} \to \vec{\mathbf{r}}'|\vec{\mathbf{r}}'\right) dS'}_{\text{Integrated Analytically}} \tag{2.134}$$

where $\vec{\mathbf{f}}(\vec{\mathbf{r}}')$ represents the basis function. After applying this subtraction for the central cell ($m = n = 0$), the first term of the right-hand side of (2.134) becomes regular. The

second term of the equation is singular and analytically evaluated for linear basis functions. It should be noted that all other terms except the central cell have a finite value, and numerical quadrature methods can directly evaluate the regular terms. If (2.134) is applied to Kummer's transform in the central cell, the decomposition for the spatial term can be written as

$$G_{Kummer}^{spatial(0,0)} = \frac{1}{4\pi}\left[\frac{e^{-uR}-1}{R}\right] + \frac{1}{4\pi R} \tag{2.135}$$

and the spatial term of Ewald's transformation is found similarly

$$G_{Ewald}^{spatial(0,0)} = \frac{1}{8\pi}\left[\sum_{\pm}\frac{e^{\pm j\beta_0 R}}{R}\mathrm{erfc}\left(RE \pm j\beta_0/2E\right) - \frac{2}{R}\right] + \frac{1}{4\pi R} \tag{2.136}$$

Here, the first terms are integrated numerically, or the limit values of them are obtained for electrically very small triangles reported as [85]—the second term of (2.135) and (2.136) are integrated analytically [84]. Although a more general approach based on purely numerical quadrature schemes is reported in [86, 87], the singularity subtraction method given above still works well for this thesis's problems.

2.2 Numerical Results

Many researchers have only focused on acceleration techniques to speed up convergence. We will discuss whether fast convergence is the main factor in determining the performance of the numerical code in a complete MoM solution for realistic scattering problems. In combination with two primary acceleration techniques, the height of the surface, mesh sizes, unit cell dimension and frequency, and quality of the numerical integration are discussed in detail to assess the performance of periodic EFIE-MoM formulations. For this purpose, the MoM formulations are compared for periodic flat, 1-D and 2-D sinusoidal, and arbitrary rough surfaces in this section. Herein, the performance analyses of numerical techniques in previous sections are performed, and the most appropriate solution approach for different scattering cases is explored.

However, before numerical calculations are carried out, it can be useful to mention the cutoff phenomena for scattering fields from an infinite periodic structure. Condition to propagate Floquet modes is $\|\beta_{mn}\| < k$, otherwise evanescent waves will be occur ($\|\beta_{mn}\| > k$). Hence, cutoff frequencies for each Floquet mode can be estimated as given in (2.138), and this formula will be employed in finding analytical values

for scattering fields from various periodic surface samples. Besides, all numerical calculations are conducted by Ryzen 3900x processor (24 cores) with 128 RAM, and MATLAB software is used in this thesis.

2.2.1 Performance analyses of periodic EFIE-MoM formulations

In this subsection, the performance analyses of the periodic EFIE-MoM formulations alluded to in the previous sections start with a flat surface case since a flat surface can be considered a periodic surface. Also, one can easily find the analytical solution to this problem, and the flat surfaces in the z-axis complicate the achievement of acceleration techniques. For these reasons, Table 2.1 is first prepared for the numerical approaches' performance test in the periodic EFIE-MoM formulations. For this purpose, dimensions and types of surfaces, singularity extraction, and acceleration technique are changed, and relative errors of solutions and solution times are evaluated. Here, the definition of the relative error is given in (2.137). In the numerical simulations used in the preparation of Table 2.1, the incident angle of the plane wave is selected as $\theta^i = 60^\circ$ and $\phi^i = 0^\circ$, the polarization is horizontal, and triangles discretize the flat surface with an edge length of about 0.1λ. Finally, the results are analytically compared in the far-field region ($\vec{\mathbf{r}} = \hat{\mathbf{z}}101$ m) for the total scattered E-field that is the sum of all Floquet modes. Also, henceforth, the amplitude of the incident plane wave is determined as a unit in all simulations, i.e., $E_0 = 1$ V/m. Unless otherwise stated in this chapter, the free space wavelength is denoted as λ in all scattering examples and numerical results.

Commercial software with a similar periodic-MoM approach with linear basis functions is also employed to compare the periodic-MoM formulations [88] better. For this purpose, FEKO software was used for comparison for various scattering cases in Table 2.1. Thus, as seen from Table 2.1, the solution time is worse than FEKO, while the accuracy of our formulations is much better. However, this shortcoming can be remedied, as discussed in the following sections. In this thesis, the exact value of PGF was calculated for each point in the triangle facets. Also, the quality of the numerical quadrature used in this thesis is very high to achieve desired accuracy levels compared to analytical solutions. This high-quality numerical integration increases numerical quadrature points and improves the overall computation time in calculating the PGF values for all source and observation triangles. Besides, pre-calculated PGF values for several sample points can even be utilized to create a look-up table [63], and an interpolation algorithm estimates any other points outside these sample points. The accuracy and solution speed will depend on the efficiency and ability of this interpolation algorithm. FEKO may use a look-table and an interpolation algorithm

Table 2.1 Comparison of periodic EFIE-MoM solutions on flat surfaces

Frequency (MHz)	L_x (λ)	L_y (λ)	This work					FEKO	
			Singular Integration	PGF Error	Acceleration Technique	Relative Error	Solution Time (s)	Relative Error	Solution Time (s)
3	0.1	0.1	Khayat [86]	10^{-3}	Ewald	8.22×10^{-7}	3.50	5.31×10^{-4}	0.012
					Kummer	7.33×10^{-7}	2.00		
300					Ewald	8.16×10^{-7}	3.60	8.8×10^{-3}	0.176
					Kummer	7.27×10^{-7}	2.38		
300000					Ewald	8.16×10^{-7}	3.51	8.8×10^{-3}	0.175
					Kummer	7.27×10^{-7}	1.95		
300	0.5	0.5		10^{-1}	Ewald	8.21×10^{-7}	262	9.9×10^{-3}	0.443
				10^{-3}		8.20×10^{-7}	328		
				10^{-4}		8.21×10^{-7}	348		
				10^{-1}	Kummer	1.30×10^{-4}	124		
				10^{-3}		7.38×10^{-7}	277		
				10^{-4}		8.23×10^{-7}	908		
			Singularity Subtraction	10^{-1}	Ewald	8.62×10^{-7}	257		
				10^{-3}		8.61×10^{-7}	319		
				10^{-4}		8.62×10^{-7}	343		
1500	1.5	1.5	Khayat [86]	10^{-3}	Ewald	1.29×10^{-5}	3085	8.9×10^{-3}	5.636
					Kummer	5.82×10^{-6}	3271		
3000					Ewald	1.48×10^{-5}	2811	8.7×10^{-3}	5.646
					Kummer	7.52×10^{-6}	2809		
30000					Ewald	3.90×10^{-5}	899	8.8×10^{-3}	5.646
					Kummer	3.86×10^{-5}	997		

to reduce the solution time. Since our interpolation algorithm is not fast and efficient enough for large matrices, this technique is not added to the table.

Moreover, one can easily see from Table 2.1 the solution's accuracy does not change significantly with the choice of the acceleration technique. Regardless of the acceleration technique, the convergence error of the PGF may have little effect on the accuracy of the solution. On the other hand, the solution time is highly dependent on the chosen acceleration technique, frequency, size of the unit cell, and the total number of unknowns. As can be seen from Table 2.1, Kummer's transform can yield faster results at lower frequencies. Still, it should be noted that Ewald's transform becomes faster than Kummer's decomposition for large unit cell sizes. Similarly, if the convergence error of PGF is reduced by 10^{-3}, Kummer's transform gives prolonged results compared to Ewald's decomposition.

$$\text{Relative Error} = \frac{\left|\left\|\vec{\mathbf{E}}^{s}_{analytical}(\vec{\mathbf{r}})\right\| - \left\|\vec{\mathbf{E}}^{s}_{numerical}(\vec{\mathbf{r}})\right\|\right|}{\left\|\vec{\mathbf{E}}^{s}_{analytical}(\vec{\mathbf{r}})\right\|} \tag{2.137}$$

2.2.1.1 Effect of mesh size and cutoff phenomena for periodic surfaces

Comparing the effect of mesh size is also performed in Table 2.2 to assess the solution's accuracy. The incident angle stays the same as the previous calculations. A sinusoidal surface whose function is $\mathfrak{s}(x) = -h\cos(2\pi x/L_x)$ is employed, where $h = 0.1$ m and $L_x = L_y = 0.5$ m. The solution frequency is determined as 300 MHz to stay outside the cutoff frequency range as reported in [13, 16]. Thus, the cutoff frequencies will have emerged for each Floquet mode, and if $\|\beta_{mn}\| = k$, the minimum cutoff frequency can be obtained. If this equation is rearranged in order to obtain the minimum cutoff frequency (f_c) as follows

$$\left|\sin^2\theta_i + 2\sin\theta_i\left[\frac{mc}{f_c L_x}\cos\phi_i + \frac{nc}{f_c L_y}\sin\phi_i\right] + \left(\frac{mc}{f_c L_x}\right)^2 + \left(\frac{nc}{f_c L_y}\right)^2\right| = 1 \tag{2.138}$$

where c is the velocity of light in free space. For $\theta^i = 60°$, $\phi^i = 0°$, $L_x = L_y = 0.5$ m and $m = -1$, $n = 0$, the cutoff frequency (f_c) is found as 321.5 GHz from (2.138). Thus, the scattered E-field aroused from this sinusoidal surface will behave like a flat surface for 300 MHz. It should be noted that the cutoff frequency is dependent on the incident angles and the dimensions of the unit cell, not the surface height. As

seen from Table 2.2, the solution's accuracy increases depending on the mesh size. Here, PGF's convergence error is constant, and the acceleration technique is Kummer's transform, while Khayat's formulation is used for singularity extraction. The definition of the relative error is as given in (2.137). Besides, the same surface is also solved by FEKO software with the RWG (linear and first-order) basis functions for different mesh lengths to obtain a reasonable comparison. As seen from Table 2.2, although FEKO is faster when comparing our formulations, the relative error results do not converge as desired, even using a fairly dense mesh in contrast to our study. As a result, the formulations used in FEKO do not achieve high accuracy, and the solution time is also longer when it uses dense mesh in order to improve accuracy.

Table 2.2 Comparison of EFIE-MoM solutions for several mesh sizes

This work					FEKO		
Mesh Length	PGF Error	Acceleration Technique	Relative Error	Solution Time (s)	Mesh Length	Relative Error	Solution Time (s)
$\lambda/10$	10^{-3}	Kummer	3.07×10^{-5}	249	$\lambda/10$	0.0223	0.355
					$\lambda/20$	0.0143	0.549
$\lambda/20$			6.63×10^{-7}	2442.9	$\lambda/30$	0.0115	1.148
					$\lambda/50$	0.0088	10.68
$\lambda/30$			4.40×10^{-7}	10832.9	$\lambda/100$	0.0063	242.9
					$\lambda/200$	0.0048	9465.7

2.2.1.2 Effect of surface height

In order to compare the effects of acceleration techniques on the surface height, a 1-D sinusoidal surface is defined with a function $\mathfrak{s}(x) = -h\cos(2\pi x/L_x)$. Here, the lengths of the unit cell are $L_x = L_y = 0.5$ m, and the h parameter is changed with $h = 0.001$ m, $h = 0.01$ m, $h = 0.1$ m, and $h = 0.2$ m. The performance results of the Kummer's and Ewald's transformations with 10^{-1} and 10^{-3} convergence errors are given in Figures 2.5, 2.6, respectively. The incident angle of the plane wave is selected as $\theta^i = 30°$ and $\phi^i = 0°$, the polarization is horizontal, and the flat surface is discretized by triangles with an edge length of about 0.1λ. The solution frequency is selected as 300 MHz, and the minimum cutoff frequency (f_c) is found as 400 MHz from (2.138). As seen from Figure 2.5, Kummer's transformation is always faster than Ewald's decomposition for high convergence error 10^{-1}, and, on the other hand, the accuracy for Ewald's transformation is always better.

However, when $|z - z'| \to 0$, Ewald's transform may converge faster than Kummer's for convergence errors less than 10^{-3}.

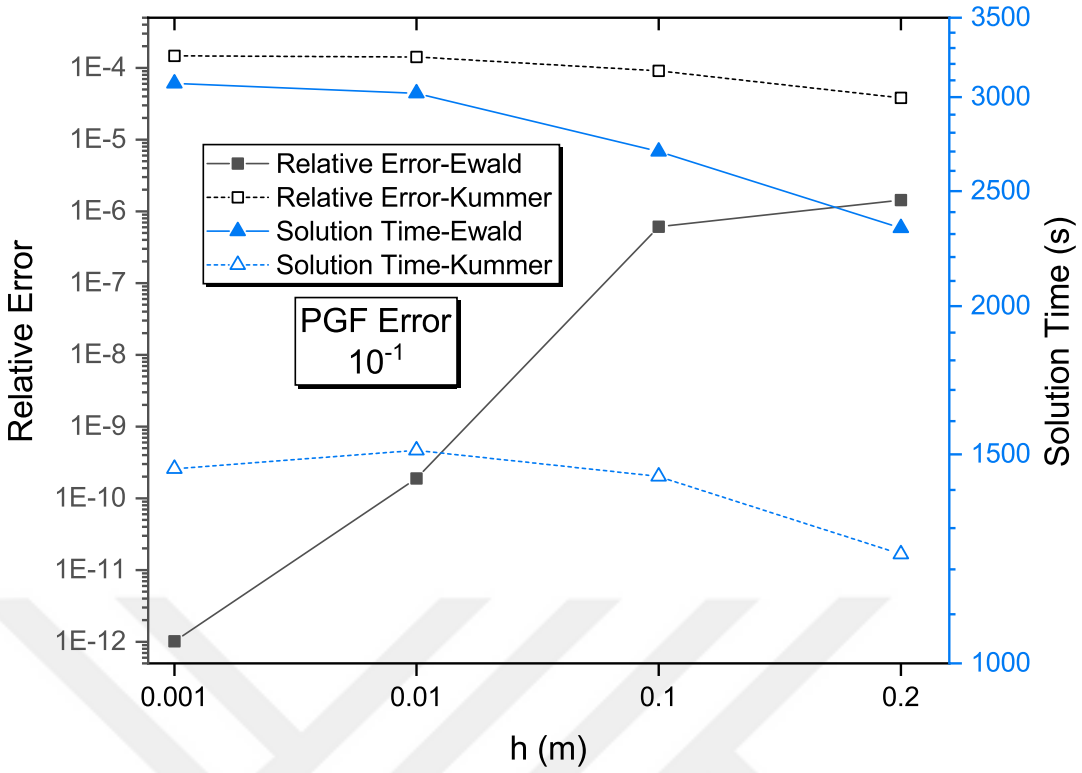

Figure 2.5 Relative error and solution time results for a sinusoidal surface with various h values at 300 MHz (PGF error 10^{-1})

2.2.1.3 Effect of unit cell size

The size of a unit cell of a periodic surface can affect the performance of the acceleration techniques. For this analysis, a 1-D sinusoidal surface is utilized with a function $s(x) = -h\cos(2\pi x/L_x)$, where $h = 0.01$ m, $L_x = L_y = 0.0852$ m. The incident angle of the plane wave is chosen as $\theta^i = 10°$, $\phi^i = 0°$, and the mesh average length is about 0.00852 m. Therefore, the minimum cutoff frequency is adjusted to 3000 MHz for easier relative error comparison. The solution frequency is altered between 300-2900 MHz with 200 MHz intervals. This provides that the unit cell dimensions are electrically changing between about 0.0852λ and 0.8λ. For the 300 – 2900 MHz range, the relative errors and solution times are demonstrated in Figures 2.7 and 2.8. Herein, Kummer's and Ewald's transformations with 10^{-1} and 10^{-3} convergence errors are compared in Figures 2.7 and 2.8, respectively. For high convergence errors, Kummer's transformation is always faster than Ewald's with similar accuracy values. Besides, as seen from previous and present results, lower convergence errors are not necessary to achieve the desired accuracy. When comparing solution times, Kummer's transform with 10^{-1} convergence error is always shorter. However, for larger unit cell dimensions, Ewald's transform can be faster for lower convergence errors than 10^{-3}.

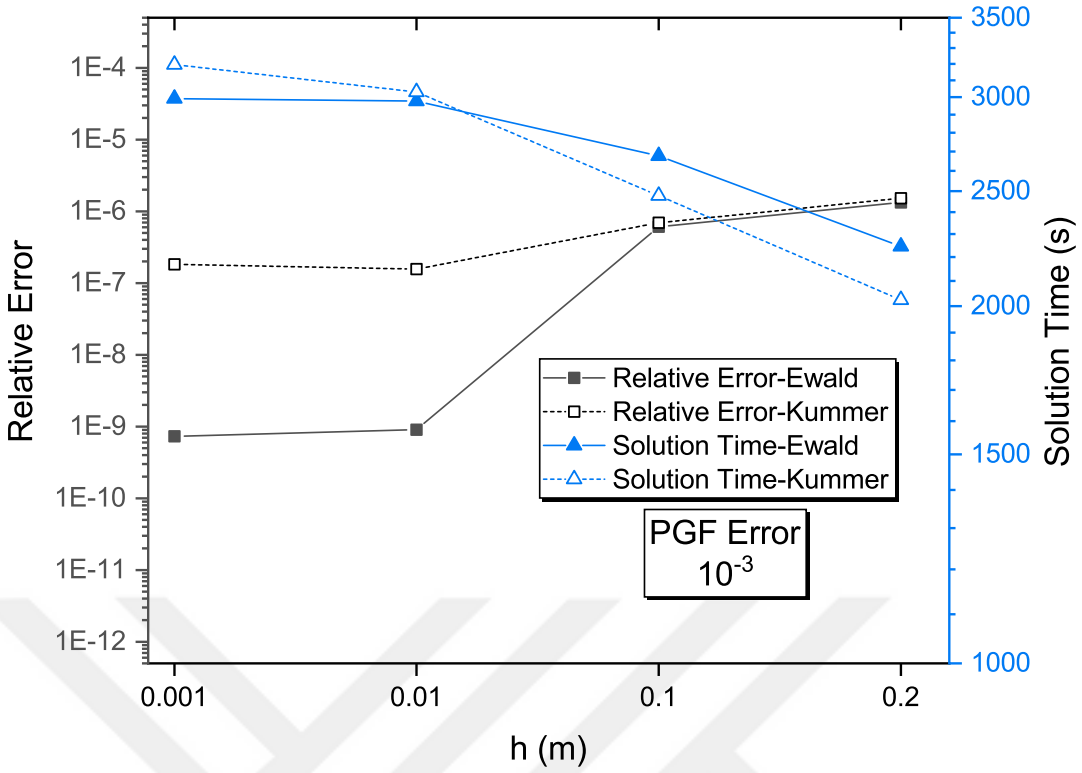

Figure 2.6 Relative error and solution time results for a sinusoidal surface with various h values at 300 MHz (PGF error 10^{-3})

2.2.1.4 Effect of numerical integration

The quality of numerical integration is also vitally important. In order to achieve high accuracy, the points used in numerical quadrature were initially used in high numbers. In addition, the number of these points changes dynamically according to the distance between the observation and source triangle facets. Hence, the total number of points in numerical integration in this study changes between 36, 169, 361, 729, and 3318 for near and far triangles facets. These values are considered a reference to assure high accuracy. In Figures 2.9 and 2.10, these point numbers are reduced as a percentage, and the results are analyzed in terms of accuracy and solution time. The surface function is selected again $\mathfrak{s}(x) = -h\cos(2\pi x/L_x)$, where $h = 0.01$ m, $L_x = L_y = 0.0852$ m. The solution frequency is selected as 1500 MHz, the incident angle of the plane wave is $\theta^i = 10°$, $\phi^i = 0°$, and for the mesh size, the length of one side of the triangles is about 0.00852 m. Kummer's and Ewald's transformations with 10^{-1} and 10^{-3} convergence errors are also depicted in Figures 2.9 and 2.10, respectively. As seen from this figure, the solution time can be increased excessively by decreasing the quality of numerical integration if one releases the desire for high accuracy. However, if high accuracy is entailed, adjusting PGF convergence error, reducing points of numerical quadrature, and determining an intelligent choice of the acceleration technique for some instances make the speed of the numerical code

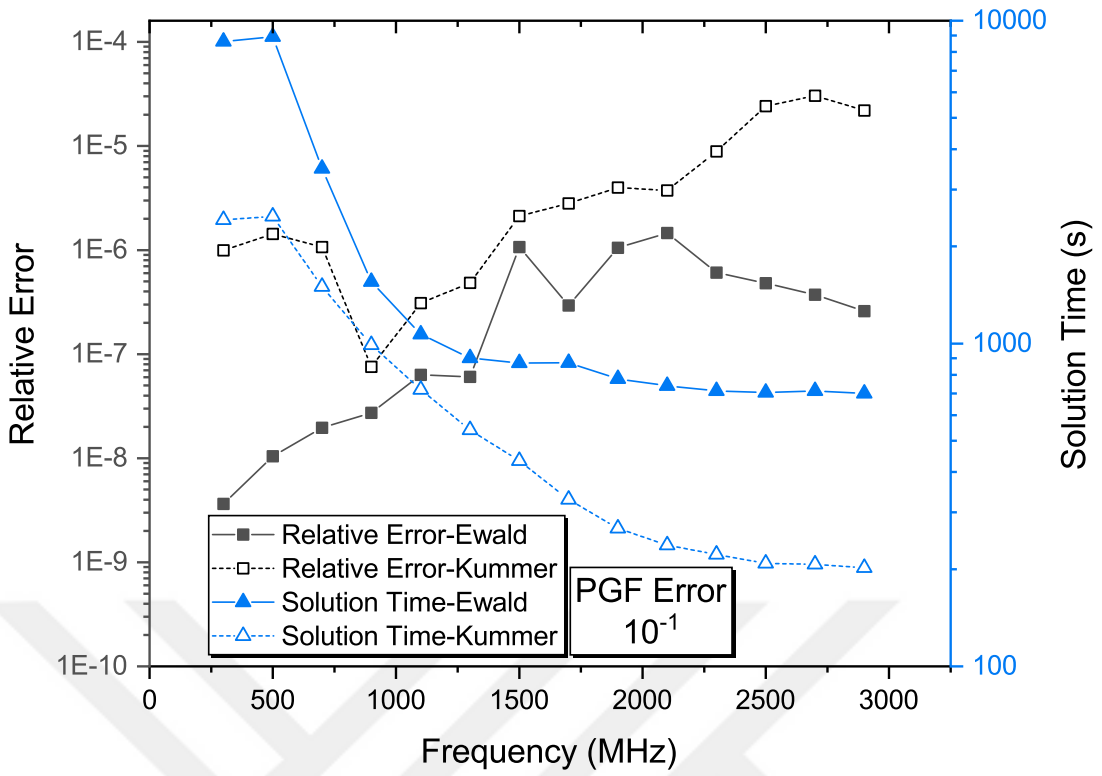

Figure 2.7 Relative error and solution time results of a sinusoidal surface with $L_x = L_y = 0.0852$ m and $h = 0.01$ m for various operating frequencies (PGF error 10^{-1})

faster while maintaining considerable accuracy.

2.2.2 Comparison of the proposed EFIE-MoM formulations with analytical results for various slightly rough surfaces

Herein, the accuracy test of the periodic-MoM solution is conducted for various periodic rough surface problems. To perform this validation, the rough surface height is chosen to be small compared to the wavelength. In this way, the solution region, wherein Rayleigh's assumption is valid, is preserved, and the analytical and semi-analytical equations can be obtained as shared in Section 2.1.1.

2.2.2.1 Comparative results for a 2-D sinusoidal surface

The periodic rough surface is assumed as a simple well-known sinusoidal that avoids the complexity of the IE method's validation with the Rayleigh-based methods. Selecting sinusoidal functions as a surface model facilitates calculating Rayleigh-based methods' coefficients analytically (see Section 2.1.1). Thus, the surface function is considered as $z = \mathfrak{s}(x, y) = -h\left[\cos(2\pi x/L_x) + \cos\left(2\pi y/L_y\right)\right]$, where $h = 0.0016$ m, $L_x = L_y = 0.1016$ m. The incident wave is horizontal polarization and is about at a

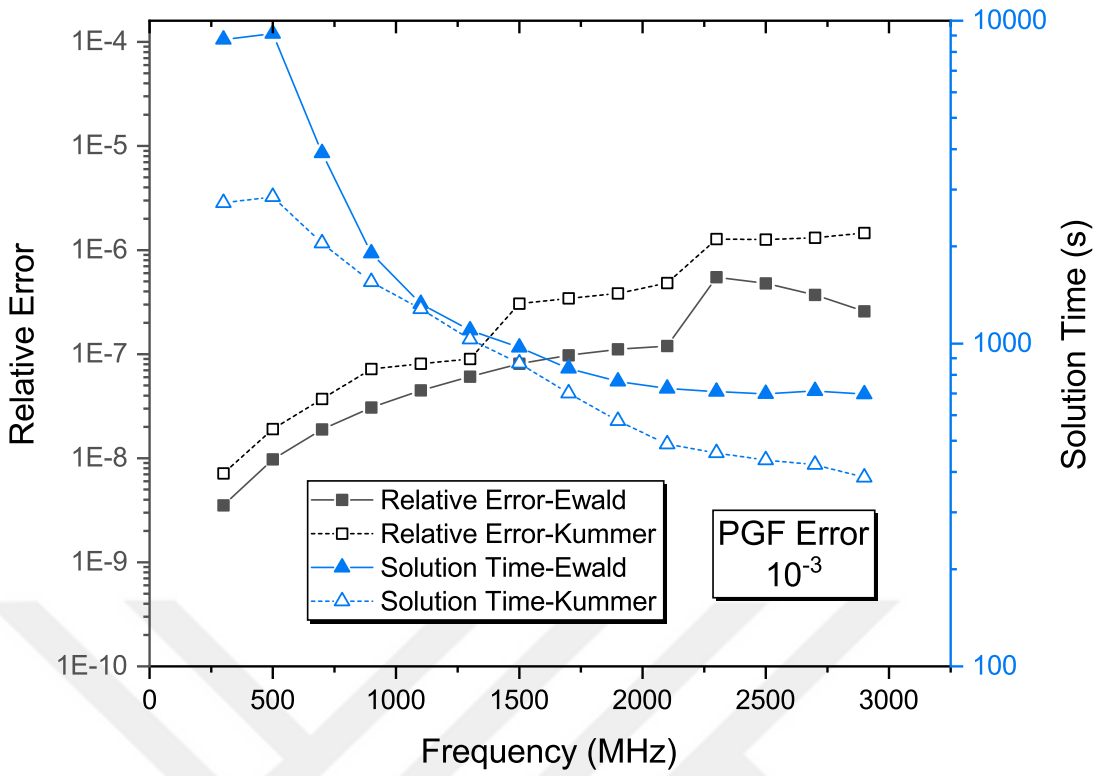

Figure 2.8 Relative error and solution time results of a sinusoidal surface with $L_x = L_y = 0.0852$ m and $h = 0.01$ m for various operating frequencies (PGF error 10^{-3})

low-grazing angle of 85°. As seen in Figures 2.11, 2.11, and 2.13, the surface current densities are demonstrated by calculating the FMMM, the periodic-MoM, and FEKO, respectively. The numerical surface current in this work agrees well with the analytic one.

The total scattered fields are also calculated for several frequencies in Figure 2.14, where the observation point is at $x = y = 0$ m and $z = 100$ m. In this figure, the EFIE-MoM solution's validation is ensured in a proper frequency region for the SPM and FMMM. The derivation of the FMMM is given to calculate the unknown coefficients of (2.3) using numerical integration for any surface function in Section 2.1.1.2. An analytical formulation is also derived for this sinusoidal surface with Bessel identity in this section. The arbitrary-order SPM solution is acquired by an iterative solution [7, 10]. Consequently, FMMM offers a more straightforward formulation than higher-order SPM, and the solution time is slower in the SPM. These two Rayleigh based-methods are also compared within themselves for this surface (see Figure 2.14). Furthermore, for several observation points at x-and z-directions, the scattered fields are also compared with the analytical solution given in Section 2.1.1.2. The magnitudes of scattered E-fields are compared for observation points at z-direction by starting from the locations where they are very close to the surface in Figure 2.15.

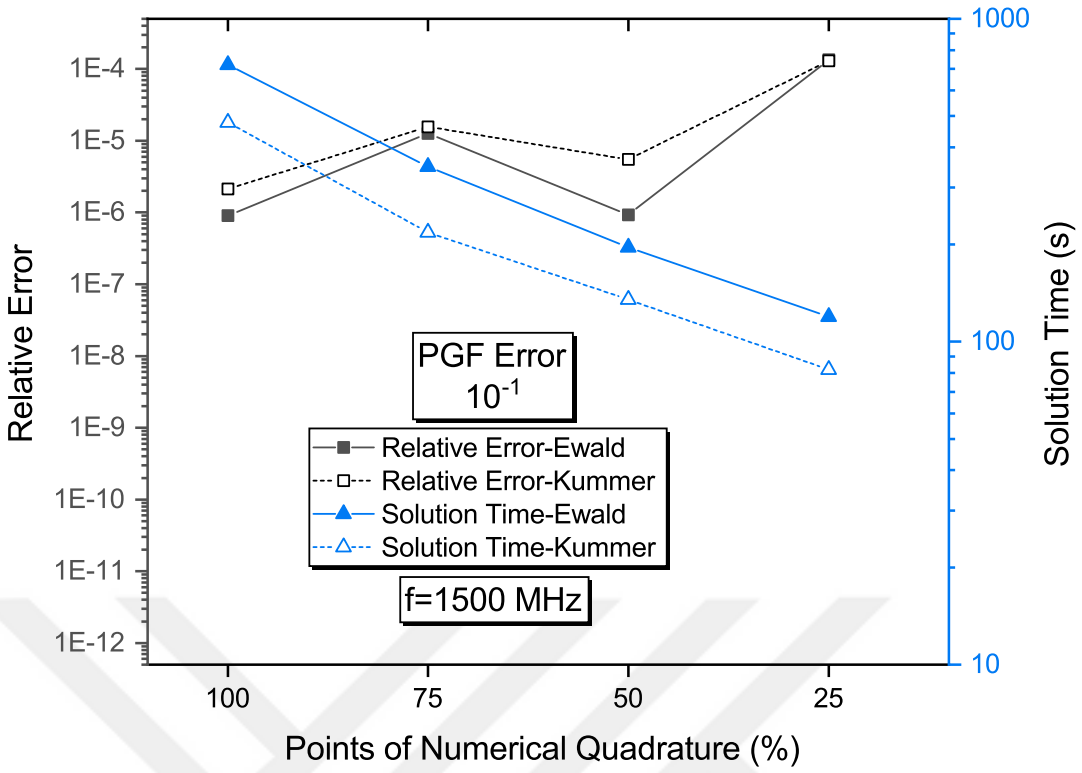

Figure 2.9 Relative error and solution time results for a sinusoidal surface with various numerical quadrature points as percentages(PGF error 10^{-1})

The scattered E-fields are also evaluated for x-direction in Figure 2.16. Here, FEKO results are also given in the figures for comparison. In Figure 2.14, the averaged edge lengths of triangles in the meshed structure are about 0.01 m in the EFIE-MoM solution and 0.0025 m in the FEKO simulation to obtain the expected accuracy. On the other hand, for the solutions of several observation points at 1500 MHz, the mesh structure used in the EFIE-MoM and FEKO solutions is the same as depicted in Figure 2.16, where the averaged triangle edge length corresponds to about $\lambda/20$. As a result, as seen from the figures, all the numerical results of the EFIE-MoM formulation are very satisfactory.

2.2.2.2 Comparative results for an arbitrarily rough periodic surface

A random surface is also generated by a Gaussian correlation function with an RMS height of $h = 0.0032$ m and a correlation length of $l = 0.09$ m to compare the semi-analytical formulation in Section 2.1.1.2 with the periodic-MoM solution. The lengths of the unit cell are $L_x = L_y = 0.1016$ m and computed scattering E-fields are shown in Figures 2.17and 2.18. Here, the incident wave is horizontally polarized and at a low grazing angle of approximately 85°. The results agree well with EFIE-MoM solutions. A numerical quadrature with 25 points is used in calculating integrals of

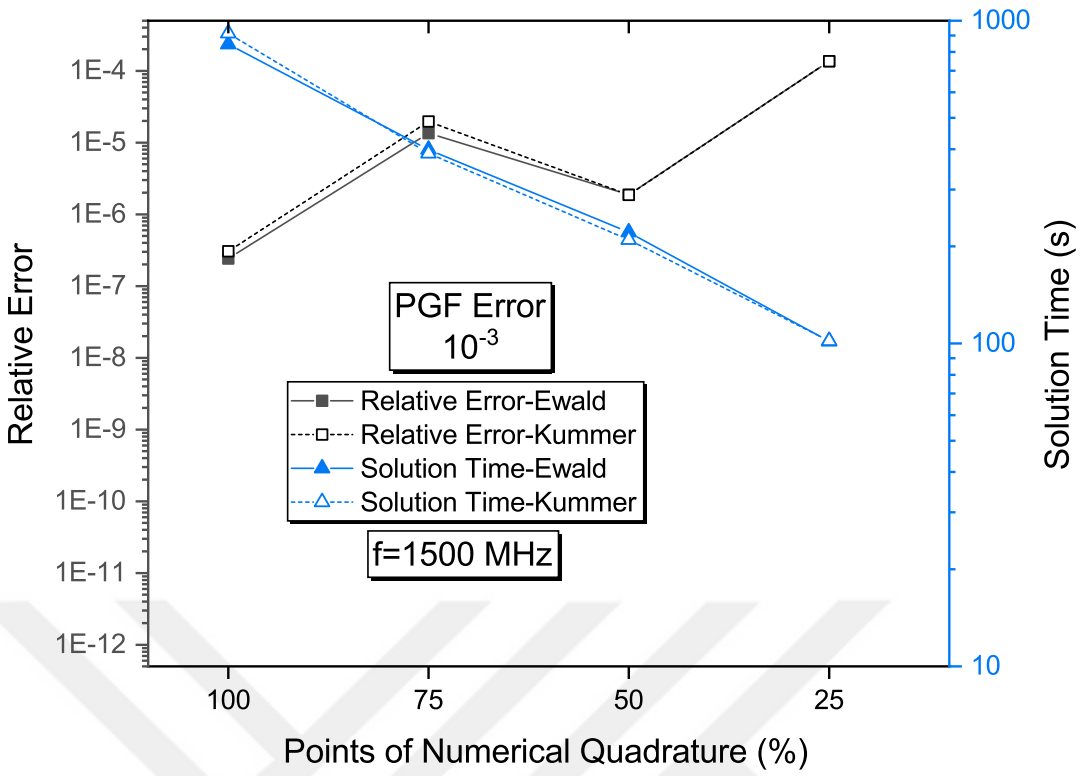

Figure 2.10 Relative error and solution time results for a sinusoidal surface with various numerical quadrature points as percentages (PGF error 10^{-3})

in (2.41)–(2.46), and the total solution time of the FMMM takes 8.6 seconds. The numerical derivative is also employed in this semi-analytical solution. Compared to the EFIE-MoM solution in terms of solution time, the full-wave solution takes about 8523 seconds. The results are shown that the full-wave periodic-MoM solution provides enough accuracy. In contrast, the solution time of this full-wave method can be reduced, as well as the semi-analytical solution can be employed for any rough surface having a small height and slope. Besides, the results from FEKO are also given in Figures 2.17and 2.18 for a mesh size with an average triangle edge length of $\lambda/20$, where the RWG basis function is also employed in obtaining numerical results. The unit cell with its mesh structure utilized in the EFIE-MoM and FEKO solutions is depicted in Figure 2.18.

2.2.3 Comparison of the proposed EFIE-MoM formulations with FEKO results for highly rough surfaces

In this subsection, the degree of roughness of the periodic surface is increased to a level where the Rayleigh hypothesis is not valid. As shown in Figures 2.19 and 2.20, a pyramidal surface $L_x = L_y = 0.499$ m is chosen in this context. This rough surface is singular, and its height is 0.499 m. The observation points and the incident angle

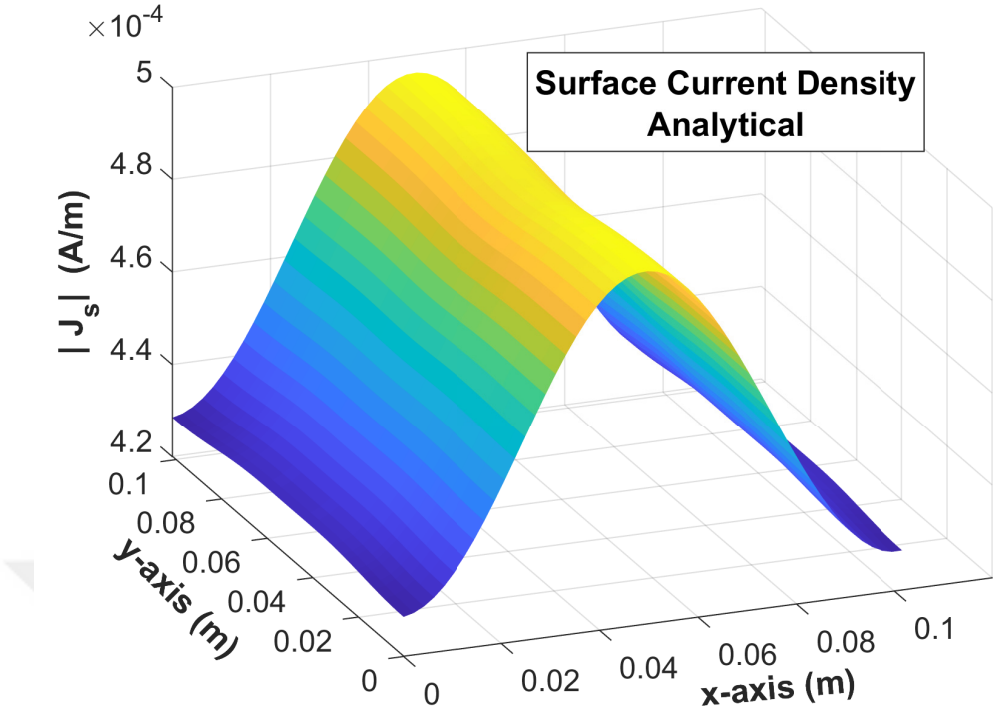

Figure 2.11 Induced surface current densities on one period of an infinite, conductive sinusoidal surface at 1.5 GHz (FMMM)

of the plane wave are similar to the previous simulations, and the solution frequency is 600 MHz. Figures 2.19 and 2.20 show the total scattered E-fields in the z-direction and the x-direction, respectively. In the first EFIE-MoM solution, the number of points used in the numerical integration is reduced by 50%, and Kummer's transform is employed with a convergence error of 10^{-1}. Secondly, the convergence error is reduced to 10^{-3} without decreasing numerical integration points. In addition, to compare the EFIE-MoM results, FEKO software is used with several mesh types and sizes. The first comparison uses the RWG basis functions with the same mesh structure as the EFIE-MoM solution. Then, a higher-order basis function (HOBF) with the same mesh size and a very dense mesh ($\lambda/80$) with the RWG basis functions are employed respectively to provide higher accuracy. The unit cell, the mesh structure, and the elapsed times for the computations are also demonstrated in Figure 2.19. It should be noted that for the same mesh type and size, the accuracy of the present work for this example is better than the FEKO simulation results, as can be seen from Figures 2.19 and 2.20 (the red-colored dotted line). On the other hand, as discussed in detail in Section 2.2.1, the solution time is considerably shorter for Kummer's transform with a 10^{-1} high error level.

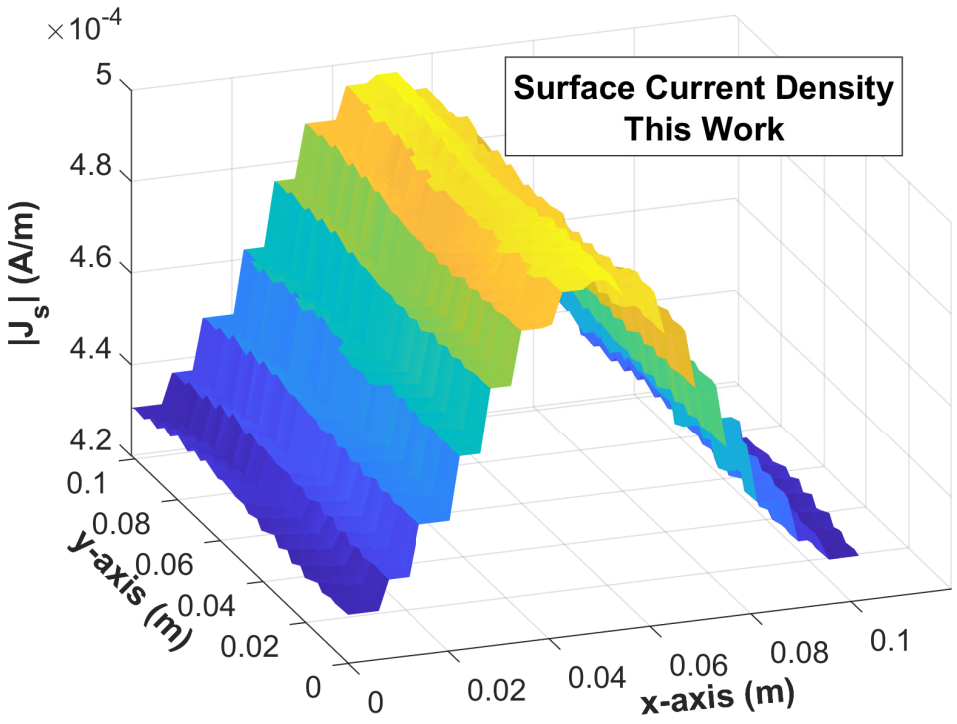

Figure 2.12 Induced surface current densities on one period of an infinite, conductive sinusoidal surface at 1.5 GHz (This work/EFIE-MoM)

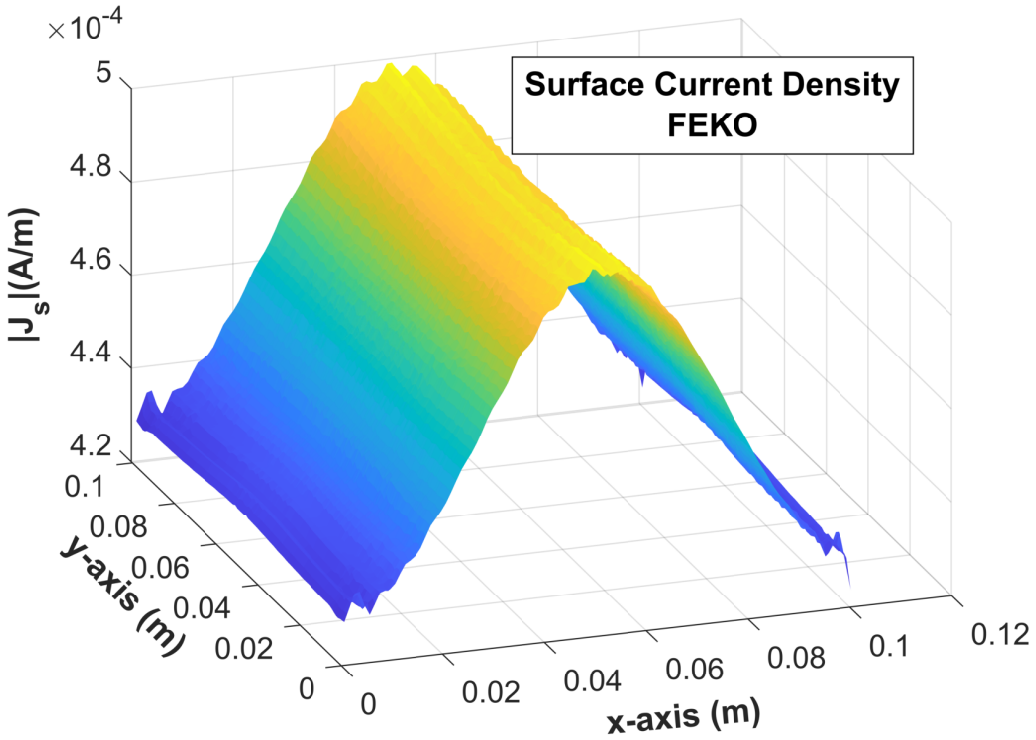

Figure 2.13 Induced surface current densities on one period of an infinite, conductive sinusoidal surface at 1.5 GHz (FEKO)

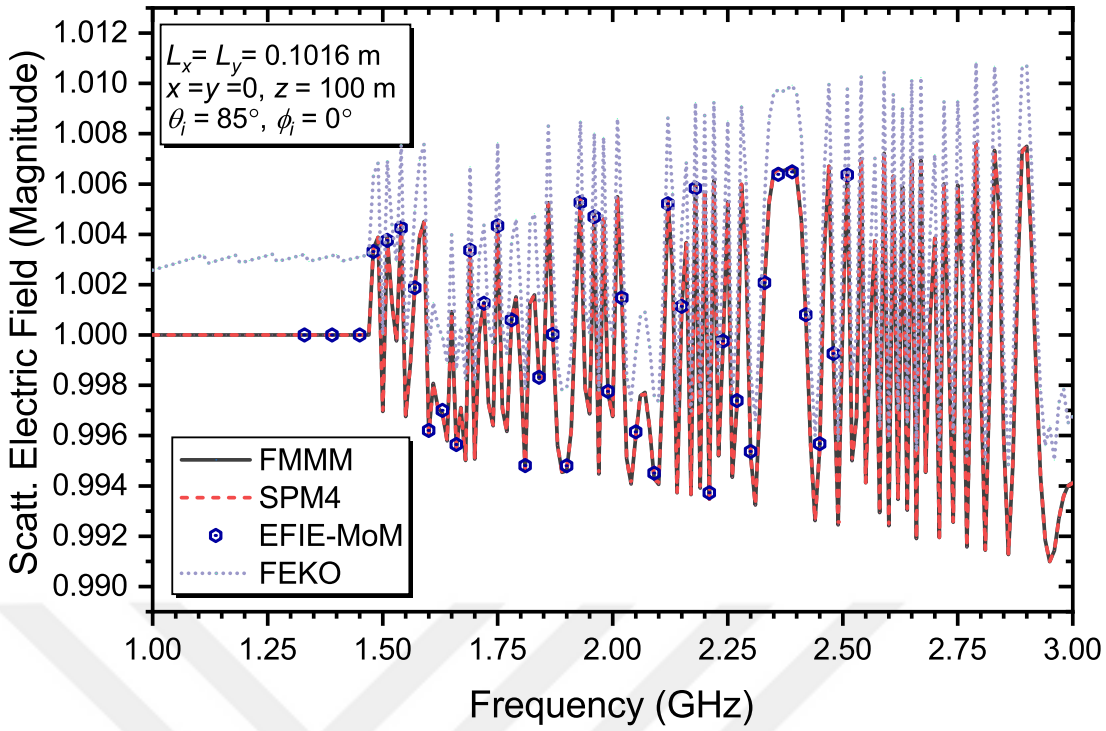

Figure 2.14 Magnitude of total scattered E-field from infinite, conducting sinusoidal surface as a function of frequency for TE polarization

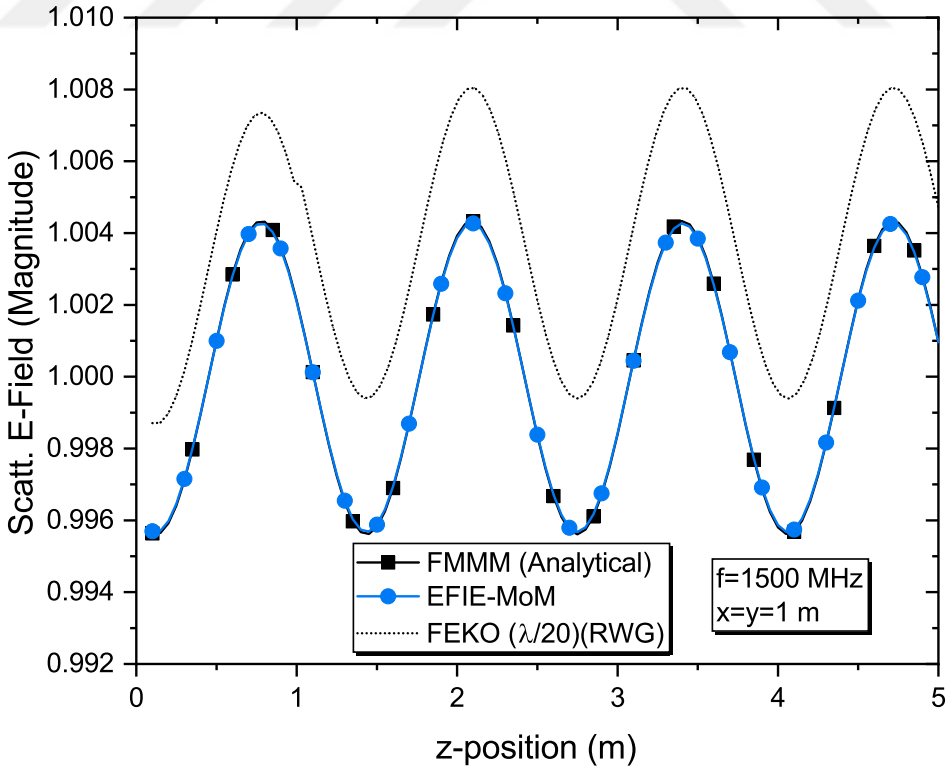

Figure 2.15 Total scattered E-field with respect to several observation points for a sinusoidal surface (Along z-axis)

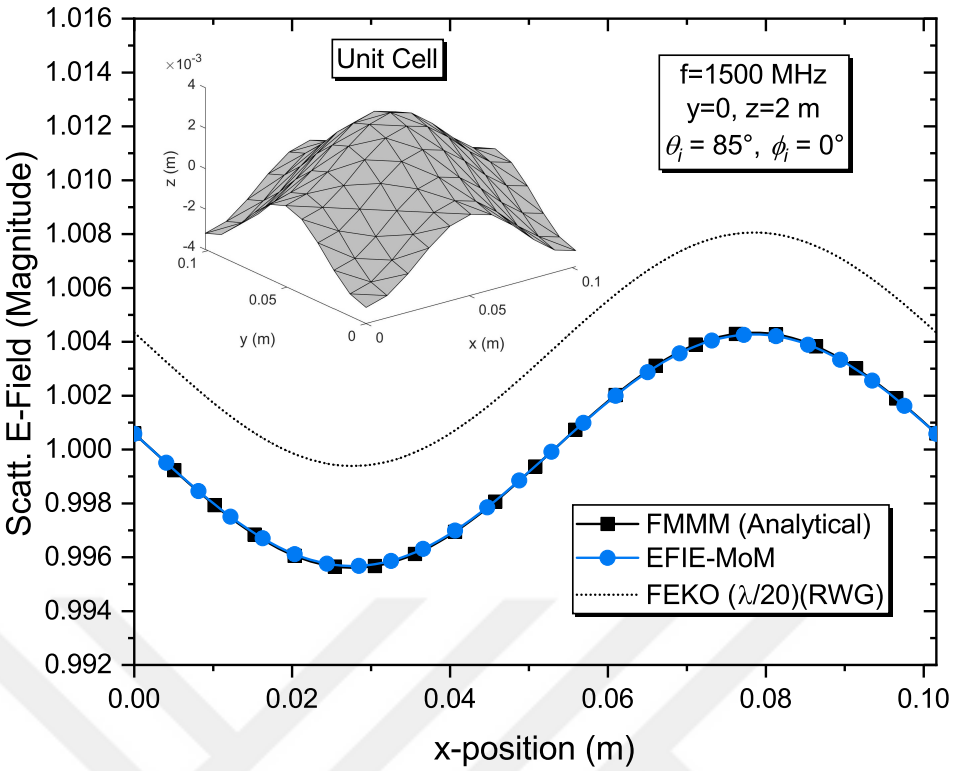

Figure 2.16 Total scattered E-field with respect to several observation points for a sinusoidal surface (Along x-axis)

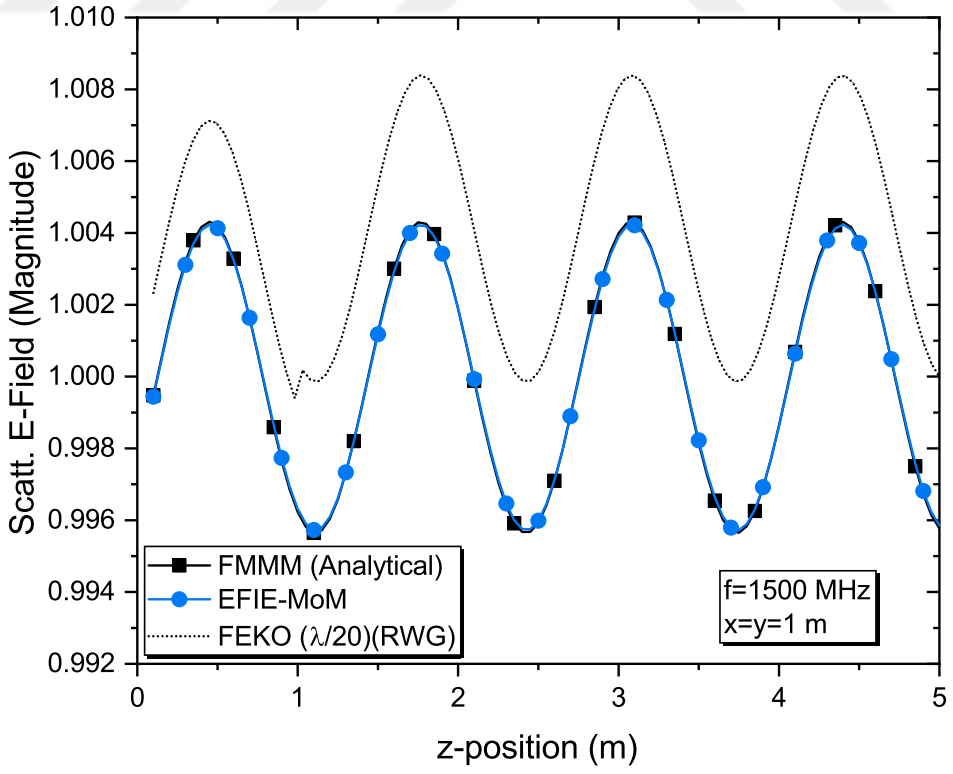

Figure 2.17 Total scattered E-field concerning several observation points for a random surface (Along z-axis)

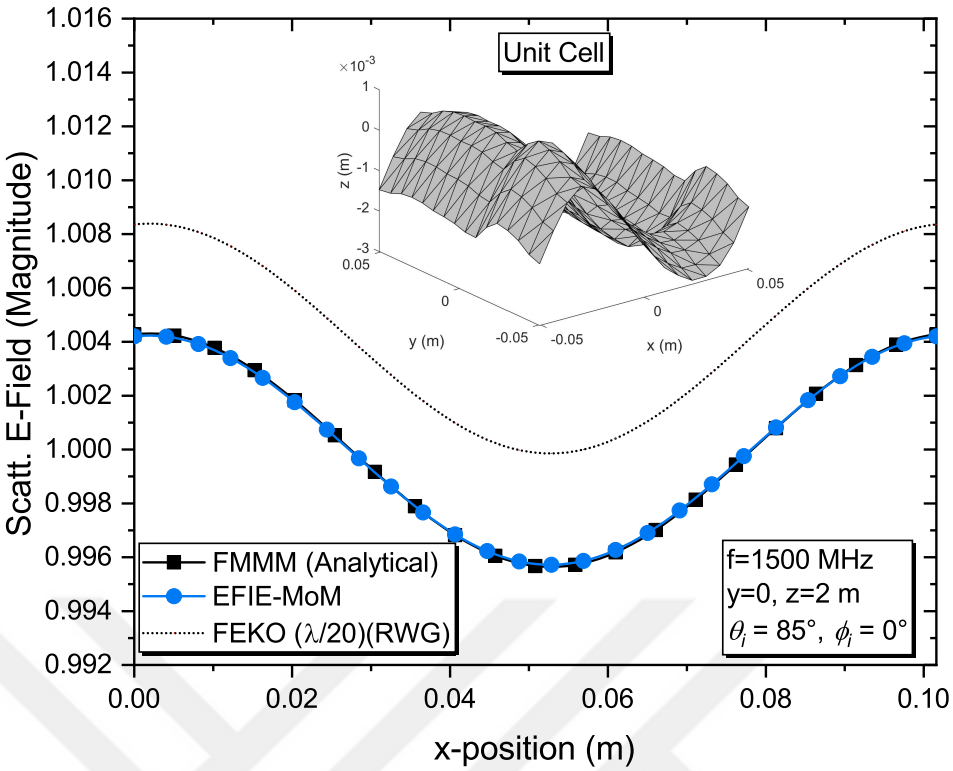

Figure 2.18 Total scattered E-field with respect to several observation points for a random surface (Along x-axis)

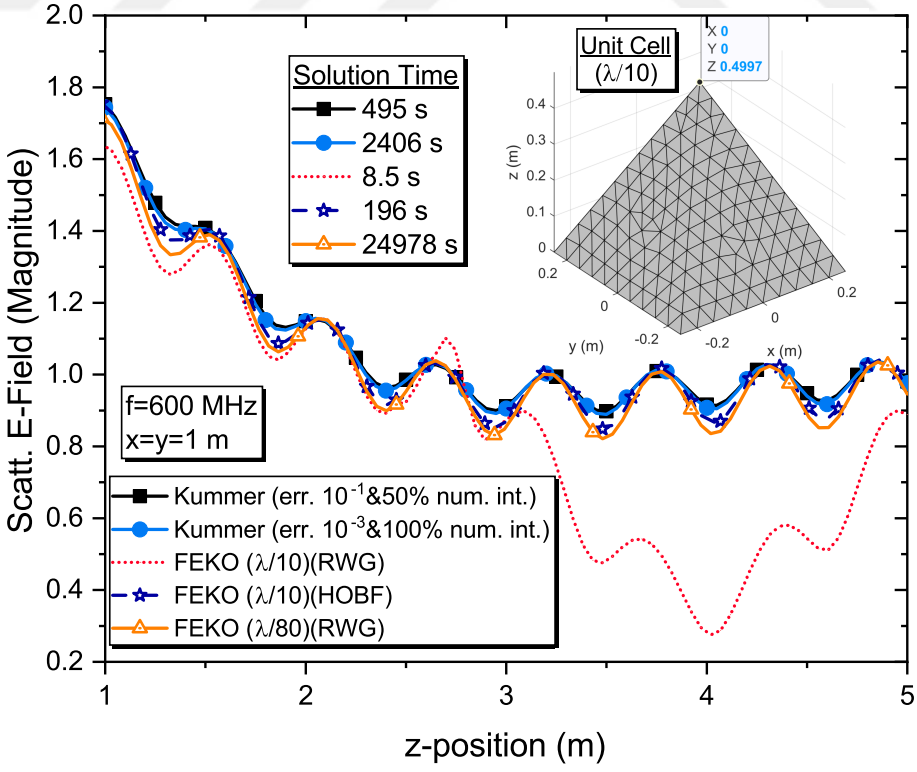

Figure 2.19 Total scattered E-field with respect to several observation points for a rough pyramidal surface (Along z-axis)

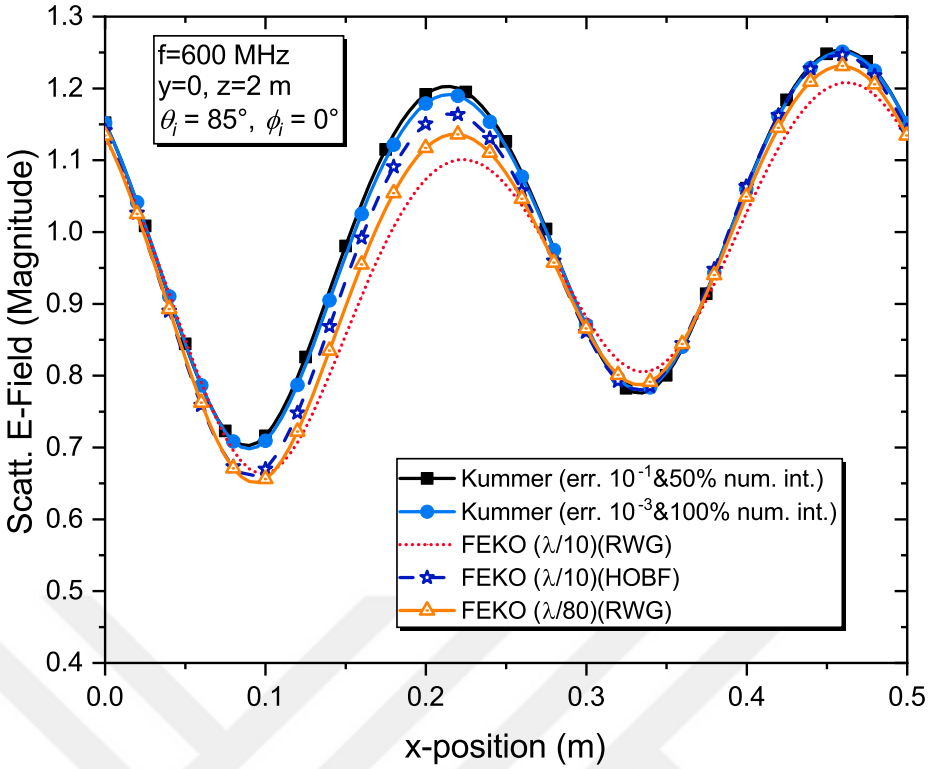

Figure 2.20 Total scattered E-field concerning several observation points for a rough pyramidal surface (Along x-axis)

3
MOM SOLUTIONS OF SCATTERING PROBLEMS FROM CONDUCTING OBJECTS ABOVE CONDUCTING FLAT HALF-SPACE: IMAGE METHOD AND PERTURBATION APPROACH

Based on the current decomposition on the ground surface, a practical solution approach, named the perturbation method, is introduced to handle several scattering problems from targets placed on any half-space. In this chapter, the scattering problem of an inserted PEC object above a flat and infinite PEC interface is addressed by this method. In this solution, the surface current on the infinite surface is decomposed as induced current without the object present and perturbed current caused by the object on a limited area of the infinite surface. The perturbed current is dominant only limited area on the infinite surface, decaying rapidly on the ground surface while far away from the object. It is assumed that the perturbed current density is zero except for the perturbation surface. However, the image theory is employed to compare and prove the achievements of the proposed approach. Hence, our method achieves considerable accuracy while providing an effortless computation without entailing to attain a half-space Green's function or exercise a tapered wave illumination. Also, in contrast to a tapered wave approach for illumination at low-grazing angles, this method provides a significantly superior solution even when using a plane wave.

A general scattering scenario is depicted in Figure 3.1, where the object shape can be arbitrary, and the half-space is selected as flat. As seen from the figure, the object is PEC and inserted with a h m above from the infinite flat surface. Next, EFIEs of unknown surface currents are solved using the MoM. Finally, the unknown surface currents are discretized using RWG basis functions and Galerkin-type testing.

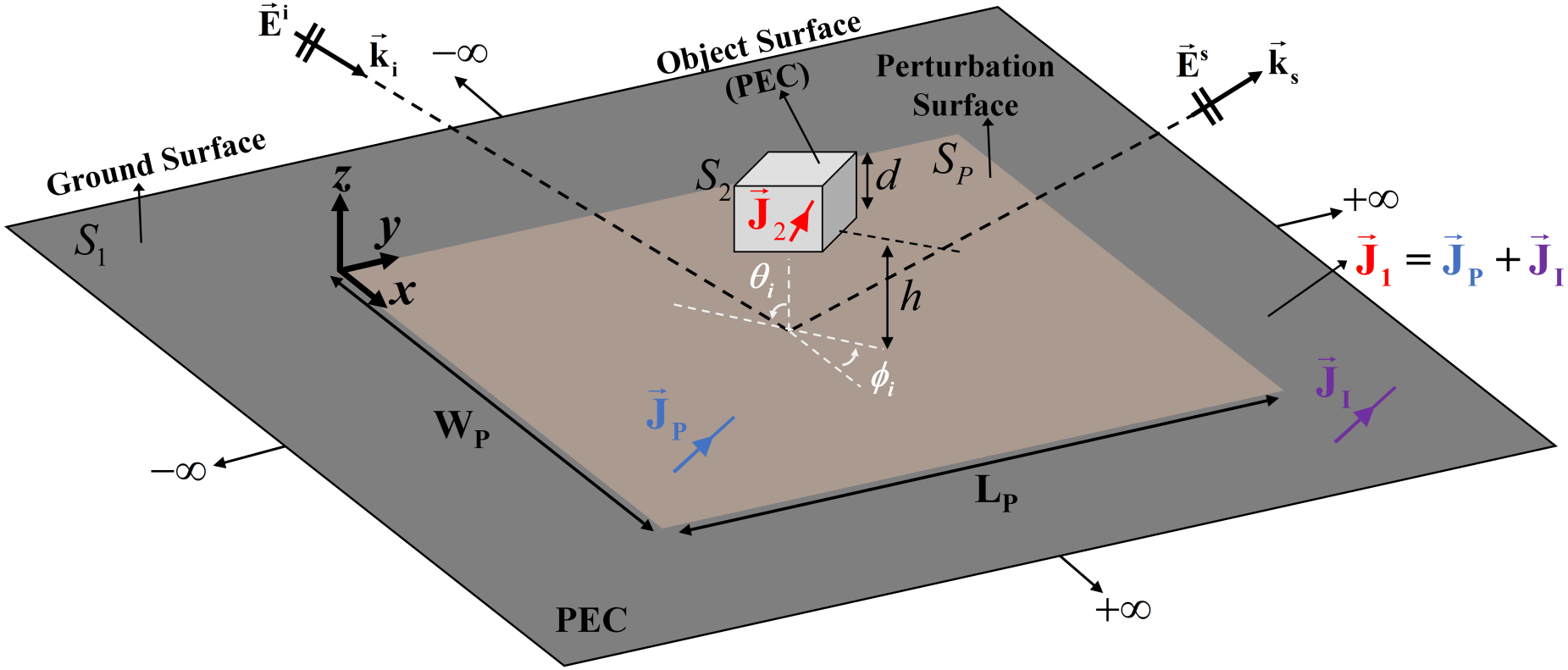

Figure 3.1 Configuration of a scattering problem from a PEC object above an infinite, flat, and PEC surface

3.1 Formulations

For a scattering example, if it is assumed that a plane wave is an incident on an infinite, flat, and PEC surface with an incidence angle of θ_i and ϕ_i as represented in Figure 3.1, the incident electric field is expressed as follows:

$$\vec{\mathbf{E}}_i = \hat{\mathbf{e}}_i E_0 e^{-j\vec{\mathbf{k}}_i\cdot\vec{\mathbf{r}}} = (\hat{\boldsymbol{\theta}}\cos\alpha + \hat{\boldsymbol{\phi}}\sin\alpha)E_0 e^{-j\beta_0\hat{\mathbf{k}}_i\cdot\vec{\mathbf{r}}} = (\hat{\mathbf{v}}_i + \hat{\mathbf{h}}_i)E_0 e^{-j\beta_0\hat{\mathbf{k}}_i\cdot\vec{\mathbf{r}}} \tag{3.1}$$

As shown in Figure 3.1, as well as a PEC target is placed on the infinite plane, and the upper half-space is the vacuum. Here, α is the polarization angle and $\vec{\mathbf{k}}_i = \beta_0\hat{\mathbf{k}}_i$ is the incident vector of the wave. $\alpha = 0°$ is θ-polarization (vertical $\hat{\mathbf{v}}_i$ or TM polarization), and $\alpha = 90°$ is ϕ-polarization (horizontal $\hat{\mathbf{h}}_i$ or TE polarization). In (3.1), the incident wave vector is $\vec{\mathbf{k}}_i = \beta_x\hat{\mathbf{x}} + \beta_y\hat{\mathbf{y}} - \beta_z\hat{\mathbf{z}}$, and the incident wave number is $k_i = \beta_0 = \omega\sqrt{\mu_0\epsilon_0}$, where $\beta_x = \beta_0\sin\theta_i\cos\phi_i$, $\beta_y = \beta_0\sin\theta_i\sin\phi_i$, and $\beta_z = \beta_0\cos\theta_i$. Besides, the scattered electric fields from the surface current densities can be written as given in (2.58). At this point, this scattering problem is solved by the image and perturbation method. The formulations for these methods are given, and the results are compared to each other.

3.1.1 Image Method

Using the image theory, the GF (Green's Function) of the scattering problem is found, as given in Figure 3.1. This method is straightforward, effective, and conventional for these scattering scenarios. It is the fastest solution because the mirrored image of the target is assumed to be located below the surface. The unknown surface currents originate only from the object and its sub-surface image. The tangential components of the generated electric fields on the infinite surface must be continuous, as shown in Figure 3.2. In dyadic form, the derived GF after applied image theory is given as follows [89]

$$\overline{\overline{\mathbf{G}}}_e(\vec{\mathbf{r}}|\vec{\mathbf{r}}') = \left(\bar{\bar{\mathbf{I}}} - \frac{1}{\beta_0^2}\nabla\nabla'\right)\left[G_0(\vec{\mathbf{r}}|\vec{\mathbf{r}}') - G_0(\vec{\mathbf{r}}|\vec{\mathbf{r}}_i')\right] + 2\hat{\mathbf{z}}\hat{\mathbf{z}}G_0(\vec{\mathbf{r}}|\vec{\mathbf{r}}_i') \tag{3.2}$$

where $G_0(\vec{\mathbf{r}}|\vec{\mathbf{r}}')$ is the free-space scalar GF, and $\bar{\bar{\mathbf{I}}}$ is the unit dyad. $\vec{\mathbf{r}}_i' = x\hat{\mathbf{x}} + y\hat{\mathbf{z}} - z\hat{\mathbf{z}}$ is the position vector that extends from the coordinate origin to a point on the object, indicating the source.

Furthermore, in the image domain scalar GF in (3.2)

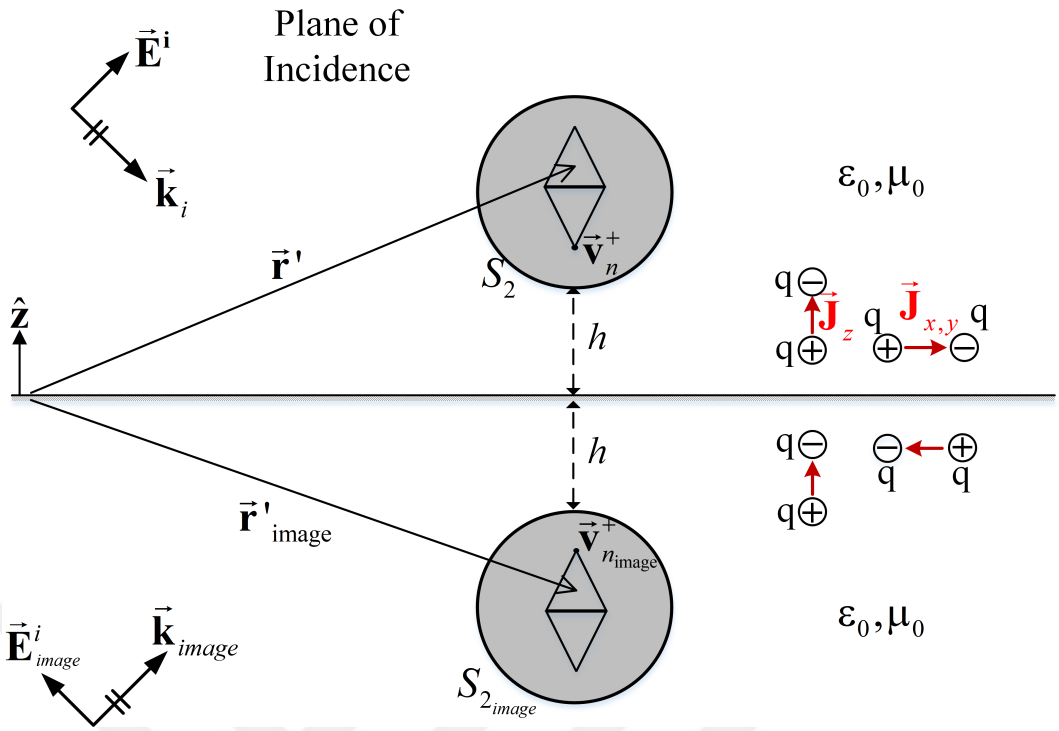

Figure 3.2 Diagram of the image theory adoption for an object above a flat, infinite, and PEC surface

$$G_0(\vec{\mathbf{r}}|\vec{\mathbf{r}}_i') = \frac{e^{-jk\left\|\vec{\mathbf{r}}-\vec{\mathbf{r}}_i'\right\|}}{4\pi\left\|\vec{\mathbf{r}}-\vec{\mathbf{r}}_i'\right\|} \tag{3.3}$$

with

$$\left\|\vec{\mathbf{r}}-\vec{\mathbf{r}}_i'\right\| = \sqrt{(x-x')^2+(y-y')^2+(z+z')^2} \tag{3.4}$$

is defined. Similarly, the wave vector in the image domain is

$$\vec{\mathbf{k}}_{image} = \beta_x\hat{\mathbf{x}} + \beta_y\hat{\mathbf{z}} + \beta_z\hat{\mathbf{z}} \tag{3.5}$$

and, as seen in Figure 3.2, the horizontal components of the electric field change direction, while the vertical components in the z-direction remain the same. After utilizing the image theory, if the boundary conditions are subjected on S_2:

$$\hat{\mathbf{n}}_2 \times \left[\vec{\mathbf{E}}^i + \vec{\mathbf{E}}^i_{image} + \vec{\mathbf{E}}^s\left(\vec{\mathbf{J}}_2\right)\right]\Big|_{\text{on } S_2} = \vec{\mathbf{0}} \tag{3.6}$$

is obtained. $\hat{\mathbf{t}}$ is the unit tangent vector of the surface S_2, and the IE of the scattered electric field $\vec{\mathbf{E}}^s\left(\vec{\mathbf{J}}_2\right)$ can be written in dyadic representation

$$\vec{\mathbf{E}}^s(\vec{\mathbf{r}}) = -j\omega\mu_0 \int_{S_2'} \overline{\overline{\mathbf{G}}}_e \cdot \vec{\mathbf{J}}_2\left(\vec{\mathbf{r}}'\right) dS_2' \tag{3.7}$$

Here, it should be noted that the unknown surface current is only on S_2 surface by means of employing the GF in (3.2). The current density $\vec{\mathbf{J}}_2$ on S_2 surface has expanded to a set of basis function:

$$\vec{\mathbf{J}}_2(\vec{\mathbf{r}}') = \sum_{\psi=1}^{N} I_\psi \vec{\mathbf{f}}_\psi(\vec{\mathbf{r}}') \tag{3.8}$$

where, $\vec{\mathbf{f}}_\psi(\vec{\mathbf{r}}')$ is RWG basis function and given in (2.67). Equation (3.6) can be written with a set of linear equations as follows

$$\overline{\overline{\mathbf{Z}}}_{(\zeta\psi)}\bar{\mathbf{I}}_{(\psi)} = \overline{\mathbf{V}}_{(\zeta)} \tag{3.9}$$

and each $Z_{\zeta\psi}$ term

$$\begin{aligned} Z_{\zeta\psi} = & j\beta_0\eta_0 \left[\int_{T_\zeta^\pm} \int_{T_\psi^\pm} \vec{\mathbf{f}}_\zeta(\vec{\mathbf{r}}) \cdot \vec{\mathbf{f}}_\psi(\vec{\mathbf{r}}') \left[G_0(\vec{\mathbf{r}}|\vec{\mathbf{r}}') - G_0(\vec{\mathbf{r}}|\vec{\mathbf{r}}_i') \right] dS_{T_\psi^\pm}' dS_{T_\zeta^\pm} \right. \\ & - \frac{1}{\beta_0^2} \int_{T_\zeta^\pm} \int_{T_\psi^\pm} \left[\nabla_s \cdot \vec{\mathbf{f}}_\zeta(\vec{\mathbf{r}}) \right] \left[\nabla_s' \cdot \vec{\mathbf{f}}_\psi(\vec{\mathbf{r}}') \right] \left[G_0(\vec{\mathbf{r}}|\vec{\mathbf{r}}') - G_0(\vec{\mathbf{r}}|\vec{\mathbf{r}}_i') \right] dS_{T_\psi^\pm}' dS_{T_\zeta^\pm} \\ & \left. + 2 \int_{T_\zeta^\pm} \int_{T_\psi^\pm} \left[\vec{\mathbf{f}}_\zeta(\vec{\mathbf{r}}) \cdot \hat{\mathbf{z}} \right] \left[\vec{\mathbf{f}}_\psi(\vec{\mathbf{r}}') \cdot \hat{\mathbf{z}} \right] G_0(\vec{\mathbf{r}}|\vec{\mathbf{r}}_i') dS_{T_\psi^\pm}' dS_{T_\zeta^\pm} \right] \end{aligned} \tag{3.10}$$

It should be noted here that each $Z_{\zeta\psi}$ term is created for a test and a basis function and is calculated by summing four different triangular surface integrals

$$Z_{\zeta\psi} = Z_{\zeta\psi}^{--} + Z_{\zeta\psi}^{+-} + Z_{\zeta\psi}^{-+} + Z_{\zeta\psi}^{++} \tag{3.11}$$

$T_\zeta^\pm$ and $T_\psi^\pm$ represent the test and basis functions' plus and minus triangles for the

adjacent edges on the discretized surface S_2. Also, each edge on the S_2 surface is discretized with the test function in creating $\overline{\mathbf{V}}$ array:

$$V_\zeta = \int_{T_\zeta^\pm} \vec{\mathbf{f}}_\zeta(\vec{\mathbf{r}}) \cdot \left[\vec{\mathbf{E}}^i + \vec{\mathbf{E}}^i_{image}\right] dS_{T_\zeta^\pm} \tag{3.12}$$

where

$$\vec{\mathbf{E}}^i + \vec{\mathbf{E}}^i_{image} = 2E_0 e^{-j\left(\beta_x x + \beta_y y\right)} \left[(\hat{\mathbf{h}}_i + \hat{\mathbf{v}}_i \times \hat{\mathbf{z}}) j \sin(\cos\theta_i \beta_0 z) + \hat{\mathbf{z}} \cos\theta_i \cos(\cos\theta_i \beta_0 z)\right] \tag{3.13}$$

After obtaining the unknown current density coefficients in (3.9), the scattered electric field expression for the far field region can be specified as:

$$\vec{\mathbf{E}}^s_{far\text{-}field}(\vec{\mathbf{r}}) = j\beta_0\eta \frac{e^{-j\beta_0 r}}{4\pi r} \left[\int_{S'} \hat{\mathbf{r}} \times \left[\hat{\mathbf{r}} \times \vec{\mathbf{J}}(\vec{\mathbf{r}}')\right]\left[e^{j\beta_0 \vec{\mathbf{r}}' \cdot \hat{\mathbf{r}}} - e^{j\beta_0 \vec{\mathbf{r}}'_i \cdot \hat{\mathbf{r}}}\right] dS' + \hat{\mathbf{z}} 2 \int_{S'} J_z(\vec{\mathbf{r}}') e^{j\beta_0 \vec{\mathbf{r}}'_i \cdot \hat{\mathbf{r}}} dS'\right] \tag{3.14}$$

In addition to these, the detailed acquisitions of (3.10) and (3.14) are presented in Appendix B.

3.1.2 Perturbation Method

In this section, a 3-D scattering example, as described in Figure 3.1, is handled by employing a current decomposition approach named the perturbation method. This method allows the equivalent current density of the infinite surface to be separated as induced (without the object present) and perturbed (with the object present) current densities. Also, with a simple assumption, the perturbed current density is strongly dominant in just a small ground surface region, and its intensity will rapidly decrease above the infinite surface. The perturbation method thereby assumes that the perturbed current density is zero except for the limited area of the infinite surface. As a result of this helpful assumption, the infinite solution domain can be restricted. This restricted perturbation domain is an area on the infinite ground surface where the object is closest to this ground surface, as shown in Figure 3.1. Finally, in the

numerical solution, the RWG basis function discretizes these surface currents, and the MoM is exploited to solve the resulting surface EFIEs.

As seen in Figure 3.1, W_P and L_P are the dimensions of the restricted perturbation surface in $\hat{\mathbf{x}}$ and $\hat{\mathbf{y}}$ directions, respectively. Also, in this scattering scenario, the object is a cube, and d is the length of one side of it. Furthermore, $\vec{\mathbf{J}}_P$ represents the perturbed current density on the S_P restricted surface called perturbation surface. $\vec{\mathbf{J}}_1$ is the total current density on S_1 infinite, flat, and PEC surface. $\vec{\mathbf{J}}_I$ specifies the induced current density on the S_1 surface without the object is present. The surface current density $\vec{\mathbf{J}}_1$, defined on the surface S_1, can now be decomposed

$$\lim_{W_p, L_p \to \infty} \vec{\mathbf{J}}_1 = \vec{\mathbf{J}}_I + \vec{\mathbf{J}}_P \tag{3.15}$$

and with our assumption for a finite perturbation region

$$\vec{\mathbf{J}}_1 \approx \vec{\mathbf{J}}_I + \vec{\mathbf{J}}_P \tag{3.16}$$

At this point, our assumption should be reminded again that $\vec{\mathbf{J}}_P$ is defined for only a finite S_P surface and is zero for others. Indeed, this perturbed current density does not entirely disappear on S_1 ground surface as given (3.15). However, the intensity of its distribution is minimal except for S_p and can be therefore considered nonexistent. To summarize, (3.16) is an approximation and is more convergent if the perturbation region is carefully determined. Now, if the boundary condition on the ground plane is applied while the object is present, then

$$\hat{\mathbf{n}}_1 \times \left[\vec{\mathbf{E}}^i + \vec{\mathbf{E}}^s\left(\vec{\mathbf{J}}_1\right) + \vec{\mathbf{E}}^s\left(\vec{\mathbf{J}}_2\right)\right]\Big|_{\text{on } S_1} = \vec{\mathbf{0}} \tag{3.17}$$

and without the object above the ground plane

$$\hat{\mathbf{n}}_1 \times \left[\vec{\mathbf{E}}^i + \vec{\mathbf{E}}^s\left(\vec{\mathbf{J}}_I\right)\right]\Big|_{\text{on } S_1} = \vec{\mathbf{0}} \tag{3.18}$$

This equation is also valid for S_p surface

$$\hat{\mathbf{n}}_P \times \left[\vec{\mathbf{E}}^i + \vec{\mathbf{E}}^s\left(\vec{\mathbf{J}}_I\right)\right]\Big|_{\text{on } S_p} = \vec{\mathbf{0}} \tag{3.19}$$

where, $\hat{\mathbf{n}}_P$ is unit normal vector of the S_P surface. If (3.16) is substituted in (3.17), on S_p

$$\hat{\mathbf{n}}_P \times \left[\vec{\mathbf{E}}^i + \vec{\mathbf{E}}^s\left(\vec{\mathbf{J}}_I\right) + \vec{\mathbf{E}}^s\left(\vec{\mathbf{J}}_P\right) + \vec{\mathbf{E}}^s\left(\vec{\mathbf{J}}_2\right)\right]\Big|_{\text{on } S_P} = \vec{\mathbf{0}} \tag{3.20}$$

Then, if we employ (3.19) in (3.16) for S_p surface

$$\hat{\mathbf{n}}_P \times \left[\vec{\mathbf{E}}^s\left(\vec{\mathbf{J}}_P\right) + \vec{\mathbf{E}}^s\left(\vec{\mathbf{J}}_2\right)\right]\Big|_{\text{on } S_P} = \vec{\mathbf{0}} \tag{3.21}$$

The boundary condition on S_2

$$\hat{\mathbf{n}}_2 \times \left[\vec{\mathbf{E}}^i + \vec{\mathbf{E}}^s\left(\vec{\mathbf{J}}_I\right) + \vec{\mathbf{E}}^s\left(\vec{\mathbf{J}}_P\right) + \vec{\mathbf{E}}^s\left(\vec{\mathbf{J}}_2\right)\right]\Big|_{\text{on } S_2} = \vec{\mathbf{0}} \tag{3.22}$$

and, if it is rearranged

$$\hat{\mathbf{n}}_2 \times \left[\vec{\mathbf{E}}^s\left(\vec{\mathbf{J}}_P\right) + \vec{\mathbf{E}}^s\left(\vec{\mathbf{J}}_2\right)\right]\Big|_{\text{on } S_2} = -\hat{\mathbf{n}}_2 \times \left[\vec{\mathbf{E}}^i + \vec{\mathbf{E}}^s\left(\vec{\mathbf{J}}_I\right)\right]\Big|_{\text{on } S_2} \tag{3.23}$$

Here, $\vec{\mathbf{E}}^s\left(\vec{\mathbf{J}}_I\right)$ can be calculated analytically. This is the electric field of the reflected plane wave for a flat PEC surface. Therefore, just as in (3.13), the total electric field on S_2 can be found for both polarization

$$\vec{\mathbf{E}}^i + \vec{\mathbf{E}}^r = 2E_0 e^{-j\left(\beta_x x + \beta_y y\right)}\left[(\hat{\mathbf{h}}_i + \hat{\mathbf{v}}_i \times \hat{\mathbf{z}}) j \sin(\cos\theta_i \beta_0 z) + \hat{\mathbf{z}} \cos\theta_i \cos(\cos\theta_i \beta_0 z)\right] \tag{3.24}$$

(3.21) and (3.23) are utilized to solve the unknown surface currents on S_p and S_2 surfaces. The right side of the equations shows the known, while the left side consists of the unknowns. With this vector identity $\hat{\mathbf{n}} \times \left(\hat{\mathbf{n}} \times \vec{\mathbf{J}}\right) = -\left[\vec{\mathbf{J}}\right]_{tan}$, these equations can be re-expressed

$$\left[\vec{\mathbf{E}}^s\left(\vec{\mathbf{J}}_P\right) + \vec{\mathbf{E}}^s\left(\vec{\mathbf{J}}_2\right)\right]_{\text{tan}} = \vec{\mathbf{0}} \quad \text{on } S_P \tag{3.25}$$

$$\left[\vec{\mathbf{E}}^s\left(\vec{\mathbf{J}}_P\right) + \vec{\mathbf{E}}^s\left(\vec{\mathbf{J}}_2\right)\right]_{\text{tan}} = -\left[\vec{\mathbf{E}}^i + \vec{\mathbf{E}}^r\right]_{\text{tan}} \quad \text{on } S_2 \tag{3.26}$$

We can now apply the MoM solution to (3.25) and (3.26). Therefore, if these currents are expanded with RWG basis functions and exploiting Galerkin-type testing functions, they will yield a matrix system as in (3.9)

$$\begin{bmatrix} \overline{\overline{\mathbf{Z}}}_{11}^{(\vec{\mathbf{J}}_P)} & \overline{\overline{\mathbf{Z}}}_{12}^{(\vec{\mathbf{J}}_2)} \\ \overline{\overline{\mathbf{Z}}}_{21}^{(\vec{\mathbf{J}}_P)} & \overline{\overline{\mathbf{Z}}}_{12}^{(\vec{\mathbf{J}}_2)} \end{bmatrix} \begin{bmatrix} \overline{\mathbf{I}}_{\psi_{11}}^{(P)} \\ \overline{\mathbf{I}}_{\psi_{21}}^{(2)} \end{bmatrix} = \begin{bmatrix} \overline{\mathbf{V}}_{\zeta_{11}}^{(P)} \\ \overline{\mathbf{V}}_{\zeta_{21}}^{(2)} \end{bmatrix} \tag{3.27}$$

where, a general statement of any edge of $\overline{\overline{\mathbf{Z}}}$ matrices for plus or minus and testing or basis triangle surfaces on S_p and S_2

$$Z_{\zeta\psi} = j\beta_0\eta_0 \Bigg[\int_{T_\zeta^\pm} \int_{T_\psi^\pm} \vec{\mathbf{f}}_\zeta(\vec{\mathbf{r}}) \cdot \vec{\mathbf{f}}_\psi(\vec{\mathbf{r}}') G_0(\vec{\mathbf{r}}|\vec{\mathbf{r}}') dS'_{T_\psi^\pm} dS_{T_\zeta^\pm} - \frac{1}{\beta_0^2} \int_{T_\zeta^\pm} \int_{T_\psi^\pm} \left[\nabla_s \cdot \vec{\mathbf{f}}_\zeta(\vec{\mathbf{r}})\right] \left[\nabla'_s \cdot \vec{\mathbf{f}}_\psi(\vec{\mathbf{r}}')\right] G_0(\vec{\mathbf{r}}|\vec{\mathbf{r}}') dS'_{T_\psi^\pm} dS_{T_\zeta^\pm} \Bigg] \tag{3.28}$$

Similarly, if these general expressions for $\overline{\mathbf{V}}$ arrays on S_p and S_2 surfaces

$$V_{\zeta 11}^{(P)} = 0 \tag{3.29}$$

$$V_{\zeta 11}^{(2)} = \int_{S_{T_\zeta^\pm}^{(2)}} \vec{\mathbf{f}}_\zeta(\vec{\mathbf{r}}) \cdot \left[\vec{\mathbf{E}}^i + \vec{\mathbf{E}}^r\right] dS_{T_\zeta^\pm}^{(2)} \tag{3.30}$$

is written. After solving this linear equation system, the unknown current coefficients will be acquired. Hence, the scattering electric field in the far field region can be stated for $\vec{\mathbf{J}}_P$ and $\vec{\mathbf{J}}_2$ on S_P and S_2 surfaces, respectively:

$$\vec{\mathbf{E}}^s_{far\text{-}field}(\vec{\mathbf{r}}) = j\beta_0\eta \frac{e^{-j\beta_0 r}}{4\pi r} \left[\int_{S'} \hat{\mathbf{r}} \times \left[\hat{\mathbf{r}} \times \vec{\mathbf{J}}(\vec{\mathbf{r}}')\right] \left[e^{j\beta_0 \vec{\mathbf{r}}' \cdot \hat{\mathbf{r}}}\right] dS' \right] \tag{3.31}$$

It should be noted that (3.31) is a general expression based on the current densities under the far-field condition. The total electric field at a position in the far-field region is calculated by the current densities on the surfaces, and finally, the surface effect on the the radar echo of the object can be observed. The Radar Cross Section (RCS) of an object is thereby defined as follows

$$\mathrm{RCS} = \lim_{r\to\infty} 4\pi r^2 \frac{\left\|\vec{\mathbf{E}}^{s}_{far\text{-}field}\right\|^2}{\left\|\vec{\mathbf{E}}^{i}\right\|^2} \tag{3.32}$$

where $\vec{\mathbf{E}}^{s}_{far\text{-}field}$ is the total electrical field at an observation point in the far-field region caused by $\vec{\mathbf{J}}_P$ and $\vec{\mathbf{J}}_2$ current densities. $\vec{\mathbf{E}}^{i}$ is the incident plane-wave defined in (3.1). Besides, the RCS of the object can be calculated by employing the total scattered electric field as given in (3.14) with the image method mentioned in the previous subsection. The image method will be used to prove the accuracy performance of the perturbation method.

3.2 Numerical Results

In order to compare the precision of the proposed perturbation approach and determine the right perturbation domain for various scattering circumstances, this section examines the numerical results of the formulations. The RCS results to be obtained using image theorem and perturbation methods are illustrated, and the impact of the chosen area for the perturbation region is carefully evaluated. In order to assess solution correctness and limitations, the object's height, size, and incidence angles are also considered. Following these projections, a proper empirical formula for choosing the perturbation region is offered.

3.2.1 Determination of Perturbation Region

In order to present the proposed perturbation method with acceptable accuracy, the size of the perturbation surface area needs to be determined intelligently. Examining the perturbed current distribution on the infinite ground plane may be helpful. For this purpose, as demonstrated in Figures 3.3,3.4,3.5,3.6,3.7, and 3.8 several scattering scenarios with a selection perturbation area of $12.5\lambda \times 12.5\lambda$ are performed to evaluate the perturbed current distribution on this truncated surface. Initially, a PEC cube with a side length of 0.3λ ($d = 0.3\lambda$) is placed above the surface at a distance of 0.1λ ($h = 0.1\lambda$), where the incidence angle is 0°. Secondly, the incidence angle is changed to 85°, and the current density result on the surface is depicted in Figure 3.4. For the third simulation, as shown in Figure 3.5, the h parameter is increased to 0.2λ, where the incidence angle is set to 0° again. Also, in the fourth scenario, the d parameter is altered to 0.6λ when the angle of incidence is 0°. Here the h parameter is 0.1λ again. So far, all simulations are illuminated by a linearly polarized plane wave in the negative y-direction ($\theta_i = 0°$, $\phi_i = 0°$, and $\alpha_i = 90°$). In Figure 3.7, the polarization of the plane wave is shifted to the positive x-direction for the fifth example ($\theta_i = 0°$, $\phi_i = 0°$,

and $\alpha_i = 0°$), while other parameters remain the same. In Figure 3.8, the horizontal polarization in the second example is converted vertically. The average mesh length of a triangle for the surface is 0.2λ. The cube is discretized with triangles of 0.1λ average length. The distributions of each current density on this truncated surface are given in Figure 3.4 for these five cases, respectively. Unless otherwise stated in this chapter, the free space wavelength is denoted as λ in all scattering examples and numerical results.

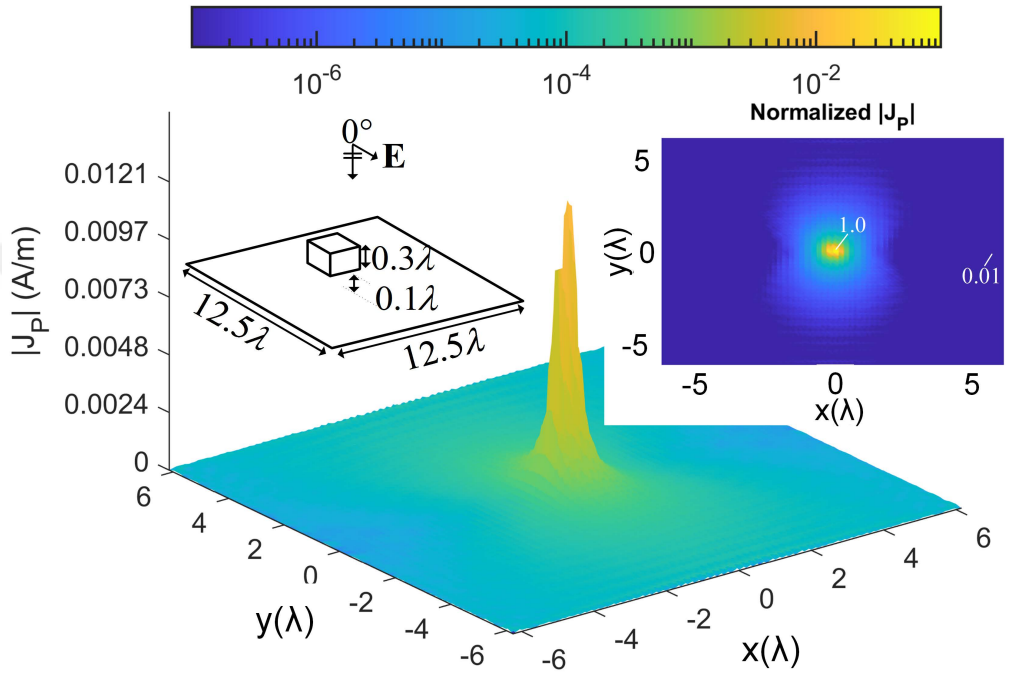

Figure 3.3 Perturbed electric current density for a limited region on the infinite ground plane ($d = 0.3$ m, $h = 0.1$ m, $\theta_i = 0°$, $\phi_i = 0°$, $\alpha_i = 90°$)

As can be easily seen from Figures 3.3,3.4,3.5,3.6,3.7, and 3.8, the perturbation current distributions predominate only in a limited region where the objects are closest to the infinite surface. These perturbed currents spread on the infinite surface depending on object size, distance from the surface, incidence angle, and polarization. As in our experiments, the spreading region of the perturbation current increases dramatically with the object's distance from the surface and the object's dimension. In contrast, the maximum amplitude of the current equally decreases. Furthermore, as expected, the distribution of the perturbation current density is also dependent on the polarization of the incident wave, as demonstrated in Figures 3.4,3.5,3.6,3.7, and 3.8. The vertical polarization distributes the current more than the horizontal polarization along the infinite surface, which is expected to increase the effect of perturbation current in the total scattering electric field.

Moreover, in these experiments, the normalized current densities are also shared

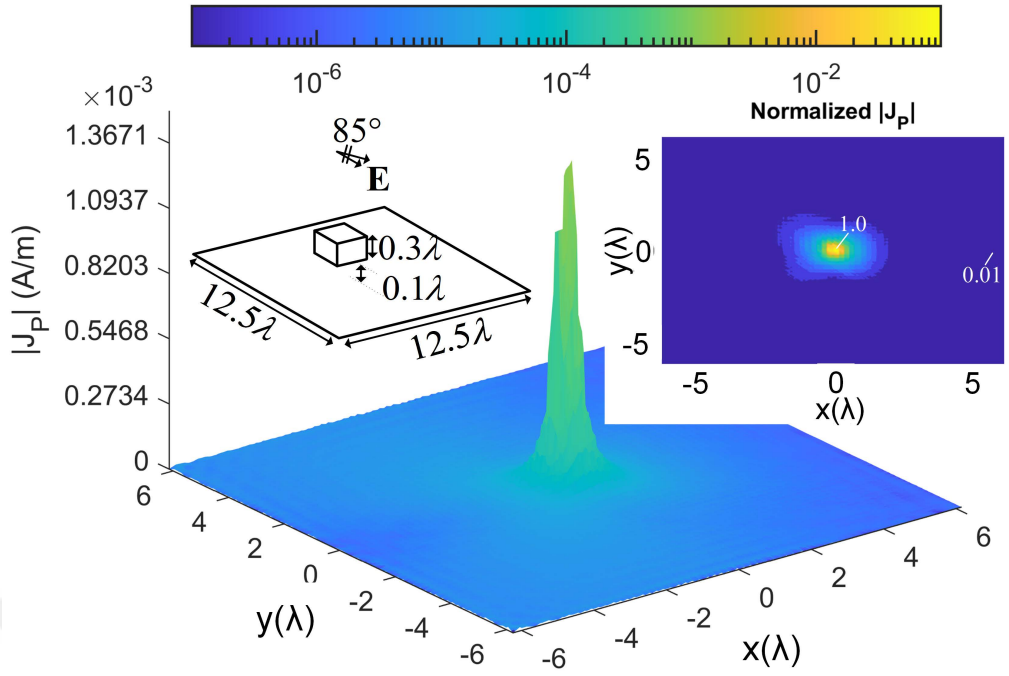

Figure 3.4 Perturbed electric current density for a limited region on the infinite ground plane ($d = 0.3$ m, $h = 0.1$ m, $\theta_i = 85°$, $\phi_i = 0°$, $\alpha_i = 90°$)

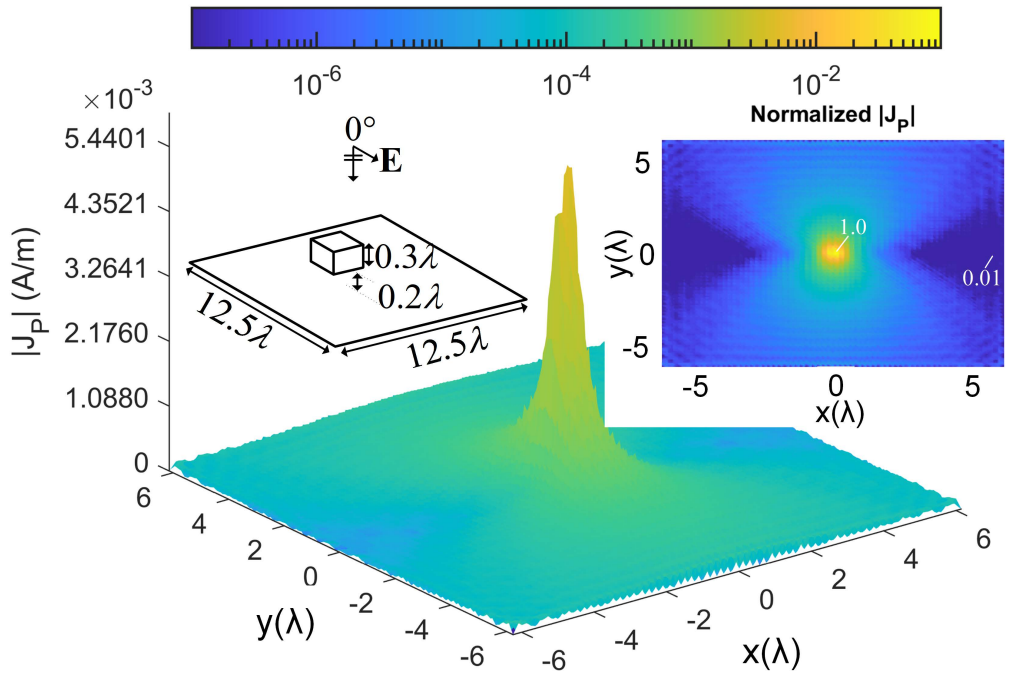

Figure 3.5 Perturbed electric current density for a limited region on the infinite ground plane ($d = 0.3$ m, $h = 0.2$ m, $\theta_i = 0°$, $\phi_i = 0°$, $\alpha_i = 90°$)

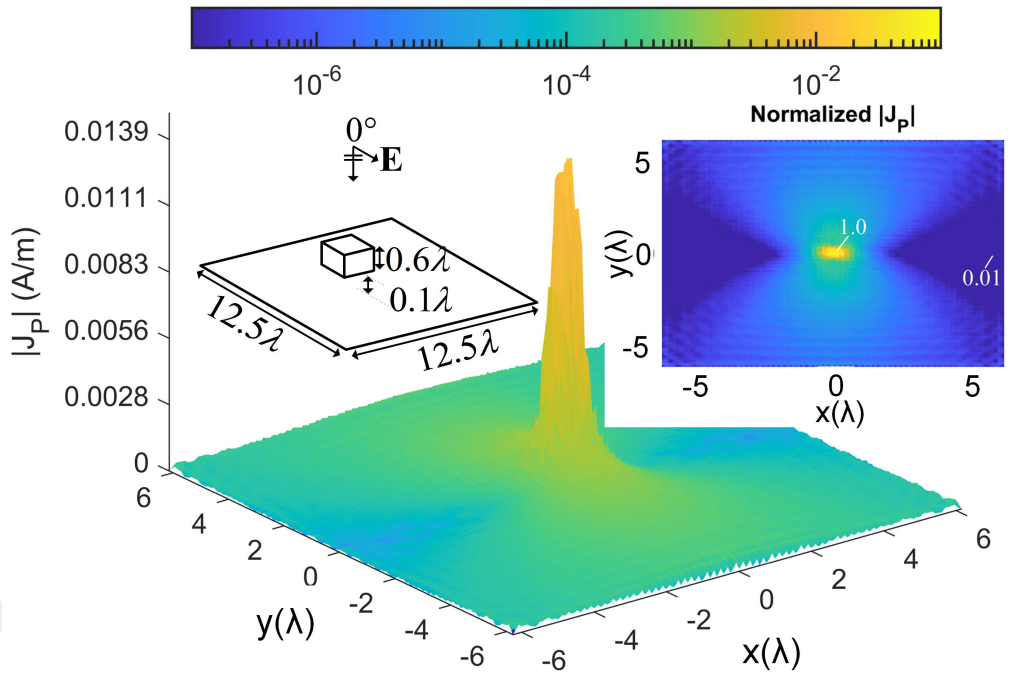

Figure 3.6 Perturbed electric current density for a limited region on the infinite ground plane ($d = 0.6$ m, $h = 0.1$ m, $\theta_i = 0°$, $\phi_i = 0°$, $\alpha_i = 90°$)

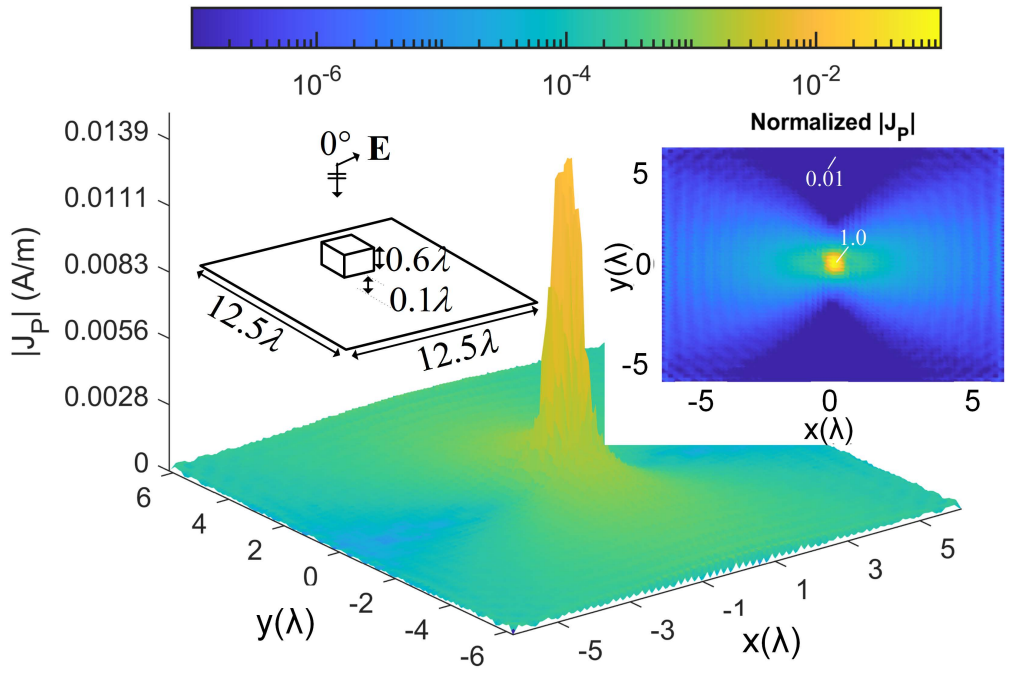

Figure 3.7 Perturbed electric current density for a limited region on the infinite ground plane ($d = 0.6$ m, $h = 0.1$ m, $\theta_i = 0°$, $\phi_i = 0°$, $\alpha_i = 0°$)

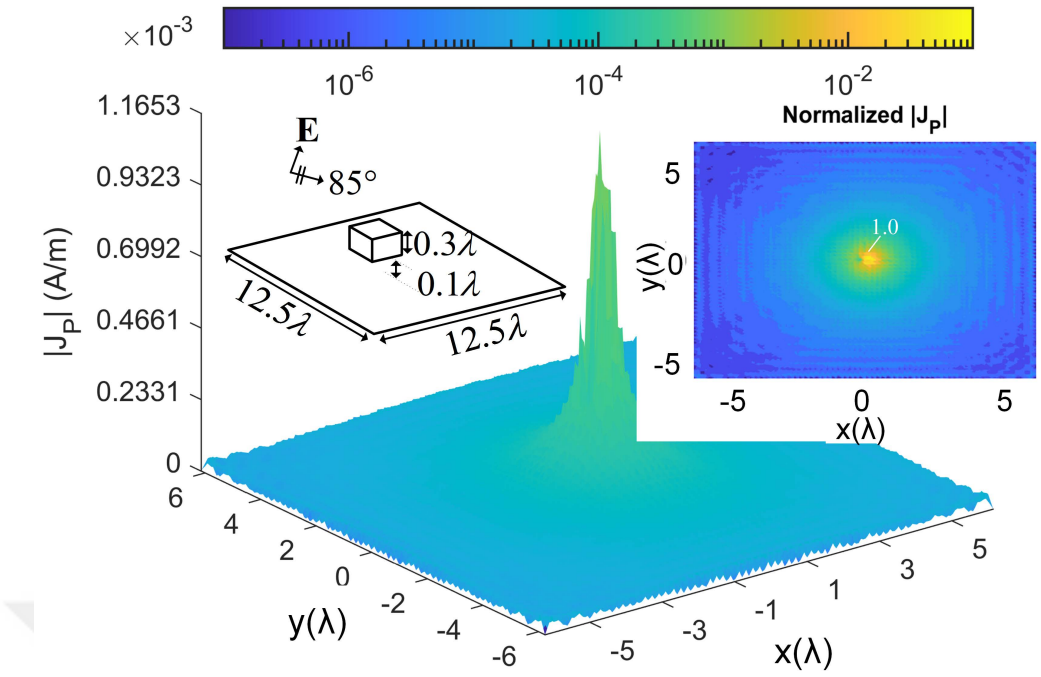

Figure 3.8 Perturbed electric current density for a limited region on the infinite ground plane ($d = 0.3$ m, $h = 0.1$ m, $\theta_i = 85°$, $\phi_i = 0°$, $\alpha_i = 90°$)

in Figures 3.3,3.4,3.5,3.6,3.7, and 3.8. Here, a 1% value of the maximum current density is accepted as a reference to ensure a reliable solution when truncating the solution region. Also, an important observation is obtained such that the oblique incidence to the surface reduces the dominant region of the current density while the normal incidence increases significantly. Accordingly, an appropriate empirical formula for which the mentioned parameters should be included can be derived in order to estimate the minimum length of the perturbation region in the x-direction

$$W_p \geq 4.3\pi \sqrt[4]{\frac{16h_{(\lambda)}^3 d_{(\lambda)} + h_{(\lambda)} d_{(\lambda)}^3}{\left(\theta_i^{(rad)}\right)^4 (|\hat{\mathbf{e}}_i \cdot \hat{\mathbf{x}}|) + 6.41\pi^4 \times 10^{-4}}} (|\hat{\mathbf{e}}_i \cdot (\hat{\mathbf{x}} + 3\hat{\mathbf{z}})| + 1) \tag{3.33}$$

and this formula in the y-direction is as follows

$$L_p \geq 4.3\pi \sqrt[4]{\frac{16h_{(\lambda)}^3 d_{(\lambda)} + h_{(\lambda)} d_{(\lambda)}^3}{\left(\theta_i^{(rad)}\right)^4 (|\hat{\mathbf{e}}_i \cdot \hat{\mathbf{y}}|) + 6.41\pi^4 \times 10^{-4}}} (|\hat{\mathbf{e}}_i \cdot (\hat{\mathbf{y}} + 3\hat{\mathbf{z}})| + 1) \tag{3.34}$$

Since the perturbed current distribution on the surface appears pretty similar to a Dirac delta distribution, the above equations in (3.33) and (3.34) are experimentally derived based on a resonance function representing the Dirac delta distribution. It

should be noticed that the calculated lengths of the perturbation region determine the current error level, which must be carefully decided—also, (3.33) and (3.34) should be tested for several scattering examples.

3.2.2 Validation of Perturbation Approach

A validation of the proposed method with a selection of perturbation domain is required by utilizing (3.33) and (3.34) to evaluate approximate lengths. For this purpose, the RCS and relative error results of scattering electric fields are initially discussed for different object sizes and distances from the surface. Here, the definition of the relative error is specified as follows

$$\varepsilon(\theta_s, \phi_s) = \frac{\left\| \vec{\mathbf{E}}^s_{image}(\theta_s, \phi_s) - \vec{\mathbf{E}}^s_{perturbation}(\theta_s, \phi_s) \right\|}{\left\| \vec{\mathbf{E}}^s_{image}(\theta_s, \phi_s) \right\|} \tag{3.35}$$

In order to verify the perturbation method whose region size was discussed above, the RCS and relative error results for the $x-z$ and $y-z$ planes are depicted in Figures 3.9–3.12 and 3.13–3.16 for various h (0.1λ, 0.2λ, 0.4λ, and 0.6λ) and d (0.3λ, 0.6λ, and 0.9λ) values. All scattering examples after this point are illuminated to a cube object above a flat plane with an incident angle of $\theta_i = 85^\circ, \phi_i = 30^\circ$, and $\alpha_i = 90^\circ$. The lengths of the perturbation area are determined as $18\lambda \times 18\lambda$ for $h = 0.6\lambda$, $d = 0.3\lambda$ by using (3.33) and (3.34). The dimension of the perturbation region remains the same in all simulations.

As shown in Figures 3.9 and 3.10, the perturbed current exists dominantly only within the selected perturbation region. This selection enables the scattered electric field to be highly compatible with the solution found by the image theorem. The parameter d is constant with 0.3λ, and h is altered as 0.2λ, 0.4λ, and 0.6λ. The compatibility of the object's RCS results with the image theorem in both the $x-z$ and $y-z$ planes is highly satisfactory except for scattering angles near the surface, as seen in Figures 3.9 and 3.10, respectively. In Figures 3.11 and 3.12, the relative error graphs of the electric fields scattered by the decomposition and image theorem are plotted depending on the angle in the $x-z$ and $y-z$ planes. Thanks to the selected perturbation region, by using (3.33) and (3.34), high accuracy is achieved at a wide scattering angle range. In Figures 3.13–3.16, h is fixed at 0.1λ, and d is replaced 0.3λ, 0.6λ, and 0.9λ to plot the graphs of the RCS and relative error results. Despite the perturbed current widely spreading over the infinite surface, the results are entirely satisfactory in these experiments.

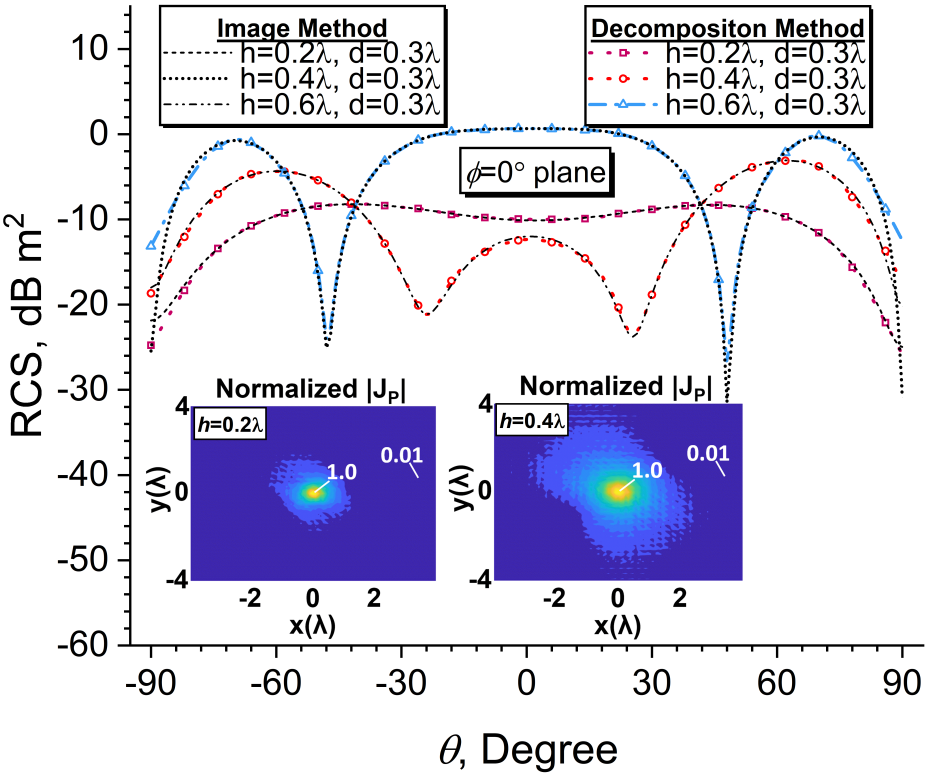

Figure 3.9 RCS result of the perturbation method with image theorem for various h values in $\phi = 0°$ plane

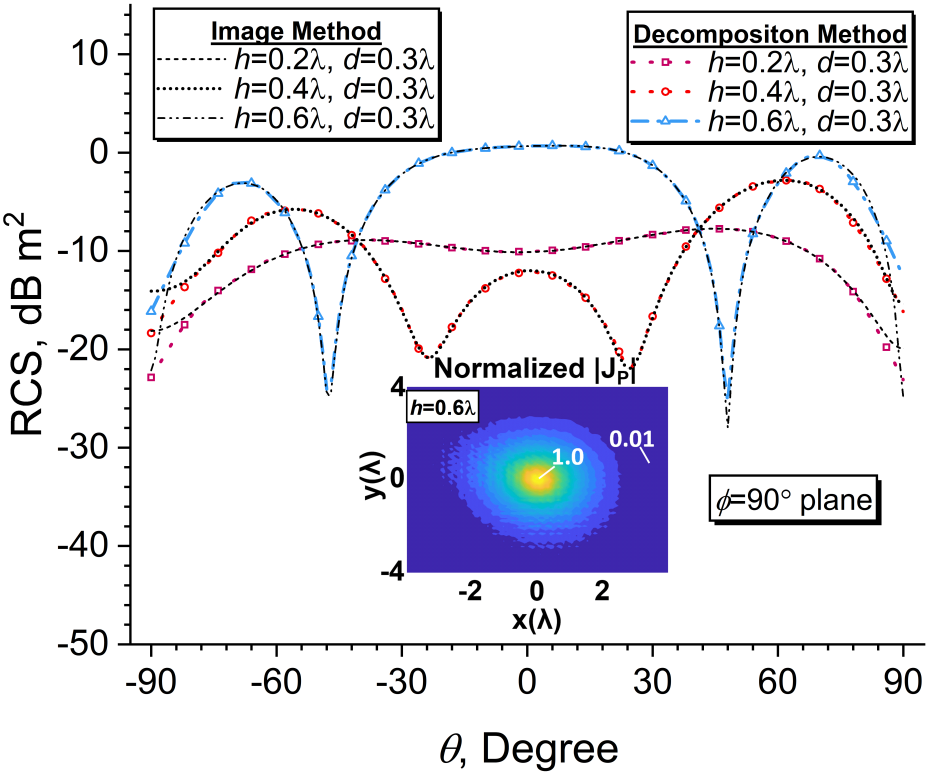

Figure 3.10 RCS result of the perturbation method with image theorem for various h values in $\phi = 90°$ plane

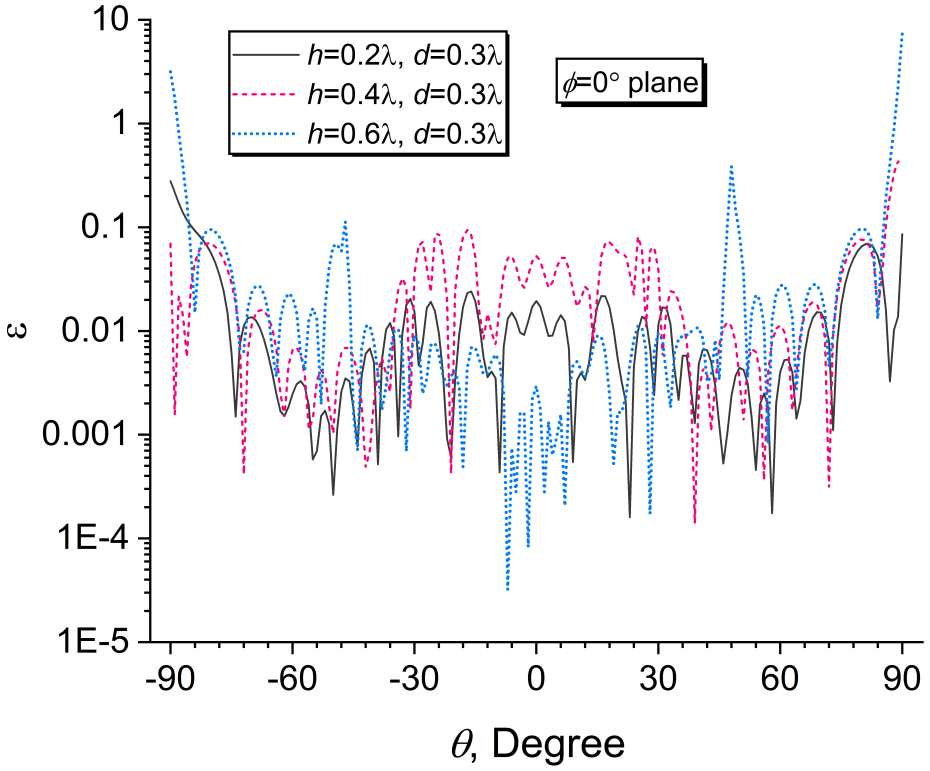

Figure 3.11 Relative error result of the perturbation method with image theorem for various h values in $\phi = 0°$ plane

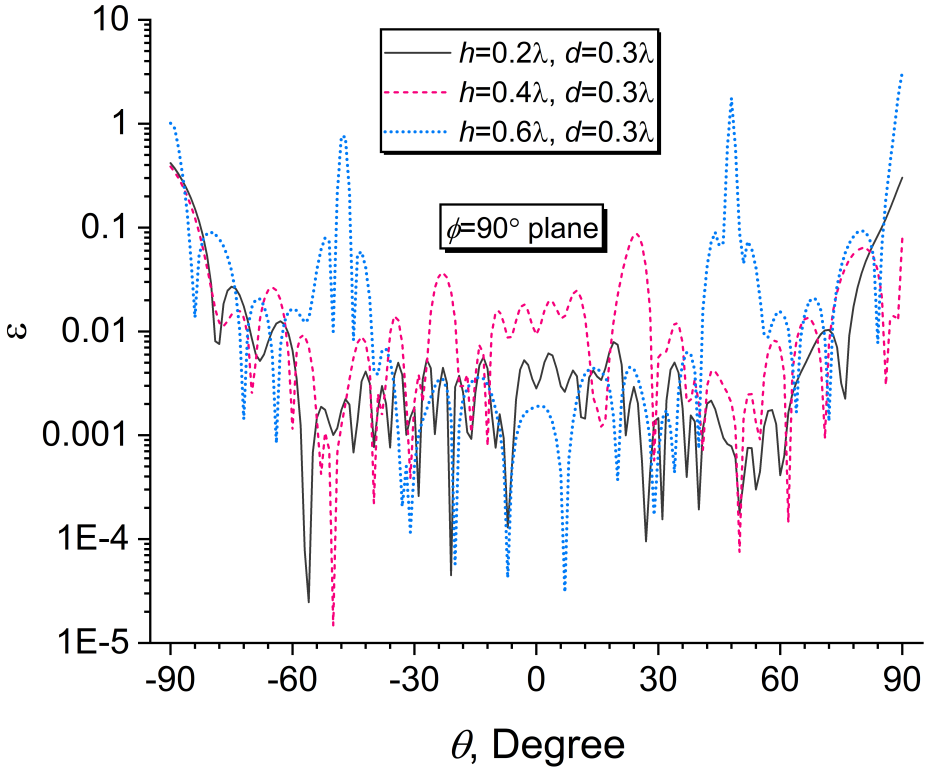

Figure 3.12 Relative error result of the perturbation method with image theorem for various h values in $\phi = 90°$ plane

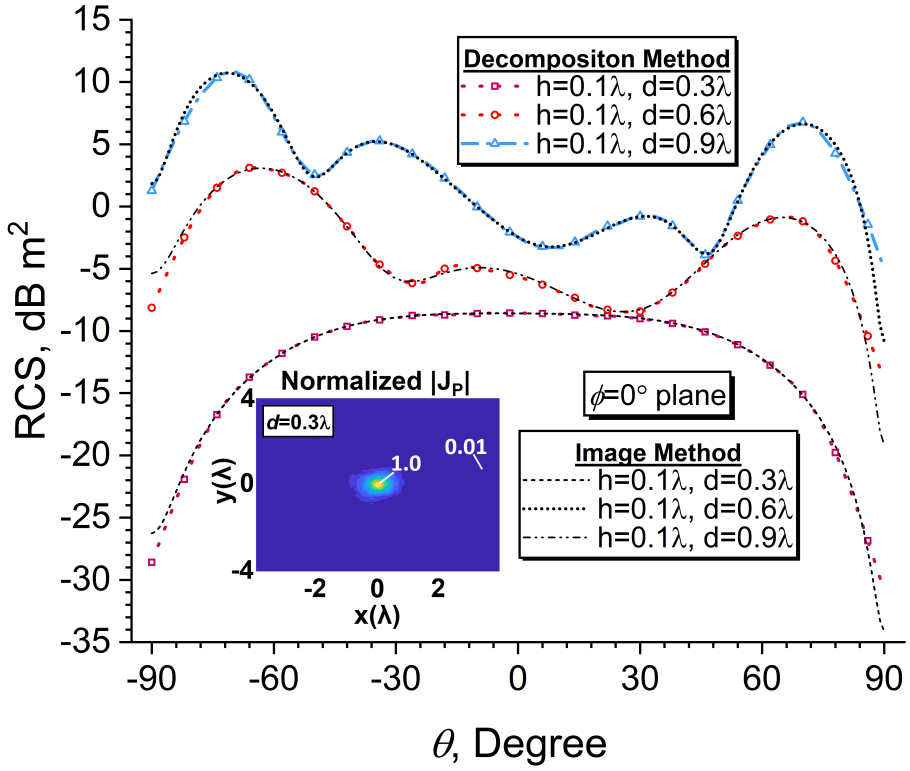

Figure 3.13 RCS result of perturbation method with image theorem for various d values in $\phi = 0°$ plane

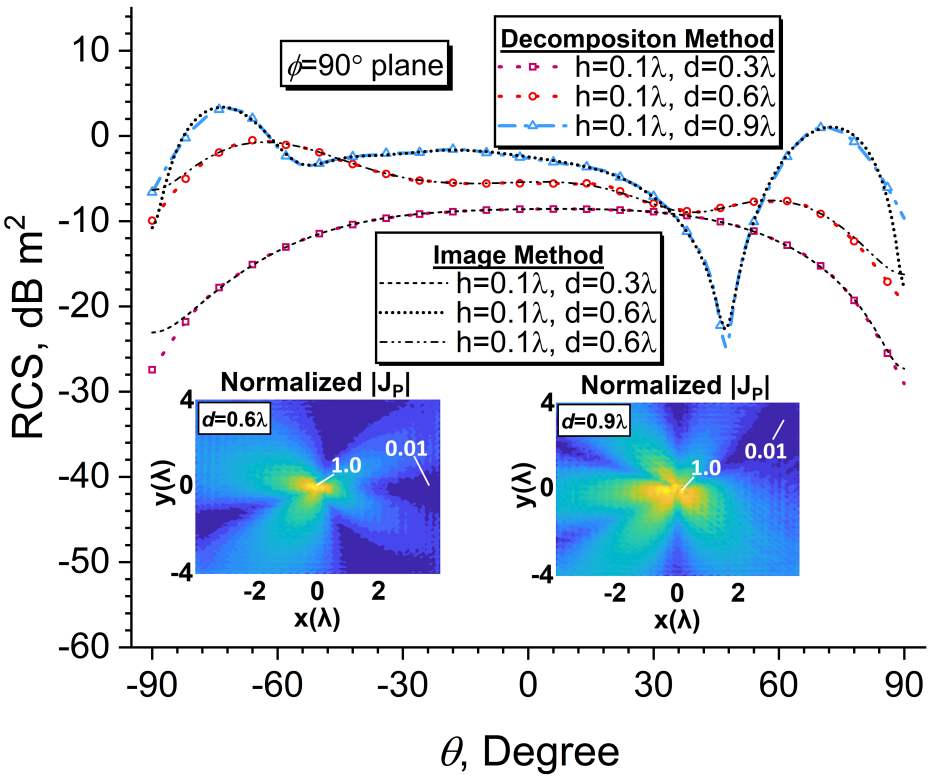

Figure 3.14 RCS result of perturbation method with image theorem for various d values in $\phi = 90°$ plane

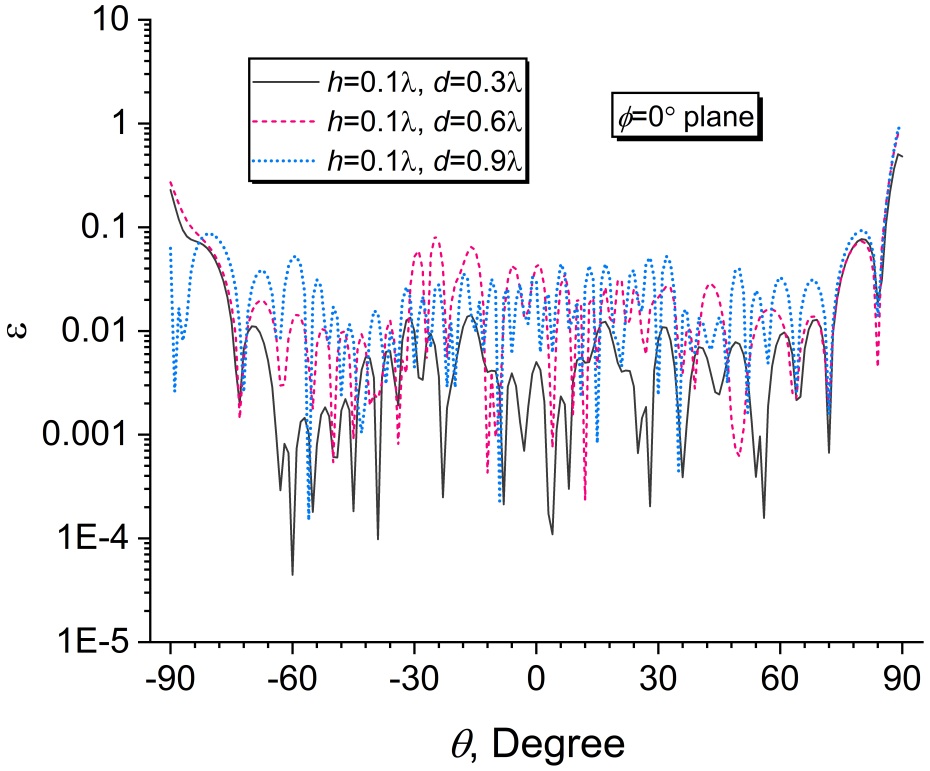

Figure 3.15 Relative error result of the perturbation method with image theorem for various d values in $\phi = 0°$ plane

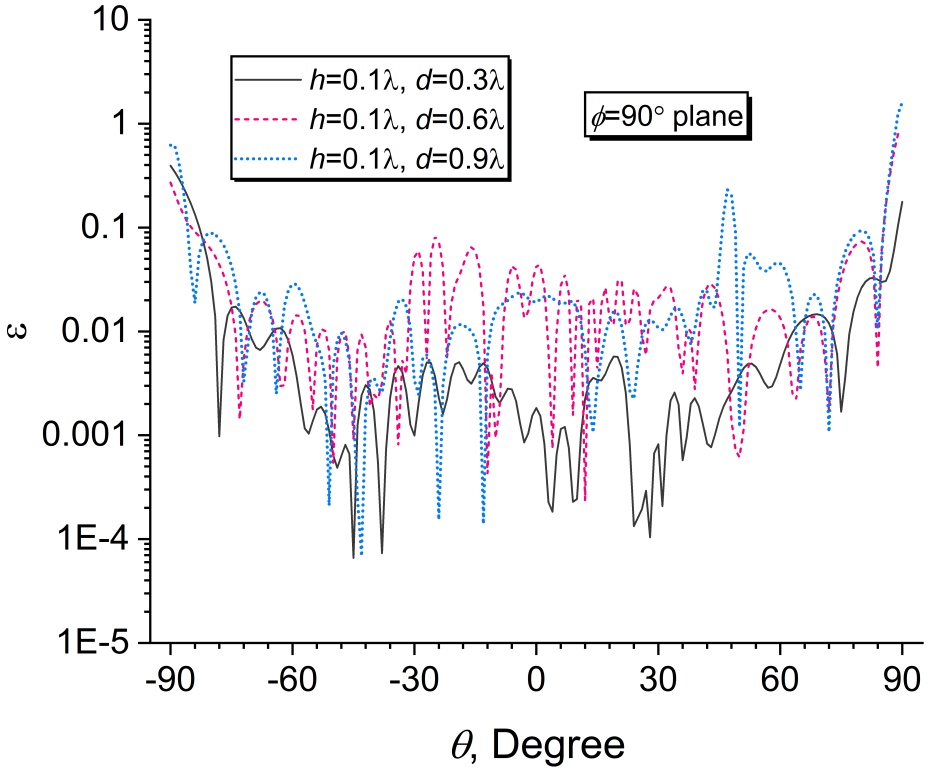

Figure 3.16 Relative error result of perturbation method with image theorem for various $d$values in $\phi = 90°$ plane

4
EFIE ANALYSES FOR PEC OBJECT SCATTERING ABOVE ARBITRARILY ROUGH CONDUCTIVE PERIODIC SURFACES WITH PERTURBATION APPROACH

In this chapter, a three-dimensional scattering problem from a PEC object above a periodic conductive rough surface is addressed using a current decomposition method (perturbation method) based on the separation of equivalent current density on the periodic surface as induced and perturbed current densities. The infinite solution domain is bounded so that the perturbed current density caused by the object is firmly dominant only in a limited area on the periodic surface. Besides, the RWG basis function is utilized to discretize currents. The MoM solves the resulting EFIE equations for these currents on the surface of the object and the bounded domain for the periodic surface. In addition, the induced current on the periodic surface in the absence of the object was found as described in Chapter 2.

In contrast to the previous chapter, this induced current with the absence of the object on half-space will be calculated fully numerically. Again, as mentioned in the previous Chapter 2, although there are analytical solutions, it is not valid for all surface roughness. For these reasons, the proposed solution method offers a unique approach to calculating the RCS of an object placed on an arbitrarily rough surface. Since this rough surface and object interact electromagnetically, significant changes will occur in the RCS of the object. Nevertheless, the proposed approach handles this challenging and crucial scattering problem with sufficient accuracy.

4.1 Formulation

The infinite PEC surface is modeled as periodic to solve the half-space problem as represented in Figure 4.1. The total induced current without the object present is found through this model as discussed in Chapter 2. The rough surface is periodic with L_x and L_y, and the surface function satisfies the condition of the periodicity

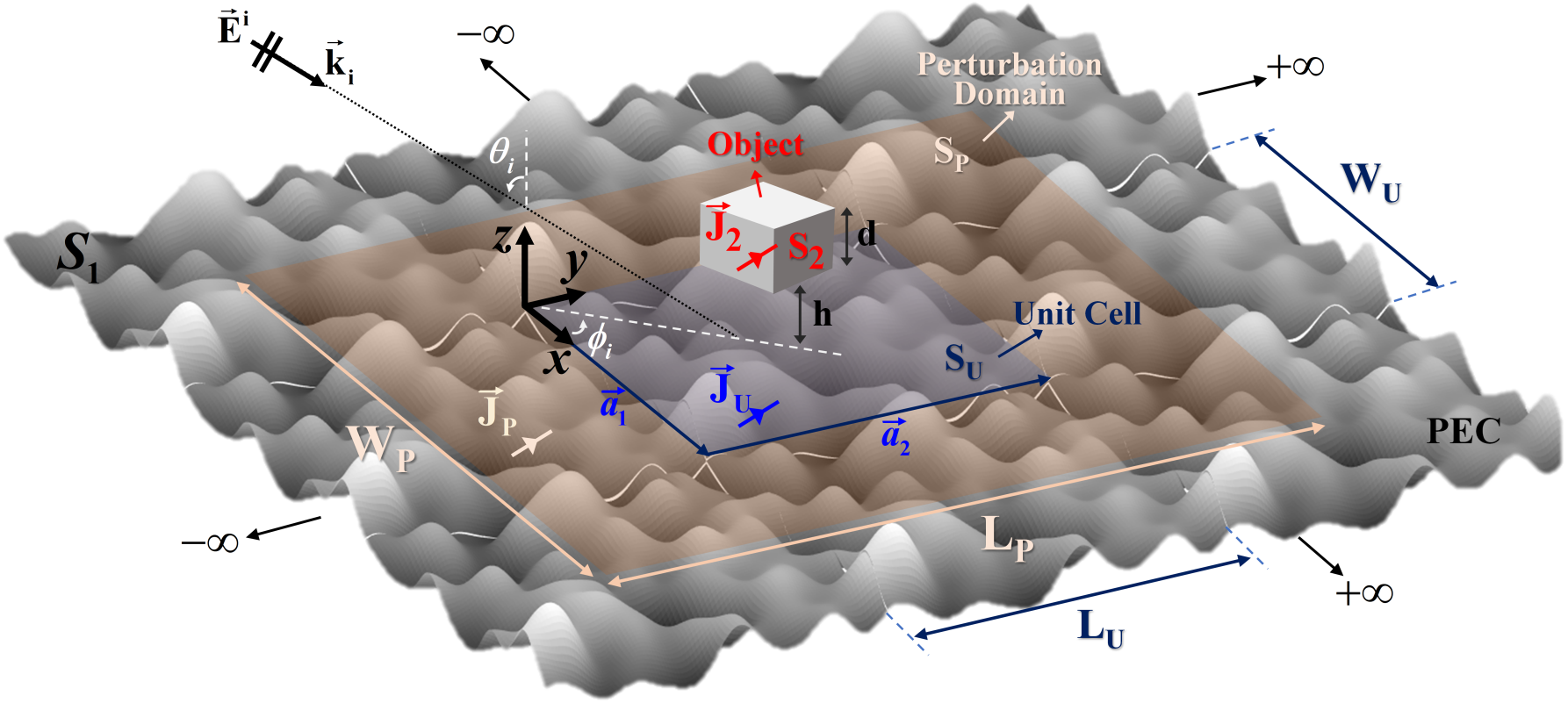

Figure 4.1 Configuration of a scattering problem from a PEC object above a periodic, arbitrarily rough, and PEC surface

$\{z = \mathfrak{s}(x,y) = f(x + L_x, y + L_y)\}$. Similar to previous chapters, here, assume that a plane wave is an incident on a periodic conductive rough surface $\{z = \mathfrak{s}(x,y)\}$ with the incidence angles of θ_i and ϕ_i. The PEC surface is located on the x– y plane, and the upper region of this surface is the vacuum, as shown in Figure 4.1. $\vec{\mathbf{a}}_1$ and $\vec{\mathbf{a}}_2$ are the primitive lattice vectors, and L_x and L_y are the dimensions of the unit cell.

As seen in Figure 4.1, W_P and L_P are the dimensions of the bounded perturbation surface. $\vec{\mathbf{J}}_U$ shows the periodic induced current density defined on the S_U surface from the illumination with a plane wave without the object present. $\vec{\mathbf{J}}_P$ specifies the perturbed current density on the rough surface with the object's presence. It is assumed that this current density is dominant in only the S_P truncated domain and is zero on the remaining rough surface. $\vec{\mathbf{J}}_2$ is the total induced current density defined on the S_2 surface. The polarization of the incident plane wave can be determined according to the transverse to incident plane. Again, the incident electric field can be written as

$$\vec{\mathbf{E}}_i = \hat{\mathbf{e}}_i E_0 e^{-j\vec{\mathbf{k}}_i \cdot \vec{\mathbf{r}}} = (\hat{\boldsymbol{\theta}} \cos\alpha + \hat{\boldsymbol{\phi}} \sin\alpha) E_0 e^{-j\beta_0 \hat{\mathbf{k}}_i \cdot \vec{\mathbf{r}}} = (\hat{\mathbf{v}}_i + \hat{\mathbf{h}}_i) E_0 e^{-j\beta_0 \hat{\mathbf{k}}_i \cdot \vec{\mathbf{r}}} \tag{4.1}$$

where α is the polarization angle and $\vec{\mathbf{k}}_i = \beta_0 \hat{\mathbf{k}}_i$ is the incident vector of the wave. $\alpha = 0°$ is θ-polarization (vertical $\hat{\mathbf{v}}_i$ or TM polarization), and $\alpha = 90°$ is ϕ-polarization (horizontal $\hat{\mathbf{h}}_i$ or TE polarization). In (4.1), the incident wave vector is $\vec{\mathbf{k}}_i = \beta_x \hat{\mathbf{x}} + \beta_y \hat{\mathbf{y}} - q\hat{\mathbf{z}}$, and the wave number is $k = \beta_0 = \omega\sqrt{\mu_0 \epsilon_0}$, where $\beta_x = \beta_0 \sin\theta_i \cos\phi_i$, $\beta_y = \beta_0 \sin\theta_i \sin\phi_i$, and $q = \beta_0 \cos\theta_i$. At this point, the derivation of the current decomposition approach is pretty similar to the previous chapter. The total surface current density on the S_1 surface is defined as $\vec{\mathbf{J}}_1$, and it can be decomposed as

$$\lim_{W_p, L_p \to \infty} \vec{\mathbf{J}}_1 = \vec{\mathbf{J}}_U + \vec{\mathbf{J}}_P \tag{4.2}$$

where $\vec{\mathbf{J}}_U$ is periodic throughout the infinite ground, and it should satisfy (2.59). Then, if our assumption is applied

$$\vec{\mathbf{J}}_1 \approx \vec{\mathbf{J}}_U + \vec{\mathbf{J}}_P \tag{4.3}$$

on S_1. Now, if the boundary condition on the ground plane is applied while the object is present, then

$$\hat{\mathbf{n}}_1 \times \left[\vec{\mathbf{E}}^i + \vec{\mathbf{E}}^s\left(\vec{\mathbf{J}}_1\right) + \vec{\mathbf{E}}^s\left(\vec{\mathbf{J}}_2\right)\right]\Big|_{\text{on } S_1} = \vec{\mathbf{0}} \tag{4.4}$$

and without the object above the ground plane

$$\hat{\mathbf{n}}_1 \times \left[\vec{\mathbf{E}}^i + \vec{\mathbf{E}}^s\left(\vec{\mathbf{J}}_U\right)\right]\Big|_{\text{on } S_1} = \vec{\mathbf{0}} \tag{4.5}$$

This equation is also valid on S_p

$$\hat{\mathbf{n}}_P \times \left[\vec{\mathbf{E}}^i + \vec{\mathbf{E}}^s\left(\vec{\mathbf{J}}_U\right)\right]\Big|_{\text{on } S_p} = \vec{\mathbf{0}} \tag{4.6}$$

where, $\hat{\mathbf{n}}_P$ is unit normal vector of the S_P surface. If (4.3) is substituted in (4.4), on S_p

$$\hat{\mathbf{n}}_P \times \left[\vec{\mathbf{E}}^i + \vec{\mathbf{E}}^s\left(\vec{\mathbf{J}}_U\right) + \vec{\mathbf{E}}^s\left(\vec{\mathbf{J}}_P\right) + \vec{\mathbf{E}}^s\left(\vec{\mathbf{J}}_2\right)\right]\Big|_{\text{on } S_P} = \vec{\mathbf{0}} \tag{4.7}$$

Then, one exploits (4.6) in (4.7)

$$\hat{\mathbf{n}}_P \times \left[\vec{\mathbf{E}}^s\left(\vec{\mathbf{J}}_P\right) + \vec{\mathbf{E}}^s\left(\vec{\mathbf{J}}_2\right)\right]\Big|_{\text{on } S_p} = \vec{\mathbf{0}} \tag{4.8}$$

is finally found for the S_p surface. Also, the boundary condition on S_2

$$\hat{\mathbf{n}}_2 \times \left[\vec{\mathbf{E}}^i + \vec{\mathbf{E}}^s\left(\vec{\mathbf{J}}_U\right) + \vec{\mathbf{E}}^s\left(\vec{\mathbf{J}}_P\right) + \vec{\mathbf{E}}^s\left(\vec{\mathbf{J}}_2\right)\right]\Big|_{\text{on } S_2} = \vec{\mathbf{0}} \tag{4.9}$$

and, rearranging the equation

$$\hat{\mathbf{n}}_2 \times \left[\vec{\mathbf{E}}^s\left(\vec{\mathbf{J}}_P\right) + \vec{\mathbf{E}}^s\left(\vec{\mathbf{J}}_2\right)\right]\Big|_{\text{on } S_2} = -\hat{\mathbf{n}}_2 \times \left[\vec{\mathbf{E}}^i + \vec{\mathbf{E}}^s\left(\vec{\mathbf{J}}_U\right)\right]\Big|_{\text{on } S_2} \tag{4.10}$$

is eventually found on S_2. These equations are similar to the previous chapter since only the right-hand side of (4.10) changes with induction in the case of no object. Besides, a flat surface can also be modeled periodically. (4.8) and (4.10) can be also written as follows

$$\left[\vec{\mathbf{E}}^s\left(\vec{\mathbf{J}}_P\right)+\vec{\mathbf{E}}^s\left(\vec{\mathbf{J}}_2\right)\right]_{\tan}=\vec{\mathbf{0}}\quad \text{on } S_P \tag{4.11}$$

$$\left[\vec{\mathbf{E}}^s\left(\vec{\mathbf{J}}_P\right)+\vec{\mathbf{E}}^s\left(\vec{\mathbf{J}}_2\right)\right]_{\tan}=-\left[\vec{\mathbf{E}}^i+\vec{\mathbf{E}}^s\left(\vec{\mathbf{J}}_U\right)\right]_{\tan}\quad \text{on } S_2 \tag{4.12}$$

Moreover, the unknown surface current density $\vec{\mathbf{J}}_U$ will firstly resolve without the object present, as discussed in Chapter 2. $\vec{\mathbf{J}}_U$ can be calculated semi-analytical or purely numerically according to the degree of surface roughness. In this thesis, we want to address any degree of roughness, so from now on, we will only use the numerical solution of it. After calculating $\vec{\mathbf{J}}_U$ without the object present, the scattered electric field on S_2 resulting from the current density $\vec{\mathbf{J}}_U$ is expressed as follows

$$\vec{\mathbf{E}}^s\left(\vec{\mathbf{J}}_U\right)\Big|_{\text{on } S_2}=-j\omega\mu_0\int_{S'_U}\left[\bar{\bar{\mathbf{I}}}+\frac{1}{\beta_0^2}\nabla\nabla\right]G_p\left(\vec{\mathbf{r}}|\vec{\mathbf{r}}'\right)\cdot\vec{\mathbf{J}}_U\left(\vec{\mathbf{r}}'\right)dS'_U \tag{4.13}$$

where G_p is the FS-PGF. To find this scattered electric field, we will utilize the spectral form of it as given in (A.45) after calculating the induced periodic current density $\vec{\mathbf{J}}_U$ on S_U. The MoM solution is applied to (4.11) and (4.12). Expanding the currents with RWG basis functions and exploiting Galerkin-type testing functions, a matrix system

$$\begin{bmatrix}\bar{\bar{\mathbf{Z}}}_{11}^{(\vec{\mathbf{J}}_P)} & \bar{\bar{\mathbf{Z}}}_{12}^{(\vec{\mathbf{J}}_2)}\\ \bar{\bar{\mathbf{Z}}}_{21}^{(\vec{\mathbf{J}}_P)} & \bar{\bar{\mathbf{Z}}}_{12}^{(\vec{\mathbf{J}}_2)}\end{bmatrix}\begin{bmatrix}\bar{\mathbf{I}}_{\psi_{11}}^{(P)}\\ \bar{\mathbf{I}}_{\psi_{21}}^{(2)}\end{bmatrix}=\begin{bmatrix}\bar{\mathbf{V}}_{\zeta_{11}}^{(P)}\\ \bar{\mathbf{V}}_{\zeta_{21}}^{(2)}\end{bmatrix} \tag{4.14}$$

is produced. Then, a general expression of any edge of $\bar{\bar{\mathbf{Z}}}$ matrices for plus or minus and testing or basis triangle surfaces on S_p and S_2

$$\begin{aligned}Z_{\zeta\psi}=j\beta_0\eta_0\Bigg[&\int_{T_\zeta^\pm}\int_{T_\psi^\pm}\vec{\mathbf{f}}_\zeta(\vec{\mathbf{r}})\cdot\vec{\mathbf{f}}_\psi(\vec{\mathbf{r}}')G_0(\vec{\mathbf{r}}|\vec{\mathbf{r}}')dS'_{T_\psi^\pm}dS_{T_\zeta^\pm}\\ &-\frac{1}{\beta_0^2}\int_{T_\zeta^\pm}\int_{T_\psi^\pm}\left[\nabla_s\cdot\vec{\mathbf{f}}_\zeta(\vec{\mathbf{r}})\right]\left[\nabla'_s\cdot\vec{\mathbf{f}}_\psi(\vec{\mathbf{r}}')\right]G_0(\vec{\mathbf{r}}|\vec{\mathbf{r}}')dS'_{T_\psi^\pm}dS_{T_\zeta^\pm}\Bigg]\end{aligned} \tag{4.15}$$

are obtained. Then, $\bar{\mathbf{V}}$ arrays on S_p and S_2 surfaces, respectively

$$V_{\zeta 11}^{(P)}=0 \tag{4.16}$$

$$V_{\zeta 21}^{(2)} = \int_{S_{T_\zeta^\pm}^{(2)}} \vec{\mathbf{f}}_\zeta(\vec{\mathbf{r}}) \cdot \left[\vec{\mathbf{E}}^i + \vec{\mathbf{E}}^s\left(\vec{\mathbf{J}}_U\right)\right] dS_{T_\zeta^\pm}^{(2)} \tag{4.17}$$

are defined. Here, if the current density vector $\vec{\mathbf{J}}_U$ is discretized with basis functions

$$\vec{\mathbf{J}}_U(\vec{\mathbf{r}}') = \sum_{\psi=1}^{N_U} I_\psi^{(J_U)} \vec{\mathbf{f}}_\psi(\vec{\mathbf{r}}') \tag{4.18}$$

and

$$\begin{aligned} V_{\zeta 21}^{(2)} = & \int_{S_{T_\zeta^\pm}^{(2)}} \vec{\mathbf{f}}_\zeta(\vec{\mathbf{r}}) \cdot \vec{\mathbf{E}}^i dS_{T_\zeta^\pm}^{(2)} \\ & - j\omega\mu_0 \sum_{\psi=1}^{N_U} I_\psi^{(J_U)} \int_{S_{T_\zeta^\pm}^{(2)}} \vec{\mathbf{f}}_\zeta(\vec{\mathbf{r}}) \cdot \int_{S_{T_\psi^\pm}^{(U)}} \left[\bar{\bar{\mathbf{I}}} + \frac{1}{\beta_0^2}\nabla\nabla\right] G_p\left(\vec{\mathbf{r}}|\vec{\mathbf{r}}'\right) \cdot \vec{\mathbf{f}}_\psi(\vec{\mathbf{r}}') dS_{T_\psi^\pm}^{(U)} dS_{T_\zeta^\pm}^{(2)} \end{aligned} \tag{4.19}$$

Since the object is always above the rough surface, the double sum of the spectral form of GF can converge

$$G_p\left(\vec{\mathbf{r}}|\vec{\mathbf{r}}'\right) = \frac{-j}{2L_x L_y} \sum_{m=-\infty}^{+\infty} \sum_{n=-\infty}^{+\infty} \frac{e^{-j\beta_m(x-x')} e^{-j\beta_n(y-y')} e^{-jq_{mn}(z-z')}}{q_{mn}} \tag{4.20}$$

and

$$\nabla\nabla G_p\left(\vec{\mathbf{r}}|\vec{\mathbf{r}}'\right) = -G_p\left(\vec{\mathbf{r}}|\vec{\mathbf{r}}'\right) \vec{\mathbf{k}}_{mn} \otimes \vec{\mathbf{k}}_{mn} \tag{4.21}$$

The detailed information is given in Chapter 2. Furthermore, the unknown current coefficients will be found after solving the linear equation system. Eventually, the total scattered electric field in the far field region

$$\vec{\mathbf{E}}^{s}_{far\text{-}field}(\vec{\mathbf{r}}) = j\beta_0\eta\frac{e^{-j\beta_0 r}}{4\pi r}\left[\int_{S'_P}\hat{\mathbf{r}}\times\left[\hat{\mathbf{r}}\times\vec{\mathbf{J}}_P(\vec{\mathbf{r}}')\right]\left[e^{j\beta_0\vec{\mathbf{r}}'\cdot\hat{\mathbf{r}}}\right]dS'_P + \int_{S'_2}\hat{\mathbf{r}}\times\left[\hat{\mathbf{r}}\times\vec{\mathbf{J}}_2(\vec{\mathbf{r}}')\right]\left[e^{j\beta_0\vec{\mathbf{r}}'\cdot\hat{\mathbf{r}}}\right]dS'_2\right] \quad (4.22)$$

can be written. With the RWG basis function for any edge

$$\vec{\mathbf{J}}_P(\vec{\mathbf{r}}') = \sum_{\psi=1}^{N_1} I_\psi^{(J_P)}\vec{\mathbf{f}}_\psi(\vec{\mathbf{r}}') \quad (4.23)$$

$$\vec{\mathbf{J}}_2(\vec{\mathbf{r}}') = \sum_{\psi=1}^{N_2} I_\psi^{(J_2)}\vec{\mathbf{f}}_\psi(\vec{\mathbf{r}}') \quad (4.24)$$

thereby

$$\vec{\mathbf{E}}^{s}_{far\text{-}field}(\vec{\mathbf{r}}) = j\beta_0\eta\frac{e^{-j\beta_0 r}}{4\pi r}\left[\sum_{\psi=1}^{N_1} I_\psi^{(J_P)}\int_{dS^{(P)}_{T^{\pm}_{\psi}}}\hat{\mathbf{r}}\times\left[\hat{\mathbf{r}}\times\vec{\mathbf{f}}_\psi(\vec{\mathbf{r}}')\right]\left[e^{j\beta_0\vec{\mathbf{r}}'\cdot\hat{\mathbf{r}}}\right]dS^{(P)}_{T^{\pm}_{\psi}} + \sum_{\psi=1}^{N_2} I_\psi^{(J_2)}\int_{dS^{(2)}_{T^{\pm}_{\psi}}}\hat{\mathbf{r}}\times\left[\hat{\mathbf{r}}\times\vec{\mathbf{f}}_\psi(\vec{\mathbf{r}}')\right]\left[e^{j\beta_0\vec{\mathbf{r}}'\cdot\hat{\mathbf{r}}}\right]dS^{(2)}_{T^{\pm}_{\psi}}\right] \quad (4.25)$$

Also, the RCS of the object

$$\mathrm{RCS} = \lim_{r\to\infty} 4\pi r^2\frac{\left\|\vec{\mathbf{E}}^{s}_{far\text{-}field}\right\|^2}{\left\|\vec{\mathbf{E}}^{i}\right\|^2} \quad (4.26)$$

is similarly defined.

4.2 Numerical Results

After the preliminary validations of the proposed perturbation approach in Chapter (3), a rough ground surface example can be realized through a pre-calculated periodic surface current by the periodic-MoM formulation as discussed in detail in

Chapter (2). For this purpose, the surface function of the unit cell of the ground plane is simply chosen as a sinusoidal function

$$z = s(x, y) = -h_s \left[\cos\left(\frac{2\pi x}{W_U}\right) + \cos\left(\frac{2\pi y}{L_U}\right) \right] \tag{4.27}$$

where h_s is the height of the rough surface, and this surface is periodic with W_U and L_U.

Similar to the flat surface case, a converge test should be performed to determine a reasonable choice of the perturbation region before investigating the effects of the rough surface on the scattering from the object. Additionally, the RAM requirement in the MoM solution can be extremely high due to employing highly dense mesh at some rough surface examples to model surface slopes correctly. Therefore, the surface parameters of the unit cell are determined as $h_s = 0.15\lambda$, $W_U = L_U = 1.5\lambda$. The dimensions of the perturbation region are changed with $4\lambda \times 4\lambda$, $8\lambda \times 8\lambda$, $16\lambda \times 16\lambda$, and $24\lambda \times 24\lambda$. Finally, the object with $d = 0.3\lambda$ is inserted at the height of $h = 0.1\lambda$ above the top of the rough surface. Unless otherwise stated in this chapter, the free space wavelength is denoted as λ in all scattering examples and numerical results.

The RCS results of these four perturbation region selections in the $x-z$ and $y-z$ planes are demonstrated in Figures 4.2 and 4.3, respectively. According to these results, a perturbation surface of $8\lambda \times 8\lambda$ was chosen because there was no significant difference except for small fluctuations. Also, this choice allows for employing smaller mesh sizes for the perturbation surface. On the other hand, the accuracy can be increased by extending the perturbation region when higher accuracy is desired. Furthermore, considering the solution region, the proposed method is still advantageous compared to the tapered wave approach for near-grazing angle illumination [28].

In Figures 4.4– 4.7, a cube object with $d = 0.3\lambda$ is employed to observe the effects of a rough surface defining in (4.27). Here, the object is again positioned at the height of $h = 0.1\lambda$ above the surface top, and perturbation region size is $8\lambda \times 8\lambda$ as determined in the preceding scattering scenario. The effect of the surface height is discussed in the $x - z$ and $y - z$ planes for several surface heights of the sinusoidal surface in Figure 4.4 and 4.5. As seen from the figures, when the surface height is decreased, the RCS of the object is converged to the flat case. In contrast, the RCS is subject to change as the perturbation current density spreads over the surface when the surface height increases. Under the same conditions, the effect of the surface gradient is demonstrated by changing the unit cell dimensions in Figures 4.6 and 4.7. Significant changes occur when the surface gradient becomes comparable to the object's size. In

other cases, the surface current is concentrated on the rough top of the surface.

Moreover, the last experiments are carried out on the effects of rough surface shape in Figures 4.8 and 4.9. In these experiments, the unit cell dimension is $1.5\lambda \times 1.5\lambda$, and other parameters remain the same as the previous two scattering examples except for the surface roughness. Here, for these four test cases, as seen in Figures 4.8 and 4.9, the surface roughnesses are randomly obtained a Gaussian correlation function with the surface height $h_s = 0.1\lambda$ and a correlation length 0.3λ. The distribution of the perturbed current on the ground surface changes concerning the surface variation. Consequently, the roughness can considerably modify the RCS results of the object.

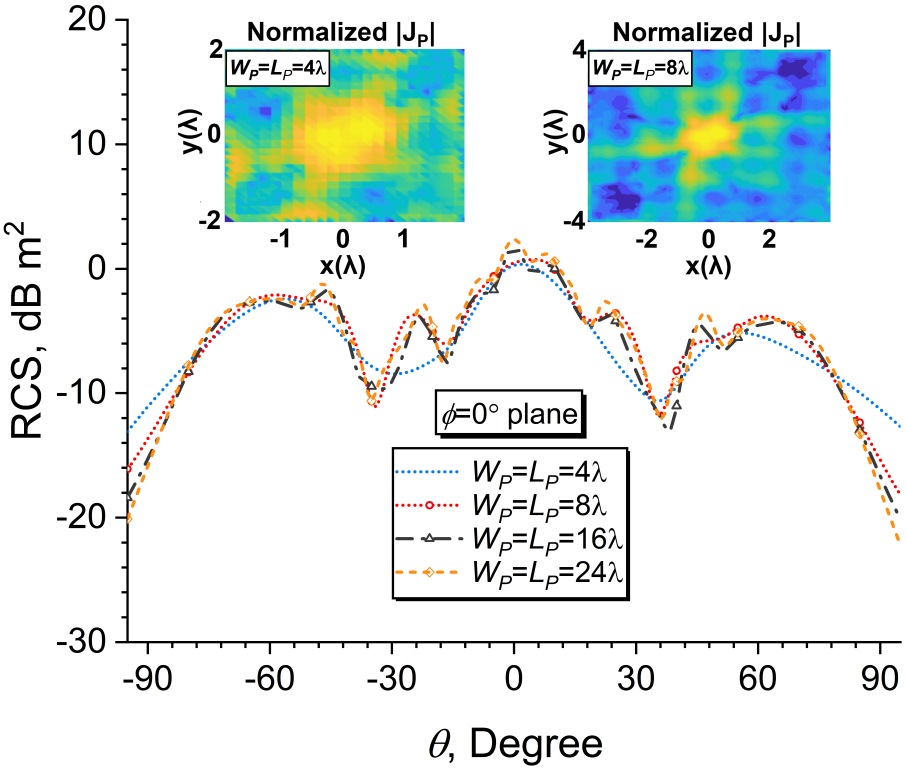

Figure 4.2 Changes on the RCS of the object according to the size of the perturbation region in $\phi = 0°$ plane

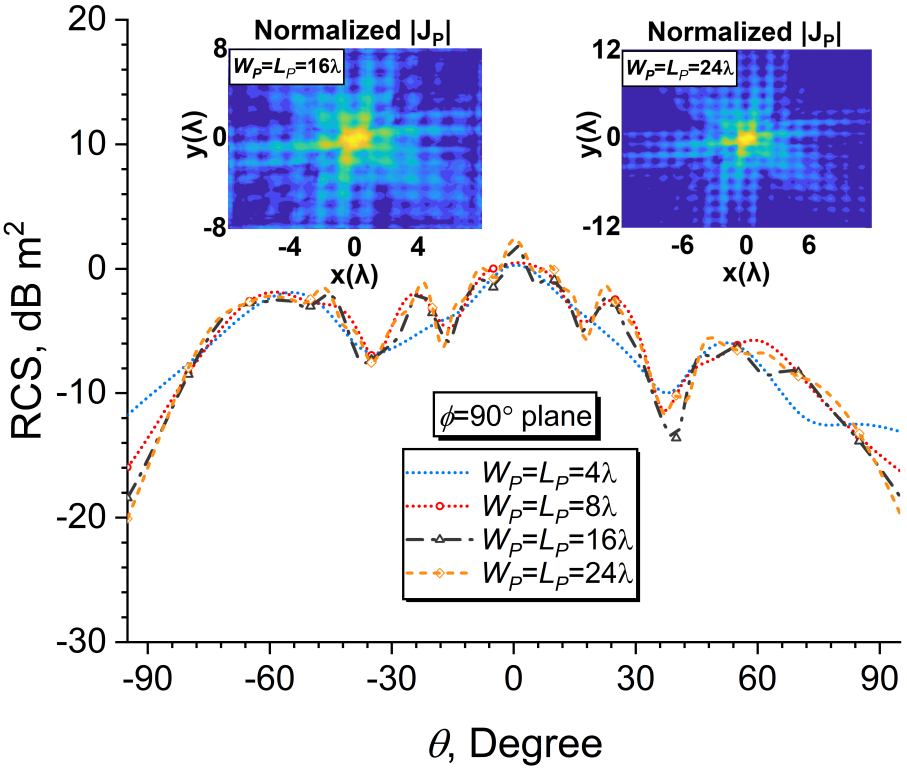

Figure 4.3 Changes on the RCS of the object according to the size of the perturbation region in $\phi = 90°$ plane

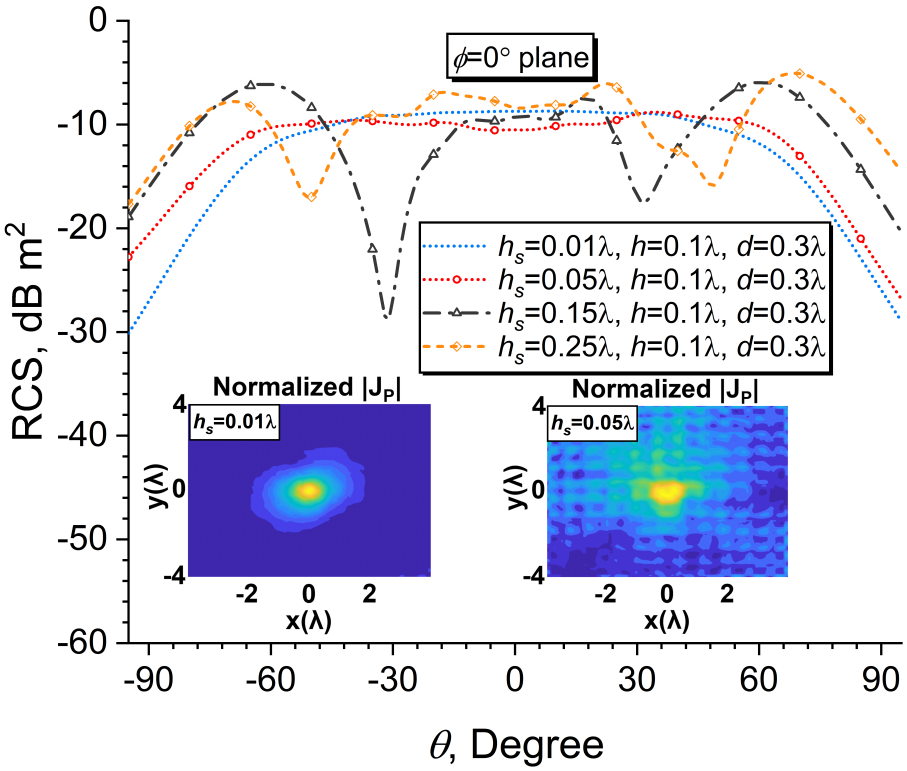

Figure 4.4 Effect of surface height on the RCS of the object in $\phi = 0°$ plane

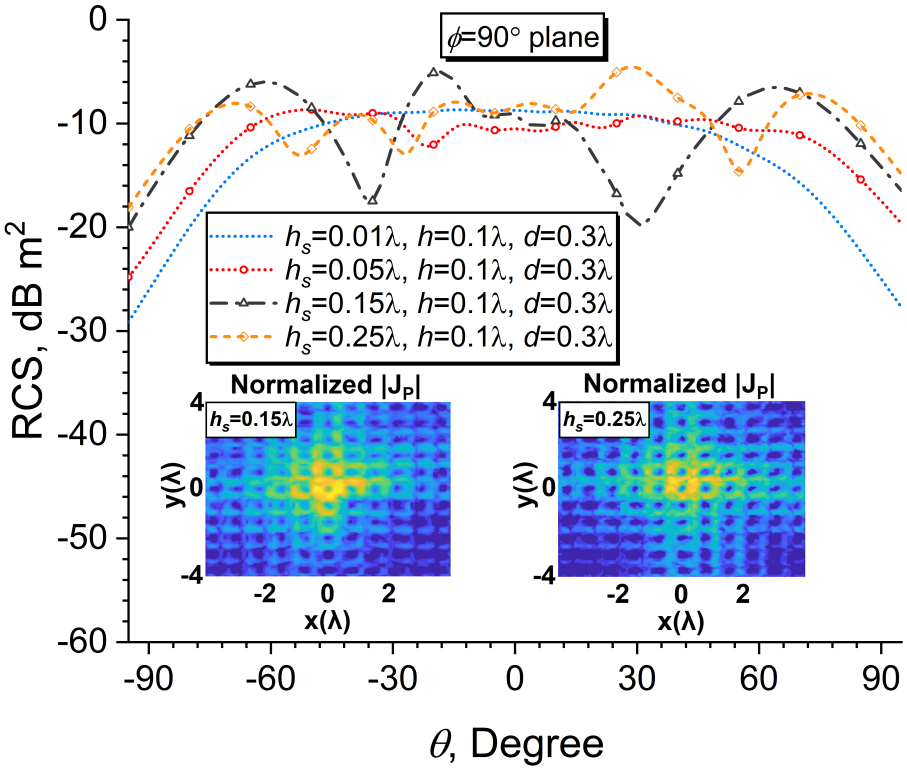

Figure 4.5 Effect of surface height on the RCS of the object in $\phi = 90°$ plane

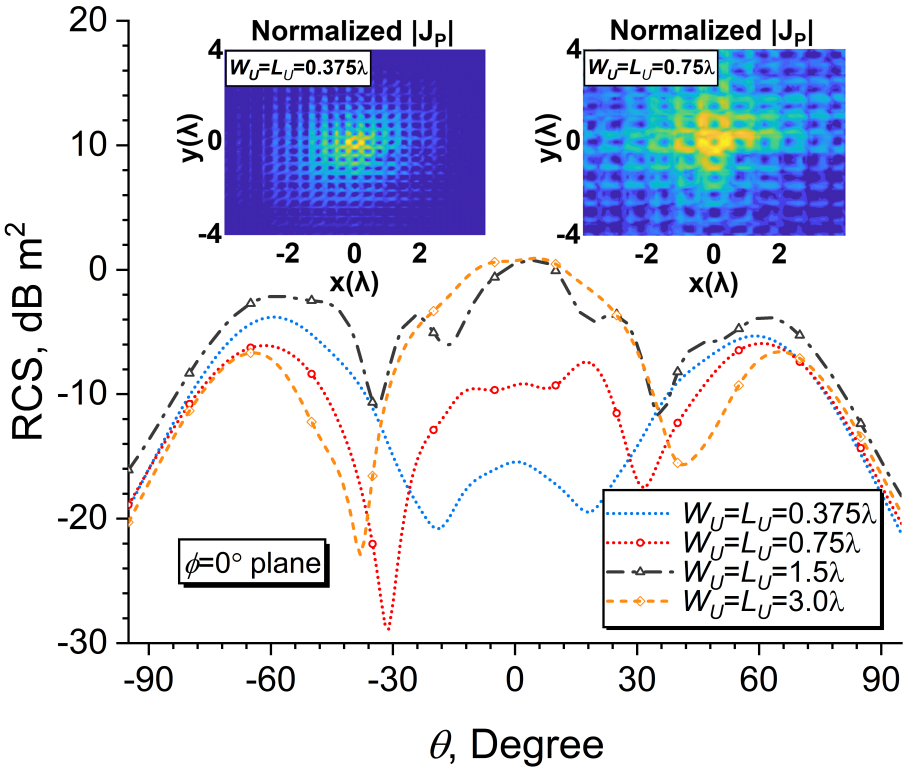

Figure 4.6 Effect of unit cell dimension on the RCS of the object in $\phi = 0°$ plane

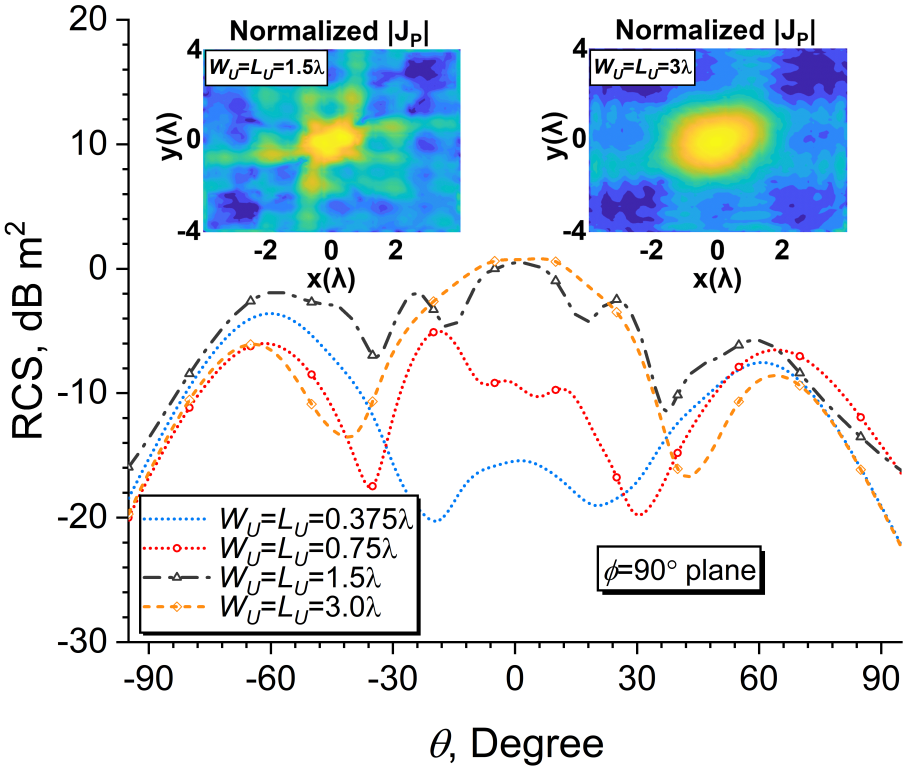

Figure 4.7 Effect of unit cell dimension on the RCS of the object in $\phi = 90°$ plane

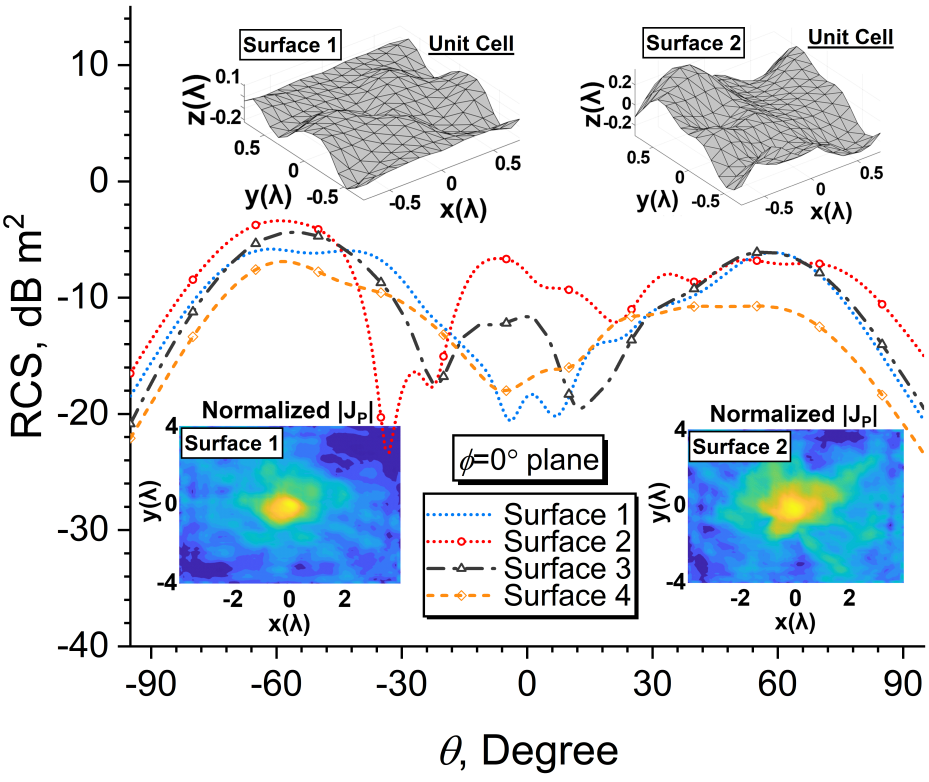

Figure 4.8 Effect of rough surface shape on the RCS of the object in $\phi = 0°$ plane

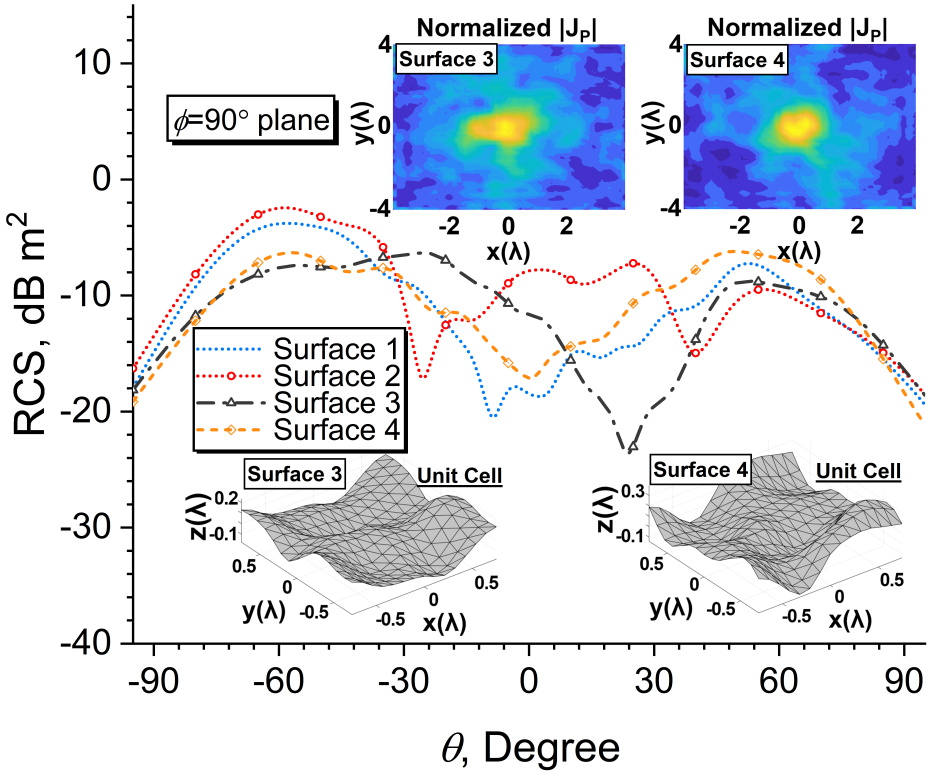

Figure 4.9 Effect of rough surface shape on the RCS of the object in $\phi = 90^\circ$ plane

5
SCATTERING ANALYSES OF A PEC OBJECT ABOVE A DIELECTRIC FLAT HALF-SPACE

In this chapter, as depicted in Figure 5.1, an electromagnetic scattering problem from an arbitrary-shaped PEC object above lossy or lossless dielectric flat half-spaces is treated by using the same perturbation approach as represented in the former chapters. Despite the earlier calculations, a new perturbed surface current occurs on the dielectric ground surface. The EFIE and MFIE are thereby exploited with the PMCHWT formulation to calculate the equivalent surface currents for the dielectric interface. The object is chosen as PEC for simplification, and the induced electric current is attained by solving the EFIE on the surface. Lastly, the validation of the proposed method is realized by commercial software.

Before starting the formulation, it will be useful to give the general expressions of the scattered electric and magnetic fields from electric $\vec{\mathbf{J}}$ and magnetic $\vec{\mathbf{M}}$ current densities in the integral form

$$\vec{\mathbf{E}}^s(\vec{\mathbf{r}}) = -jk\eta \int_{S'} \left[1 + \frac{1}{k^2}\nabla\nabla\cdot\right] \vec{\mathbf{J}}(\vec{\mathbf{r}}')G(\vec{\mathbf{r}},\vec{\mathbf{r}}')dS' - \nabla \times \int_{S'} \vec{\mathbf{M}}(\vec{\mathbf{r}}')G(\vec{\mathbf{r}},\vec{\mathbf{r}}')dS' \tag{5.1}$$

$$\vec{\mathbf{H}}^s(\vec{\mathbf{r}}) = -j\frac{k}{\eta} \int_{S'} \left[1 + \frac{1}{k^2}\nabla\nabla\cdot\right] \vec{\mathbf{M}}(\vec{\mathbf{r}}')G(\vec{\mathbf{r}},\vec{\mathbf{r}}')dS' + \nabla \times \int_{S'} \vec{\mathbf{J}}(\vec{\mathbf{r}}')G(\vec{\mathbf{r}},\vec{\mathbf{r}}')dS' \tag{5.2}$$

and, these equations can be represented plainly in the form of integral operators

$$\vec{\mathbf{E}}^s = -jk\eta\mathfrak{L}[\vec{\mathbf{J}}] - \mathfrak{K}[\vec{\mathbf{M}}] \tag{5.3}$$

$$\vec{\mathbf{H}}^s = -j\frac{k}{\eta}\mathfrak{L}[\vec{\mathbf{M}}] + \mathfrak{K}[\vec{\mathbf{J}}] \tag{5.4}$$

where, $\vec{\mathbf{J}}$ and $\vec{\mathbf{M}}$ are electric and magnetic current densities on the dielectric interface.

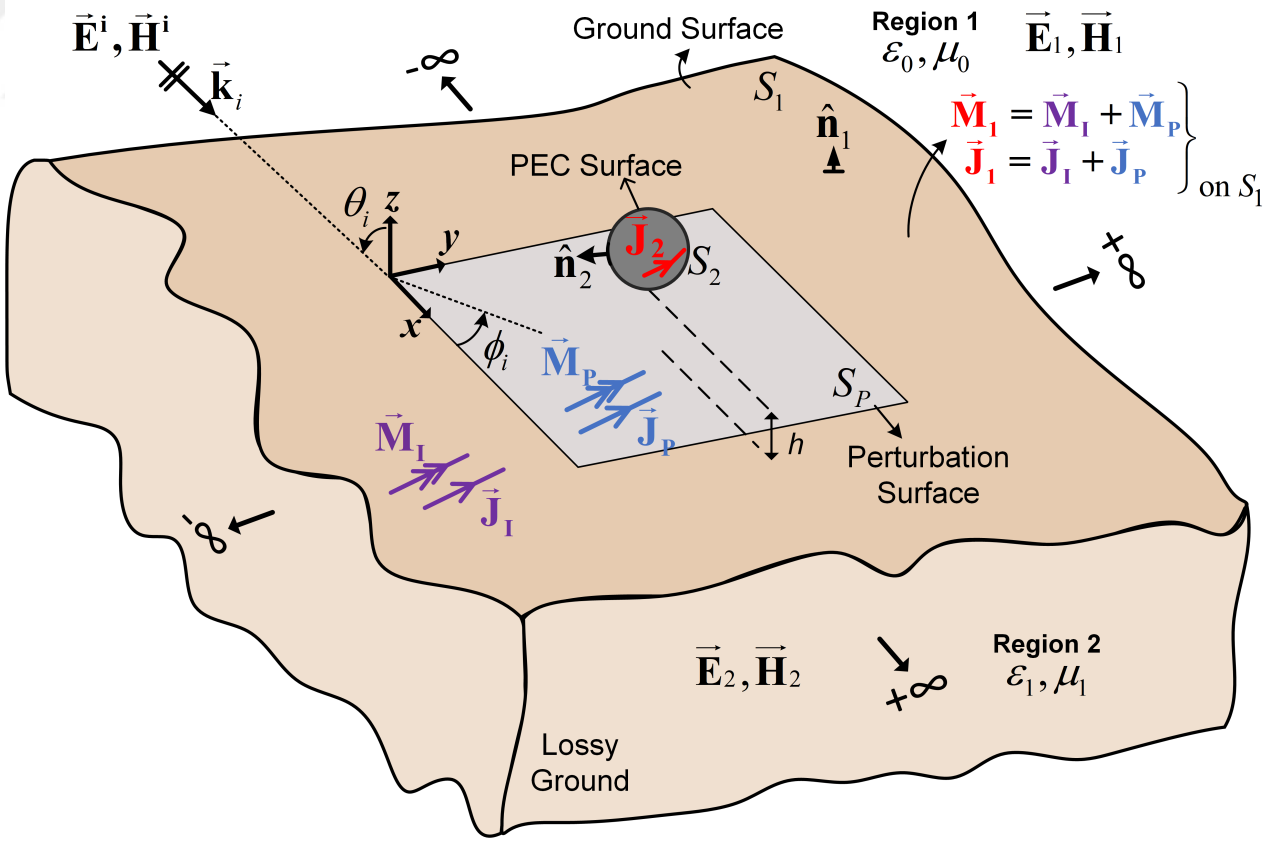

Figure 5.1 Configuration of a scattering problem from a PEC object above an infinite, flat, and dielectric surface

5.1 Formulation

As shown in Figure 5.1, an object is inserted above a flat dielectric surface, and a plane wave illuminates it. Here, the dielectric ground can be lossy or lossless, and the PEC object can be selected as any arbitrary shape. The plane wave definition is as (3.1) in the former chapter. In Figure 5.1, since the perturbed surface current on the dielectric interface aroused from the object is only dominant in a limited surface region, the perturbation region should be therefore determined carefully. Once more, under this assumption, we must use the formulations with and without the target, as in the earlier chapters. Subsequently, we will utilize inner and outer equivalence theorems for the dielectric interface.

5.1.1 Formulations without Target

Initially, the case without the target is formulated. After applying the outer equivalence to the ground interface in which the target is not present:

$$\hat{\mathbf{n}}_1 \times \left[\vec{\mathbf{E}}_1\right]\Big|_{S_1^+} = -\vec{\mathbf{M}}_I, \quad \text{and} \quad \hat{\mathbf{n}}_1 \times \left[\vec{\mathbf{H}}_1\right]\Big|_{S_1^+} = \vec{\mathbf{J}}_I \tag{5.5}$$

is written through the boundary conditions. Here, $\vec{\mathbf{J}}_I$ and $\vec{\mathbf{M}}_I$ represent the electric and magnetic currents induced on the ground plane in the absence of the object. $\hat{\mathbf{n}}_1$ is the unit normal vector of the ground surface. $\vec{\mathbf{E}}_1$ and $\vec{\mathbf{H}}_1$ are the total electric and magnetic fields in the free-space region, respectively. Therefore, the total electric field is in the free-space region (in Region 1)

$$\vec{\mathbf{E}}_1 = \vec{\mathbf{E}}_1^s(\vec{\mathbf{J}}_I, \vec{\mathbf{M}}_I) + \vec{\mathbf{E}}^i \tag{5.6}$$

where the superscript s indicates the scattered field, as well as the total magnetic field in Region 1 is

$$\vec{\mathbf{H}}_1 = \vec{\mathbf{H}}_1^s(\vec{\mathbf{J}}_I, \vec{\mathbf{M}}_I) + \vec{\mathbf{H}}^i \tag{5.7}$$

Also, as depicted in the fields and regions in Figure 5.1, utilizing the extinction theorem, the total electric and magnetic fields in Region 2

$$\vec{\mathbf{E}}_2 = \vec{\mathbf{H}}_2 = \vec{\mathbf{0}} \tag{5.8}$$

will simply become. Now, (5.6) are substituted in (5.5)

$$\hat{\mathbf{n}}_1 \times \left[\vec{\mathbf{E}}_1^s(\vec{\mathbf{J}}_I, \vec{\mathbf{M}}_I) + \vec{\mathbf{E}}^i\right]\Big|_{S_1^+} = -\vec{\mathbf{M}}_I \tag{5.9}$$

and, it is rearranged on S_1^+

$$\left[\vec{\mathbf{E}}_1^s(\vec{\mathbf{J}}_I, \vec{\mathbf{M}}_I) + \vec{\mathbf{E}}^i\right]_{\tan} - \hat{\mathbf{n}}_1 \times \vec{\mathbf{M}}_I = \vec{\mathbf{0}} \quad \text{on } S_1^+ \tag{5.10}$$

Furthermore, (5.7) are substituted in (5.5)

$$\hat{\mathbf{n}}_1 \times \left[\vec{\mathbf{H}}_1^s(\vec{\mathbf{J}}_I, \vec{\mathbf{M}}_I) + \vec{\mathbf{H}}^i\right]\Big|_{S_1^+} = \vec{\mathbf{J}}_I \tag{5.11}$$

and, it is again rearranged on S_1^+

$$\left[\vec{\mathbf{H}}_1^s(\vec{\mathbf{J}}_I, \vec{\mathbf{M}}_I) + \vec{\mathbf{H}}^i\right]_{\tan} + \hat{\mathbf{n}}_1 \times \vec{\mathbf{J}}_I = \vec{\mathbf{0}} \quad \text{on } S_1^+ \tag{5.12}$$

is obtained. On the other hand, we can now employ the inner equivalence theorem to the dielectric interface in a similar way. The boundary conditions on S_1^- as follows

$$-\hat{\mathbf{n}}_1 \times \left[\vec{\mathbf{E}}_2\right]\Big|_{S_1^-} = \vec{\mathbf{M}}_I, \quad \text{and} \quad -\hat{\mathbf{n}}_1 \times \left[\vec{\mathbf{H}}_2\right]\Big|_{S_1^-} = -\vec{\mathbf{J}}_I \tag{5.13}$$

where, the total electric and magnetic fields in the second region

$$\vec{\mathbf{E}}_2 = \vec{\mathbf{E}}_2^s(-\vec{\mathbf{J}}_I, -\vec{\mathbf{M}}_I) \tag{5.14}$$

$$\vec{\mathbf{H}}_2 = \vec{\mathbf{H}}_2^s(-\vec{\mathbf{J}}_I, -\vec{\mathbf{M}}_I) \tag{5.15}$$

and, the total electric and magnetic fields in the first region

$$\vec{\mathbf{E}}_1 = \vec{\mathbf{H}}_1 = \vec{\mathbf{0}} \tag{5.16}$$

Here, it should be noted that the constitutive parameters of the first region are considered the same as the second region in the inner equivalence. On the contrary, this situation is the opposite of the outer equivalence theorem. In addition, if (5.14)

and (5.15) are substituted in (5.13)

$$-\hat{\mathbf{n}}_1 \times \left[\vec{\mathbf{E}}_2^s(-\vec{\mathbf{J}}_I, -\vec{\mathbf{M}}_I)\right]\Big|_{S_1^-} = \vec{\mathbf{M}}_I \tag{5.17}$$

and

$$-\hat{\mathbf{n}}_1 \times \left[\vec{\mathbf{H}}_2^s(-\vec{\mathbf{J}}_I, -\vec{\mathbf{M}}_I)\right]\Big|_{S_1^-} = -\vec{\mathbf{J}}_I \tag{5.18}$$

If they can be expressed on S_1^- as follows

$$\left[\vec{\mathbf{E}}_2^s(-\vec{\mathbf{J}}_I, -\vec{\mathbf{M}}_I)\right]_{\tan} - \hat{\mathbf{n}}_1 \times \vec{\mathbf{M}}_I = \vec{\mathbf{0}} \quad \text{on } S_1^- \tag{5.19}$$

as well as

$$\left[\vec{\mathbf{H}}_2^s(-\vec{\mathbf{J}}_I, -\vec{\mathbf{M}}_I)\right]_{\tan} + \hat{\mathbf{n}}_1 \times \vec{\mathbf{J}}_I = \vec{\mathbf{0}} \quad \text{on } S_1^- \tag{5.20}$$

(5.10), (5.12) on S_1^+ and (5.19), (5.20) on S_1^- will be employed in the derivation of the perturbation approach for the problem shown in Figure (5.1).

5.1.2 Analytical Solution without Target

The reflected and transmitted fields can be obtained analytically for a flat dielectric interface. For this purpose, the incident electric field should be decomposed to the vertical and horizontal components as follows

$$\vec{\mathbf{E}}_1^i = (\vec{\mathbf{E}}_1^i \cdot \hat{\mathbf{v}}_i)\hat{\mathbf{v}}_i + (\vec{\mathbf{E}}_1^i \cdot \hat{\mathbf{h}})\hat{\mathbf{h}} = E_{1,v}^i \hat{\mathbf{v}}_i + E_{1,h}^i \hat{\mathbf{h}} \tag{5.21}$$

Therefore, the reflected and transmitted fields from the infinite dielectric surface will be comprised of vertical and horizontal components

$$\vec{\mathbf{E}}_1^r = R_{\parallel} E_{1,v}^i \hat{\mathbf{v}}_r + R_{\perp} E_{1,h}^i \hat{\mathbf{h}} \tag{5.22}$$

$$\vec{\mathbf{E}}_2^t = T_{\parallel} E_{1,v}^i \hat{\mathbf{v}}_t + T_{\perp} E_{1,h}^i \hat{\mathbf{h}} \tag{5.23}$$

Here, subscripts 1 and 2 imply the regions, respectively. Also, $\perp$ and $\parallel$ show horizontal

and vertical polarizations, and R and T mean reflection and transmission, respectively. Consequently, if the reflection and transmission coefficients are written for both polarization

$$R_{\perp} = \frac{\eta_1 \cos\theta^i - \eta_0 \cos\theta^t}{\eta_1 \cos\theta^i + \eta_0 \cos\theta^t} \tag{5.24}$$

$$R_{\parallel} = \frac{\eta_1 \cos\theta^t - \eta_0 \cos\theta^i}{\eta_1 \cos\theta^t + \eta_0 \cos\theta^i} \tag{5.25}$$

$$T_{\perp} = \frac{2\eta_1 \cos\theta^i}{\eta_1 \cos\theta^i + \eta_0 \cos\theta^t} \tag{5.26}$$

$$T_{\parallel} = \frac{2\eta_1 \cos\theta^i}{\eta_0 \cos\theta^i + \eta_1 \cos\theta^t} \tag{5.27}$$

Here, the intrinsic impedances of these two mediums

$$\eta_0 = \sqrt{\frac{\mu_0}{\epsilon_0}}, \quad \text{and} \quad \eta_1 = \sqrt{\frac{\mu_1}{\epsilon_1}} \tag{5.28}$$

Then, if we define the scattered and transmitted fields in terms of the surface current densities

$$\vec{\mathbf{E}}_1^r = \vec{\mathbf{E}}_1(\vec{\mathbf{J}}_I, \vec{\mathbf{M}}_I), \quad \text{and} \quad \vec{\mathbf{H}}_1^r = \vec{\mathbf{H}}_1(\vec{\mathbf{J}}_I, \vec{\mathbf{M}}_I) \tag{5.29}$$

$$\vec{\mathbf{E}}_2^t = \vec{\mathbf{E}}_2(-\vec{\mathbf{J}}_I, -\vec{\mathbf{M}}_I), \quad \text{and} \quad \vec{\mathbf{H}}_2^t = \vec{\mathbf{H}}_2(-\vec{\mathbf{J}}_I, -\vec{\mathbf{M}}_I) \tag{5.30}$$

it will be helpful for the subsequent formulations.

5.1.3 Current Decomposition Solution

A PEC cube is placed h m above the ground surface as the target. For the problem represented in Figure 5.1, the total induced current on the ground surface is $\vec{\mathbf{J}}_1$ and $\vec{\mathbf{M}}_1$. In addition, $\vec{\mathbf{J}}_2$ indicates the induced electric current density on the PEC target. The currents on the ground surface can be decomposed as follows

$$\lim_{W_p, L_p \to \infty} \vec{\mathbf{J}}_1 = \vec{\mathbf{J}}_I + \vec{\mathbf{J}}_P \tag{5.31}$$

and

$$\lim_{W_p, L_p \to \infty} \vec{\mathbf{M}}_1 = \vec{\mathbf{M}}_I + \vec{\mathbf{M}}_P \tag{5.32}$$

where $\vec{\mathbf{J}}_P$ and $\vec{\mathbf{M}}_P$ are the perturbed electric and magnetic current density vectors, respectively. Besides, as we know from the former chapters, we can forcibly restrict the perturbation surface since the perturbation currents strongly exist for a limited area on the infinite surface. Hence, this assumption gives us a sufficiently accurate approximate solution:

$$\vec{\mathbf{J}}_1 \approx \vec{\mathbf{J}}_I + \vec{\mathbf{J}}_P \tag{5.33}$$

$$\vec{\mathbf{M}}_1 \approx \vec{\mathbf{M}}_I + \vec{\mathbf{M}}_P \tag{5.34}$$

Here, it assumes that $\vec{\mathbf{J}}_P$ and $\vec{\mathbf{M}}_P$ are defined only in the perturbation region. At this point, the outer and inner equivalence theorems will be employed once more on the infinite ground surface for the currents $\vec{\mathbf{J}}_1$ and $\vec{\mathbf{M}}_1$. Through the inner equivalence theorem, the electric and magnetic fields inside each region

$$\vec{\mathbf{E}}_1 = \vec{\mathbf{E}}_1^s(\vec{\mathbf{J}}_1, \vec{\mathbf{M}}_1) + \vec{\mathbf{E}}_1^s(\vec{\mathbf{J}}_2) + \vec{\mathbf{E}}^i, \quad \text{and} \quad \vec{\mathbf{E}}_2 = \vec{\mathbf{0}} \tag{5.35}$$

$$\vec{\mathbf{H}}_1 = \vec{\mathbf{H}}_1^s(\vec{\mathbf{J}}_1, \vec{\mathbf{M}}_1) + \vec{\mathbf{H}}_1^s(\vec{\mathbf{J}}_2) + \vec{\mathbf{H}}^i, \quad \text{and} \quad \vec{\mathbf{H}}_2 = \vec{\mathbf{0}} \tag{5.36}$$

is given. Using the boundary conditions with the outer equivalence,

$$\hat{\mathbf{n}}_1 \times \left[\vec{\mathbf{E}}_1^s(\vec{\mathbf{J}}_1, \vec{\mathbf{M}}_1) + \vec{\mathbf{E}}_1^s(\vec{\mathbf{J}}_2) + \vec{\mathbf{E}}^i\right]\Big|_{S_1^+} = -\vec{\mathbf{M}}_1 \tag{5.37}$$

and

$$\hat{\mathbf{n}}_1 \times \left[\vec{\mathbf{H}}_1^s(\vec{\mathbf{J}}_1, \vec{\mathbf{M}}_1) + \vec{\mathbf{H}}_1^s(\vec{\mathbf{J}}_2) + \vec{\mathbf{H}}^i\right]\Big|_{S_1^+} = \vec{\mathbf{J}}_1 \tag{5.38}$$

are written. (5.34) is substituted in (5.37) for S_P^+

$$\hat{\mathbf{n}}_1 \times \left[\vec{\mathbf{E}}_1^s(\vec{\mathbf{J}}_I, \vec{\mathbf{M}}_I) + \vec{\mathbf{E}}_1^s(\vec{\mathbf{J}}_P, \vec{\mathbf{M}}_P) + \vec{\mathbf{E}}_1^s(\vec{\mathbf{J}}_2) + \vec{\mathbf{E}}^i\right]\Big|_{S_P^+} = -\vec{\mathbf{M}}_I - \vec{\mathbf{M}}_P \tag{5.39}$$

and if it is rearranged

$$\left[\vec{\mathbf{E}}_1^s(\vec{\mathbf{J}}_I,\vec{\mathbf{M}}_I)+\vec{\mathbf{E}}_1^s(\vec{\mathbf{J}}_P,\vec{\mathbf{M}}_P)+\vec{\mathbf{E}}_1^s(\vec{\mathbf{J}}_2)+\vec{\mathbf{E}}^i\right]_{\tan}-\hat{\mathbf{n}}_1\times\vec{\mathbf{M}}_I-\hat{\mathbf{n}}_1\times\vec{\mathbf{M}}_P=\vec{\mathbf{0}}\quad\text{on } S_P^+ \tag{5.40}$$

Also, (5.33) is substituted in (5.38) for S_P^+

$$\hat{\mathbf{n}}_1\times\left[\vec{\mathbf{H}}_1^s(\vec{\mathbf{J}}_I,\vec{\mathbf{M}}_I)+\vec{\mathbf{H}}_1^s(\vec{\mathbf{J}}_P,\vec{\mathbf{M}}_P)+\vec{\mathbf{H}}_1^s(\vec{\mathbf{J}}_2)+\vec{\mathbf{H}}^i\right]\Big|_{S_p^+}=\vec{\mathbf{J}}_I+\vec{\mathbf{J}}_P \tag{5.41}$$

by rearranging this

$$\left[\vec{\mathbf{H}}_1^s(\vec{\mathbf{J}}_I,\vec{\mathbf{M}}_I)+\vec{\mathbf{H}}_1^s(\vec{\mathbf{J}}_P,\vec{\mathbf{M}}_P)+\vec{\mathbf{H}}_1^s(\vec{\mathbf{J}}_2)+\vec{\mathbf{H}}^i\right]_{\tan}+\hat{\mathbf{n}}_1\times\vec{\mathbf{J}}_I+\hat{\mathbf{n}}_1\times\vec{\mathbf{J}}_P=\vec{\mathbf{0}}\quad\text{on } S_P^+ \tag{5.42}$$

can be written. Finally, employing (5.10) with (5.40) on S_p^+ surface

$$\left[\vec{\mathbf{E}}_1^s(\vec{\mathbf{J}}_P,\vec{\mathbf{M}}_P)+\vec{\mathbf{E}}_1^s(\vec{\mathbf{J}}_2)\right]_{\tan}-\hat{\mathbf{n}}_1\times\vec{\mathbf{M}}_P=\vec{\mathbf{0}}\quad\text{on } S_P^+ \tag{5.43}$$

also, employing (5.12) with (5.42) on S_p^+

$$\left[\vec{\mathbf{H}}_1^s(\vec{\mathbf{J}}_P,\vec{\mathbf{M}}_P)+\vec{\mathbf{H}}_1^s(\vec{\mathbf{J}}_2)\right]_{\tan}+\hat{\mathbf{n}}_1\times\vec{\mathbf{J}}_P=\vec{\mathbf{0}}\quad\text{on } S_P^+ \tag{5.44}$$

are found. Utilizing from inner equivalence theorem, the electric and magnetic fields inside each region

$$\vec{\mathbf{E}}_2=\vec{\mathbf{E}}_2^s(-\vec{\mathbf{J}}_1,-\vec{\mathbf{M}}_1),\quad\text{and}\quad\vec{\mathbf{E}}_1=\vec{\mathbf{0}} \tag{5.45}$$

$$\vec{\mathbf{H}}_2=\vec{\mathbf{H}}_2^s(-\vec{\mathbf{J}}_1,-\vec{\mathbf{M}}_1),\quad\text{and}\quad\vec{\mathbf{H}}_1=\vec{\mathbf{0}} \tag{5.46}$$

is expressed, and employing the boundary conditions on S_1^-

$$(-\hat{\mathbf{n}}_1)\times\left[\vec{\mathbf{E}}_2^s(-\vec{\mathbf{J}}_1,-\vec{\mathbf{M}}_1)\right]\Big|_{S_1^-}=\vec{\mathbf{M}}_1 \tag{5.47}$$

$$(-\hat{\mathbf{n}}_1)\times\left[\vec{\mathbf{H}}_2^s(-\vec{\mathbf{J}}_1,-\vec{\mathbf{M}}_1)\right]\Big|_{S_1^-}=-\vec{\mathbf{J}}_1 \tag{5.48}$$

can be written. (5.34) in (5.47) and (5.33) in (5.48) are substituted on S_P^-

$$(-\hat{\mathbf{n}}_1) \times \left[\vec{\mathbf{E}}_2^s(-\vec{\mathbf{J}}_I, -\vec{\mathbf{M}}_I) + \vec{\mathbf{E}}_2^s(-\vec{\mathbf{J}}_P, -\vec{\mathbf{M}}_P)\right]\Big|_{S_P^-} = \vec{\mathbf{M}}_I + \vec{\mathbf{M}}_P \tag{5.49}$$

$$(-\hat{\mathbf{n}}_1) \times \left[\vec{\mathbf{H}}_2^s(-\vec{\mathbf{J}}_I, -\vec{\mathbf{M}}_I) + \vec{\mathbf{H}}_2^s(-\vec{\mathbf{J}}_P, -\vec{\mathbf{M}}_P)\right]\Big|_{S_P^-} = -\vec{\mathbf{J}}_I - \vec{\mathbf{J}}_P \tag{5.50}$$

Eventually, in a similar way, if we apply (5.19) and (5.20) in (5.49) and (5.50), respectively

$$\left[\vec{\mathbf{E}}_2^s(-\vec{\mathbf{J}}_P, -\vec{\mathbf{M}}_P)\right]_{\tan} - \hat{\mathbf{n}}_1 \times \vec{\mathbf{M}}_P = \vec{\mathbf{0}} \quad \text{on } S_P^- \tag{5.51}$$

$$\left[\vec{\mathbf{H}}_2^s(-\vec{\mathbf{J}}_P, -\vec{\mathbf{M}}_P)\right]_{\tan} + \hat{\mathbf{n}}_1 \times \vec{\mathbf{J}}_P = \vec{\mathbf{0}} \quad \text{on } S_P^- \tag{5.52}$$

will be obtained. Therefore, the EFIEs and MFIEs can be used together with the PMCHWT formulation by adding them to the dielectric interface. As a result, the electric fields

$$\left[\vec{\mathbf{E}}_1^s(\vec{\mathbf{J}}_P, \vec{\mathbf{M}}_P) + \vec{\mathbf{E}}_1^s(\vec{\mathbf{J}}_2) + \vec{\mathbf{E}}_2^s(\vec{\mathbf{J}}_P, \vec{\mathbf{M}}_P)\right]_{\tan} = \vec{\mathbf{0}} \quad \text{on } S_P \tag{5.53}$$

as well as magnetic fields

$$\left[\vec{\mathbf{H}}_1^s(\vec{\mathbf{J}}_P, \vec{\mathbf{M}}_P) + \vec{\mathbf{H}}_1^s(\vec{\mathbf{J}}_2) + \vec{\mathbf{H}}_2^s(\vec{\mathbf{J}}_P, \vec{\mathbf{M}}_P)\right]_{\tan} = \vec{\mathbf{0}} \quad \text{on } S_P \tag{5.54}$$

are found on S_P surface. Lastly, we will employ the EFIE for the target surface. Thereby, the electric fields caused by the surface currents on S_2 surface

$$\left[\vec{\mathbf{E}}_1^s(\vec{\mathbf{J}}_P, \vec{\mathbf{M}}_P) + \vec{\mathbf{E}}_1^s(\vec{\mathbf{J}}_2) + \vec{\mathbf{E}}_1^s(\vec{\mathbf{J}}_I, \vec{\mathbf{M}}_I) + \vec{\mathbf{E}}^i\right]_{\tan} = \vec{\mathbf{0}} \quad \text{on } S_2 \tag{5.55}$$

rearranging this by using (5.29)

$$\left[\vec{\mathbf{E}}_1^s(\vec{\mathbf{J}}_P, \vec{\mathbf{M}}_P) + \vec{\mathbf{E}}_1^s(\vec{\mathbf{J}}_2)\right]_{\tan} = -\left[\vec{\mathbf{E}}^r + \vec{\mathbf{E}}^i\right]_{\tan} \quad \text{on } S_2 \tag{5.56}$$

is finally obtained. Here, $\vec{\mathbf{E}}^r$ is considered analytically solvable and precomputed. As a result, if we substitute (5.3) and (5.4) in (5.53), (5.54), and (5.56):

$$\Big\{j\omega\mu_0\mathfrak{L}^{(1)}[\vec{\mathbf{J}}_P]+j\omega\mu_1\mathfrak{L}^{(2)}[\vec{\mathbf{J}}_P] + \mathfrak{K}^{(1)}[\vec{\mathbf{M}}_P]+\mathfrak{K}^{(2)}[\vec{\mathbf{M}}_P]+j\omega\mu_1\mathfrak{L}^{(2)}[\vec{\mathbf{J}}_2]\Big\}_{\tan}=\vec{\mathbf{0}} \quad \text{on } S_P \tag{5.57}$$

$$\Big\{-j\omega\epsilon_0\mathfrak{L}^{(1)}[\vec{\mathbf{M}}_P]-j\omega\epsilon_1\mathfrak{L}^{(2)}[\vec{\mathbf{M}}_P]+\mathfrak{K}^{(1)}[\vec{\mathbf{J}}_P] + \mathfrak{K}^{(2)}[\vec{\mathbf{J}}_P]+\mathfrak{K}^{(2)}[\vec{\mathbf{J}}_2]\Big\}_{\tan}=\vec{\mathbf{0}} \quad \text{on } S_P \tag{5.58}$$

$$\Big\{j\omega\mu_1\mathfrak{L}^{(2)}[\vec{\mathbf{J}}_P]+\mathfrak{K}^{(2)}[\vec{\mathbf{M}}_P]+j\omega\mu_1\mathfrak{L}^{(2)}[\vec{\mathbf{J}}_2]\Big\}_{\tan}=\big[\vec{\mathbf{E}}^r+\vec{\mathbf{E}}^i\big]_{\tan} \quad \text{on } S_2 \tag{5.59}$$

will be found. Here, the superscripts (1) and (2) show the regions, and ϵ_1 and μ_1 can be complex and dependent on frequency. The principal value theorem was applied to the $\mathfrak{K}$ operator as in [78]

$$\lim_{\vec{\mathbf{r}}\to\vec{\mathbf{r}}'}\big[\hat{\mathbf{n}}\times\mathfrak{K}[\vec{\mathbf{X}}]\big]=\frac{1}{2}\vec{\mathbf{X}} \tag{5.60}$$

and

$$\lim_{\vec{\mathbf{r}}\to\vec{\mathbf{r}}'}\big[\mathfrak{K}[\vec{\mathbf{X}}]\big]_{\tan}=-\frac{1}{2}\hat{\mathbf{n}}\times\vec{\mathbf{X}} \tag{5.61}$$

thus, $\mathfrak{K}$ operator can be written as

$$\mathfrak{K}[\vec{\mathbf{X}}]_{\tan}=\mathfrak{K}_{P.V.}[\vec{\mathbf{X}}]_{\tan}-\frac{1}{2}\hat{\mathbf{n}}\times\vec{\mathbf{X}} \tag{5.62}$$

Finally, using (5.62) in (5.57), (5.58), and (5.59)

$$\Big\{j\omega\mu_0\mathfrak{L}^{(1)}[\vec{\mathbf{J}}_P]+j\omega\mu_1\mathfrak{L}^{(2)}[\vec{\mathbf{J}}_P] + \mathfrak{K}^{(1)}_{P.V.}[\vec{\mathbf{M}}_P]+\mathfrak{K}^{(2)}_{P.V.}[\vec{\mathbf{M}}_P]+j\omega\mu_1\mathfrak{L}^{(2)}[\vec{\mathbf{J}}_2]\Big\}_{\tan}=\vec{\mathbf{0}} \quad \text{on } S_P \tag{5.63}$$

$$\Big\{-j\omega\epsilon_0\mathfrak{L}^{(1)}[\vec{\mathbf{M}}_P]-j\omega\epsilon_1\mathfrak{L}^{(2)}[\vec{\mathbf{M}}_P]+\mathfrak{K}^{(1)}_{P.V.}[\vec{\mathbf{J}}_P] + \mathfrak{K}^{(2)}_{P.V.}[\vec{\mathbf{J}}_P]+\mathfrak{K}^{(2)}[\vec{\mathbf{J}}_2]\Big\}_{\tan}=\vec{\mathbf{0}} \quad \text{on } S_P \tag{5.64}$$

$$\Big\{j\omega\mu_1\mathfrak{L}^{(2)}[\vec{\mathbf{J}}_P]+\mathfrak{K}^{(2)}[\vec{\mathbf{M}}_P]+j\omega\mu_1\mathfrak{L}^{(2)}[\vec{\mathbf{J}}_2]\Big\}_{\tan}=\big[\vec{\mathbf{E}}^r+\vec{\mathbf{E}}^i\big]_{\tan} \quad \text{on } S_2 \tag{5.65}$$

are found. Moreover, if the unknown currents are expanded with RWG basis functions

$$\vec{\mathbf{J}}_P(\vec{\mathbf{r}}') = \sum_{\psi=1}^{N_P} I_{\psi}^{(J_P)} \vec{\mathbf{f}}_{\psi}(\vec{\mathbf{r}}') \tag{5.66}$$

$$\vec{\mathbf{M}}_P(\vec{\mathbf{r}}') = \sum_{\psi=1}^{N_P} I_{\psi}^{(M_P)} \vec{\mathbf{g}}_{\psi}(\vec{\mathbf{r}}') \tag{5.67}$$

$$\vec{\mathbf{J}}_2(\vec{\mathbf{r}}') = \sum_{\psi=1}^{N_2} I_{\psi}^{(J_2)} \vec{\mathbf{f}}_{\psi}(\vec{\mathbf{r}}') \tag{5.68}$$

where, $\vec{\mathbf{g}}_{\psi}(\vec{\mathbf{r}}')$ is the magnetic basis function. Actually, the RWG basis function is divergence-conforming but not curl-conforming. However, it is the same as $\vec{\mathbf{f}}_{\psi}(\vec{\mathbf{r}}')$ since the PMCHWT formulation can be handled without applying the curl operator. Furthermore, exploiting Galerkin-type testing functions, a matrix system

$$\begin{bmatrix} \overline{\overline{\mathbf{Z}}}_{11}^{(\vec{\mathbf{J}}_P)} & \overline{\overline{\mathbf{Z}}}_{12}^{(\vec{\mathbf{M}}_P)} & \overline{\overline{\mathbf{Z}}}_{13}^{(\vec{\mathbf{J}}_2)} \\ \overline{\overline{\mathbf{Z}}}_{21}^{(\vec{\mathbf{J}}_P)} & \overline{\overline{\mathbf{Z}}}_{22}^{(\vec{\mathbf{M}}_P)} & \overline{\overline{\mathbf{Z}}}_{23}^{(\vec{\mathbf{J}}_2)} \\ \overline{\overline{\mathbf{Z}}}_{31}^{(\vec{\mathbf{J}}_P)} & \overline{\overline{\mathbf{Z}}}_{32}^{(\vec{\mathbf{M}}_P)} & \overline{\overline{\mathbf{Z}}}_{33}^{(\vec{\mathbf{J}}_2)} \end{bmatrix} \begin{bmatrix} \overline{\mathbf{I}}_{\psi_{11}}^{(\vec{\mathbf{J}}_P)} \\ \overline{\mathbf{I}}_{\psi_{21}}^{(\vec{\mathbf{M}}_P)} \\ \overline{\mathbf{I}}_{\psi_{31}}^{(\vec{\mathbf{J}}_2)} \end{bmatrix} = \begin{bmatrix} \overline{\mathbf{V}}_{\zeta_{11}}^{(\vec{\mathbf{J}}_P)} \\ \overline{\mathbf{V}}_{\zeta_{21}}^{(\vec{\mathbf{M}}_P)} \\ \overline{\mathbf{V}}_{\zeta_{31}}^{(\vec{\mathbf{J}}_2)} \end{bmatrix} \tag{5.69}$$

are produced. At this point, we use $\vec{\mathbf{g}}_{\psi}(\vec{\mathbf{r}}') = \eta_0 \vec{\mathbf{f}}_{\psi}(\vec{\mathbf{r}}')$ for basis and $\vec{\mathbf{g}}_{\zeta}(\vec{\mathbf{r}}) = \eta_0 \vec{\mathbf{f}}_{\zeta}(\vec{\mathbf{r}})$ for testing to obtain the diagonal Z matrix. Here, the general expressions for $\mathfrak{L}$ and $\mathfrak{K}$

$$\begin{aligned} \mathfrak{L}[\vec{\mathbf{X}}] = \Bigg[& \int_{T_{\zeta}^{\pm}} \int_{T_{\psi}^{\pm}} \vec{\mathbf{f}}_{\zeta}(\vec{\mathbf{r}}) \cdot \vec{\mathbf{f}}_{\psi}(\vec{\mathbf{r}}') \frac{e^{-jk_l \left\| \vec{\mathbf{r}} - \vec{\mathbf{r}}' \right\|}}{4\pi \left\| \vec{\mathbf{r}} - \vec{\mathbf{r}}' \right\|} dS'_{T_{\psi}^{\pm}} dS_{T_{\zeta}^{\pm}} \\ & - \frac{1}{k_l^2} \int_{T_{\zeta}^{\pm}} \int_{T_{\psi}^{\pm}} \left[\nabla_s \cdot \vec{\mathbf{f}}_{\zeta}(\vec{\mathbf{r}}) \right] \left[\nabla'_s \cdot \vec{\mathbf{f}}_{\psi}(\vec{\mathbf{r}}') \right] \frac{e^{-jk_l \left\| \vec{\mathbf{r}} - \vec{\mathbf{r}}' \right\|}}{4\pi \left\| \vec{\mathbf{r}} - \vec{\mathbf{r}}' \right\|} dS'_{T_{\psi}^{\pm}} dS_{T_{\zeta}^{\pm}} \Bigg] \end{aligned} \tag{5.70}$$

and

$$\mathfrak{K}[\vec{\mathbf{X}}] = -\frac{1}{4\pi} \int_{T_{\zeta}^{\pm}} \int_{T_{\psi}^{\pm}} \vec{\mathbf{f}}_{\zeta}(\vec{\mathbf{r}}) \cdot \left[\left(\vec{\mathbf{r}} - \vec{\mathbf{r}}' \right) \times \vec{\mathbf{g}}_{\psi}(\vec{\mathbf{r}}') \right] \frac{1 + jk_l \left\| \vec{\mathbf{r}} - \vec{\mathbf{r}}' \right\|}{\left\| \vec{\mathbf{r}} - \vec{\mathbf{r}}' \right\|^3} e^{-jk_l \left\| \vec{\mathbf{r}} - \vec{\mathbf{r}}' \right\|} dS'_{T_{\psi}^{\pm}} dS_{T_{\zeta}^{\pm}} \tag{5.71}$$

can be given. Here, k_l indicates the wave number for a region. As a result, it can be helpful for the reader to give detailed expressions each Z component for any edge

$$Z_{11}^{(\zeta\psi)} = jk_0\eta_0 \left[\int_{T_\zeta^\pm} \int_{T_\psi^\pm} \vec{\mathbf{f}}_\zeta(\vec{\mathbf{r}}) \cdot \vec{\mathbf{f}}_\psi(\vec{\mathbf{r}}') \frac{e^{-jk_0\left\|\vec{\mathbf{r}}-\vec{\mathbf{r}}'\right\|}}{4\pi\left\|\vec{\mathbf{r}}-\vec{\mathbf{r}}'\right\|} dS_{T_\psi^\pm}^{\prime(P)} dS_{T_\zeta^\pm}^{(P)} \right.$$
$$\left. -\frac{1}{k_0^2} \int_{T_\zeta^\pm} \int_{T_\psi^\pm} \left[\nabla_s \cdot \vec{\mathbf{f}}_\zeta(\vec{\mathbf{r}})\right]\left[\nabla_s' \cdot \vec{\mathbf{f}}_\psi(\vec{\mathbf{r}}')\right] \frac{e^{-jk_0\left\|\vec{\mathbf{r}}-\vec{\mathbf{r}}'\right\|}}{4\pi\left\|\vec{\mathbf{r}}-\vec{\mathbf{r}}'\right\|} dS_{T_\psi^\pm}^{\prime(P)} dS_{T_\zeta^\pm}^{(P)} \right]$$
$$jk_1\eta_1 \left[\int_{T_\zeta^\pm} \int_{T_\psi^\pm} \vec{\mathbf{f}}_\zeta(\vec{\mathbf{r}}) \cdot \vec{\mathbf{f}}_\psi(\vec{\mathbf{r}}') \frac{e^{-jk_1\left\|\vec{\mathbf{r}}-\vec{\mathbf{r}}'\right\|}}{4\pi\left\|\vec{\mathbf{r}}-\vec{\mathbf{r}}'\right\|} dS_{T_\psi^\pm}^{\prime(P)} dS_{T_\zeta^\pm}^{(P)} \right.$$
$$\left. -\frac{1}{k_1^2} \int_{T_\zeta^\pm} \int_{T_\psi^\pm} \left[\nabla_s \cdot \vec{\mathbf{f}}_\zeta(\vec{\mathbf{r}})\right]\left[\nabla_s' \cdot \vec{\mathbf{f}}_\psi(\vec{\mathbf{r}}')\right] \frac{e^{-jk_1\left\|\vec{\mathbf{r}}-\vec{\mathbf{r}}'\right\|}}{4\pi\left\|\vec{\mathbf{r}}-\vec{\mathbf{r}}'\right\|} dS_{T_\psi^\pm}^{\prime(P)} dS_{T_\zeta^\pm}^{(P)} \right] \quad \text{on } S_P \quad (5.72)$$

$$Z_{12}^{(\zeta\psi)} = -\frac{1}{4\pi} \int_{T_\zeta^\pm} \int_{T_\psi^\pm} \vec{\mathbf{f}}_\zeta(\vec{\mathbf{r}}) \cdot \left[\left(\vec{\mathbf{r}}-\vec{\mathbf{r}}'\right) \times \vec{\mathbf{g}}_\psi(\vec{\mathbf{r}}')\right] \frac{1+jk_0\left\|\vec{\mathbf{r}}-\vec{\mathbf{r}}'\right\|}{\left\|\vec{\mathbf{r}}-\vec{\mathbf{r}}'\right\|^3} e^{-jk_0\left\|\vec{\mathbf{r}}-\vec{\mathbf{r}}'\right\|} dS_{T_\psi^\pm}^{\prime(P)} dS_{T_\zeta^\pm}^{(P)}$$
$$-\frac{1}{4\pi} \int_{T_\zeta^\pm} \int_{T_\psi^\pm} \vec{\mathbf{f}}_\zeta(\vec{\mathbf{r}}) \cdot \left[\left(\vec{\mathbf{r}}-\vec{\mathbf{r}}'\right) \times \vec{\mathbf{g}}_\psi(\vec{\mathbf{r}}')\right] \frac{1+jk_1\left\|\vec{\mathbf{r}}-\vec{\mathbf{r}}'\right\|}{\left\|\vec{\mathbf{r}}-\vec{\mathbf{r}}'\right\|^3} e^{-jk_1\left\|\vec{\mathbf{r}}-\vec{\mathbf{r}}'\right\|} dS_{T_\psi^\pm}^{\prime(P)} dS_{T_\zeta^\pm}^{(P)} \quad \text{on } S_P \quad (5.73)$$

$$Z_{13}^{(\zeta\psi)} = jk_1\eta_1 \left[\int_{T_\zeta^\pm} \int_{T_\psi^\pm} \vec{\mathbf{f}}_\zeta(\vec{\mathbf{r}}) \cdot \vec{\mathbf{f}}_\psi(\vec{\mathbf{r}}') \frac{e^{-jk_1\left\|\vec{\mathbf{r}}-\vec{\mathbf{r}}'\right\|}}{4\pi\left\|\vec{\mathbf{r}}-\vec{\mathbf{r}}'\right\|} dS_{T_\psi^\pm}^{\prime(2)} dS_{T_\zeta^\pm}^{(P)} \right.$$
$$\left. -\frac{1}{k_1^2} \int_{T_\zeta^\pm} \int_{T_\psi^\pm} \left[\nabla_s \cdot \vec{\mathbf{f}}_\zeta(\vec{\mathbf{r}})\right]\left[\nabla_s' \cdot \vec{\mathbf{f}}_\psi(\vec{\mathbf{r}}')\right] \frac{e^{-jk_1\left\|\vec{\mathbf{r}}-\vec{\mathbf{r}}'\right\|}}{4\pi\left\|\vec{\mathbf{r}}-\vec{\mathbf{r}}'\right\|} dS_{T_\psi^\pm}^{\prime(2)} dS_{T_\zeta^\pm}^{(P)} \right] \quad \text{on } S_P \quad (5.74)$$

$$Z_{21}^{(\zeta\psi)} = -\frac{1}{4\pi} \int_{T_\zeta^\pm} \int_{T_\psi^\pm} \vec{\mathbf{g}}_\zeta(\vec{\mathbf{r}}) \cdot \left[\left(\vec{\mathbf{r}}-\vec{\mathbf{r}}'\right) \times \vec{\mathbf{f}}_\psi(\vec{\mathbf{r}}')\right] \frac{1+jk_0\left\|\vec{\mathbf{r}}-\vec{\mathbf{r}}'\right\|}{\left\|\vec{\mathbf{r}}-\vec{\mathbf{r}}'\right\|^3} e^{-jk_0\left\|\vec{\mathbf{r}}-\vec{\mathbf{r}}'\right\|} dS_{T_\psi^\pm}^{\prime(P)} dS_{T_\zeta^\pm}^{(P)}$$
$$-\frac{1}{4\pi} \int_{T_\zeta^\pm} \int_{T_\psi^\pm} \vec{\mathbf{g}}_\zeta(\vec{\mathbf{r}}) \cdot \left[\left(\vec{\mathbf{r}}-\vec{\mathbf{r}}'\right) \times \vec{\mathbf{f}}_\psi(\vec{\mathbf{r}}')\right] \frac{1+jk_1\left\|\vec{\mathbf{r}}-\vec{\mathbf{r}}'\right\|}{\left\|\vec{\mathbf{r}}-\vec{\mathbf{r}}'\right\|^3} e^{-jk_1\left\|\vec{\mathbf{r}}-\vec{\mathbf{r}}'\right\|} dS_{T_\psi^\pm}^{\prime(P)} dS_{T_\zeta^\pm}^{(P)} \quad \text{on } S_P \quad (5.75)$$

$$Z_{22}^{(\zeta\psi)} = -j\frac{k_0}{\eta_0}\left[\int_{T_\zeta^\pm}\int_{T_\psi^\pm}\vec{\mathbf{g}}_\zeta(\vec{\mathbf{r}})\cdot\vec{\mathbf{g}}_\psi(\vec{\mathbf{r}}')\frac{e^{-jk_0\|\vec{\mathbf{r}}-\vec{\mathbf{r}}'\|}}{4\pi\|\vec{\mathbf{r}}-\vec{\mathbf{r}}'\|}dS_{T_\psi^\pm}^{\prime(P)}dS_{T_\zeta^\pm}^{(P)}\right.$$
$$\left.-\frac{1}{k_0^2}\int_{T_\zeta^\pm}\int_{T_\psi^\pm}\left[\nabla_s\cdot\vec{\mathbf{g}}_\zeta(\vec{\mathbf{r}})\right]\left[\nabla_s'\cdot\vec{\mathbf{g}}_\psi(\vec{\mathbf{r}}')\right]\frac{e^{-jk_0\|\vec{\mathbf{r}}-\vec{\mathbf{r}}'\|}}{4\pi\|\vec{\mathbf{r}}-\vec{\mathbf{r}}'\|}dS_{T_\psi^\pm}^{\prime(P)}dS_{T_\zeta^\pm}^{(P)}\right]$$
$$-j\frac{k_1}{\eta_1}\left[\int_{T_\zeta^\pm}\int_{T_\psi^\pm}\vec{\mathbf{g}}_\zeta(\vec{\mathbf{r}})\cdot\vec{\mathbf{g}}_\psi(\vec{\mathbf{r}}')\frac{e^{-jk_1\|\vec{\mathbf{r}}-\vec{\mathbf{r}}'\|}}{4\pi\|\vec{\mathbf{r}}-\vec{\mathbf{r}}'\|}dS_{T_\psi^\pm}^{\prime(P)}dS_{T_\zeta^\pm}^{(P)}\right.$$
$$\left.-\frac{1}{k_1^2}\int_{T_\zeta^\pm}\int_{T_\psi^\pm}\left[\nabla_s\cdot\vec{\mathbf{g}}_\zeta(\vec{\mathbf{r}})\right]\left[\nabla_s'\cdot\vec{\mathbf{g}}_\psi(\vec{\mathbf{r}}')\right]\frac{e^{-jk_1\|\vec{\mathbf{r}}-\vec{\mathbf{r}}'\|}}{4\pi\|\vec{\mathbf{r}}-\vec{\mathbf{r}}'\|}dS_{T_\psi^\pm}^{\prime(P)}dS_{T_\zeta^\pm}^{(P)}\right]\quad\text{on } S_P \quad (5.76)$$

$$Z_{23}^{(\zeta\psi)} = -\frac{1}{4\pi}\int_{T_\zeta^\pm}\int_{T_\psi^\pm}\vec{\mathbf{g}}_\zeta(\vec{\mathbf{r}})\cdot\left[\left(\vec{\mathbf{r}}-\vec{\mathbf{r}}'\right)\times\vec{\mathbf{f}}_\psi(\vec{\mathbf{r}}')\right]$$
$$\frac{1+jk_1\|\vec{\mathbf{r}}-\vec{\mathbf{r}}'\|}{\|\vec{\mathbf{r}}-\vec{\mathbf{r}}'\|^3}e^{-jk_1\|\vec{\mathbf{r}}-\vec{\mathbf{r}}'\|}dS_{T_\psi^\pm}^{\prime(2)}dS_{T_\zeta^\pm}^{(P)}\quad\text{on } S_P \quad (5.77)$$

$$Z_{31}^{(\zeta\psi)} = jk_1\eta_1\left[\int_{T_\zeta^\pm}\int_{T_\psi^\pm}\vec{\mathbf{f}}_\zeta(\vec{\mathbf{r}})\cdot\vec{\mathbf{f}}_\psi(\vec{\mathbf{r}}')\frac{e^{-jk_1\|\vec{\mathbf{r}}-\vec{\mathbf{r}}'\|}}{4\pi\|\vec{\mathbf{r}}-\vec{\mathbf{r}}'\|}dS_{T_\psi^\pm}^{\prime(P)}dS_{T_\zeta^\pm}^{(2)}\right.$$
$$\left.-\frac{1}{k_1^2}\int_{T_\zeta^\pm}\int_{T_\psi^\pm}\left[\nabla_s\cdot\vec{\mathbf{f}}_\zeta(\vec{\mathbf{r}})\right]\left[\nabla_s'\cdot\vec{\mathbf{f}}_\psi(\vec{\mathbf{r}}')\right]\frac{e^{-jk_1\|\vec{\mathbf{r}}-\vec{\mathbf{r}}'\|}}{4\pi\|\vec{\mathbf{r}}-\vec{\mathbf{r}}'\|}dS_{T_\psi^\pm}^{\prime(P)}dS_{T_\zeta^\pm}^{(2)}\right]\quad\text{on } S_2 \quad (5.78)$$

$$Z_{32}^{(\zeta\psi)} = -\frac{1}{4\pi}\int_{T_\zeta^\pm}\int_{T_\psi^\pm}\vec{\mathbf{f}}_\zeta(\vec{\mathbf{r}})\cdot\left[\left(\vec{\mathbf{r}}-\vec{\mathbf{r}}'\right)\times\vec{\mathbf{g}}_\psi(\vec{\mathbf{r}}')\right]$$
$$\frac{1+jk_1\|\vec{\mathbf{r}}-\vec{\mathbf{r}}'\|}{\|\vec{\mathbf{r}}-\vec{\mathbf{r}}'\|^3}e^{-jk_1\|\vec{\mathbf{r}}-\vec{\mathbf{r}}'\|}dS_{T_\psi^\pm}^{\prime(P)}dS_{T_\zeta^\pm}^{(2)}\quad\text{on } S_2 \quad (5.79)$$

$$Z_{33}^{(\zeta\psi)} = jk_1\eta_1\left[\int_{T_\zeta^\pm}\int_{T_\psi^\pm}\vec{\mathbf{f}}_\zeta(\vec{\mathbf{r}})\cdot\vec{\mathbf{f}}_\psi(\vec{\mathbf{r}}')\frac{e^{-jk_1\|\vec{\mathbf{r}}-\vec{\mathbf{r}}'\|}}{4\pi\|\vec{\mathbf{r}}-\vec{\mathbf{r}}'\|}dS_{T_\psi^\pm}^{\prime(2)}dS_{T_\zeta^\pm}^{(2)}\right.$$
$$\left.-\frac{1}{k_1^2}\int_{T_\zeta^\pm}\int_{T_\psi^\pm}\left[\nabla_s\cdot\vec{\mathbf{f}}_\zeta(\vec{\mathbf{r}})\right]\left[\nabla_s'\cdot\vec{\mathbf{f}}_\psi(\vec{\mathbf{r}}')\right]\frac{e^{-jk_1\|\vec{\mathbf{r}}-\vec{\mathbf{r}}'\|}}{4\pi\|\vec{\mathbf{r}}-\vec{\mathbf{r}}'\|}dS_{T_\psi^\pm}^{\prime(2)}dS_{T_\zeta^\pm}^{(2)}\right]\quad\text{on } S_2 \quad (5.80)$$

where, supercripts (P) and (2) imply the surfaces. In addition, $\overline{\mathbf{V}}$ array components

$$V_{\zeta 11}^{(P)} = 0 \quad \text{on } S_P \tag{5.81}$$

$$V_{\zeta 21}^{(P)} = 0 \quad \text{on } S_P \tag{5.82}$$

$$V_{\zeta 31}^{(2)} = \int_{S_{T_\zeta^\pm}^{(2)}} \vec{\mathbf{f}}_\zeta(\vec{\mathbf{r}}) \cdot \left[\vec{\mathbf{E}}^i + \vec{\mathbf{E}}^r\right] dS_{T_\zeta^\pm}^{(2)} \quad \text{on } S_2 \tag{5.83}$$

After the representation of the Z matrix, the far-field expression inside Region 1 can be no more given here as follows

$$\vec{\mathbf{E}}_{far\text{-}field}^s(\vec{\mathbf{r}}) = \vec{\mathbf{E}}_1^s(\vec{\mathbf{J}}_P, \vec{\mathbf{M}}_P) + \vec{\mathbf{E}}_1^s(\vec{\mathbf{J}}_2) \tag{5.84}$$

Thus, for S_P

$$\begin{aligned}\vec{\mathbf{E}}_1^s(\vec{\mathbf{J}}_P, \vec{\mathbf{M}}_P) = -jk_0 \frac{e^{-jk_0 r}}{4\pi r} \int_{S_P'} \left[\vec{\mathbf{M}}_P(\vec{\mathbf{r}}') \times \vec{\mathbf{r}}\right] e^{jk_0 \vec{\mathbf{r}}' \cdot \vec{\mathbf{r}}} dS_P' \\ + jk_0 \eta_0 \frac{e^{-jk_0 r}}{4\pi r} \int_{S_P'} \hat{\mathbf{r}} \times \left[\hat{\mathbf{r}} \times \vec{\mathbf{J}}_P(\vec{\mathbf{r}}')\right] \left[e^{jk_0 \vec{\mathbf{r}}' \cdot \hat{\mathbf{r}}}\right] dS_P'\end{aligned} \tag{5.85}$$

and for S_2

$$\vec{\mathbf{E}}_1^s(\vec{\mathbf{J}}_2) = jk_0 \eta_0 \frac{e^{-jk_0 r}}{4\pi r} \int_{S_2'} \hat{\mathbf{r}} \times \left[\hat{\mathbf{r}} \times \vec{\mathbf{J}}_2(\vec{\mathbf{r}}')\right] \left[e^{jk_0 \vec{\mathbf{r}}' \cdot \hat{\mathbf{r}}}\right] dS_2' \tag{5.86}$$

can be written. Finally, utilizing (5.66), (5.67), and (5.68)

$$\begin{aligned}\vec{\mathbf{E}}_1^s(\vec{\mathbf{J}}_P, \vec{\mathbf{M}}_P) = -jk_0 \frac{e^{-jk_0 r}}{4\pi r} \left[\sum_{\psi=1}^{N_P} I_\psi^{(M_P)} \int_{S_{T_\psi^\pm}^{\prime(P)}} \left[\vec{\mathbf{g}}_\psi(\vec{\mathbf{r}}') \times \vec{\mathbf{r}}\right] \left[e^{jk_0 \vec{\mathbf{r}}' \cdot \hat{\mathbf{r}}}\right] dS_{T_\psi^\pm}^{\prime(P)}\right] \\ + jk_0 \eta_0 \frac{e^{-jk_0 r}}{4\pi r} \left[\sum_{\psi=1}^{N_P} I_\psi^{(J_P)} \int_{S_{T_\psi^\pm}^{\prime(P)}} \hat{\mathbf{r}} \times \left[\hat{\mathbf{r}} \times \vec{\mathbf{f}}_\psi(\vec{\mathbf{r}}')\right] \left[e^{jk_0 \vec{\mathbf{r}}' \cdot \hat{\mathbf{r}}}\right] dS_{T_\psi^\pm}^{\prime(P)}\right]\end{aligned} \tag{5.87}$$

$$\vec{\mathbf{E}}_1^s(\vec{\mathbf{J}}_2) = jk_0\eta_0\frac{e^{-jk_0r}}{4\pi r}\left[\sum_{\psi=1}^{N_2} I_\psi^{(J_2)}\int_{S_{T_\psi^\pm}^{\prime(2)}} \hat{\mathbf{r}}\times\left[\hat{\mathbf{r}}\times\vec{\mathbf{f}}_\psi(\vec{\mathbf{r}}')\right]\left[e^{jk_0\vec{\mathbf{r}}'\cdot\hat{\mathbf{r}}}\right]dS_{T_\psi^\pm}^{\prime(2)}\right] \tag{5.88}$$

are expressed for any edge on the surfaces. Lastly, the RCS

$$\text{RCS} = \lim_{r\to\infty} 4\pi r^2 \frac{\left\|\vec{\mathbf{E}}^s_{\textit{far-field}}\right\|^2}{\left\|\vec{\mathbf{E}}^i\right\|^2} \tag{5.89}$$

is defined.

5.2 Numerical Results

As discussed in the previous chapters, we know that the size of the perturbation surface must be carefully selected to obtain the proposed method with acceptable accuracy. Therefore, starting by discussing the perturbation current distribution may be helpful. As demonstrated in Figures 5.2–5.13, several scattering scenarios with a selection perturbation area of 12.5×12.5 m^2 are conducted to evaluate the perturbed current distribution on this truncated surface. Here, the dielectric constant of the ground is selected as 4, and it has a conductivity of 0.1 S/m. In the first scattering example, a PEC cube with a side length of 0.3 m ($d = 0.3$ m) is initially placed above the surface at a distance of 0.1 m ($h = 0.1$ m) in which the incidence angle is 0°. The perturbed currents on the perturbation surface are demonstrated in Figures 5.2 and 5.3. Subsequently, the incidence angle is set to 85°, and the current density results on the surface are presented in Figures 5.4 and 5.5. As illustrated in Figures 5.6 and 5.7 for the third simulation, h is increased to 0.2 m, where the incidence angle is once more fixed to 0°. Additionally, the d parameter is revised to 0.6 m while the incidence angle is 0° as the fourth case shared in Figures 5.8 and 5.9. Here, h is 0.1 m again. So far, all simulations are illuminated by a linearly polarized plane wave in the negative y-direction ($\theta_i = 0°$, $\phi_i = 0°$, and $\alpha_i = 90°$). In Figures 5.10 and 5.11, the polarization of the plane wave is shifted to the positive x-direction for the fifth example ($\theta_i = 0°$, $\phi_i = 0°$, and $\alpha_i = 0°$), while other parameters remain the same. In Figures 5.12 and 5.13, the horizontal polarization in the second example is converted vertically. As seen from the figures, the current distribution behaves similarly to a PEC ground and continues to satisfy our assumption.

Furthermore, in these simulations, the average mesh length of a triangle for the ground surface is $0.2\lambda_0$. The cube is discretized with triangles of $0.1\lambda_0$ average

length. The distributions of each current density on this truncated surface are given in Figures 5.2–5.13 for these six cases, respectively. Also, the incident plane wave frequency was 300 MHz in all simulations.

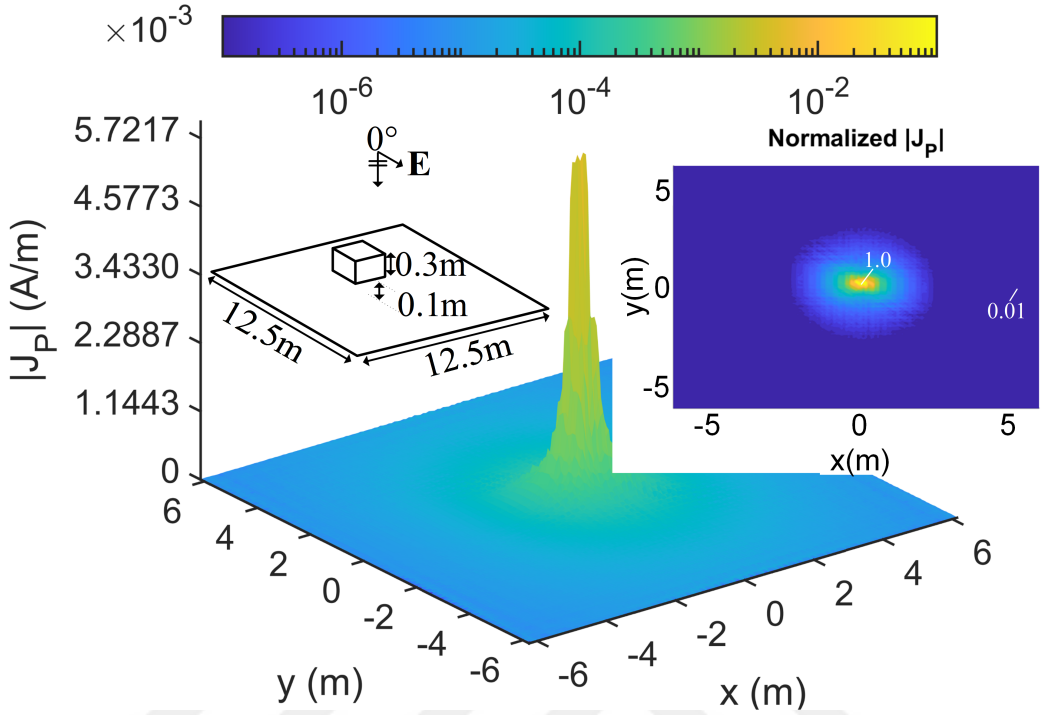

Figure 5.2 Perturbed electric current density for a limited region on an infinite ground plane ($d = 0.3$ m, $h = 0.1$ m, $\theta_i = 0°$, $\phi_i = 0°$, $\alpha_i = 90°$)

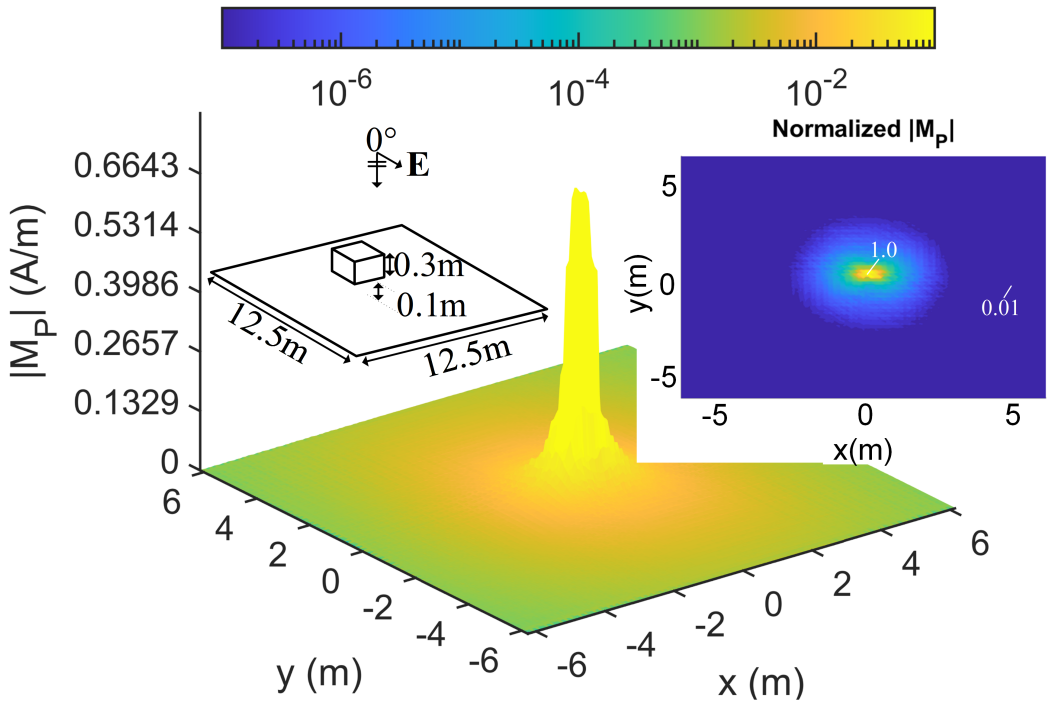

Figure 5.3 Perturbed magnetic current density for a limited region on an infinite ground plane ($d = 0.3$ m, $h = 0.1$ m, $\theta_i = 0°$, $\phi_i = 0°$, $\alpha_i = 90°$)

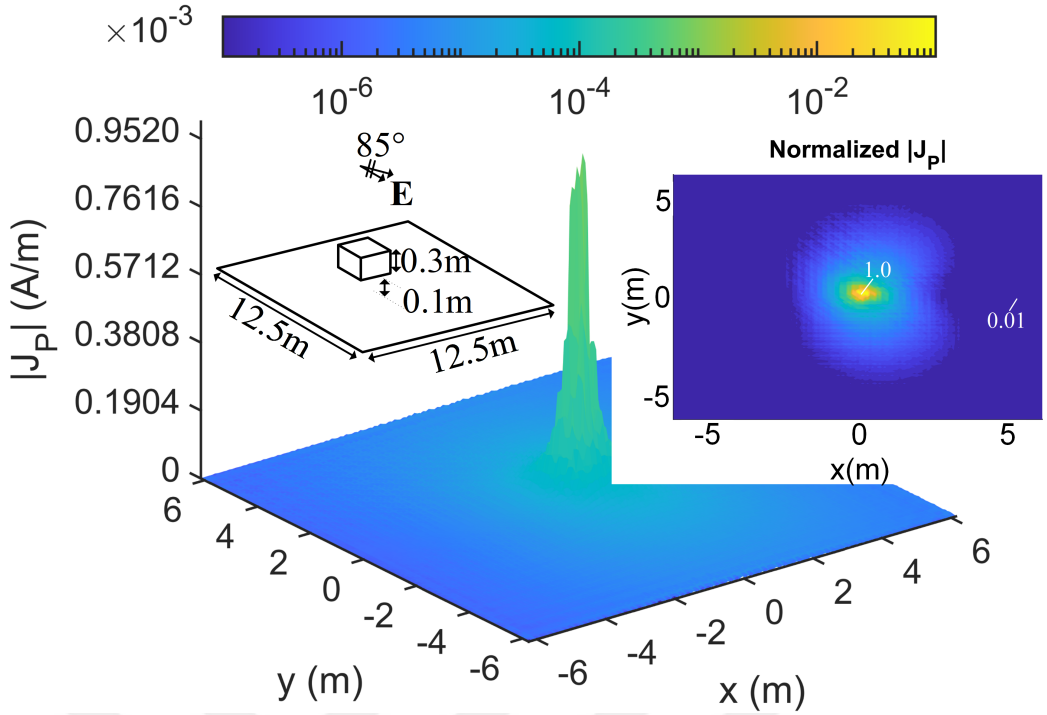

Figure 5.4 Perturbed electric current density for a limited region on an infinite ground plane ($d = 0.3$ m, $h = 0.1$ m, $\theta_i = 85°$, $\phi_i = 0°$, $\alpha_i = 90°$)

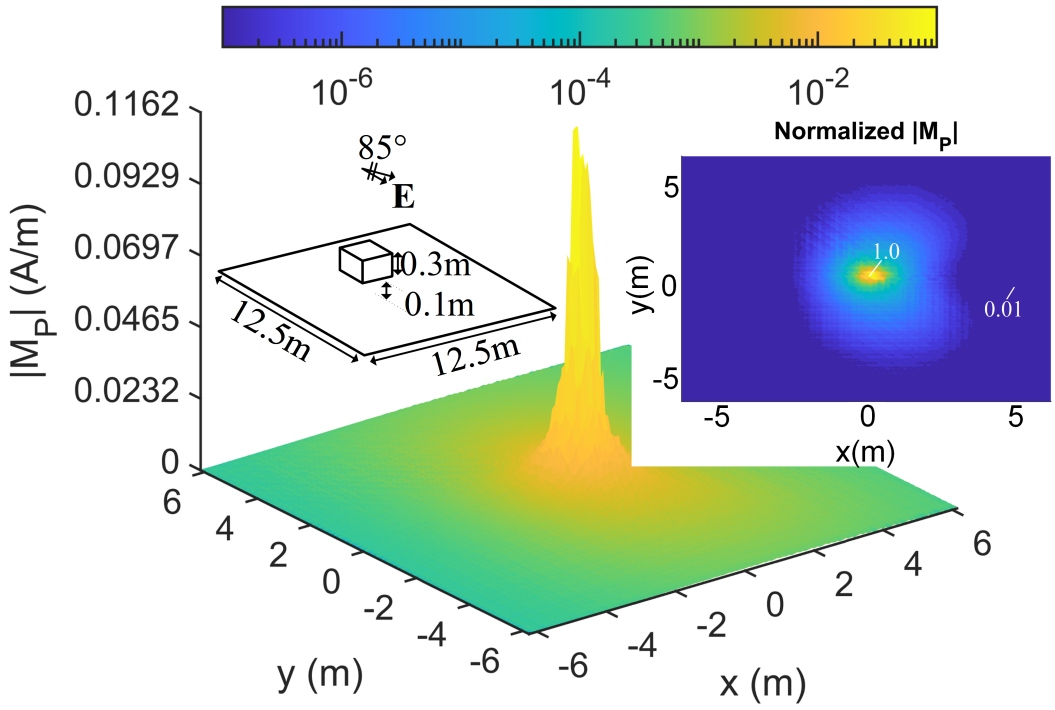

Figure 5.5 Perturbed magnetic current density for a limited region on an infinite ground plane ($d = 0.3$ m, $h = 0.1$ m, $\theta_i = 85°$, $\phi_i = 0°$, $\alpha_i = 90°$)

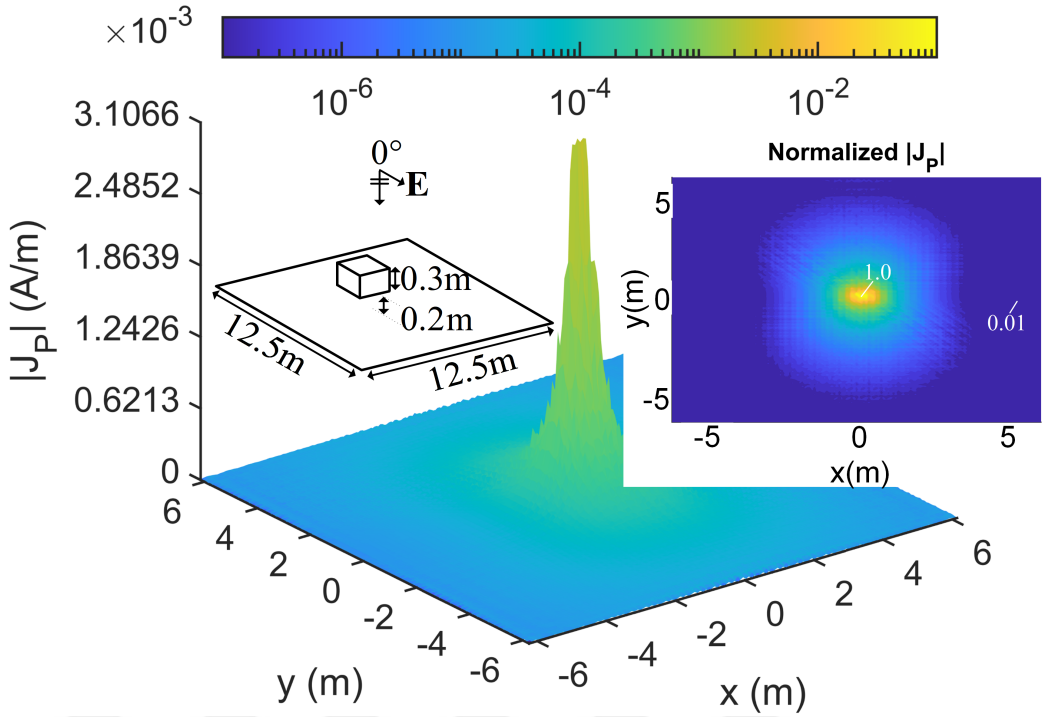

Figure 5.6 Perturbed electric current density for a limited region on an infinite ground plane ($d = 0.3$ m, $h = 0.2$ m, $\theta_i = 0°$, $\phi_i = 0°$, $\alpha_i = 90°$)

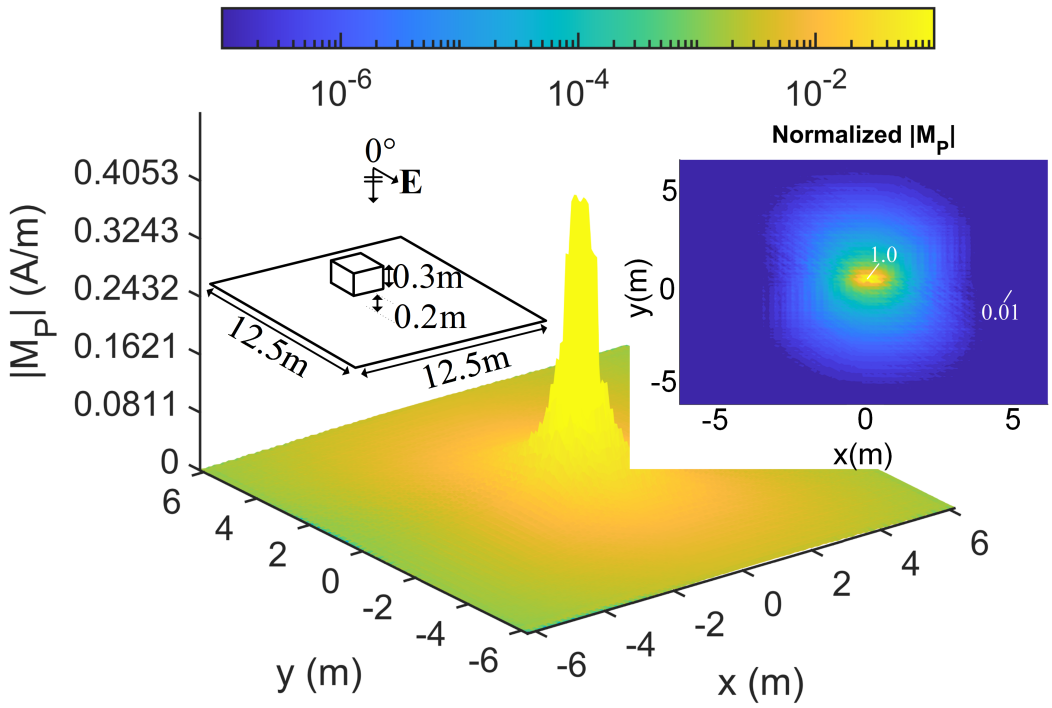

Figure 5.7 Perturbed magnetic current density for a limited region on an infinite ground plane ($d = 0.3$ m, $h = 0.2$ m, $\theta_i = 0°$, $\phi_i = 0°$, $\alpha_i = 90°$)

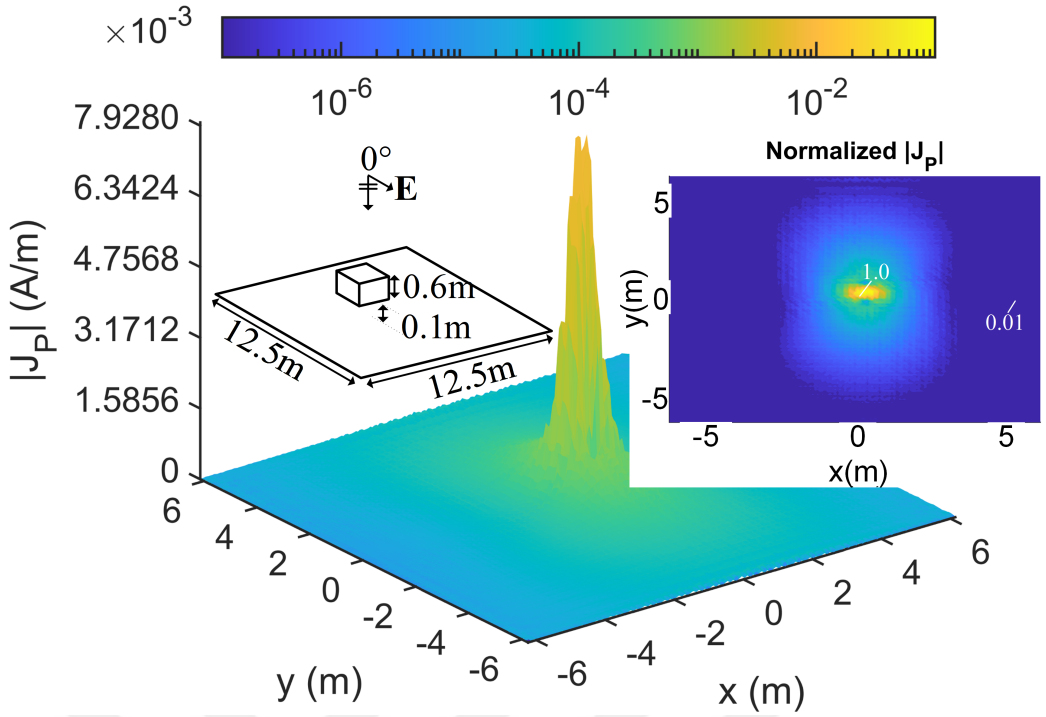

Figure 5.8 Perturbed electric current density for a limited region on an infinite ground plane ($d = 0.6$ m, $h = 0.1$ m, $\theta_i = 0°$, $\phi_i = 0°$, $\alpha_i = 90°$)

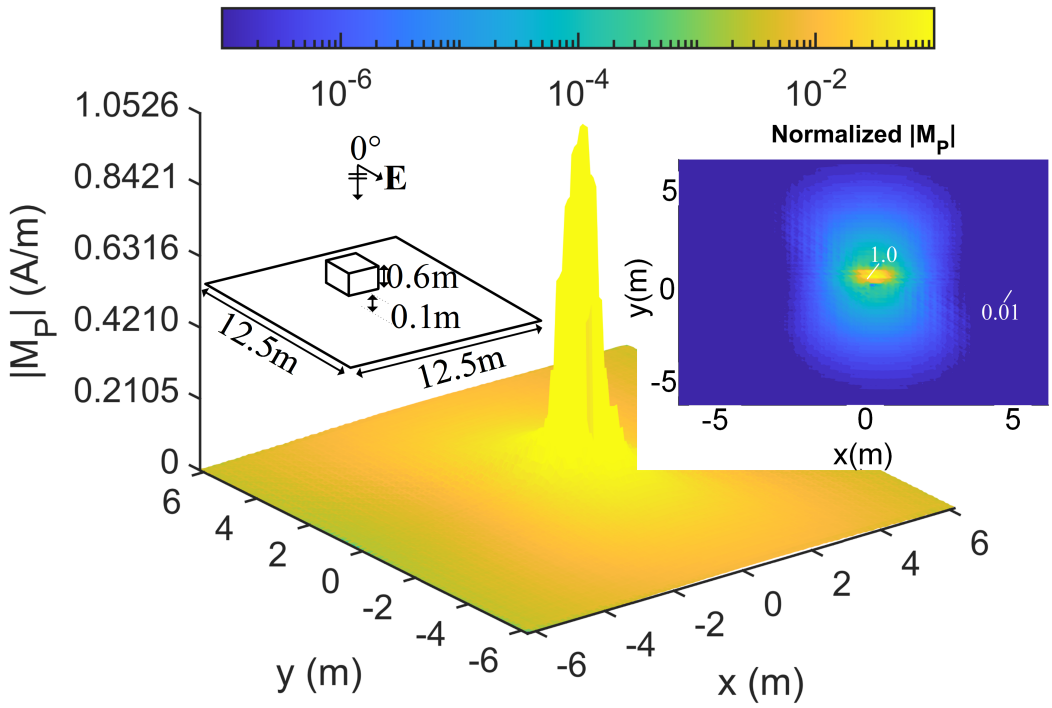

Figure 5.9 Perturbed magnetic current density for a limited region on an infinite ground plane ($d = 0.6$ m, $h = 0.1$ m, $\theta_i = 0°$, $\phi_i = 0°$, $\alpha_i = 90°$)

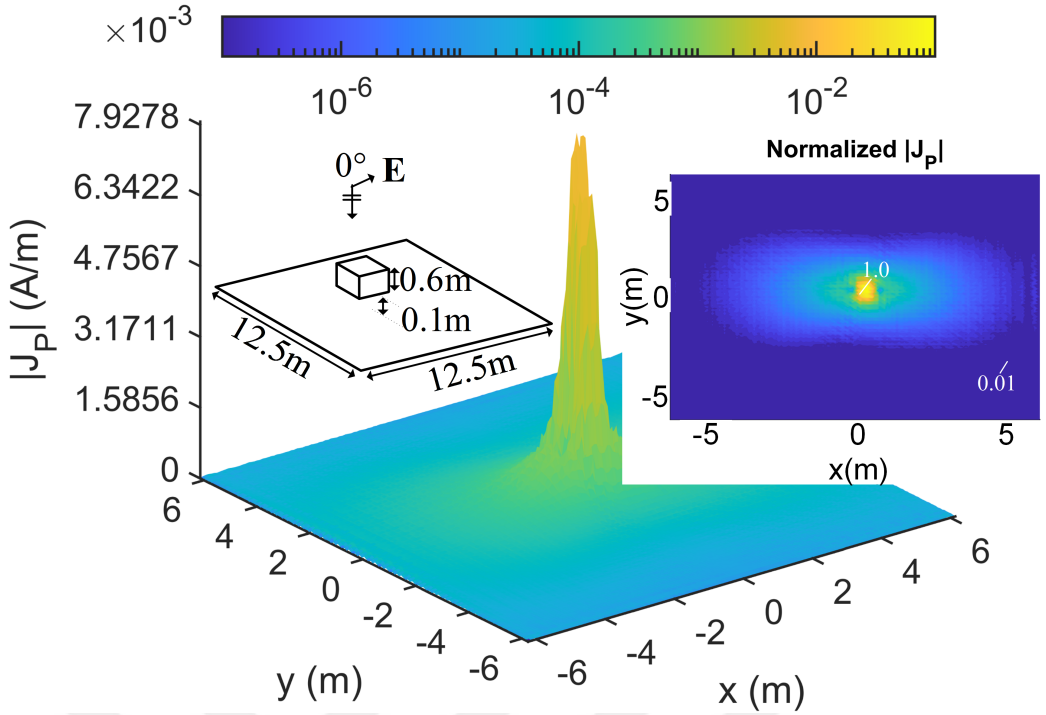

Figure 5.10 Perturbed electric current density for a limited region on an infinite ground plane ($d = 0.6$ m, $h = 0.1$ m, $\theta_i = 0°$, $\phi_i = 0°$, $\alpha_i = 0°$)

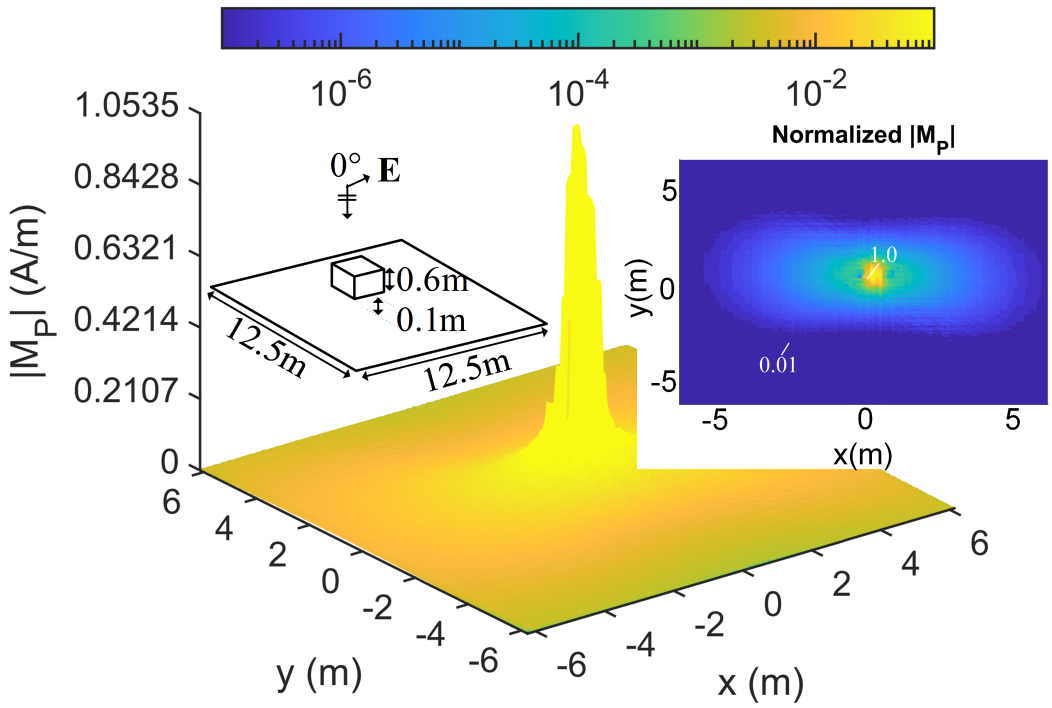

Figure 5.11 Perturbed magnetic current density for a limited region on an infinite ground plane ($d = 0.6$ m, $h = 0.1$ m, $\theta_i = 0°$, $\phi_i = 0°$, $\alpha_i = 0°$)

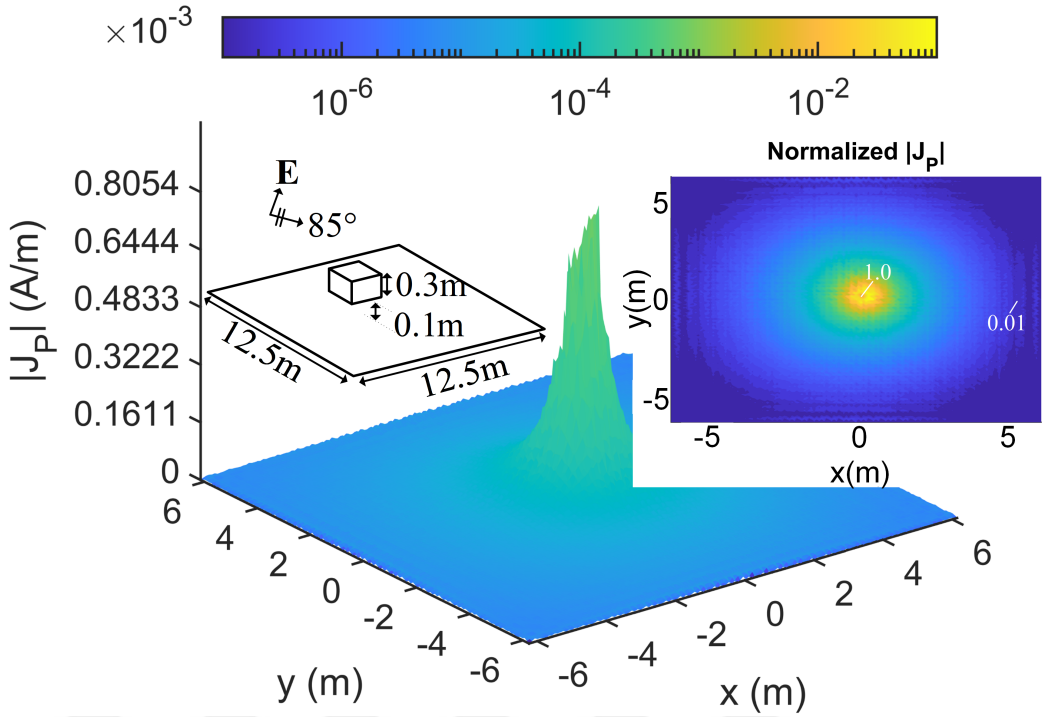

Figure 5.12 Perturbed electric current density for a limited region on an infinite ground plane ($d = 0.3$ m, $h = 0.1$ m, $\theta_i = 85°$, $\phi_i = 0°$, $\alpha_i = 0°$)

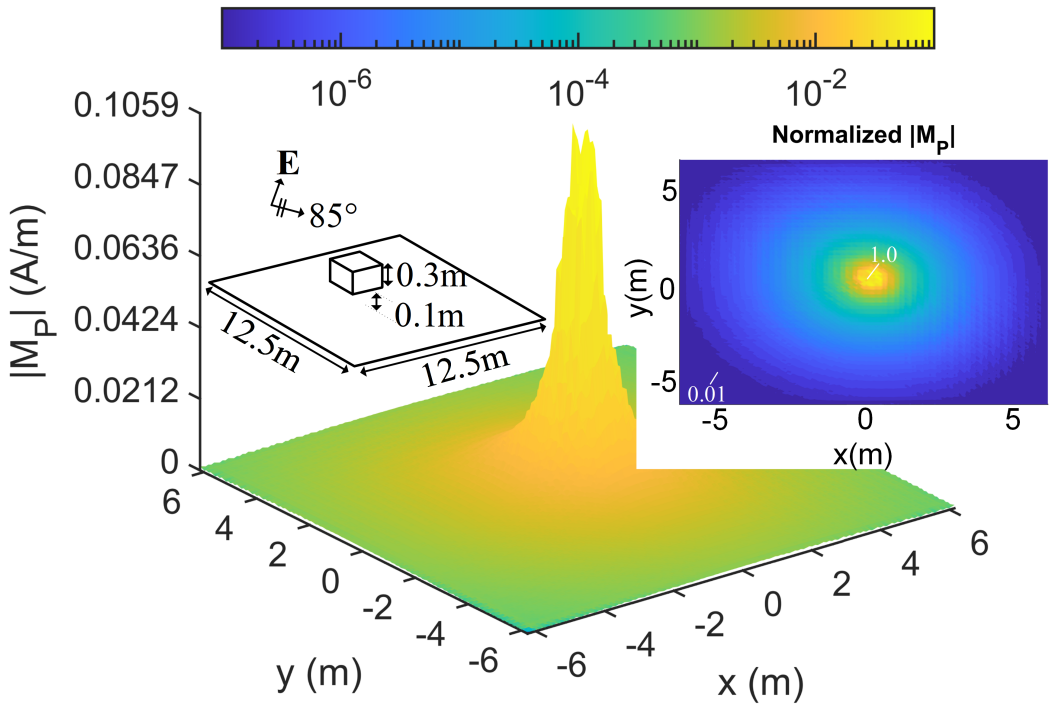

Figure 5.13 Perturbed magnetic current density for a limited region on an infinite ground plane ($d = 0.3$ m, $h = 0.1$ m, $\theta_i = 85°$, $\phi_i = 0°$, $\alpha_i = 0°$)

Now, the perturbation region is increased for validation. After this point, a plane wave illuminates all scattering examples with an incident angle of θ_i=85°, ϕ_i=30°, α_i=90°. Figures 5.14 and 5.15 demonstrate the RCS results for $\phi = 0°$ and $\phi = 90°$ planes while increasing the the perturbation surface. The frequency of the incident plane wave is 300 MHz again, and after this point, the frequency will not be changed unless otherwise stated. In addition, unless otherwise stated, the dielectric constant of the ground is 4, and the ground has a conductivity of 0.1 S/m. Also, in these simulations, the parameters are $h = 0.1$ m and $d = 0.3$ m. As seen from Figures 5.14 and 5.15, the selected perturbation area is adequate to calculate the RCSs of the object with high accuracy, and it seems that there is not a significant change in the RCS results while increasing the region. It should be noticed that minor changes in the RCS patterns are only in the scattering angles close to grazing. Besides, the current distributions are also shared on the perturbation region for $W_P = L_P = 24$ m. As can be seen from the figures, the perturbed current is diminished exponentially, and the magnetic current density on the perturbation surface is dominant.

Subsequently, the effect of the d and h parameters on the RCS of the object is given in Figures 5.16–5.19. The incident direction and polarization of the wave are the same as in the previous examples. However, the image theorem can be used for these kinds of scattering problems by finding the exact GF. Herein, the results were also compared with CST Microwave Studio for validation. The integral solver is employed with the MoM solution for this purpose. As seen from Figures 5.16–5.19, all results are very consistent. Also, since the incident wave definition is different from CST, θ angles are flipped in the results from CST.

Furthermore, as seen from the results, the proposed perturbation approach also is valid for a dielectric half-space. Therefore, even if the problem type becomes more complex, our proposed method will continue to produce high-accuracy solutions. Besides these, although the perturbed magnetic currents are more dominant on the surface, the RCS results are similar to the PEC ground case. Besides, the changes in the RCS are also observed while increasing the incident angle in Figures 5.20 and 5.21 for $\phi = 0°$ and $\phi = 90°$ planes, respectively.

Then, simulations are continued for different dielectric and conductivity values. The results are given in Figure 5.22 - 5.25. Here, as the dielectric constant and conductivity increase, the results converge to the PEC ground case. Unlike the previous chapters, the effects of object shapes on the RCSs are given in Figures 5.26 and 5.27. Here, the objects are 0.1 m above the surface, and the width of the objects is approximately 0.6 m. As seen from these figures, the object's shape also significantly affects the RCS.

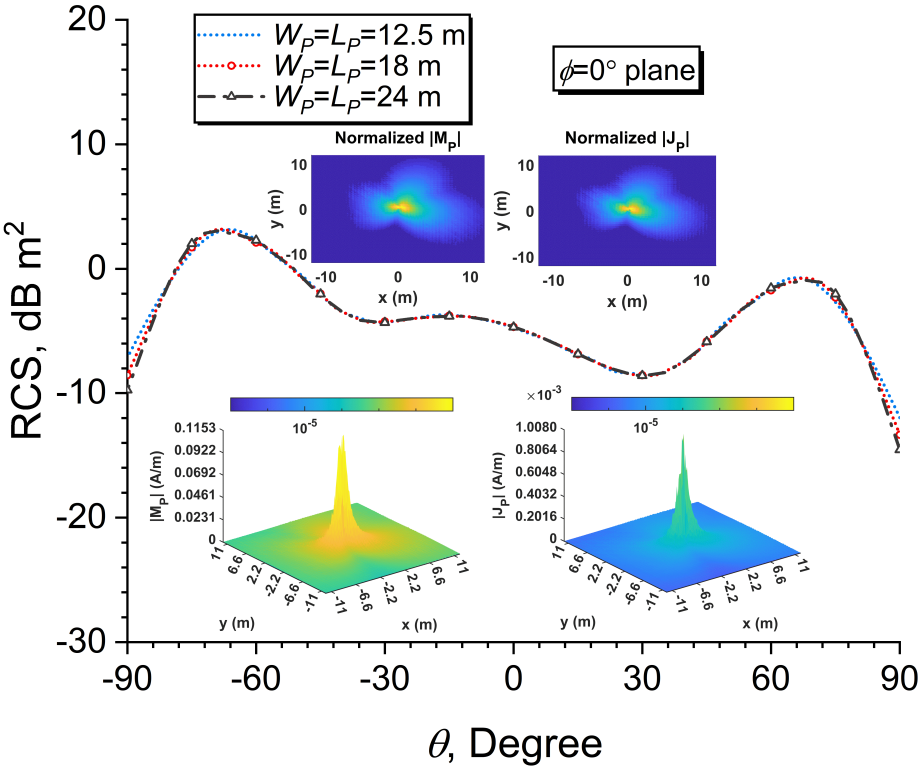

Figure 5.14 RCS results for the plane $\phi = 0°$ while increasing the perturbation region

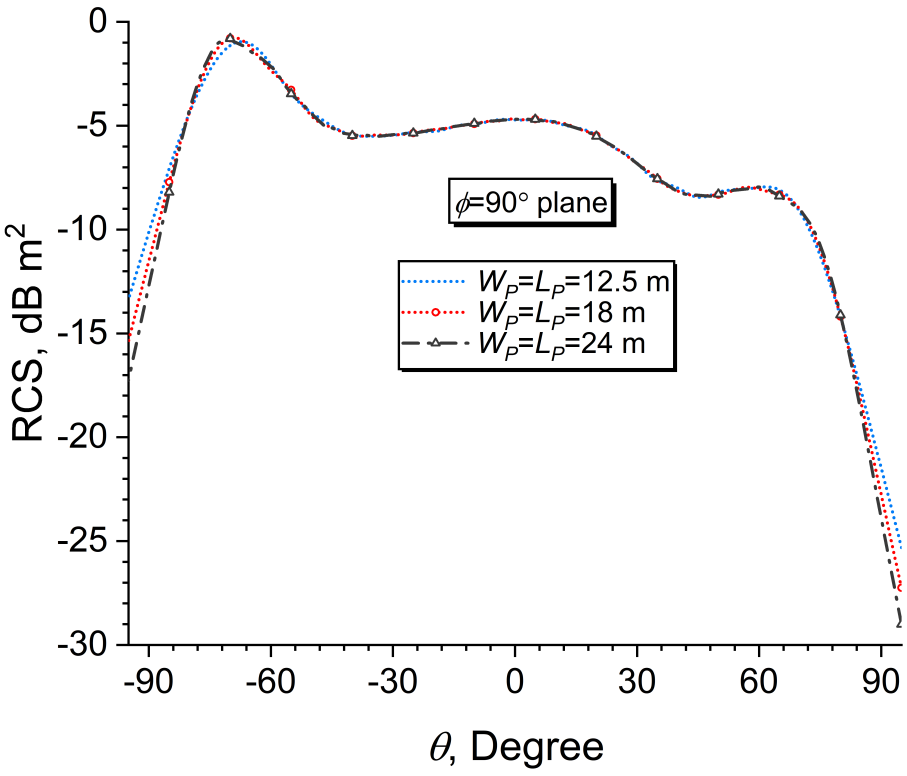

Figure 5.15 RCS results for the plane $\phi = 90°$ while increasing the perturbation region

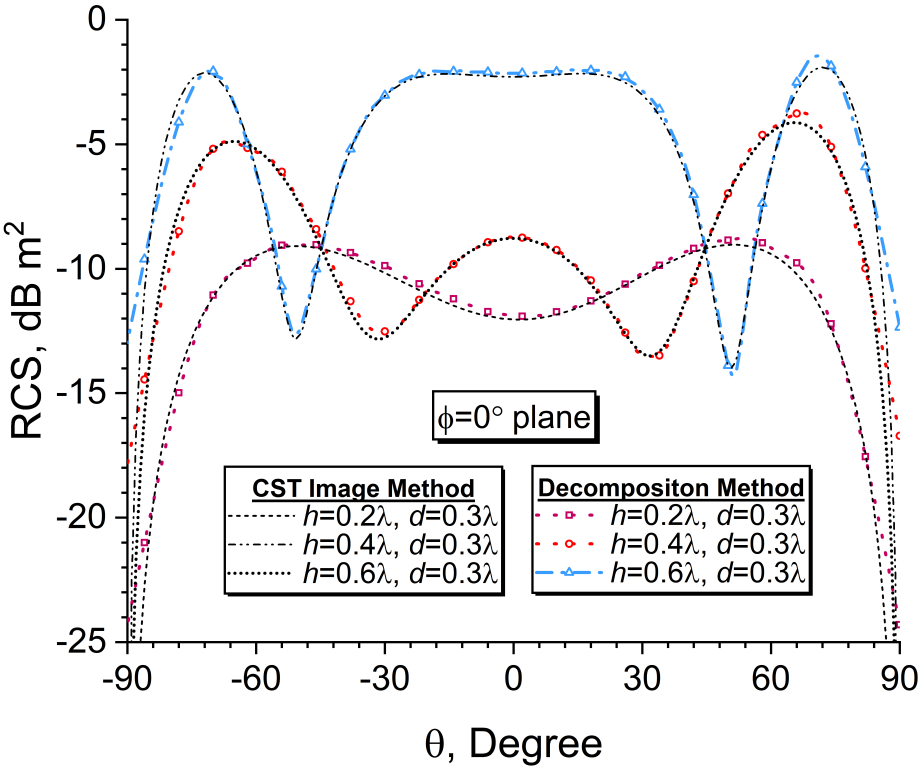

Figure 5.16 RCS results in the $\phi = 0°$ plane while increasing the height of the object from the ground surface

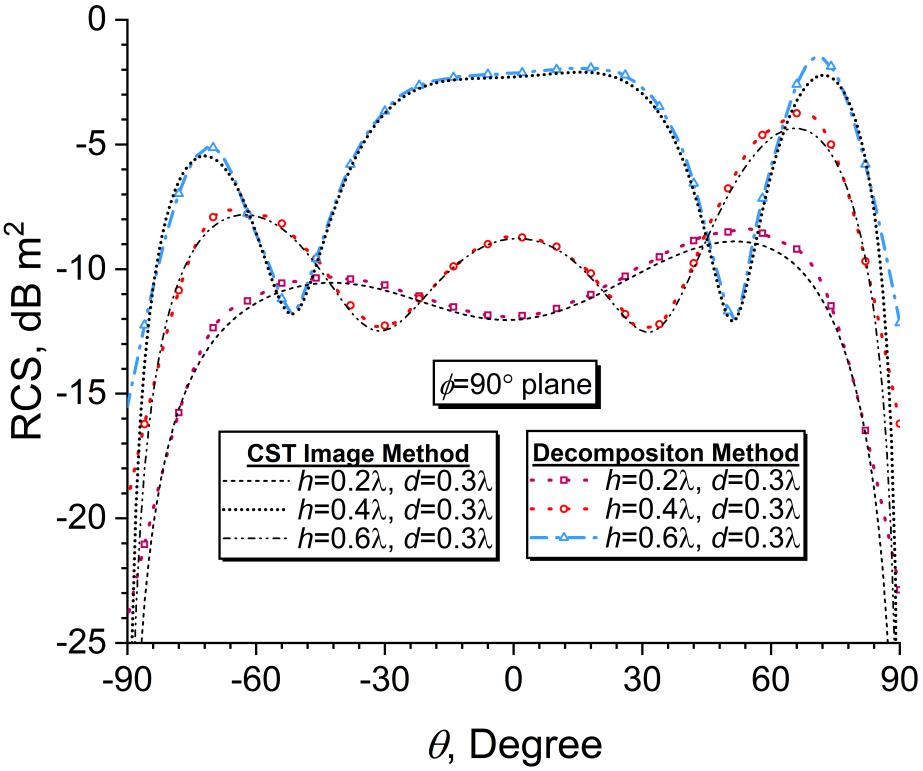

Figure 5.17 RCS results in the $\phi = 90°$ plane while increasing the height of the object from the ground surface

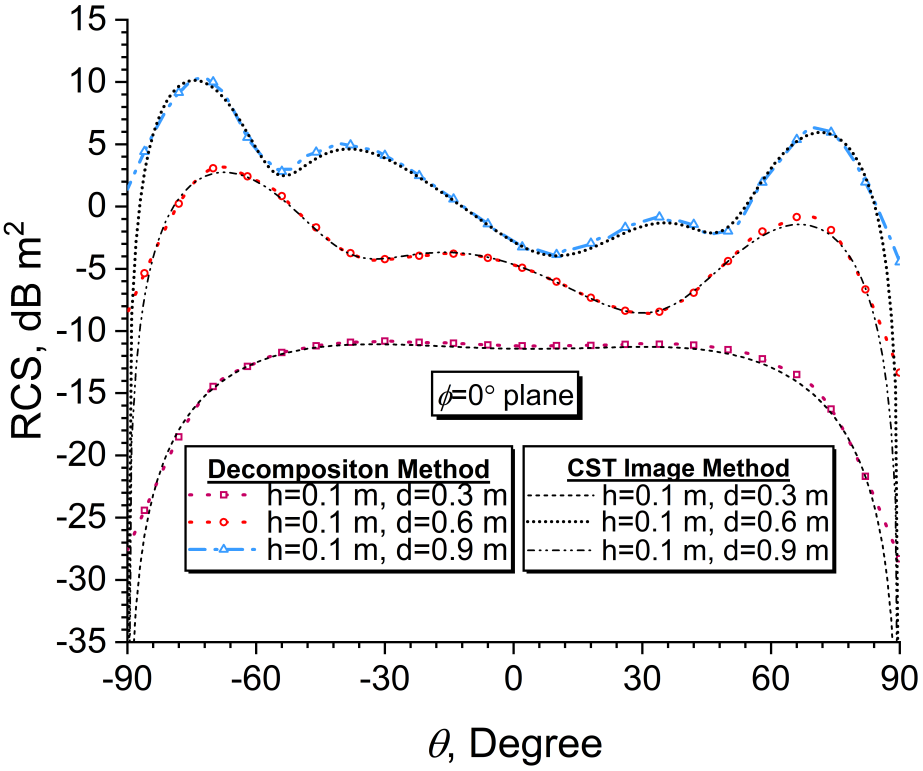

Figure 5.18 RCS results in the $\phi = 0°$ plane while increasing the size of the object

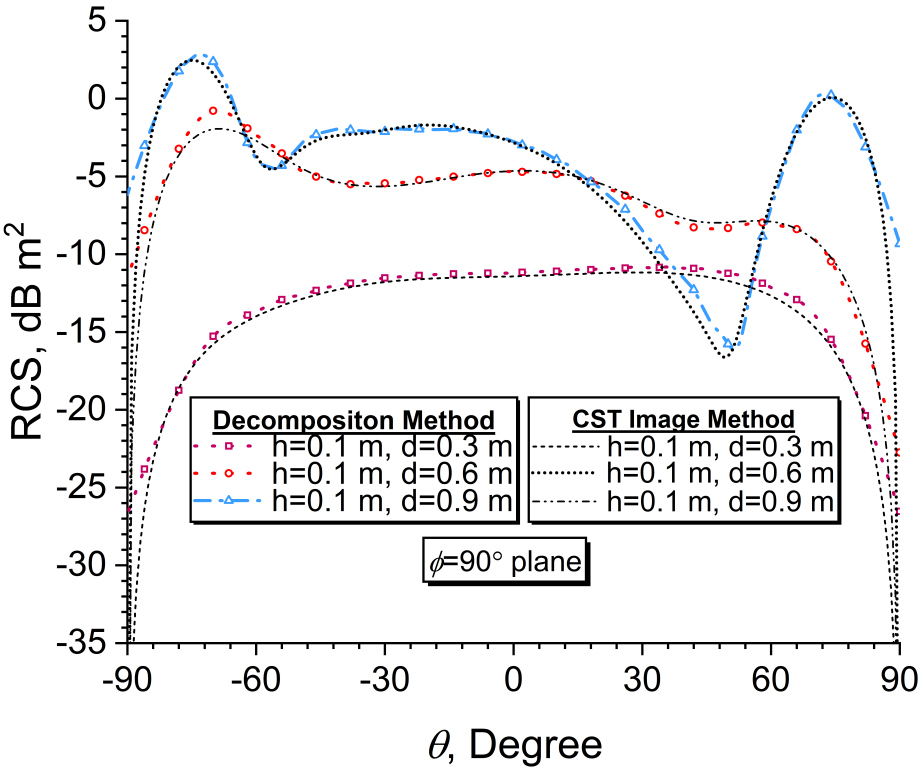

Figure 5.19 RCS results in the $\phi = 90°$ plane while increasing the size of the object

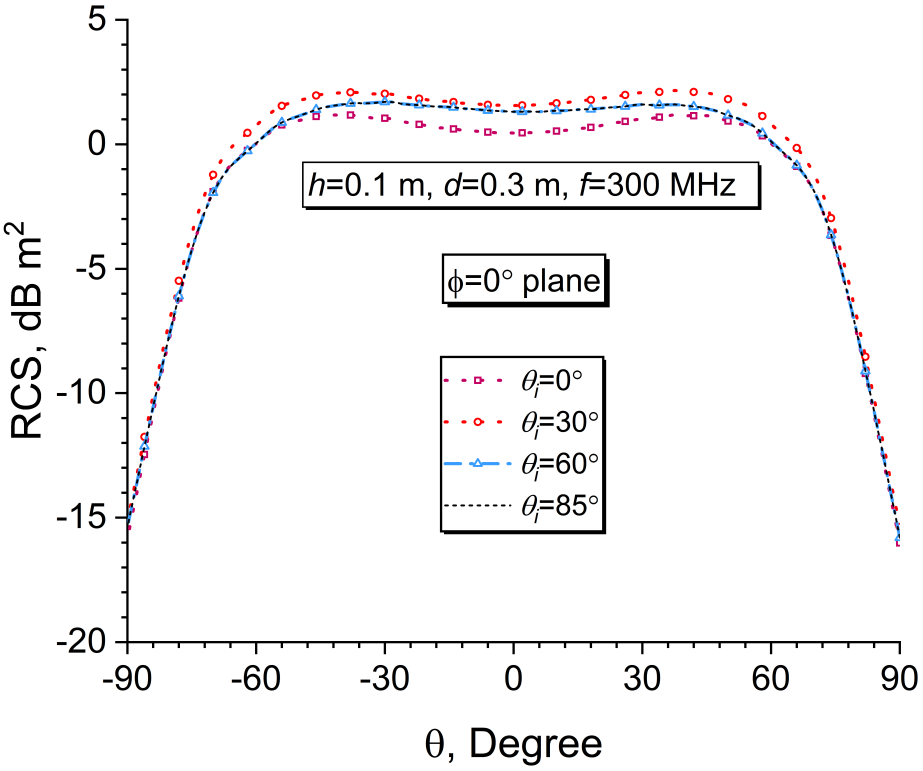

Figure 5.20 RCS results in the $\phi = 0°$ plane while increasing the incident angle

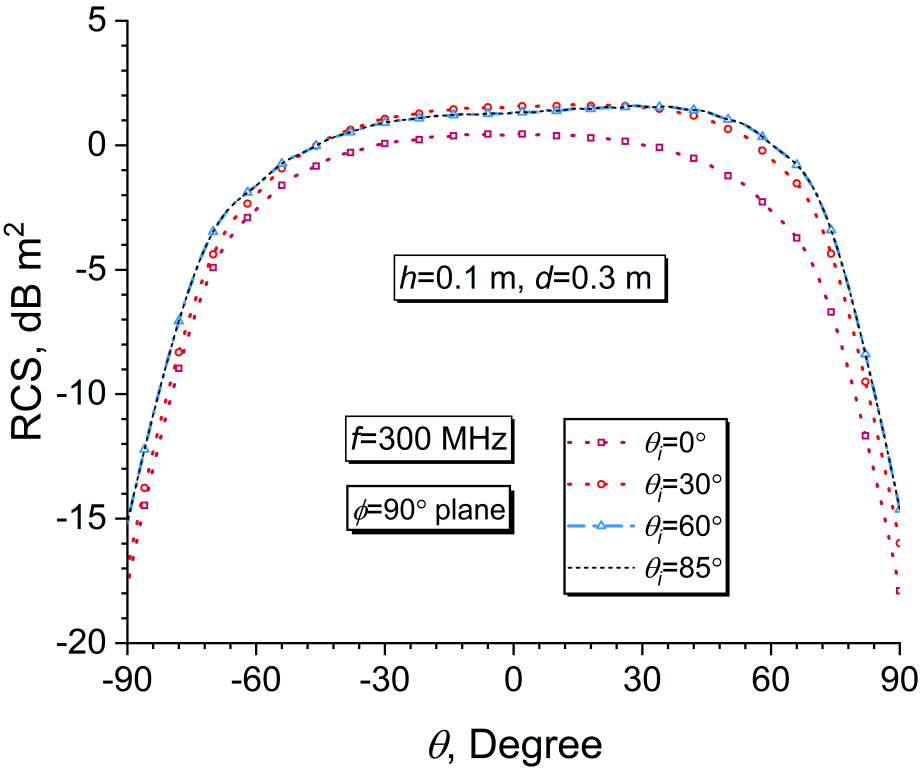

Figure 5.21 RCS results in the $\phi = 90°$ plane while increasing the incident angle

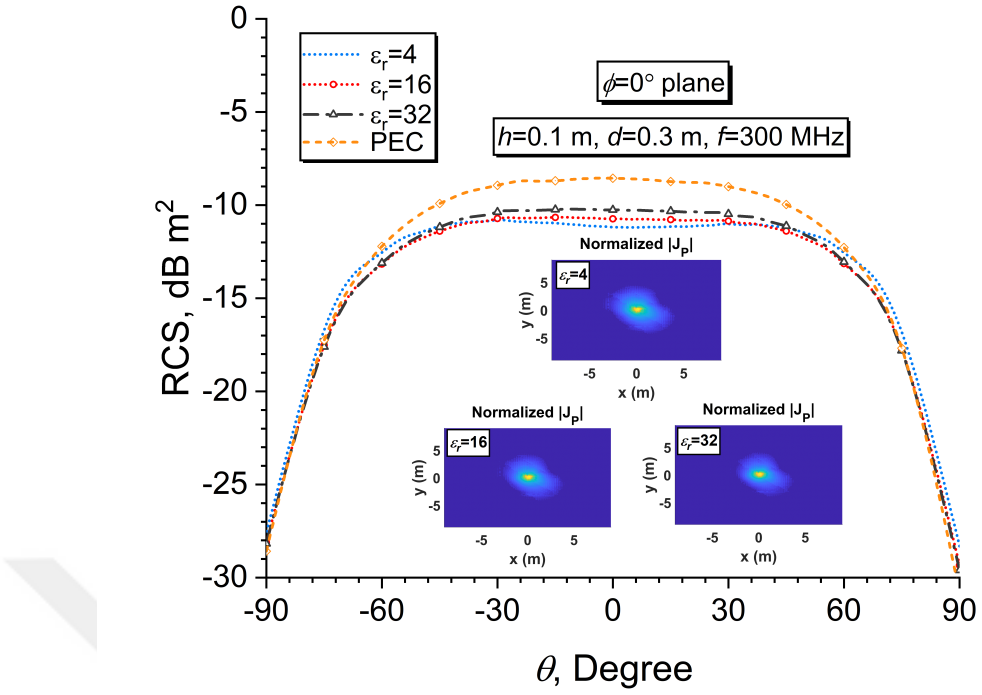

Figure 5.22 RCS results in the $\phi = 0°$ plane while increasing the dielectric constant of the dielectric medium

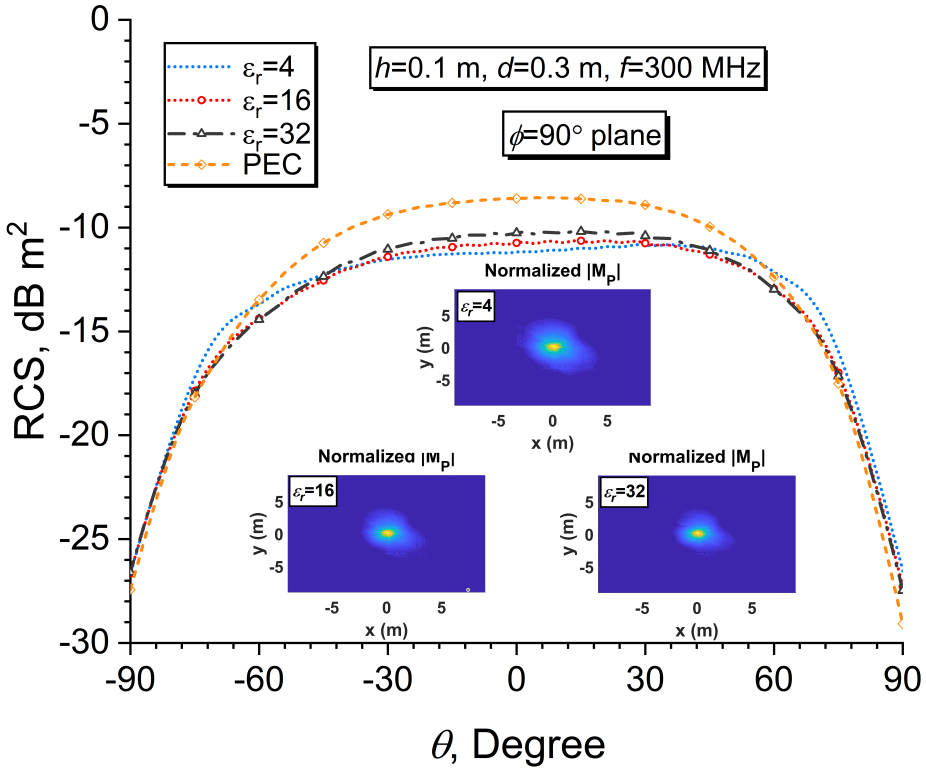

Figure 5.23 RCS results in the $\phi = 90°$ plane while increasing the dielectric constant of the dielectric medium

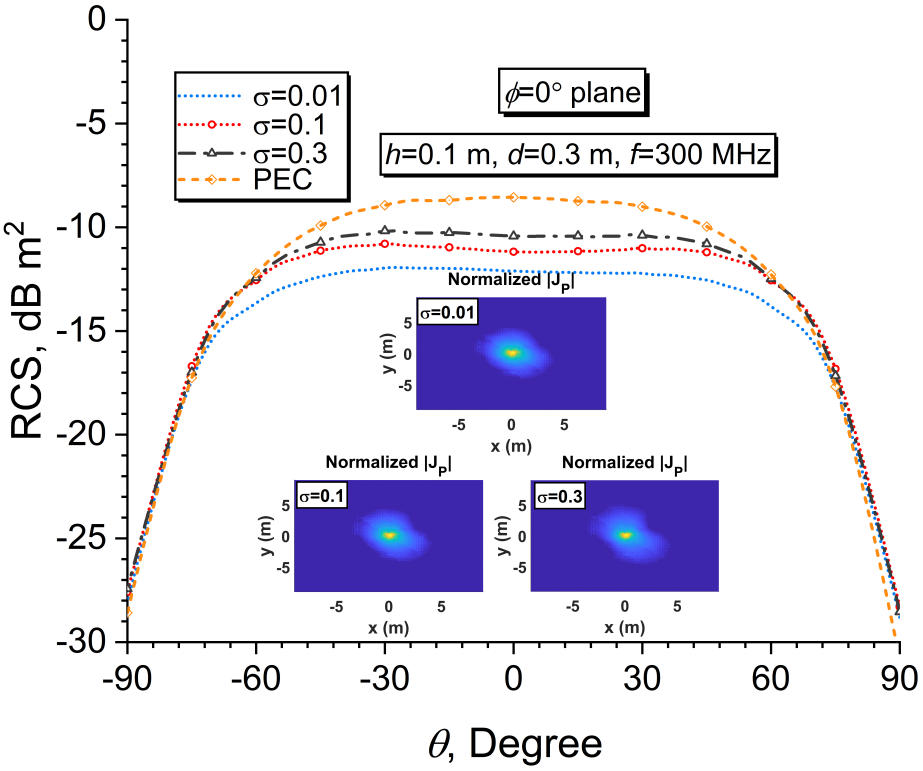

Figure 5.24 RCS results in the $\phi = 0°$ plane while increasing the conductivity of the dielectric medium

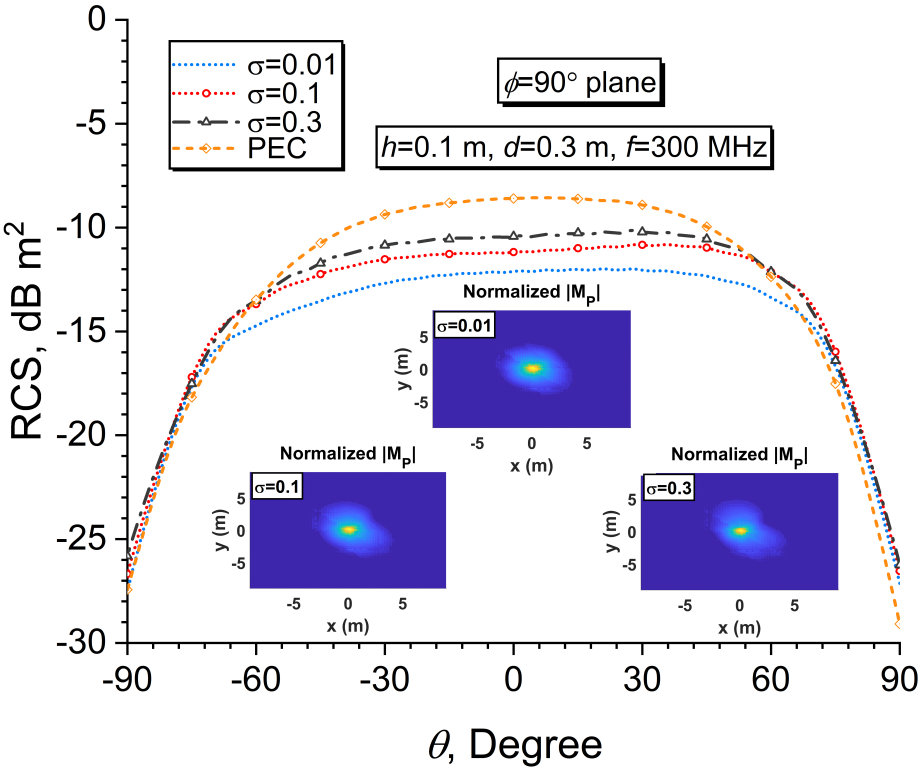

Figure 5.25 RCS results in the $\phi = 90°$ plane while increasing the conductivity of the dielectric medium

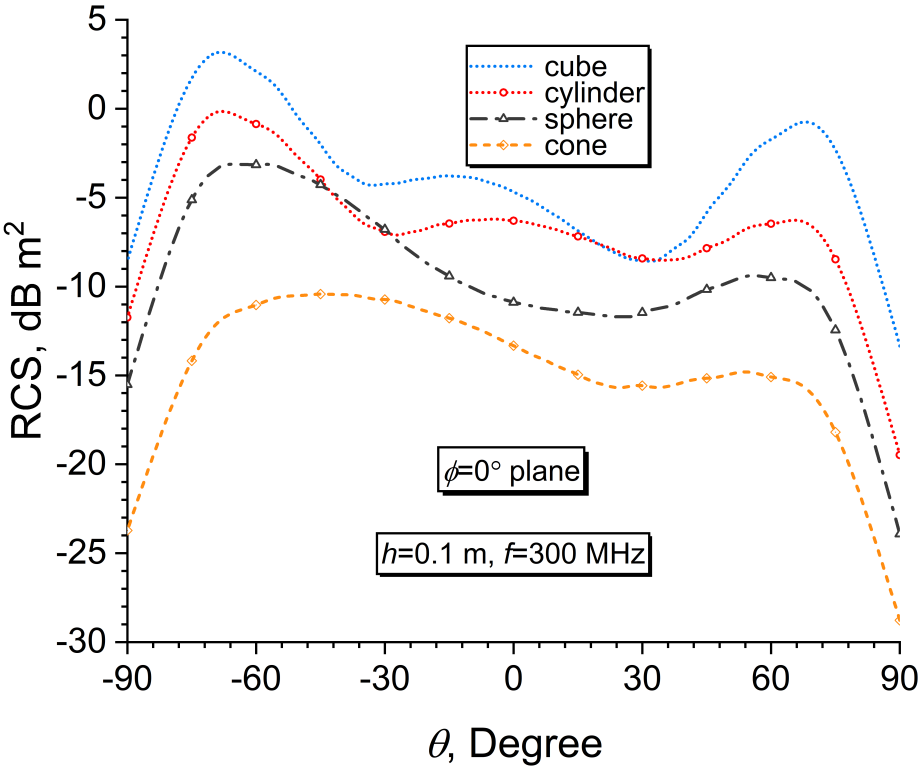

Figure 5.26 RCS results for different objects with approximately the same dimensions in the plane $\phi = 0°$.

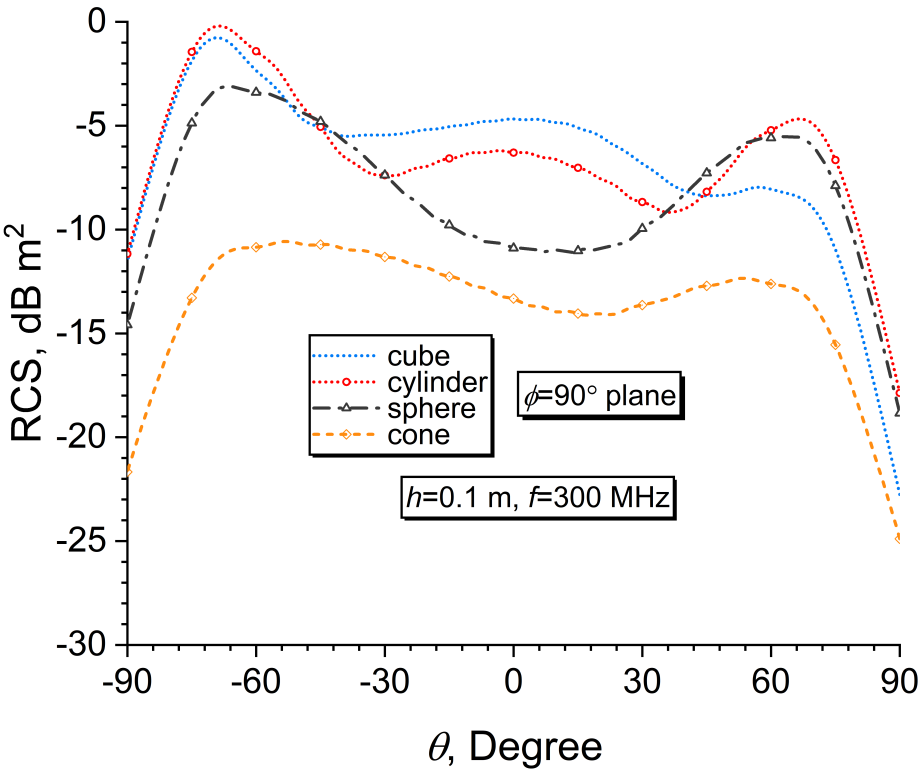

Figure 5.27 RCS results for different objects with approximately the same dimensions in the plane $\phi = 90°$.

6
SCATTERING ANALYSES OF A BURIED PEC TARGET INSIDE A LOSSY HALF-SPACE

This chapter handles an electromagnetic scattering problem from an arbitrary-shaped PEC object buried lossy or lossless dielectric flat half-spaces as depicted in Figure 6.1. The perturbation method is again employed for this purpose by decomposing the surface currents on the ground plane. The PMCHWT formulation solves these equivalent surface currents for the dielectric interface, which are discretized with RWG basis functions. In addition, for the buried PEC object, the induced electric current on it is calculated by solving the EFIE. The buried object is again chosen as PEC for an effortless calculation as well as an accessible validation with the literature.

6.1 Formulation

Since the case without the target was formulated in Chapter 5, we only discuss the perturbation method for the buried target case in this chapter. As seen in Figure 6.1, an object is placed below a flat dielectric surface when a plane wave illuminates it. The plane wave definition is the same as (3.1). The dielectric ground can be lossy or lossless, and the PEC object can be selected as any arbitrary shape.

A PEC cube is placed h m below the ground surface as the target. For the problem represented in Figure 6.1, the total induced current on the ground surface is $\vec{\mathbf{J}}_1$ and $\vec{\mathbf{M}}_1$. In addition, $\vec{\mathbf{J}}_2$ indicates the induced electric current density on the PEC target. The currents on the ground surface can be decomposed as follows

$$\lim_{W_p, L_p \to \infty} \vec{\mathbf{J}}_1 = \vec{\mathbf{J}}_I + \vec{\mathbf{J}}_P \tag{6.1}$$

and

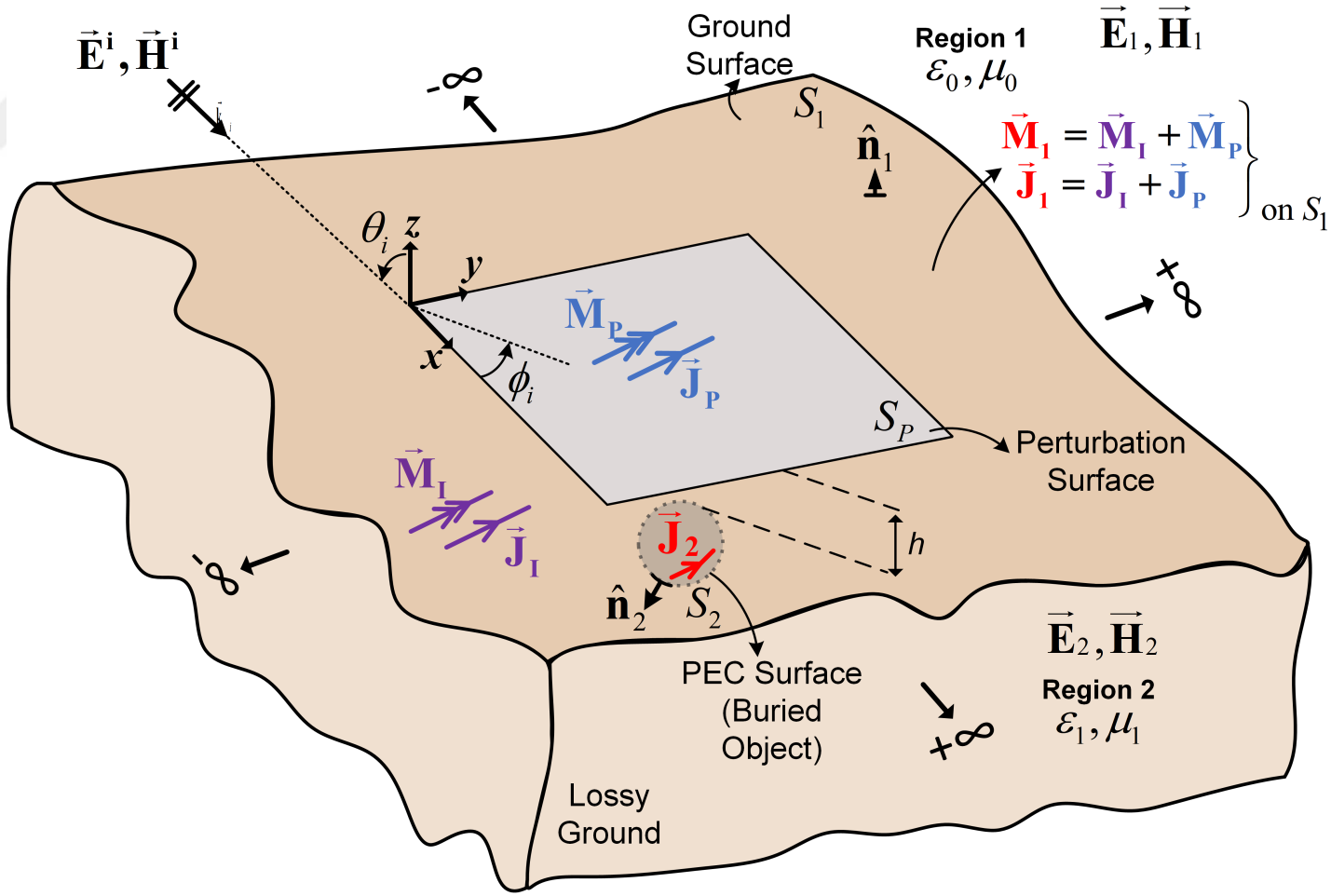

Figure 6.1 Configuration of a scattering problem from a PEC buried below an infinite, flat, and dielectric surface

$$\lim_{W_p, L_p \to \infty} \vec{\mathbf{M}}_1 = \vec{\mathbf{M}}_I + \vec{\mathbf{M}}_P \tag{6.2}$$

where W_p and L_p are lengths of the perturbation area, and the currents can be approximately written as follows

$$\vec{\mathbf{J}}_1 \approx \vec{\mathbf{J}}_I + \vec{\mathbf{J}}_P \tag{6.3}$$

$$\vec{\mathbf{M}}_1 \approx \vec{\mathbf{M}}_I + \vec{\mathbf{M}}_P \tag{6.4}$$

Here, $\vec{\mathbf{J}}_P$ and $\vec{\mathbf{M}}_P$ are defined only on the perturbation surface and zero elsewhere. Now, we can utilize from outer equivalence theorem for the dielectric interface. The boundary conditions on it is as follows

$$\hat{\mathbf{n}}_1 \times \left[\vec{\mathbf{E}}_1\right]\Big|_{S_1^+} = -\vec{\mathbf{M}}_1, \quad \text{and} \quad \hat{\mathbf{n}}_1 \times \left[\vec{\mathbf{H}}_1\right]\Big|_{S_1^+} = \vec{\mathbf{J}}_1 \tag{6.5}$$

Here, the total electric and magnetic fields in Region 1 are

$$\vec{\mathbf{E}}_1 = \vec{\mathbf{E}}_1^s(\vec{\mathbf{J}}_1, \vec{\mathbf{M}}_1) + \vec{\mathbf{E}}_i, \quad \vec{\mathbf{H}}_1 = \vec{\mathbf{H}}_1^s(\vec{\mathbf{J}}_1, \vec{\mathbf{M}}_1) + \vec{\mathbf{H}}_i \tag{6.6}$$

and, in Region 2

$$\vec{\mathbf{E}}_2 = \vec{\mathbf{H}}_2 = \vec{\mathbf{0}} \tag{6.7}$$

This produces

$$\hat{\mathbf{n}}_1 \times \left[\vec{\mathbf{E}}_1^s(\vec{\mathbf{J}}_1, \vec{\mathbf{M}}_1) + \vec{\mathbf{E}}^i\right]\Big|_{S_1^+} = -\vec{\mathbf{M}}_1 \tag{6.8}$$

by rearranging on S_1^+

$$\left[\vec{\mathbf{E}}_1^s(\vec{\mathbf{J}}_1, \vec{\mathbf{M}}_1)\right]_{\tan} = -\left[\vec{\mathbf{E}}^i\right]_{\tan} + \hat{\mathbf{n}}_1 \times \vec{\mathbf{M}}_1 \quad \text{on } S_1^+ \tag{6.9}$$

In addition, (6.6) is substituted in (6.5) for the magnetic fields as follows

$$\hat{\mathbf{n}}_1 \times \left[\vec{\mathbf{H}}_1^s(\vec{\mathbf{J}}_1, \vec{\mathbf{M}}_1) + \vec{\mathbf{H}}^i\right]\Big|_{S_1^+} = \vec{\mathbf{J}}_1 \tag{6.10}$$

$$-\left[\vec{\mathbf{H}}_1^s(\vec{\mathbf{J}}_1, \vec{\mathbf{M}}_1)\right]_{\tan} = \left[\vec{\mathbf{H}}^i\right]_{\tan} + \hat{\mathbf{n}}_1 \times \vec{\mathbf{J}}_1 \quad \text{on } S_1^+ \tag{6.11}$$

Then, through the inner equivalence theorem, the total fields

$$\vec{\mathbf{E}}_1 = \vec{\mathbf{H}}_1 = \vec{\mathbf{0}} \tag{6.12}$$

$$\vec{\mathbf{E}}_2 = \vec{\mathbf{E}}_2^s(-\vec{\mathbf{J}}_1, -\vec{\mathbf{M}}_1) + \vec{\mathbf{E}}_2^s(\vec{\mathbf{J}}_2), \quad \vec{\mathbf{H}}_2 = \vec{\mathbf{H}}_2^s(-\vec{\mathbf{J}}_1, -\vec{\mathbf{M}}_1) + \vec{\mathbf{H}}_2^s(\vec{\mathbf{J}}_2) \tag{6.13}$$

can be written for each region. Subjecting to the boundary conditions

$$-\hat{\mathbf{n}}_1 \times \left[\vec{\mathbf{E}}_2^s(-\vec{\mathbf{J}}_1, -\vec{\mathbf{M}}_1) + \vec{\mathbf{E}}_2^s(\vec{\mathbf{J}}_2)\right]\Big|_{S_1^-} = \vec{\mathbf{M}}_1 \tag{6.14}$$

$$\left[\vec{\mathbf{E}}_2^s(-\vec{\mathbf{J}}_1, -\vec{\mathbf{M}}_1) + \vec{\mathbf{E}}_2^s(\vec{\mathbf{J}}_2)\right]_{\tan} = \hat{\mathbf{n}}_1 \times \vec{\mathbf{M}}_1 \quad \text{on } S_1^- \tag{6.15}$$

and

$$-\hat{\mathbf{n}}_1 \times \left[\vec{\mathbf{H}}_2^s(-\vec{\mathbf{J}}_1, -\vec{\mathbf{M}}_1) + \vec{\mathbf{H}}_2^s(\vec{\mathbf{J}}_2)\right]\Big|_{S_1^-} = -\vec{\mathbf{J}}_1 \tag{6.16}$$

$$-\left[\vec{\mathbf{H}}_2^s(-\vec{\mathbf{J}}_1, -\vec{\mathbf{M}}_1) + \vec{\mathbf{H}}_2^s(\vec{\mathbf{J}}_2)\right]_{\tan} = \hat{\mathbf{n}}_1 \times \vec{\mathbf{J}}_1 \quad \text{on } S_1^- \tag{6.17}$$

are found on S_1^- surface.

$$\hat{\mathbf{n}}_2 \times \left[\vec{\mathbf{E}}_2^s(-\vec{\mathbf{J}}_1, -\vec{\mathbf{M}}_1) + \vec{\mathbf{E}}_2^s(\vec{\mathbf{J}}_2)\right]\Big|_{S_2^+} = \vec{\mathbf{0}} \tag{6.18}$$

Also, subjecting to the boundary condition on S_2^+ surface

$$\left[\vec{\mathbf{E}}_2^s(-\vec{\mathbf{J}}_1, -\vec{\mathbf{M}}_1) + \vec{\mathbf{E}}_2^s(\vec{\mathbf{J}}_2)\right]_{\tan} = \vec{\mathbf{0}} \quad \text{on } S_2^+ \tag{6.19}$$

will be obtained for the inner equivalence. Therefore, the scattered electric field aroused from the induced $\vec{\mathbf{J}}_1$ and $\vec{\mathbf{M}}_1$ surface current densities

$$\vec{\mathbf{E}}_1^s(\vec{\mathbf{J}}_1, \vec{\mathbf{M}}_1) = \vec{\mathbf{E}}_1^s(\vec{\mathbf{J}}_P, \vec{\mathbf{M}}_P) + \vec{\mathbf{E}}_1^s(\vec{\mathbf{J}}_I, \vec{\mathbf{M}}_I) \tag{6.20}$$

can be decomposed. In a similar way, the scattered magnetic field caused by surface currents in Region 1 can also be decomposed as follows

$$\vec{\mathbf{H}}_1^s(\vec{\mathbf{J}}_1, \vec{\mathbf{M}}_1) = \vec{\mathbf{H}}_1^s(\vec{\mathbf{J}}_P, \vec{\mathbf{M}}_P) + \vec{\mathbf{H}}_1^s(\vec{\mathbf{J}}_I, \vec{\mathbf{M}}_I) \tag{6.21}$$

Also, in Region 2, these fields are decomposed as

$$\vec{\mathbf{E}}_2^s(-\vec{\mathbf{J}}_1, -\vec{\mathbf{M}}_1) = \vec{\mathbf{E}}_2^s(-\vec{\mathbf{J}}_P, -\vec{\mathbf{M}}_P) + \vec{\mathbf{E}}_2^s(-\vec{\mathbf{J}}_I, -\vec{\mathbf{M}}_I) \tag{6.22}$$

$$\vec{\mathbf{H}}_2^s(-\vec{\mathbf{J}}_1, -\vec{\mathbf{M}}_1) = \vec{\mathbf{H}}_2^s(-\vec{\mathbf{J}}_P, -\vec{\mathbf{M}}_P) + \vec{\mathbf{H}}_2^s(-\vec{\mathbf{J}}_I, -\vec{\mathbf{M}}_I) \tag{6.23}$$

It should be noted here that the perturbed current densities are assumed to exist only on the perturbation surface and are zero for the remaining surface. Now, substituting (6.20) in (6.9), and using (5.10) on S_P^+

$$\left[\vec{\mathbf{E}}_1^s(\vec{\mathbf{J}}_P, \vec{\mathbf{M}}_P)\right]_{\tan} - \hat{\mathbf{n}}_1 \times \vec{\mathbf{M}}_P = \vec{\mathbf{0}} \quad \text{on } S_P^+ \tag{6.24}$$

will be derived. Then, substituting (6.22) in (6.15), and using (5.19) on S_P^-

$$\left[\vec{\mathbf{E}}_2^s(-\vec{\mathbf{J}}_P, -\vec{\mathbf{M}}_P) + \vec{\mathbf{E}}_2^s(\vec{\mathbf{J}}_2)\right]_{\tan} - \hat{\mathbf{n}}_1 \times \vec{\mathbf{M}}_P = \vec{\mathbf{0}} \quad \text{on } S_P^- \tag{6.25}$$

and, substituting (6.21) in (6.11), and using (5.12) on S_P^+

$$\left[\vec{\mathbf{H}}_1^s(\vec{\mathbf{J}}_P, \vec{\mathbf{M}}_P)\right]_{\tan} + \hat{\mathbf{n}}_1 \times \vec{\mathbf{J}}_P = \vec{\mathbf{0}} \quad \text{on } S_P^+ \tag{6.26}$$

as well as substituting (6.23) in (6.17), and using (5.20) on S_P^-

$$\left[\vec{\mathbf{H}}_2^s(-\vec{\mathbf{J}}_P, -\vec{\mathbf{M}}_P) + \vec{\mathbf{H}}_2^s(\vec{\mathbf{J}}_2)\right]_{\tan} + \hat{\mathbf{n}}_1 \times \vec{\mathbf{J}}_P = \vec{\mathbf{0}} \quad \text{on } S_P^- \tag{6.27}$$

will be derived. Finally, employing (6.24) and (6.25), the electric fields on S_P surface

$$\left[\vec{\mathbf{E}}_1^s(\vec{\mathbf{J}}_P, \vec{\mathbf{M}}_P)\right]_{\tan} + \left[\vec{\mathbf{E}}_2^s(\vec{\mathbf{J}}_P, \vec{\mathbf{M}}_P)\right]_{\tan} - \left[\vec{\mathbf{E}}_2^s(\vec{\mathbf{J}}_2)\right]_{\tan} = \vec{\mathbf{0}} \quad \text{on } S_P \tag{6.28}$$

are obtained. In addition, the magnetic fields in (6.26) and (6.27) are arranged on S_P

surface as follows

$$\left[\vec{\mathbf{H}}_1^s(\vec{\mathbf{J}}_P,\vec{\mathbf{M}}_P)\right]_{\tan}+\left[\vec{\mathbf{H}}_2^s(\vec{\mathbf{J}}_P,\vec{\mathbf{M}}_P)\right]_{\tan}-\left[\vec{\mathbf{H}}_2^s(\vec{\mathbf{J}}_2)\right]_{\tan}=\vec{\mathbf{0}}\quad\text{on } S_P \tag{6.29}$$

Moreover, if (6.19) is rearranged similarly for S_2

$$-\left[\vec{\mathbf{E}}_2^s(\vec{\mathbf{J}}_P,\vec{\mathbf{M}}_P)\right]_{\tan}+\left[\vec{\mathbf{E}}_2^s(\vec{\mathbf{J}}_2)\right]_{\tan}=\left[\vec{\mathbf{E}}^t\right]_{\tan}\quad\text{on } S_2 \tag{6.30}$$

will be found. Here, (6.28) and (6.29) are PMCHWT formulations for dielectric interface, and (6.30) is EFIE equation for PEC surface. (6.28), (6.29), and (6.30) can be rewritten by subjecting (5.3) and (5.4) with $\mathfrak{L}$ and $\mathfrak{K}$ operators

$$\begin{aligned}\Big\{&-j\omega\mu_0\mathfrak{L}^{(1)}[\vec{\mathbf{J}}_P]-j\omega\mu_1\mathfrak{L}^{(2)}[\vec{\mathbf{J}}_P]\\&-\mathfrak{K}^{(1)}[\vec{\mathbf{M}}_P]-\mathfrak{K}^{(2)}[\vec{\mathbf{M}}_P]+j\omega\mu_1\mathfrak{L}^{(2)}[\vec{\mathbf{J}}_2]\Big\}_{\tan}=\vec{\mathbf{0}}\quad\text{on } S_P\end{aligned} \tag{6.31}$$

$$\begin{aligned}\Big\{&-j\omega\epsilon_0\mathfrak{L}^{(1)}[\vec{\mathbf{M}}_P]-j\omega\epsilon_1\mathfrak{L}^{(2)}[\vec{\mathbf{M}}_P]+\mathfrak{K}^{(1)}[\vec{\mathbf{J}}_P]\\&+\mathfrak{K}^{(2)}[\vec{\mathbf{J}}_P]-\mathfrak{K}^{(2)}[\vec{\mathbf{J}}_2]\Big\}_{\tan}=\vec{\mathbf{0}}\quad\text{on } S_P\end{aligned} \tag{6.32}$$

$$\left\{j\omega\mu_1\mathfrak{L}^{(2)}[\vec{\mathbf{J}}_P]+\mathfrak{K}^{(2)}[\vec{\mathbf{M}}_P]-j\omega\mu_1\mathfrak{L}^{(2)}[\vec{\mathbf{J}}_2]\right\}_{\tan}=\left[\vec{\mathbf{E}}^t\right]_{\tan}\quad\text{on } S_2 \tag{6.33}$$

As a result, utilizing (5.62) in (6.31), (6.32), and (6.33)

$$\begin{aligned}\Big\{&-j\omega\mu_0\mathfrak{L}^{(1)}[\vec{\mathbf{J}}_P]-j\omega\mu_1\mathfrak{L}^{(2)}[\vec{\mathbf{J}}_P]\\&-\mathfrak{K}_{P.V.}^{(1)}[\vec{\mathbf{M}}_P]-\mathfrak{K}_{P.V.}^{(2)}[\vec{\mathbf{M}}_P]+j\omega\mu_1\mathfrak{L}^{(2)}[\vec{\mathbf{J}}_2]\Big\}_{\tan}=\vec{\mathbf{0}}\quad\text{on } S_P\end{aligned} \tag{6.34}$$

$$\begin{aligned}\Big\{&-j\omega\epsilon_0\mathfrak{L}^{(1)}[\vec{\mathbf{M}}_P]-j\omega\epsilon_1\mathfrak{L}^{(2)}[\vec{\mathbf{M}}_P]+\mathfrak{K}_{P.V.}^{(1)}[\vec{\mathbf{J}}_P]\\&+\mathfrak{K}_{P.V.}^{(2)}[\vec{\mathbf{J}}_P]-\mathfrak{K}^{(2)}[\vec{\mathbf{J}}_2]\Big\}_{\tan}=\vec{\mathbf{0}}\quad\text{on } S_P\end{aligned} \tag{6.35}$$

$$\left\{j\omega\mu_1\mathfrak{L}^{(2)}[\vec{\mathbf{J}}_P]+\mathfrak{K}^{(2)}[\vec{\mathbf{M}}_P]-j\omega\mu_1\mathfrak{L}^{(2)}[\vec{\mathbf{J}}_2]\right\}_{\tan}=\left[\vec{\mathbf{E}}^t\right]_{\tan}\quad\text{on } S_2 \tag{6.36}$$

are found. Moreover, if the unknown currents are expanded with RWG basis functions

$$\vec{\mathbf{J}}_P(\vec{\mathbf{r}}') = \sum_{\psi=1}^{N_P} I_\psi^{(J_P)} \vec{\mathbf{f}}_\psi(\vec{\mathbf{r}}') \tag{6.37}$$

$$\vec{\mathbf{M}}_P(\vec{\mathbf{r}}') = \sum_{\psi=1}^{N_P} I_\psi^{(M_P)} \vec{\mathbf{g}}_\psi(\vec{\mathbf{r}}') \tag{6.38}$$

$$\vec{\mathbf{J}}_2(\vec{\mathbf{r}}') = \sum_{\psi=1}^{N_2} I_\psi^{(J_2)} \vec{\mathbf{f}}_\psi(\vec{\mathbf{r}}') \tag{6.39}$$

where, $\vec{\mathbf{g}}_\psi(\vec{\mathbf{r}}')$ is the magnetic basis function and the same as $\vec{\mathbf{f}}_\psi(\vec{\mathbf{r}}')$ since the PMCHWT formulation can be handled without applying the curl operator. Furthermore, exploiting Galerkin-type testing functions, a matrix system

$$\begin{bmatrix} \overline{\overline{\mathbf{Z}}}_{11}^{(\vec{J}_P)} & \overline{\overline{\mathbf{Z}}}_{12}^{(\vec{M}_P)} & \overline{\overline{\mathbf{Z}}}_{13}^{(\vec{J}_2)} \\ \overline{\overline{\mathbf{Z}}}_{21}^{(\vec{J}_P)} & \overline{\overline{\mathbf{Z}}}_{22}^{(\vec{M}_P)} & \overline{\overline{\mathbf{Z}}}_{23}^{(\vec{J}_2)} \\ \overline{\overline{\mathbf{Z}}}_{31}^{(\vec{J}_P)} & \overline{\overline{\mathbf{Z}}}_{32}^{(\vec{M}_P)} & \overline{\overline{\mathbf{Z}}}_{33}^{(\vec{J}_2)} \end{bmatrix} \begin{bmatrix} \overline{\mathbf{I}}_{\psi_{11}}^{(\vec{J}_P)} \\ \overline{\mathbf{I}}_{\psi_{21}}^{(\vec{M}_P)} \\ \overline{\mathbf{I}}_{\psi_{31}}^{(\vec{J}_2)} \end{bmatrix} = \begin{bmatrix} \overline{\mathbf{V}}_{\zeta_{11}}^{(\vec{J}_P)} \\ \overline{\mathbf{V}}_{\zeta_{21}}^{(\vec{M}_P)} \\ \overline{\mathbf{V}}_{\zeta_{31}}^{(\vec{J}_2)} \end{bmatrix} \tag{6.40}$$

are produced. Again, we use $\vec{\mathbf{g}}_\psi(\vec{\mathbf{r}}') = \eta_0 \vec{\mathbf{f}}_\psi(\vec{\mathbf{r}}')$ for basis and $\vec{\mathbf{g}}_\zeta(\vec{\mathbf{r}}) = \eta_0 \vec{\mathbf{f}}_\zeta(\vec{\mathbf{r}})$ for testing to obtain the diagonal Z matrix. The general expressions for $\mathfrak{L}$ and $\mathfrak{K}$ are given in (5.70) and (5.71). If we give detailed expressions each Z component for any edge, it will be helpful

$$\begin{aligned} Z_{11}^{(\zeta\psi)} = -jk_0\eta_0 \Bigg[& \int_{T_\zeta^\pm} \int_{T_\psi^\pm} \vec{\mathbf{f}}_\zeta(\vec{\mathbf{r}}) \cdot \vec{\mathbf{f}}_\psi(\vec{\mathbf{r}}') \frac{e^{-jk_0\left\|\vec{\mathbf{r}}-\vec{\mathbf{r}}'\right\|}}{4\pi\left\|\vec{\mathbf{r}}-\vec{\mathbf{r}}'\right\|} dS_{T_\psi^\pm}^{\prime(P)} dS_{T_\zeta^\pm}^{(P)} \\ & -\frac{1}{k_0^2} \int_{T_\zeta^\pm} \int_{T_\psi^\pm} \left[\nabla_s \cdot \vec{\mathbf{f}}_\zeta(\vec{\mathbf{r}})\right]\left[\nabla_s' \cdot \vec{\mathbf{f}}_\psi(\vec{\mathbf{r}}')\right] \frac{e^{-jk_0\left\|\vec{\mathbf{r}}-\vec{\mathbf{r}}'\right\|}}{4\pi\left\|\vec{\mathbf{r}}-\vec{\mathbf{r}}'\right\|} dS_{T_\psi^\pm}^{\prime(P)} dS_{T_\zeta^\pm}^{(P)} \Bigg] \\ & - jk_1\eta_1 \Bigg[\int_{T_\zeta^\pm} \int_{T_\psi^\pm} \vec{\mathbf{f}}_\zeta(\vec{\mathbf{r}}) \cdot \vec{\mathbf{f}}_\psi(\vec{\mathbf{r}}') \frac{e^{-jk_1\left\|\vec{\mathbf{r}}-\vec{\mathbf{r}}'\right\|}}{4\pi\left\|\vec{\mathbf{r}}-\vec{\mathbf{r}}'\right\|} dS_{T_\psi^\pm}^{\prime(P)} dS_{T_\zeta^\pm}^{(P)} \\ & -\frac{1}{k_1^2} \int_{T_\zeta^\pm} \int_{T_\psi^\pm} \left[\nabla_s \cdot \vec{\mathbf{f}}_\zeta(\vec{\mathbf{r}})\right]\left[\nabla_s' \cdot \vec{\mathbf{f}}_\psi(\vec{\mathbf{r}}')\right] \frac{e^{-jk_1\left\|\vec{\mathbf{r}}-\vec{\mathbf{r}}'\right\|}}{4\pi\left\|\vec{\mathbf{r}}-\vec{\mathbf{r}}'\right\|} dS_{T_\psi^\pm}^{\prime(P)} dS_{T_\zeta^\pm}^{(P)} \Bigg] \quad \text{on } S_P \end{aligned} \tag{6.41}$$

$$Z_{12}^{(\zeta\psi)} = \frac{1}{4\pi}\int_{T_\zeta^\pm}\int_{T_\psi^\pm} \vec{\mathbf{f}}_\zeta(\vec{\mathbf{r}})\cdot\left[\left(\vec{\mathbf{r}}-\vec{\mathbf{r}}'\right)\times\vec{\mathbf{g}}_\psi(\vec{\mathbf{r}}')\right]\frac{1+jk_0\left\|\vec{\mathbf{r}}-\vec{\mathbf{r}}'\right\|}{\left\|\vec{\mathbf{r}}-\vec{\mathbf{r}}'\right\|^3}e^{-jk_0\left\|\vec{\mathbf{r}}-\vec{\mathbf{r}}'\right\|}dS_{T_\psi^\pm}^{\prime(P)}dS_{T_\zeta^\pm}^{(P)}$$
$$+\frac{1}{4\pi}\int_{T_\zeta^\pm}\int_{T_\psi^\pm} \vec{\mathbf{f}}_\zeta(\vec{\mathbf{r}})\cdot\left[\left(\vec{\mathbf{r}}-\vec{\mathbf{r}}'\right)\times\vec{\mathbf{g}}_\psi(\vec{\mathbf{r}}')\right]\frac{1+jk_1\left\|\vec{\mathbf{r}}-\vec{\mathbf{r}}'\right\|}{\left\|\vec{\mathbf{r}}-\vec{\mathbf{r}}'\right\|^3}e^{-jk_1\left\|\vec{\mathbf{r}}-\vec{\mathbf{r}}'\right\|}dS_{T_\psi^\pm}^{\prime(P)}dS_{T_\zeta^\pm}^{(P)} \quad \text{on } S_P \tag{6.42}$$

$$Z_{13}^{(\zeta\psi)} = jk_1\eta_1\left[\int_{T_\zeta^\pm}\int_{T_\psi^\pm}\vec{\mathbf{f}}_\zeta(\vec{\mathbf{r}})\cdot\vec{\mathbf{f}}_\psi(\vec{\mathbf{r}}')\frac{e^{-jk_1\left\|\vec{\mathbf{r}}-\vec{\mathbf{r}}'\right\|}}{4\pi\left\|\vec{\mathbf{r}}-\vec{\mathbf{r}}'\right\|}dS_{T_\psi^\pm}^{\prime(2)}dS_{T_\zeta^\pm}^{(P)}\right.$$
$$\left.-\frac{1}{k_1^2}\int_{T_\zeta^\pm}\int_{T_\psi^\pm}\left[\nabla_s\cdot\vec{\mathbf{f}}_\zeta(\vec{\mathbf{r}})\right]\left[\nabla_s'\cdot\vec{\mathbf{f}}_\psi(\vec{\mathbf{r}}')\right]\frac{e^{-jk_1\left\|\vec{\mathbf{r}}-\vec{\mathbf{r}}'\right\|}}{4\pi\left\|\vec{\mathbf{r}}-\vec{\mathbf{r}}'\right\|}dS_{T_\psi^\pm}^{\prime(2)}dS_{T_\zeta^\pm}^{(P)}\right] \quad \text{on } S_P \tag{6.43}$$

$$Z_{21}^{(\zeta\psi)} = -\frac{1}{4\pi}\int_{T_\zeta^\pm}\int_{T_\psi^\pm}\vec{\mathbf{g}}_\zeta(\vec{\mathbf{r}})\cdot\left[\left(\vec{\mathbf{r}}-\vec{\mathbf{r}}'\right)\times\vec{\mathbf{f}}_\psi(\vec{\mathbf{r}}')\right]\frac{1+jk_0\left\|\vec{\mathbf{r}}-\vec{\mathbf{r}}'\right\|}{\left\|\vec{\mathbf{r}}-\vec{\mathbf{r}}'\right\|^3}e^{-jk_0\left\|\vec{\mathbf{r}}-\vec{\mathbf{r}}'\right\|}dS_{T_\psi^\pm}^{\prime(P)}dS_{T_\zeta^\pm}^{(P)}$$
$$-\frac{1}{4\pi}\int_{T_\zeta^\pm}\int_{T_\psi^\pm}\vec{\mathbf{g}}_\zeta(\vec{\mathbf{r}})\cdot\left[\left(\vec{\mathbf{r}}-\vec{\mathbf{r}}'\right)\times\vec{\mathbf{f}}_\psi(\vec{\mathbf{r}}')\right]\frac{1+jk_1\left\|\vec{\mathbf{r}}-\vec{\mathbf{r}}'\right\|}{\left\|\vec{\mathbf{r}}-\vec{\mathbf{r}}'\right\|^3}e^{-jk_1\left\|\vec{\mathbf{r}}-\vec{\mathbf{r}}'\right\|}dS_{T_\psi^\pm}^{\prime(P)}dS_{T_\zeta^\pm}^{(P)} \quad \text{on } S_P \tag{6.44}$$

$$Z_{22}^{(\zeta\psi)} = -j\frac{k_0}{\eta_0}\left[\int_{T_\zeta^\pm}\int_{T_\psi^\pm}\vec{\mathbf{g}}_\zeta(\vec{\mathbf{r}})\cdot\vec{\mathbf{g}}_\psi(\vec{\mathbf{r}}')\frac{e^{-jk_0\left\|\vec{\mathbf{r}}-\vec{\mathbf{r}}'\right\|}}{4\pi\left\|\vec{\mathbf{r}}-\vec{\mathbf{r}}'\right\|}dS_{T_\psi^\pm}^{\prime(P)}dS_{T_\zeta^\pm}^{(P)}\right.$$
$$\left.-\frac{1}{k_0^2}\int_{T_\zeta^\pm}\int_{T_\psi^\pm}\left[\nabla_s\cdot\vec{\mathbf{g}}_\zeta(\vec{\mathbf{r}})\right]\left[\nabla_s'\cdot\vec{\mathbf{g}}_\psi(\vec{\mathbf{r}}')\right]\frac{e^{-jk_0\left\|\vec{\mathbf{r}}-\vec{\mathbf{r}}'\right\|}}{4\pi\left\|\vec{\mathbf{r}}-\vec{\mathbf{r}}'\right\|}dS_{T_\psi^\pm}^{\prime(P)}dS_{T_\zeta^\pm}^{(P)}\right]$$
$$-j\frac{k_1}{\eta_1}\left[\int_{T_\zeta^\pm}\int_{T_\psi^\pm}\vec{\mathbf{g}}_\zeta(\vec{\mathbf{r}})\cdot\vec{\mathbf{g}}_\psi(\vec{\mathbf{r}}')\frac{e^{-jk_1\left\|\vec{\mathbf{r}}-\vec{\mathbf{r}}'\right\|}}{4\pi\left\|\vec{\mathbf{r}}-\vec{\mathbf{r}}'\right\|}dS_{T_\psi^\pm}^{\prime(P)}dS_{T_\zeta^\pm}^{(P)}\right.$$
$$\left.-\frac{1}{k_1^2}\int_{T_\zeta^\pm}\int_{T_\psi^\pm}\left[\nabla_s\cdot\vec{\mathbf{g}}_\zeta(\vec{\mathbf{r}})\right]\left[\nabla_s'\cdot\vec{\mathbf{g}}_\psi(\vec{\mathbf{r}}')\right]\frac{e^{-jk_1\left\|\vec{\mathbf{r}}-\vec{\mathbf{r}}'\right\|}}{4\pi\left\|\vec{\mathbf{r}}-\vec{\mathbf{r}}'\right\|}dS_{T_\psi^\pm}^{\prime(P)}dS_{T_\zeta^\pm}^{(P)}\right] \quad \text{on } S_P \tag{6.45}$$

$$Z_{23}^{(\zeta\psi)} = \frac{1}{4\pi}\int_{T_\zeta^\pm}\int_{T_\psi^\pm}\vec{\mathbf{g}}_\zeta(\vec{\mathbf{r}})\cdot\left[\left(\vec{\mathbf{r}}-\vec{\mathbf{r}}'\right)\times\vec{\mathbf{f}}_\psi(\vec{\mathbf{r}}')\right]$$
$$\frac{1+jk_1\left\|\vec{\mathbf{r}}-\vec{\mathbf{r}}'\right\|}{\left\|\vec{\mathbf{r}}-\vec{\mathbf{r}}'\right\|^3}e^{-jk_1\left\|\vec{\mathbf{r}}-\vec{\mathbf{r}}'\right\|}dS_{T_\psi^\pm}^{\prime(2)}dS_{T_\zeta^\pm}^{(P)} \quad \text{on } S_P \tag{6.46}$$

$$Z_{31}^{(\zeta\psi)} = jk_1\eta_1 \left[\int_{T_\zeta^\pm} \int_{T_\psi^\pm} \vec{\mathbf{f}}_\zeta(\vec{\mathbf{r}}) \cdot \vec{\mathbf{f}}_\psi(\vec{\mathbf{r}}') \frac{e^{-jk_1\left\|\vec{\mathbf{r}}-\vec{\mathbf{r}}'\right\|}}{4\pi\left\|\vec{\mathbf{r}}-\vec{\mathbf{r}}'\right\|} dS_{T_\psi^\pm}^{\prime(P)} dS_{T_\zeta^\pm}^{(2)} \right.$$
$$\left. -\frac{1}{k_1^2} \int_{T_\zeta^\pm} \int_{T_\psi^\pm} \left[\nabla_s \cdot \vec{\mathbf{f}}_\zeta(\vec{\mathbf{r}})\right] \left[\nabla_s' \cdot \vec{\mathbf{f}}_\psi(\vec{\mathbf{r}}')\right] \frac{e^{-jk_1\left\|\vec{\mathbf{r}}-\vec{\mathbf{r}}'\right\|}}{4\pi\left\|\vec{\mathbf{r}}-\vec{\mathbf{r}}'\right\|} dS_{T_\psi^\pm}^{\prime(P)} dS_{T_\zeta^\pm}^{(2)} \right] \quad \text{on } S_2 \quad (6.47)$$

$$Z_{32}^{(\zeta\psi)} = -\frac{1}{4\pi} \int_{T_\zeta^\pm} \int_{T_\psi^\pm} \vec{\mathbf{f}}_\zeta(\vec{\mathbf{r}}) \cdot \left[\left(\vec{\mathbf{r}}-\vec{\mathbf{r}}'\right) \times \vec{\mathbf{g}}_\psi(\vec{\mathbf{r}}')\right]$$
$$\frac{1+jk_1\left\|\vec{\mathbf{r}}-\vec{\mathbf{r}}'\right\|}{\left\|\vec{\mathbf{r}}-\vec{\mathbf{r}}'\right\|^3} e^{-jk_1\left\|\vec{\mathbf{r}}-\vec{\mathbf{r}}'\right\|} dS_{T_\psi^\pm}^{\prime(P)} dS_{T_\zeta^\pm}^{(2)} \quad \text{on } S_2 \quad (6.48)$$

$$Z_{33}^{(\zeta\psi)} = -jk_1\eta_1 \left[\int_{T_\zeta^\pm} \int_{T_\psi^\pm} \vec{\mathbf{f}}_\zeta(\vec{\mathbf{r}}) \cdot \vec{\mathbf{f}}_\psi(\vec{\mathbf{r}}') \frac{e^{-jk_1\left\|\vec{\mathbf{r}}-\vec{\mathbf{r}}'\right\|}}{4\pi\left\|\vec{\mathbf{r}}-\vec{\mathbf{r}}'\right\|} dS_{T_\psi^\pm}^{\prime(2)} dS_{T_\zeta^\pm}^{(2)} \right.$$
$$\left. -\frac{1}{k_1^2} \int_{T_\zeta^\pm} \int_{T_\psi^\pm} \left[\nabla_s \cdot \vec{\mathbf{f}}_\zeta(\vec{\mathbf{r}})\right] \left[\nabla_s' \cdot \vec{\mathbf{f}}_\psi(\vec{\mathbf{r}}')\right] \frac{e^{-jk_1\left\|\vec{\mathbf{r}}-\vec{\mathbf{r}}'\right\|}}{4\pi\left\|\vec{\mathbf{r}}-\vec{\mathbf{r}}'\right\|} dS_{T_\psi^\pm}^{\prime(2)} dS_{T_\zeta^\pm}^{(2)} \right] \quad \text{on } S_2 \quad (6.49)$$

where, supercripts (P) and (2) imply the surfaces. In addition, $\overline{\mathbf{V}}$ array components

$$V_{\zeta 11}^{(P)} = 0 \quad \text{on } S_P \quad (6.50)$$

$$V_{\zeta 21}^{(P)} = 0 \quad \text{on } S_P \quad (6.51)$$

$$V_{\zeta 31}^{(2)} = \int_{S_{T_\zeta^\pm}^{(2)}} \vec{\mathbf{f}}_\zeta(\vec{\mathbf{r}}) \cdot \left[\vec{\mathbf{E}}^t\right] dS_{T_\zeta^\pm}^{(2)} \quad \text{on } S_2 \quad (6.52)$$

After the representation of the Z matrix, the far-field expression inside Region 1 can be given here as follows

$$\vec{\mathbf{E}}_{far\text{-}field}^s(\vec{\mathbf{r}}) = \vec{\mathbf{E}}_1^s(\vec{\mathbf{J}}_P, \vec{\mathbf{M}}_P) \quad (6.53)$$

Hence, on S_P surface

$$\vec{\mathbf{E}}_1^s(\vec{\mathbf{J}}_P,\vec{\mathbf{M}}_P) = -jk_0\frac{e^{-jk_0r}}{4\pi r}\int_{S'_P}\left[\vec{\mathbf{M}}_P(\vec{\mathbf{r}}')\times\vec{\mathbf{r}}\right]e^{jk_0\vec{\mathbf{r}}'\cdot\vec{\mathbf{r}}}dS'_P + jk_0\eta_0\frac{e^{-jk_0r}}{4\pi r}\int_{S'_P}\hat{\mathbf{r}}\times\left[\hat{\mathbf{r}}\times\vec{\mathbf{J}}_P(\vec{\mathbf{r}}')\right]\left[e^{jk_0\vec{\mathbf{r}}'\cdot\hat{\mathbf{r}}}\right]dS'_P \quad (6.54)$$

can be written. Finally, utilizing (6.37), and (6.38)

$$\vec{\mathbf{E}}_1^s(\vec{\mathbf{J}}_P,\vec{\mathbf{M}}_P) = -jk_0\frac{e^{-jk_0r}}{4\pi r}\left[\sum_{\psi=1}^{N_P}I_\psi^{(M_P)}\int_{S'^{(P)}_{T^\pm_\psi}}\left[\vec{\mathbf{g}}_\psi(\vec{\mathbf{r}}')\times\vec{\mathbf{r}}\right]\left[e^{jk_0\vec{\mathbf{r}}'\cdot\hat{\mathbf{r}}}\right]dS'^{(P)}_{T^\pm_\psi}\right] + jk_0\eta_0\frac{e^{-jk_0r}}{4\pi r}\left[\sum_{\psi=1}^{N_P}I_\psi^{(J_P)}\int_{S'^{(P)}_{T^\pm_\psi}}\hat{\mathbf{r}}\times\left[\hat{\mathbf{r}}\times\vec{\mathbf{f}}_\psi(\vec{\mathbf{r}}')\right]\left[e^{jk_0\vec{\mathbf{r}}'\cdot\hat{\mathbf{r}}}\right]dS'^{(P)}_{T^\pm_\psi}\right] \quad (6.55)$$

are expressed for any edge on the surface, and the RCS definition is given in (5.89).

6.2 Numerical Results

As in the previous chapters, we are starting by discussing the perturbation current distributions will help understand the scattering behavior of the buried object. Then, as demonstrated in Figures 6.2–6.13, several scattering examples with a selection perturbation area of 12.5 × 12.5 m^2 are carried out to assess the perturbed current distributions on this bounded surface. Here, as in Chapter 5, the ground has a dielectric constant of 4 and a conductivity of 0.1 S/m. Now, for the first scattering example, a PEC cube with a side length of 0.3 m ($d = 0.3$ m) is initially placed below the surface at a distance of 0.1 m ($h = 0.1$ m), where the incidence angle is 0°. The perturbed currents on the perturbation surface are demonstrated in Figures 6.2 and 6.3. Then, the incidence angle is changed to 85°, and the current density results on the surface are depicted in Figures 6.4 and 6.5. For the third simulation, as shown in Figures 6.6 and 6.7, the h parameter is increased to 0.2 m, where the incidence angle is set to 0° again. Also, in the fourth scenario given in Figures 6.8 and 6.9, the d parameter is changed to 0.6 m when the angle of incidence is 0°. Here, h is 0.1 m again. So far, all simulations are illuminated by a linearly polarized plane wave in the negative y-direction ($\theta_i = 0°$, $\phi_i = 0°$, and $\alpha_i = 90°$). In Figures 6.10 and 6.11, the polarization of the plane wave is shifted to the positive x-direction for the fifth

example ($\theta_i = 0°$, $\phi_i = 0°$, and $\alpha_i = 0°$), while other parameters remain the same. In Figures 6.12 and 6.13, the horizontal polarization in the second example is converted vertically.

Furthermore, in these simulations, the average mesh length of a triangle for the ground surface is $0.2\lambda_0$. The cube is discretized with triangles of $0.2\lambda_d$ average length. The distributions of each current density on this truncated surface are given in Figures 6.2–6.13 for these six cases, respectively. Also, the incident plane wave frequency was 300 MHz in all simulations.

A sample scattering problem is utilized from a reference work as given in [50] to validate our proposed formulation. In this example, a plate buried with a depth of 0.5 m in a lossy dielectric half-space. The electrical properties of this flat ground plane are $\epsilon = 4 - j0.01$, and $\mu = 1$. A plane wave whose amplitude is one is normal incidence to the surface. The frequency of the wave is $f = 100$ MHz. Plate dimension is 3.750×3.750 m^2. Figures 6.14 and 6.15 show the obtained results with literature comparisons. As shown from these figures, our results are very satisfactory.

Now, the perturbation region is increased for validation. After this point, a plane wave illuminates all scattering examples with an incident angle of θ_i=85°, ϕ_i=30°, α_i=90°. Figures 6.16 and 6.17 are the RCS results for $\phi = 0°$ and $\phi = 90°$ planes while increasing the the perturbation surface. The frequency of the incident plane wave is 300 MHz again, and after this point, the frequency will not be changed unless otherwise stated. In addition, unless otherwise stated, the dielectric constant of the ground is 4, and the ground has a conductivity of 0.1 S/m. Also, in these simulations, the parameters is as $h = 0.1$ m and $d = 0.3$ m.

As seen from Figures 6.16 and 6.17, the selected perturbation area is adequate to calculate the RCSs of the object with high accuracy, and it seems that there is no significant change in the RCS results while increasing the region. It should be noticed that minor changes in the RCS patterns are only in the scattering angles close to grazing. Besides, the current distributions are also shared on the perturbation region for $W_P = L_P = 24$ m. As can be seen from the figures, the perturbed current is diminished exponentially, and the magnetic current density on the perturbation surface is dominant.

Subsequently, the effect of the d and h parameters on the RCS of the object is given in Figures 6.18–6.21. Besides, the changes in the RCS are also observed while increasing the incident angle in Figures 6.22 and 6.23 for $\phi = 0°$ and $\phi = 90°$ planes, respectively.

Then, simulations are continued for different dielectric and conductivity values. The results are given in Figure 6.24 - 6.27. Here, as the dielectric constant and conductivity increase, the results converge to the PEC ground case. Unlike the previous chapters, the effects of object shapes on the RCSs are given in Figures 6.28 and 6.29. Here, the objects are 0.1 m above the surface, and the width of the objects is approximately 0.6 m. As seen from these figures, the object's shape also significantly affects the RCS.

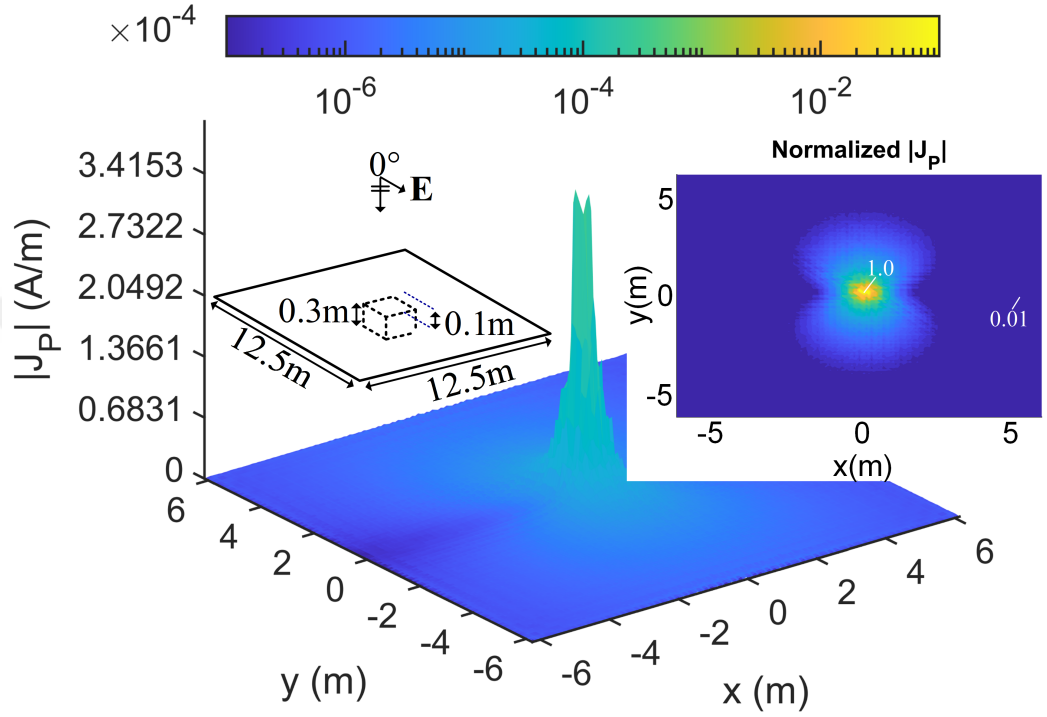

Figure 6.2 Perturbed electric current density for a limited region on an infinite ground plane ($d = 0.3$ m, $h = 0.1$ m, $\theta_i = 0°$, $\phi_i = 0°$, $\alpha_i = 90°$)

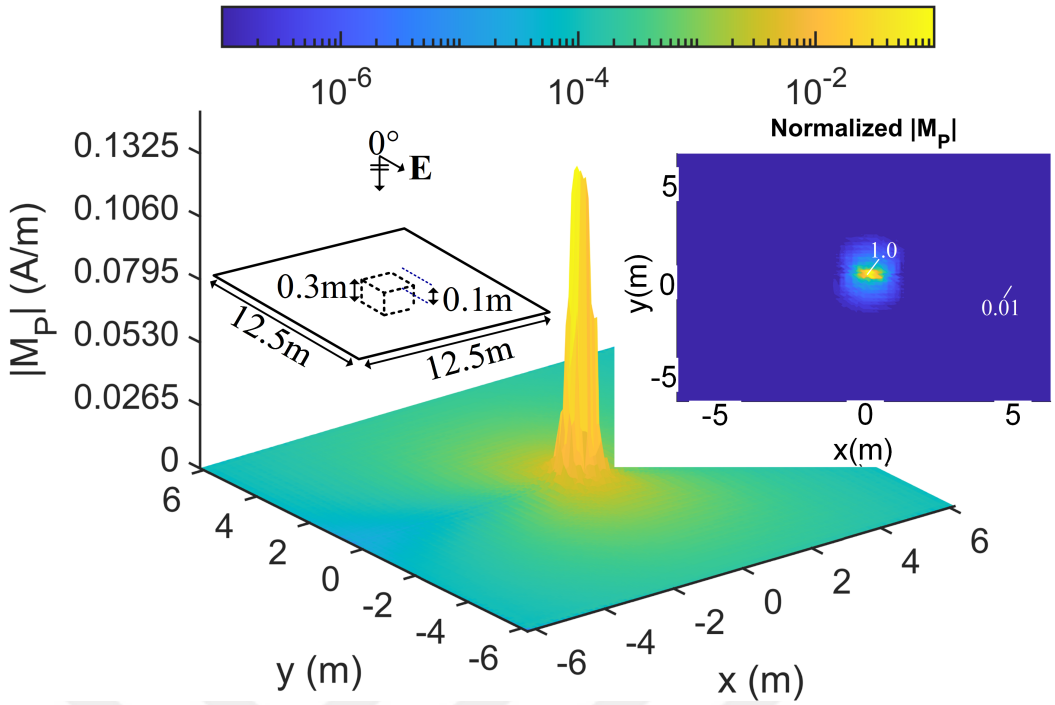

Figure 6.3 Perturbed magnetic current density for a limited region on an infinite ground plane ($d = 0.3$ m, $h = 0.1$ m, $\theta_i = 0°$, $\phi_i = 0°$, $\alpha_i = 90°$)

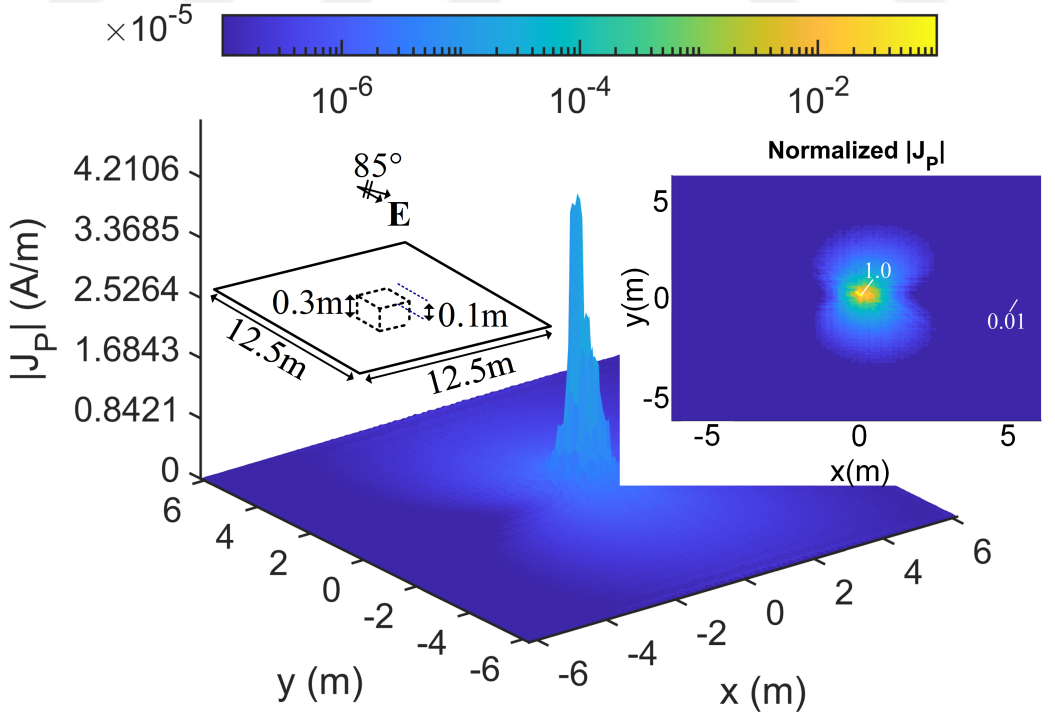

Figure 6.4 Perturbed electric current density for a limited region on an infinite ground plane ($d = 0.3$ m, $h = 0.1$ m, $\theta_i = 85°$, $\phi_i = 0°$, $\alpha_i = 90°$)

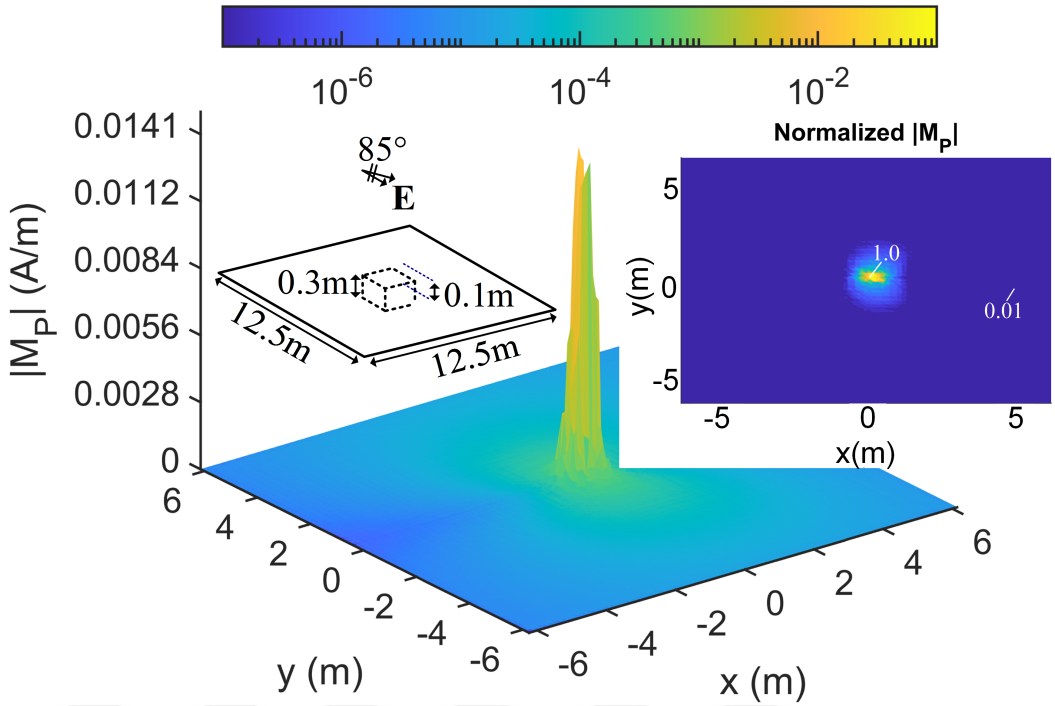

Figure 6.5 Perturbed magnetic current density for a limited region on an infinite ground plane ($d = 0.3$ m, $h = 0.1$ m, $\theta_i = 85°$, $\phi_i = 0°$, $\alpha_i = 90°$)

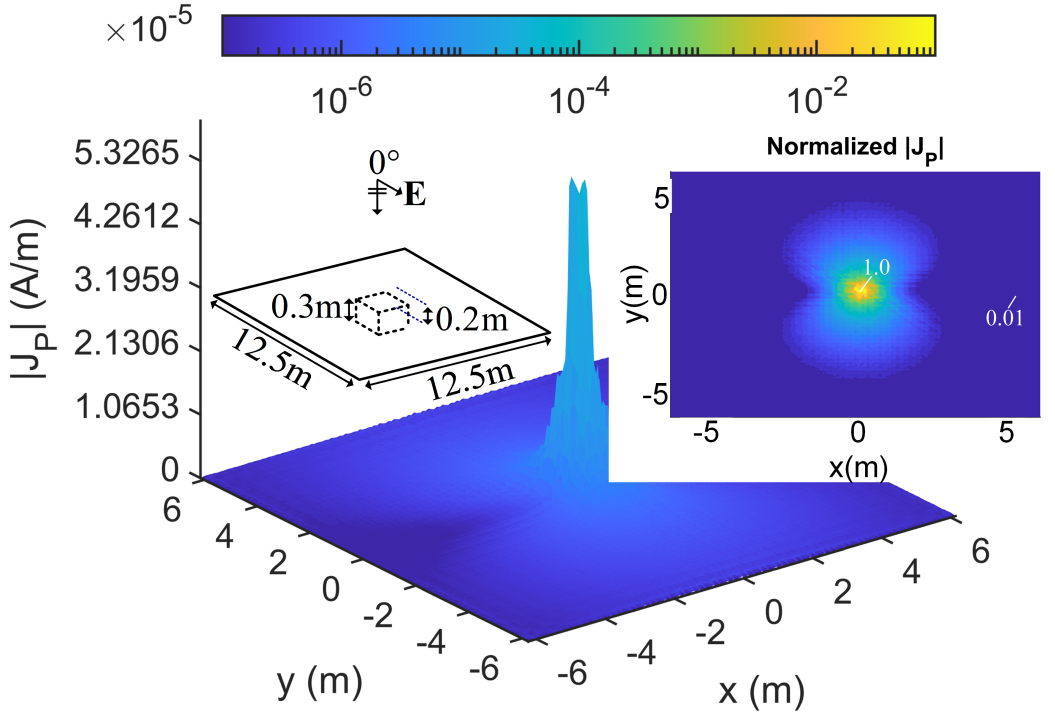

Figure 6.6 Perturbed electric current density for a limited region on an infinite ground plane ($d = 0.3$ m, $h = 0.2$ m, $\theta_i = 0°$, $\phi_i = 0°$, $\alpha_i = 90°$)

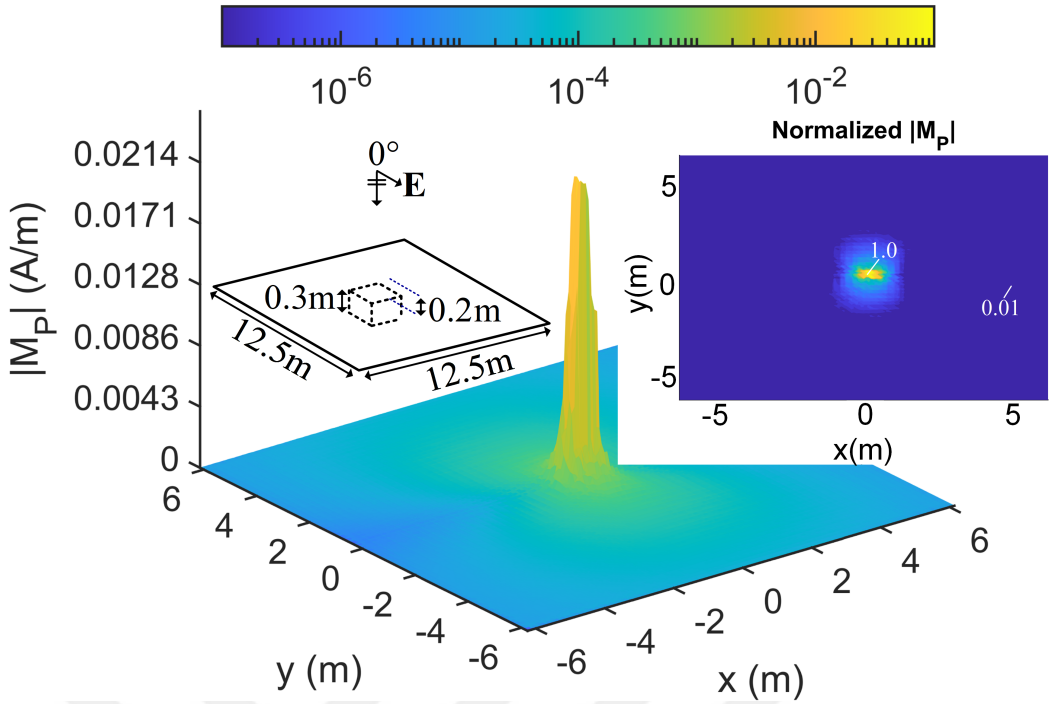

Figure 6.7 Perturbed magnetic current density for a limited region on an infinite ground plane ($d = 0.3$ m, $h = 0.2$ m, $\theta_i = 0°$, $\phi_i = 0°$, $\alpha_i = 90°$)

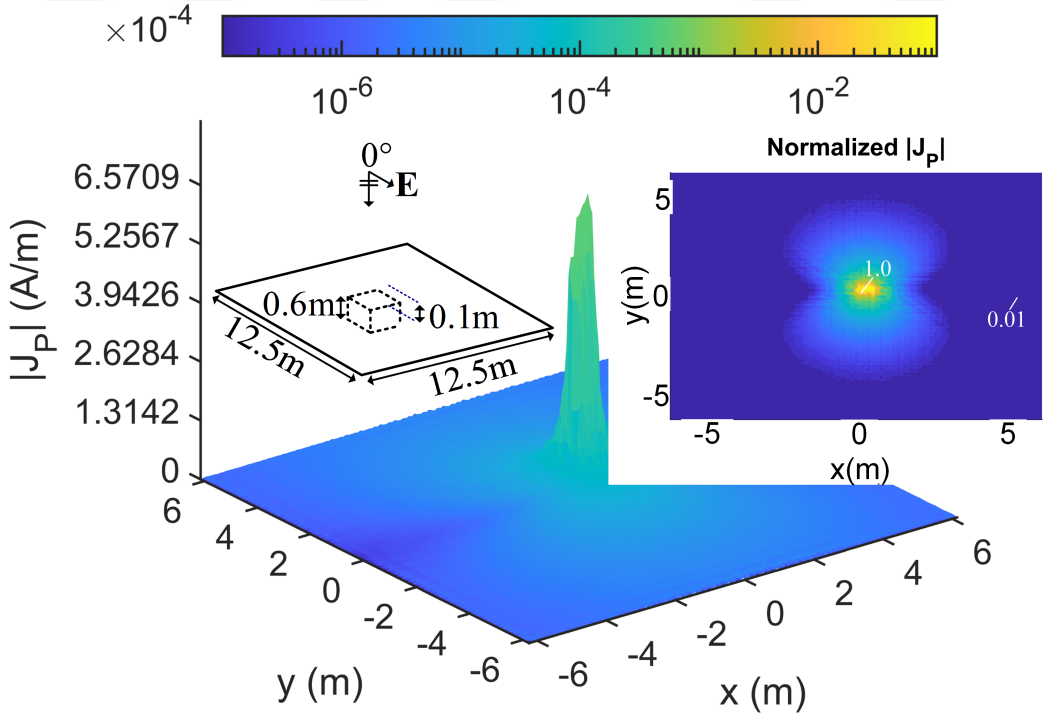

Figure 6.8 Perturbed electric current density for a limited region on an infinite ground plane ($d = 0.6$ m, $h = 0.1$ m, $\theta_i = 0°$, $\phi_i = 0°$, $\alpha_i = 90°$)

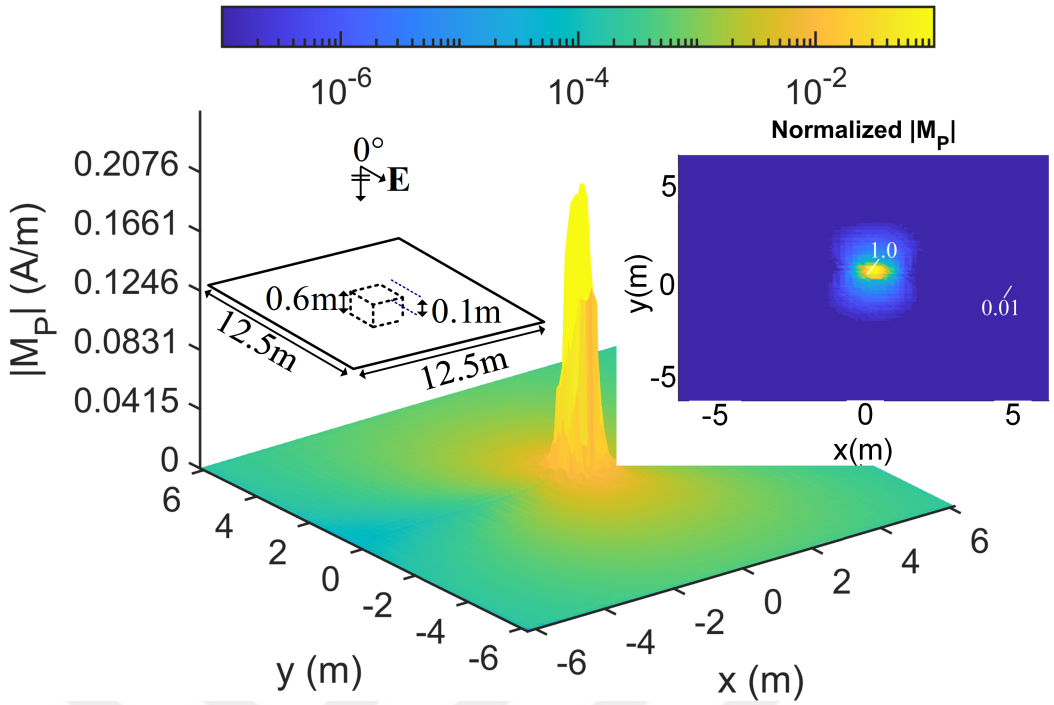

Figure 6.9 Perturbed magnetic current density for a limited region on an infinite ground plane ($d = 0.6$ m, $h = 0.1$ m, $\theta_i = 0°$, $\phi_i = 0°$, $\alpha_i = 90°$)

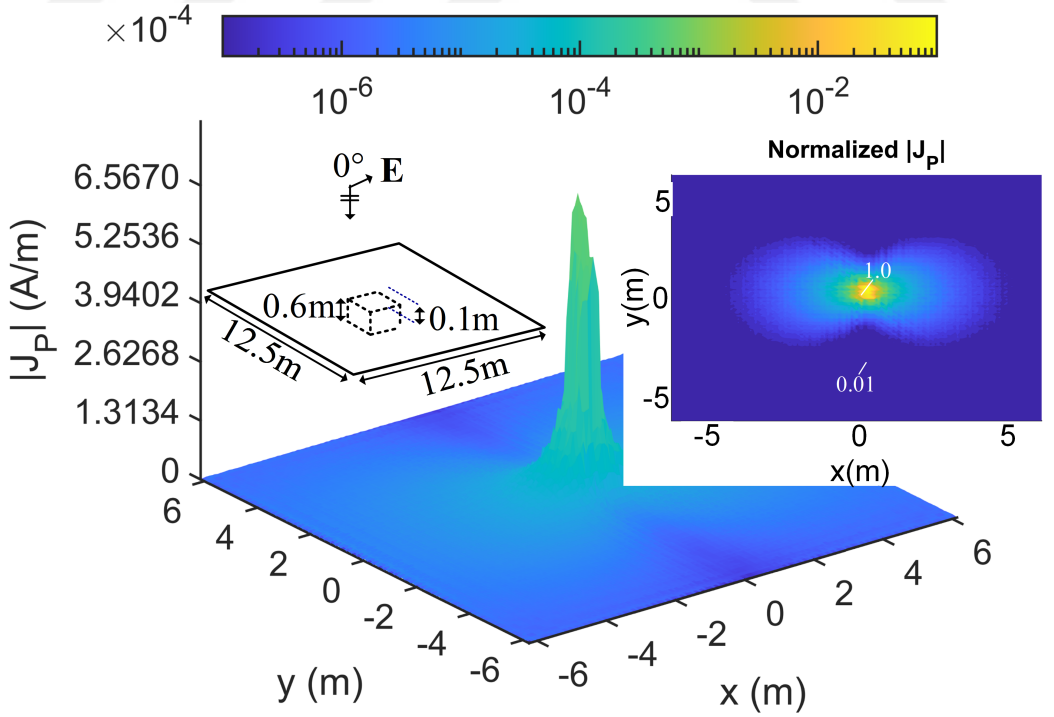

Figure 6.10 Perturbed electric current density for a limited region on an infinite ground plane ($d = 0.6$ m, $h = 0.1$ m, $\theta_i = 0°$, $\phi_i = 0°$, $\alpha_i = 0°$)

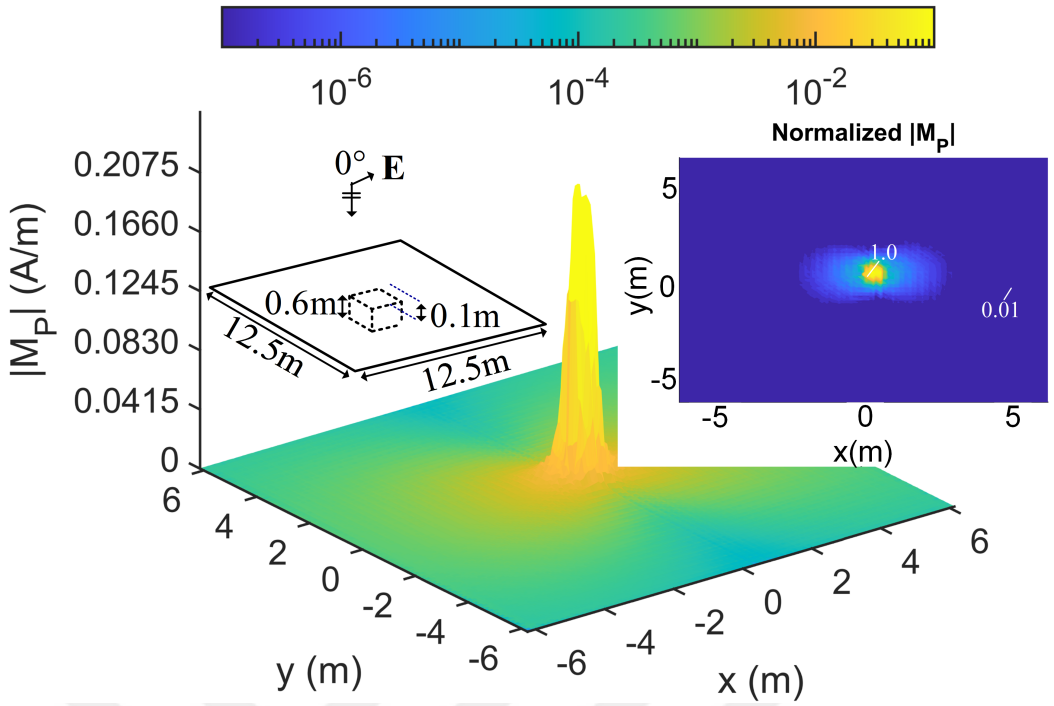

Figure 6.11 Perturbed magnetic current density for a limited region on an infinite ground plane ($d = 0.6$ m, $h = 0.1$ m, $\theta_i = 0°$, $\phi_i = 0°$, $\alpha_i = 0°$)

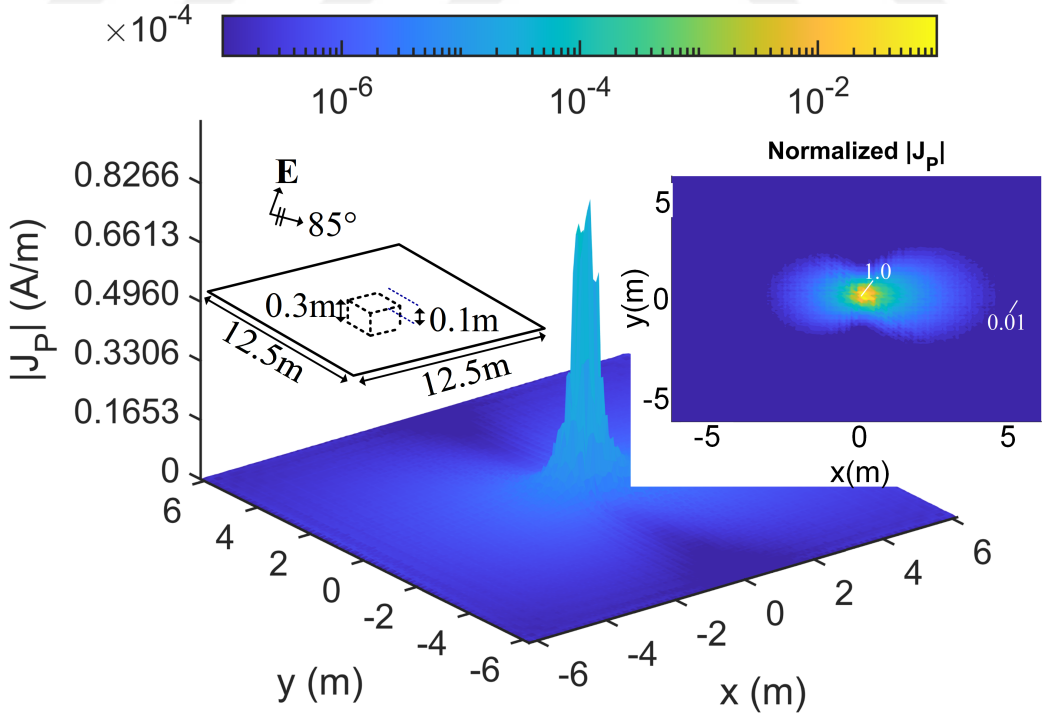

Figure 6.12 Perturbed electric current density for a limited region on an infinite ground plane ($d = 0.3$ m, $h = 0.1$ m, $\theta_i = 85°$, $\phi_i = 0°$, $\alpha_i = 0°$)

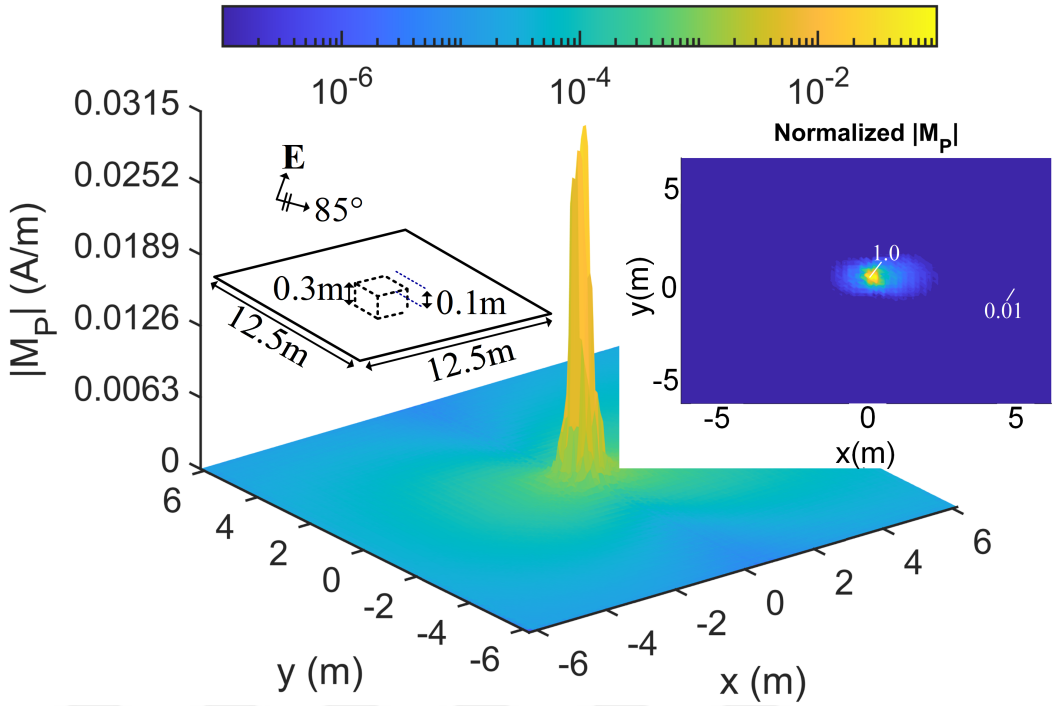

Figure 6.13 Perturbed magnetic current density for a limited region on an infinite ground plane ($d = 0.3$ m, $h = 0.1$ m, $\theta_i = 85°$, $\phi_i = 0°$, $\alpha_i = 0°$)

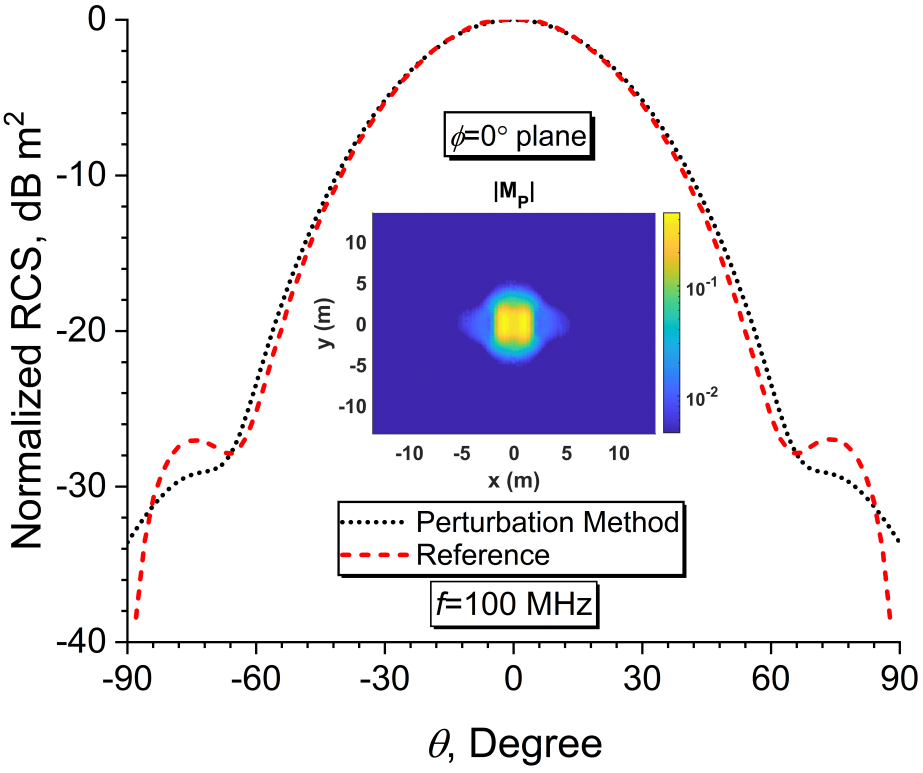

Figure 6.14 Comparative results of a buried plate inside a lossy ground for the vertical polarized scattered electric field. Plate dimension 3.750×3.750 m^2, $f = 100$ MHz, x-polarized incident plane wave.

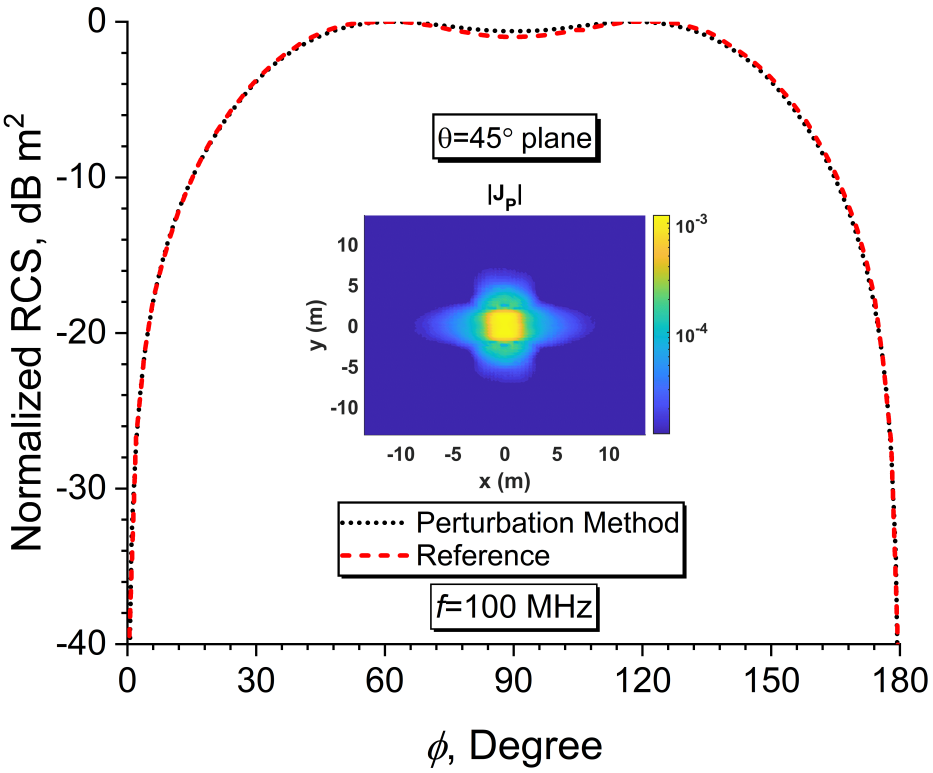

Figure 6.15 Comparative results of a buried plate inside a lossy ground for the horizontal polarized scattered electric field. Plate dimension 3.750×3.750 m^2, $f = 100$ MHz, x-polarized incident plane wave.

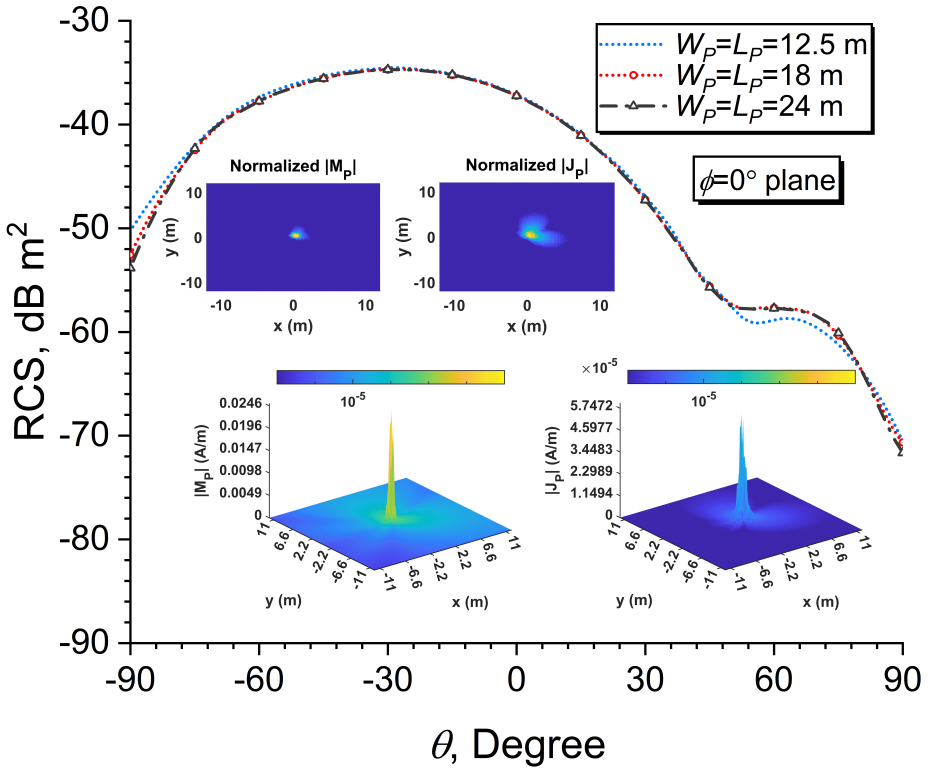

Figure 6.16 RCS results for the plane $\phi = 0°$ while increasing the perturbation region

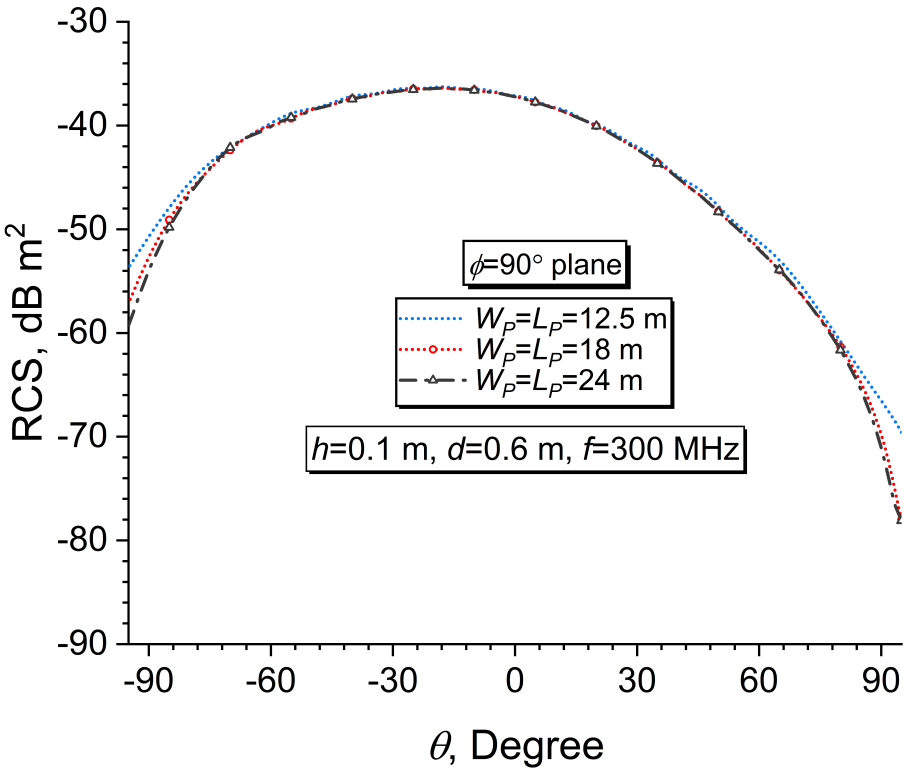

Figure 6.17 RCS results for the plane $\phi = 90°$ while increasing the perturbation region

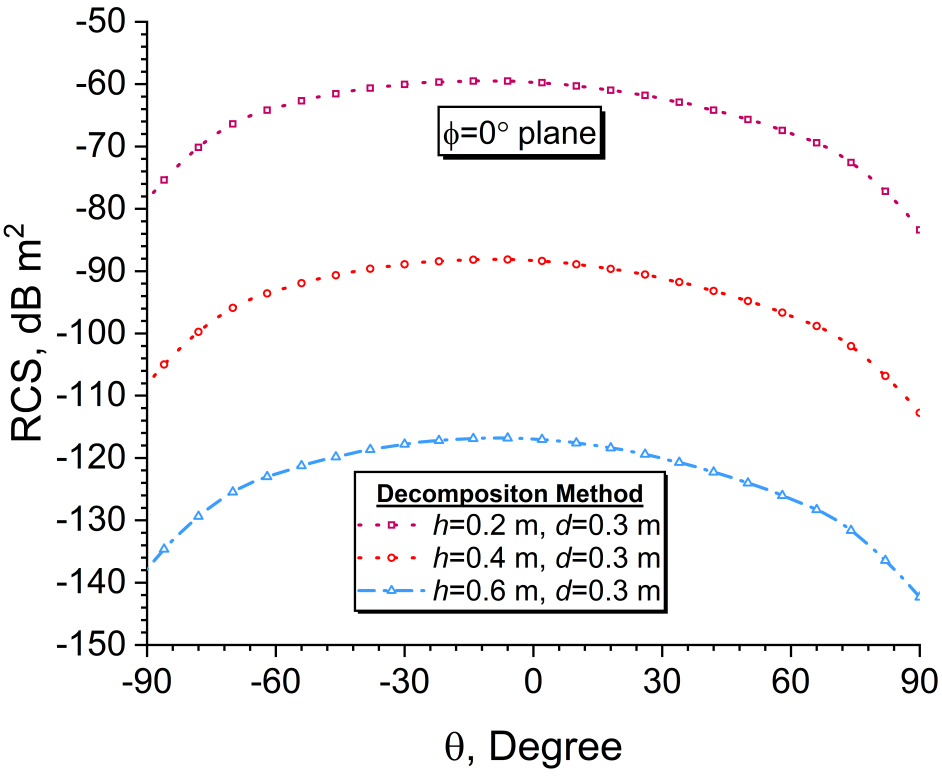

Figure 6.18 RCS results in the plane $\phi = 0°$ while increasing the depth of the object to the surface

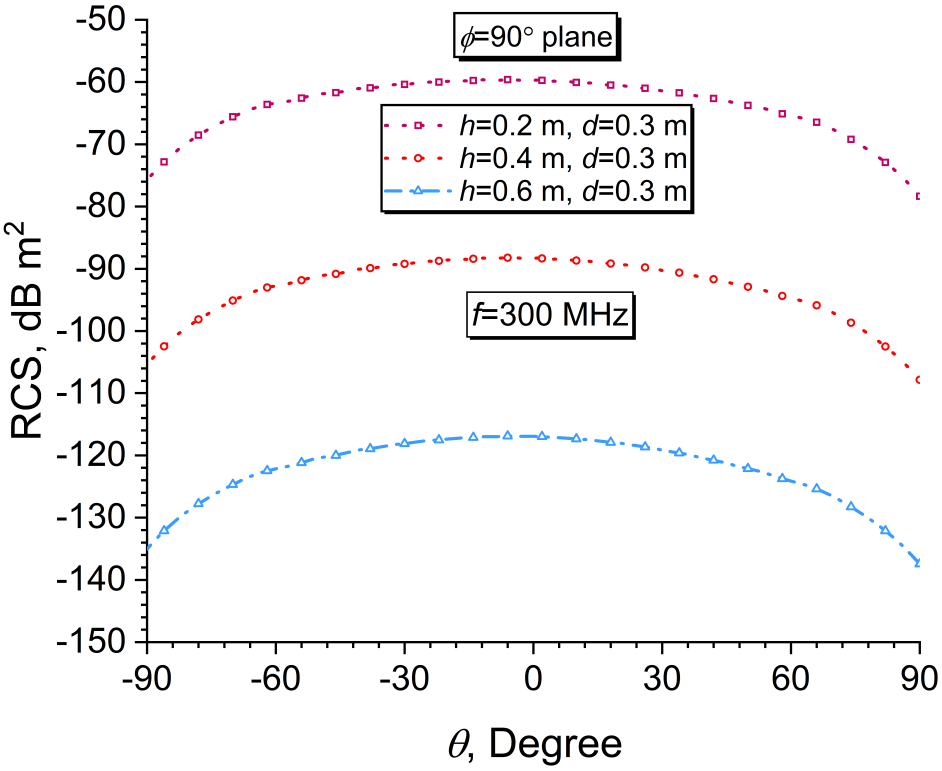

Figure 6.19 RCS results in the plane $\phi = 90°$ while increasing the depth of the object to the surface

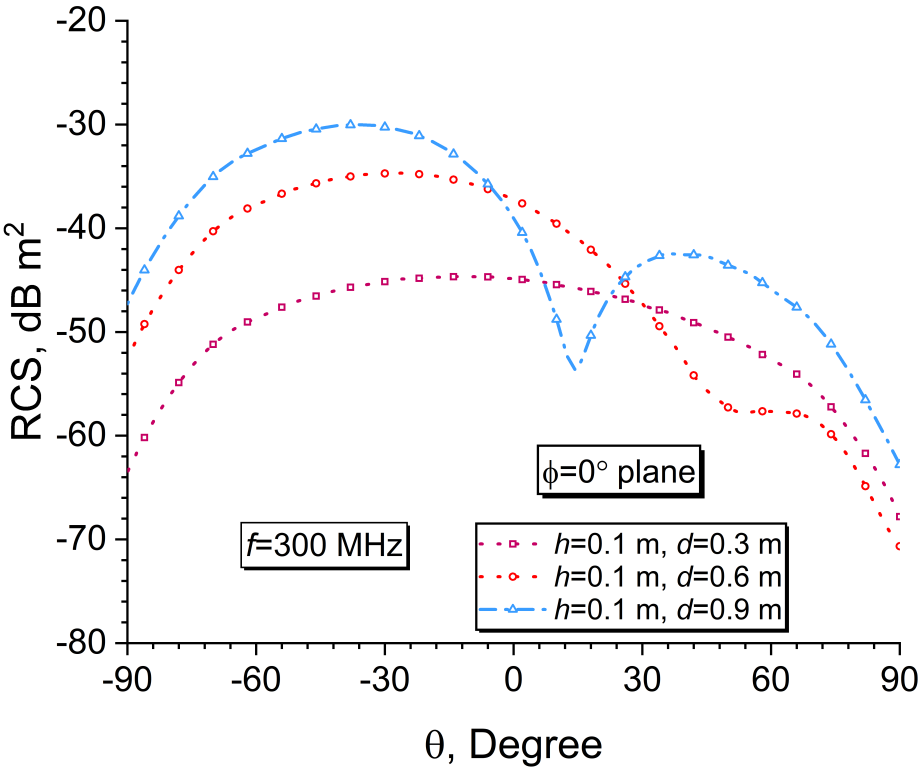

Figure 6.20 RCS results in the $\phi = 0°$ plane while increasing the size of the object

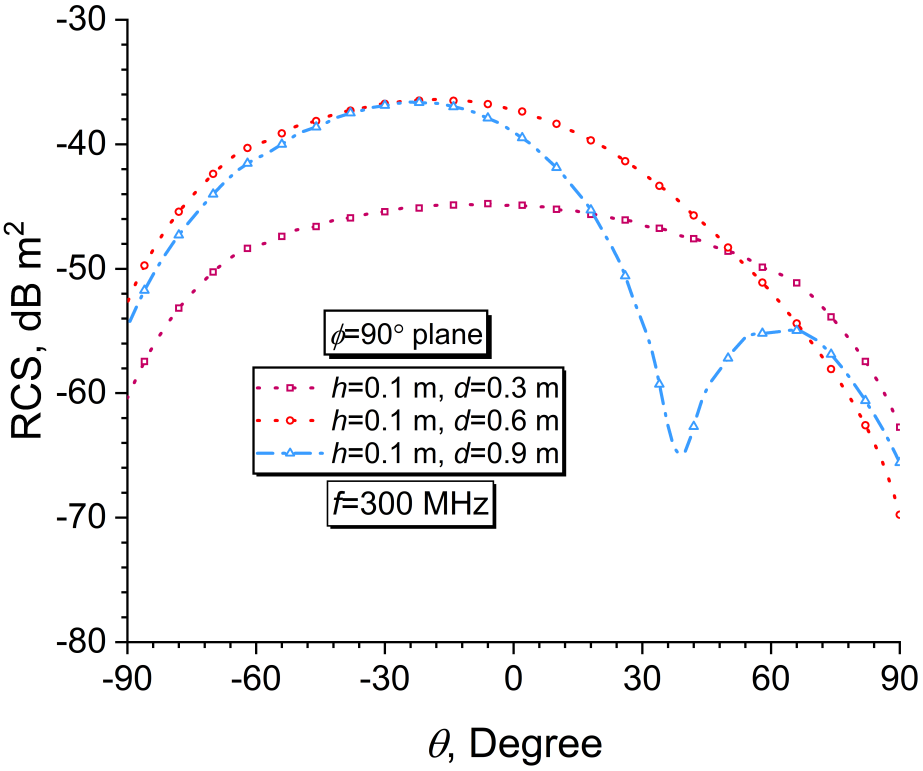

Figure 6.21 RCS results in the $\phi = 90°$ plane while increasing the size of the object

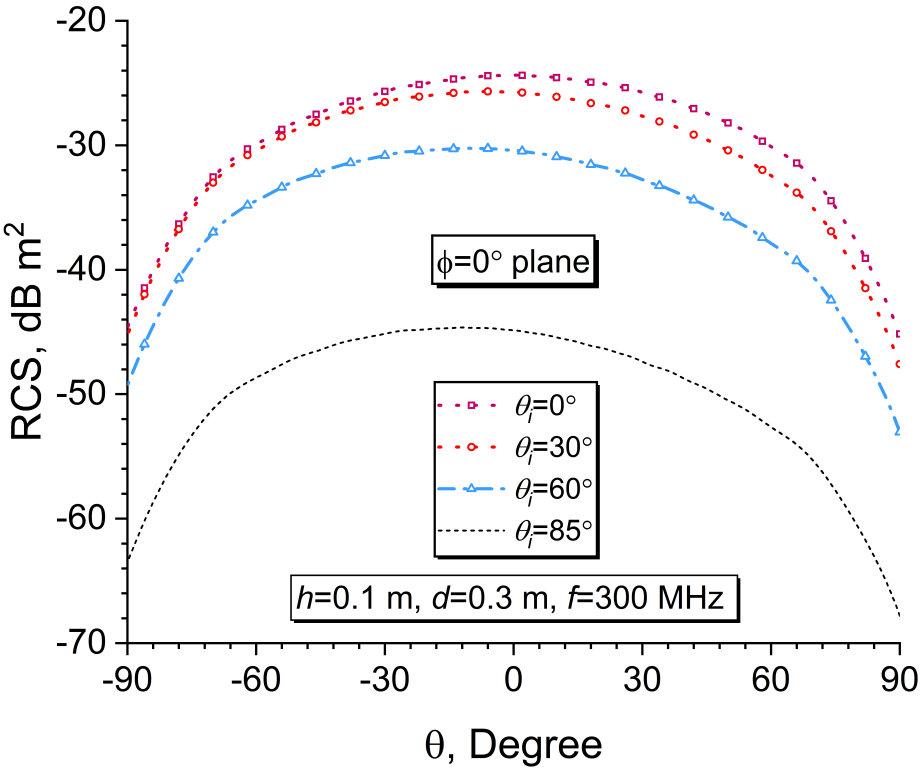

Figure 6.22 RCS results in the $\phi = 0°$ plane while increasing the incident angle

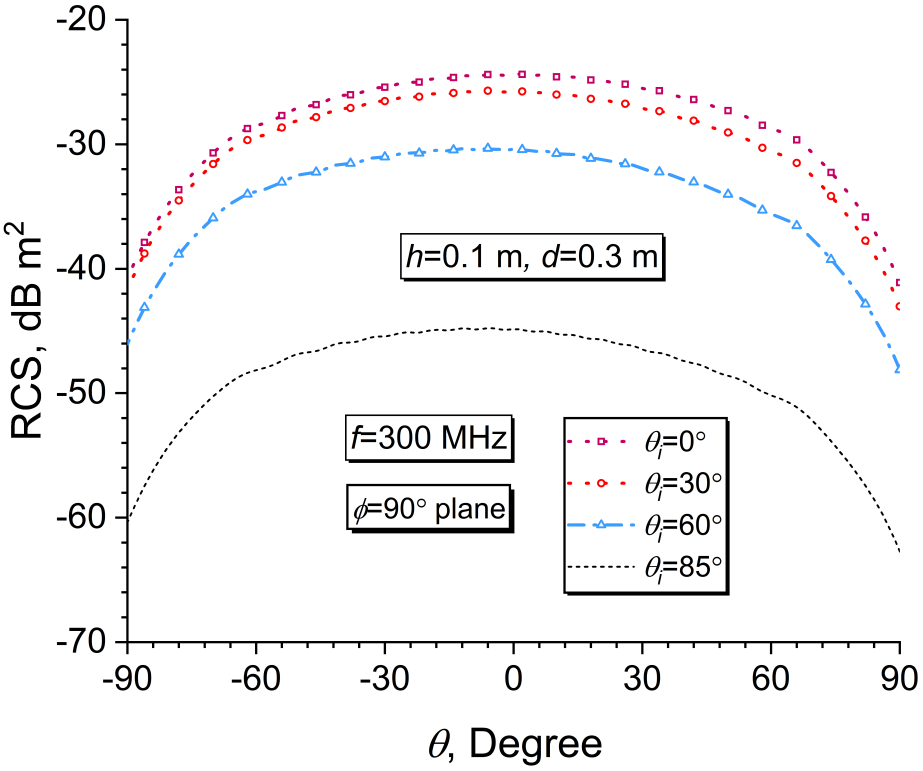

Figure 6.23 RCS results in the $\phi = 90°$ plane while increasing the incident angle

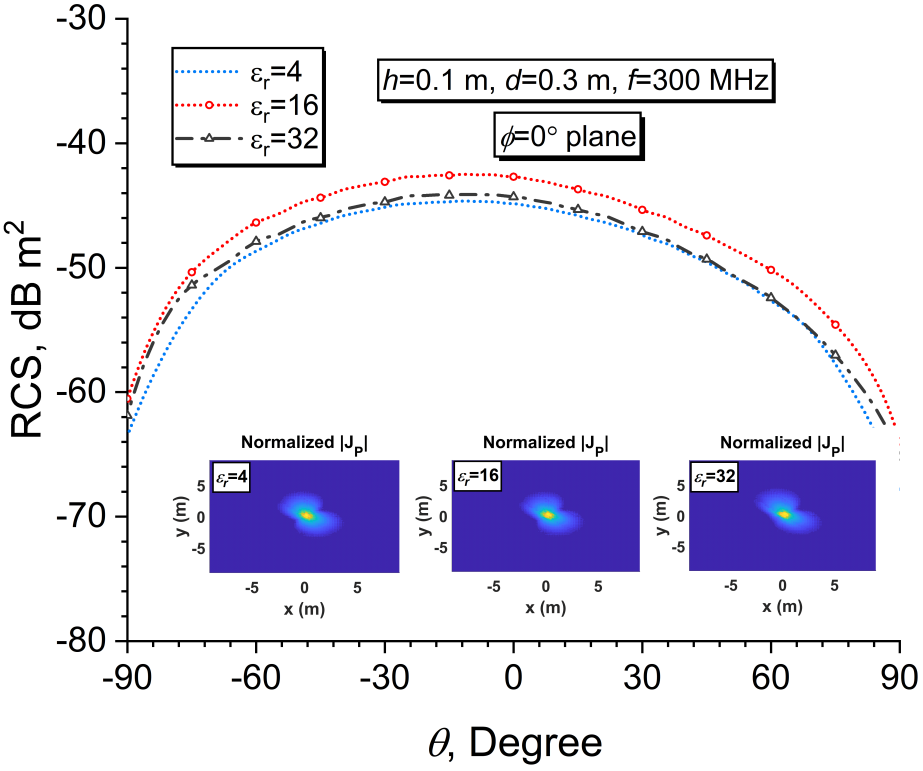

Figure 6.24 RCS results in the $\phi = 0°$ plane while increasing the dielectric constant of the dielectric medium

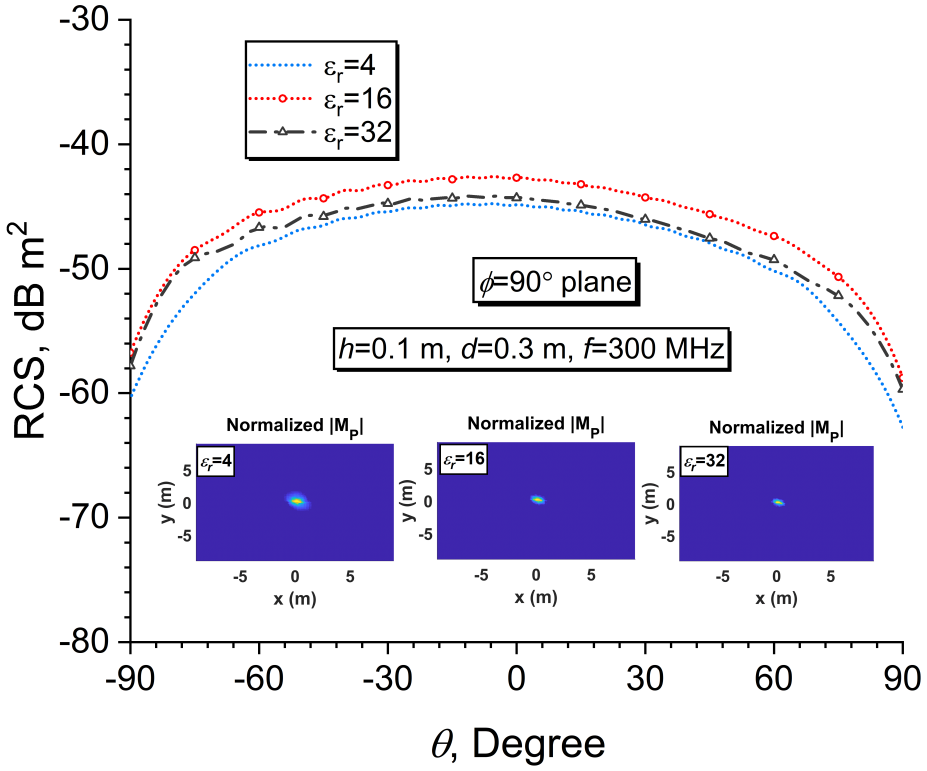

Figure 6.25 RCS results in the $\phi = 90^\circ$ plane while increasing the dielectric constant of the dielectric medium

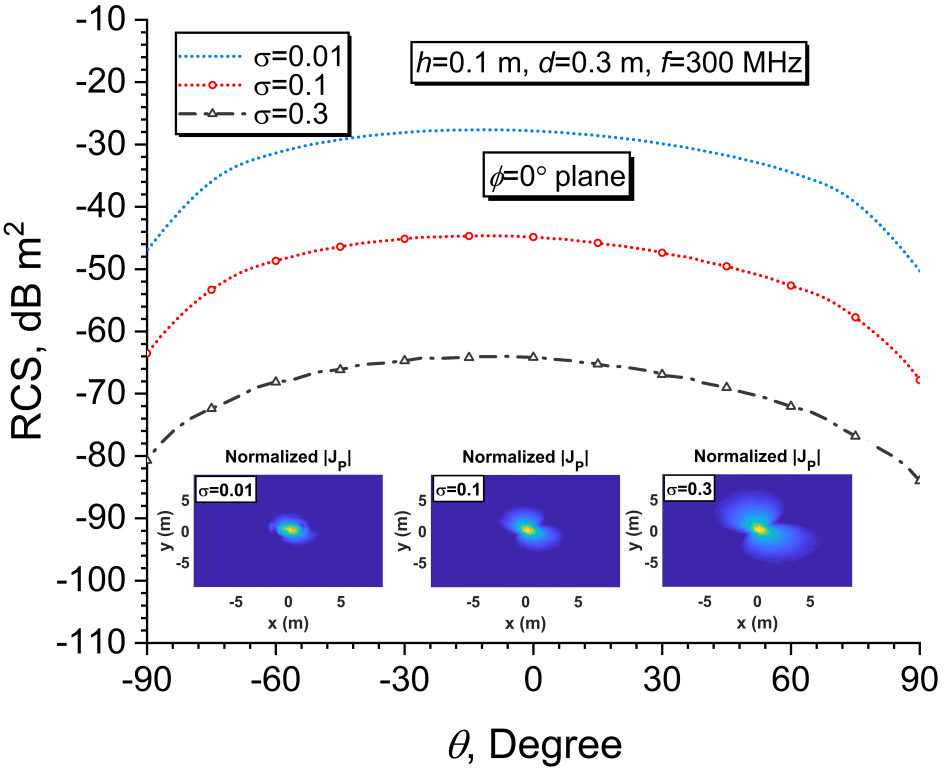

Figure 6.26 RCS results in the $\phi = 0^\circ$ plane while increasing the conductivity of the dielectric medium

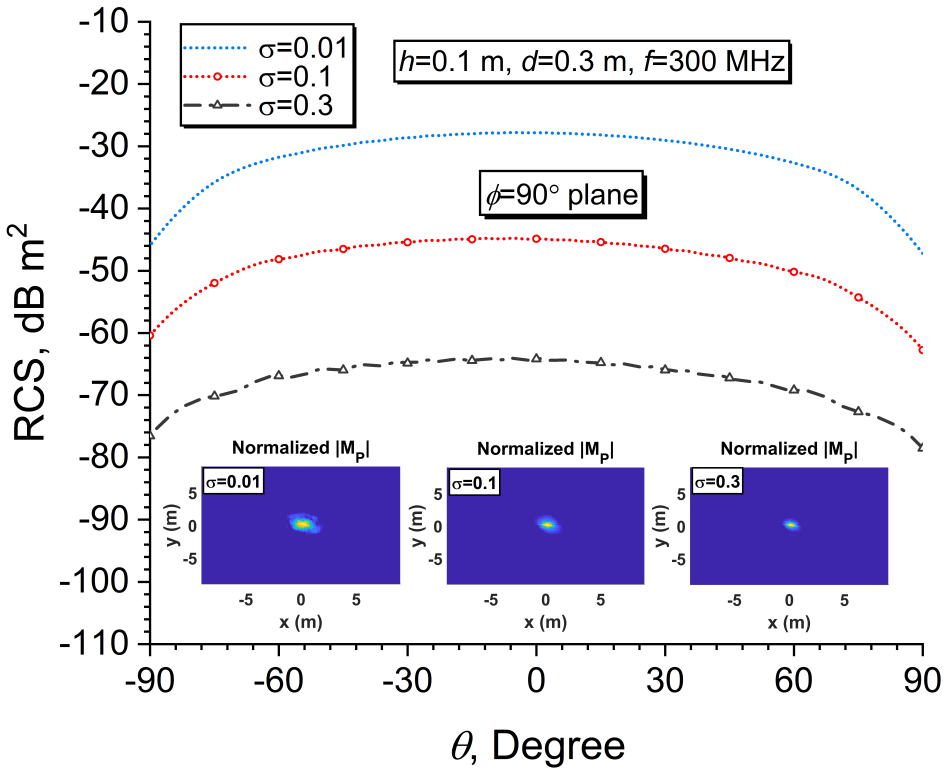

Figure 6.27 RCS results in the $\phi = 90°$ plane while increasing the conductivity of the dielectric medium

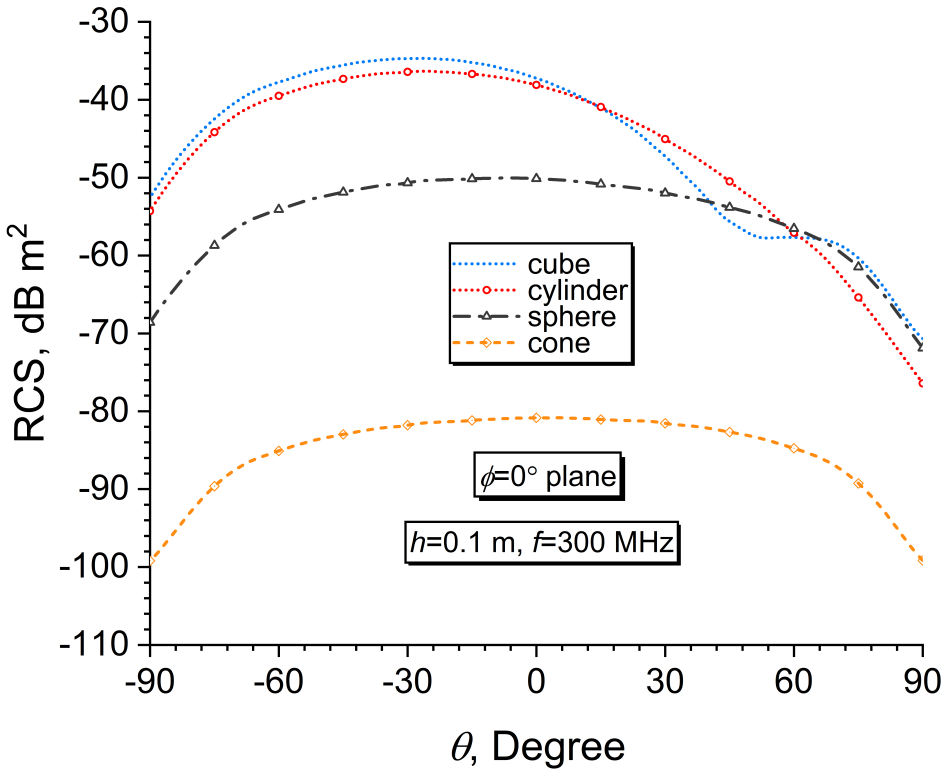

Figure 6.28 RCS results for different objects with approximately the same dimensions in the plane $\phi = 0°$

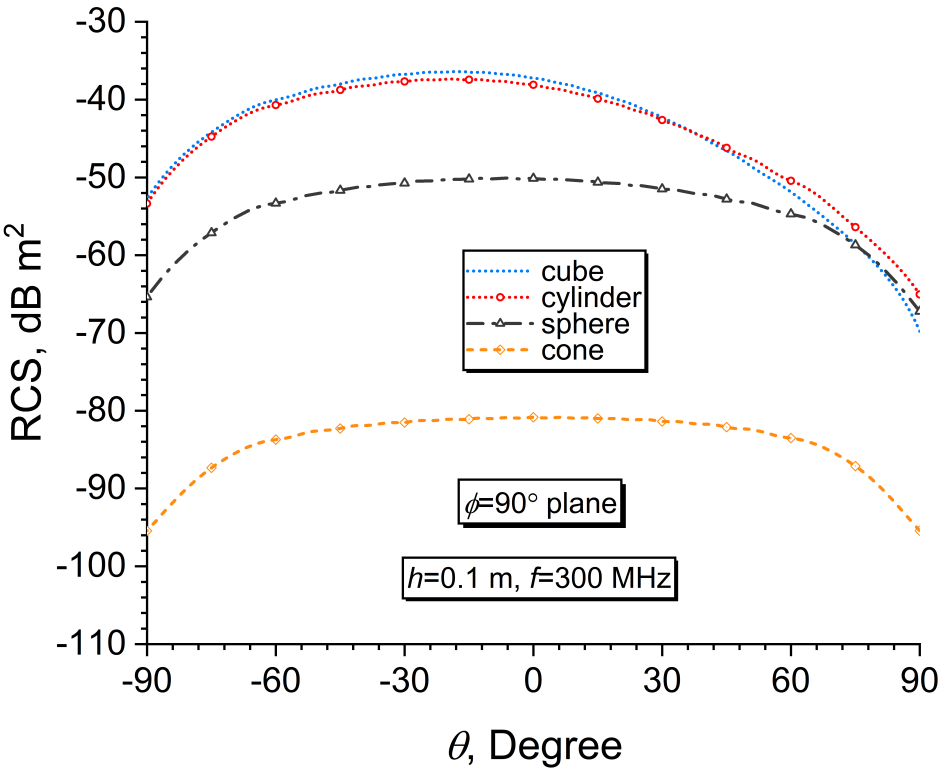

Figure 6.29 RCS results for different objects with approximately the same dimensions in the plane $\phi = 90°$

7
DISCUSSION AND FUTURE WORK

Since the interactions between the object and the surface will change the RCS of the object, this object cannot be truly recognized by a radar device. Examples of these objects are cruise missiles, helicopters flying near the surface, ships over the sea, or armed drones flying near the sea or ground surface. In addition, in GPR (Ground Penetrating Radar) applications for detecting buried objects, the targets usually interact strongly with the soil surface as well. In this thesis, the modifications in the RCS of the object due to the interactions from an infinite surface have been discussed by examining the surface currents in detail. Finally, a realistic approach to handling this critical issue has been presented.

A spatial domain solution method in which it was based on the decomposition of the surface current on an infinite ground plane has been introduced to handle any 3-D scattering problems caused by targets placed above or below several half-spaces. In this method, the surface current density on the interface is decomposed as induced current without the object and perturbed current caused by the object on a limited area of the infinite surface. This yields a solution without obtaining the GF of the problem or employing a tapered wave approach to eliminate edge effects. Although the method used is based on a simple logic based on modifying the SIE formulations, the problems that the proposed method can solve are pretty complex. Also, divergence conforming linear RWG basis function has been utilized, preventing the complexity of formulations in all scattering problems.

In this thesis, the rough half-space was chosen periodically, and the MoM could resolve an arbitrary roughness. When examining the examples in the literature, periodic selection of the rough surface is a critical approach to suppress unwanted edge currents. This thesis used this approach for the first time in the 3-D scattering problem. By periodic selection of the surface in two dimensions, the surface currents induced by the incident wave when the object is absent were found. Furthermore, by using these surface currents, the perturbed surface currents formed on the infinite surface, originating from an object placed on the infinite surface, could be separated.

The image theory, commercial EM solvers such as FEKO and CST, and the literature studies have been exploited for validation and comparison. Thus, the proposed approach and formulations accomplish noticeable accuracy while giving an effortless computation without deriving a half-space Green's function or utilizing a tapered wave illumination. Additionally, our method yields a significantly superior solution even when using a plane wave rather than a tapered wave approach for illumination at low-grazing angles.

On the other hand, considering future research, fast solution methods instead of MoM can be used to calculate perturbed current on the surface. In finding the perturbation current, high-impedance regions can be defined as the edges of the perturbation surface. Similarly, in rough surface problems, Monte Carlo simulations can be used to solve the surface roughness that should be randomly distributed. In addition, the minimum lengths at which the periodic surface must be increased to calculate the induced current on the surface accurately can be discussed for a given surface roughness.

Furthermore, it should also be noted that this method can be easily adapted and used for many radiation and scattering problems for the reasons mentioned above. This thesis's proposed formulations and method can be adapted to buried dielectric bodies, a rough dielectric interface, artificial surfaces, and objects buried under or between layered rough surfaces.

REFERENCES

[1] S. O. Rice, "Reflection of electromagnetic waves from slightly rough surfaces," *Communications on Pure and Applied Mathematics*, vol. 4, no. 2-3, pp. 351–378, 1951, ISSN: 10970312. DOI: 10.1002/cpa.3160040206.

[2] P. Spiga, G. Soriano, M. Saillard, "Scattering of electromagnetic waves from rough surfaces: A boundary integral method for low-grazing angles," *IEEE Transactions on Antennas and Propagation*, vol. 56, no. 7, pp. 2043–2050, 2008, ISSN: 0018926X. DOI: 10.1109/TAP.2008.924710.

[3] R. Chen, J. C. West, "Analysis of Scattering from Rough Surfaces at Large Incidence Angles Using a Periodic-Surface Moment Method," *IEEE Transactions on Geoscience and Remote Sensing*, vol. 33, no. 5, pp. 1206–1213, 1995, ISSN: 15580644. DOI: 10.1109/36.469484.

[4] J. DeSanto, G. Erdmann, W. Hereman, B. Krause, M. Misra, E. Swim, "Theoretical and computational aspects of scattering from periodic surfaces: Two-dimensional perfectly reflecting surfaces using the spectral-coordinate method," *Waves Random Media*, vol. 11, no. 4, pp. 455–487, 2001, ISSN: 09597174. DOI: 10.1088/0959-7174/11/4/306.

[5] S. Barzegar-Parizi, A. A. Shishegar, "Electromagnetic wave scattering analysis from 2-D periodic rough surfaces using complex images technique," *IEEE Transactions on Geoscience and Remote Sensing*, vol. 53, no. 2, pp. 862–868, 2015, ISSN: 01962892. DOI: 10.1109/TGRS.2014.2329995.

[6] S. Yildiz, Y. Altuncu, O. Ozdemir, "Scattering of Electromagnetic Waves by Periodic Rough Surfaces," *Ieee Transactions on Geoscience and Remote Sensing*, vol. 46, no. 9, pp. 2599–2606, 2008.

[7] M. A. Demir, "Perturbation theory of electromagnetic scattering from layered media with rough interfaces," Ph.D. dissertation, The Ohio State University, 2007.

[8] R. F. Millar, "On the Rayleigh assumption in scattering by a periodic surface. II," *Mathematical Proceedings of the Cambridge Philosophical Society*, vol. 69, no. 1, pp. 217–225, 1971, ISSN: 14698064. DOI: 10.1017/S0305004100046570.

[9] J. T. Johnson, "Third-order small-perturbation method for scattering from dielectric rough surfaces," *Journal of the Optical Society of America A*, vol. 16, no. 11, p. 2720, 1999, ISSN: 1084-7529. DOI: 10.1364/josaa.16.002720.

[10] M. A. Demir, J. T. Johnson, "Fourth and higher order small perturbation solution for scattering from dielectric rough surfaces," *IEEE Antennas and Propagation Society, AP-S International Symposium (Digest)*, vol. 3, pp. 412–415, 2003, ISSN: 02724693. DOI: 10.1364/josaa.20.002330.

[11] L. X. Guo, Y. Liang, J. Li, Z. S. Wu, "A high order integral SPM for the conducting rough surface scattering with the tapered wave incidence-Te case," *Progress in Electromagnetics Research*, vol. 114, pp. 333–352, 2011, ISSN: 15598985. DOI: 10.2528/PIER11011605.

[12] A. Ishimaru, "Periodic Structures and Coupled-Mode Theory," *Electromagnetic Wave Propagation, Radiation, and Scattering*, pp. 201–231, 2017. DOI: 10.1002/9781119079699.ch7.

[13] A. Norman, D. P. Nyquist, E. Rothwell, K. M. Chen, J. Ross, P. Ilavarasan, "Transient scattering of a short pulse from a conducting sinusoidal surface," *Journal of Electromagnetic Waves and Applications*, vol. 10, no. 4, pp. 461–487, 1996, ISSN: 15693937. DOI: 10.1163/156939396X01062.

[14] E. I. Thorsos, "The validity of the Kirchhoff approximation for rough surface scattering using a Gaussian roughness spectrum," *Journal of the Acoustical Society of America*, vol. 83, no. 1, pp. 78–92, 1988, ISSN: NA. DOI: 10.1121/1.396188.

[15] J. C. West, "On the Control of Edge Diffraction in Numerical Rough Surface Scattering Using Resistive Tapering," *IEEE Transactions on Antennas and Propagation*, vol. 51, no. 11, pp. 3180–3183, 2003, ISSN: 0018926X. DOI: 10.1109/TAP.2003.818775.

[16] A. J. Norman, "Transient scattering of electromagnetic waves in an ocean environment," Ph.D. dissertation, Michigan State University, 1996.

[17] A. Ishimaru, J. D. Rockway, Y. Kuga, "Rough surface Green's function based on the first-order modified perturbation and smoothed diagram methods," *Waves Random Media*, vol. 10, no. 1, pp. 17–31, 2000, ISSN: 13616676. DOI: 10.1088/0959-7174/10/1/302.

[18] Y. Altuncu, "A Numerical Method for Electromagnetic Scattering by 3-D Dielectric Objects Buried under 2-D Locally Rough Surfaces," *IEEE Transactions on Antennas and Propagation*, vol. 63, no. 8, pp. 3634–3643, 2015, ISSN: 0018926X. DOI: 10.1109/TAP.2015.2438859.

[19] B. Guan, J. F. Zhang, X. Y. Zhou, T. J. Cui, "Electromagnetic scattering from objects above a rough surface using the method of moments with half-space green's function," *IEEE Transactions on Geoscience and Remote Sensing*, vol. 47, no. 10, pp. 3399–3405, 2009, ISSN: 01962892. DOI: 10.1109/TGRS.2009.2022169.

[20] Y. Zhang, Y. E. Yang, H. Braunisch, J. A. Kong, "Electromagnetic Wave Interaction of Conducting Object with Rough Surface by Hybrid SPM/MOM Technique," *Progress In Electromagnetics Research*, vol. 22, pp. 315–335, 1999. DOI: 10.2528/pier98112506.

[21] X. M. Li, C. M. Tong, S. H. Fu, J. J. Li, "Bistatic electromagnetic scattering from a three-dimensional perfect electric conducting object above a Gaussian rough surface based on the Kirchhoff-Helmholtz and electric field integral equation," *Waves in Random and Complex Media*, vol. 21, no. 3, pp. 389–404, 2011, ISSN: 17455030. DOI: 10.1080/17455030.2011.571725.

[22] D. E. Lawrence, K. Sarabandi, "Electromagnetic scattering from a dielectric cylinder buried beneath a slightly rough surface," *IEEE Transactions on Antennas and Propagation*, vol. 50, no. 10, pp. 1368–1376, 2002, ISSN: 0018926X. DOI: 10.1109/TAP.2002.802160.

[23] H. Ye, Y. Q. Jin, "A hybrid analytic-numerical algorithm of scattering from an object above a rough surface," *IEEE Transactions on Geoscience and Remote Sensing*, vol. 45, no. 5, pp. 1174–1179, 2007, ISSN: 01962892. DOI: 10.1109/TGRS.2007.892609.

[24] H. Ye, Y. Q. Jin, "A hybrid KA-MoM algorithm for computation of scattering from a 3-D PEC target above a dielectric rough surface," *Radio Science*, vol. 43, no. 3, 2008, ISSN: 00486604. DOI: 10.1029/2007RS003702.

[25] X. Wang, C. F. Wang, Y. B. Gan, L. W. Li, "Electromagnetic scattering from a circular target above or below rough surface," *Progress in Electromagnetics Research*, vol. 40, pp. 207–227, 2003, ISSN: 10704698. DOI: 10.2528/PIER02111901.

[26] X. Wang, L. W. Li, "Numerical characterization of bistatic scattering from PEC cylinder partially embedded in a dielectric rough surface interface: Horizontal polarization," *Progress in Electromagnetics Research*, vol. 91, pp. 35–51, 2009, ISSN: 15598985. DOI: 10.2528/PIER09013001.

[27] X. Wang, Y. B. Gan, L. W. Li, "Electromagnetic scattering by partially buried PEC cylinder at the dielectric rough surface interface: TM case," *IEEE Antennas and Wireless Propagation Letters*, vol. 2, pp. 319–322, 2003, ISSN: 15361225. DOI: 10.1109/LAWP.2003.822200.

[28] L. X. Guo, A. Q. Wang, J. Ma, "Study on EM scattering from 2-D target above 1-D large scale rough surface with low grazing incidence by parallel MOM based on PC Clusters," *Progress in Electromagnetics Research*, vol. 89, pp. 149–166, 2009, ISSN: 15598985. DOI: 10.2528/PIER08121002.

[29] C. Bourlier, G. Kubické, N. Déchamps, "Fast method to compute scattering by a buried object under a randomly rough surface: PILE combined with FB-SA," *Journal of the Optical Society of America A*, vol. 25, no. 4, p. 891, 2008, ISSN: 1084-7529. DOI: 10.1364/josaa.25.000891.

[30] R. J. Burkholder, M. R. Pino, F. Obelleiro, "A Monte Carlo study of the rough-sea-surface influence on the radar scattering from two-dimensional ships," *IEEE Antennas and Propagation Magazine*, vol. 43, no. 2, pp. 25–33, 2001, ISSN: 10459243. DOI: 10.1109/74.924601.

[31] M. R. Pino, R. J. Burkholder, F. Obelleiro, "Spectral acceleration of the generalized forward-backward method," *IEEE Transactions on Antennas and Propagation*, vol. 50, no. 6, pp. 785–797, 2002, ISSN: 0018926X. DOI: 10.1109/TAP.2002.1017658.

[32] W. Luo, Z. Nie, Y. P. Chen, "Fast analysis of electromagnetic scattering from three-dimensional objects straddling the interface of a half space," *IEEE Geoscience and Remote Sensing Letters*, vol. 11, no. 7, pp. 1205–1209, 2014, ISSN: 1545598X. DOI: 10.1109/LGRS.2013.2289015.

[33] K. Zhao, M. N. Vouvakis, J. F. Lee, "The adaptive cross approximation algorithm for accelerated method of moments computations of EMC problems," *IEEE Transactions on Electromagnetic Compatibility*, vol. 47, no. 4, pp. 763–773, 2005, ISSN: 00189375. DOI: 10.1109/TEMC.2005.857898.

[34] C. Bourlier, "Scattering from Quasi-Planar and Moderate Rough Surfaces: Efficient Method to Fill the EFIE-Galerkin MoM Impedance Matrix and to Solve the Linear System," *IEEE Transactions on Antennas and Propagation*, vol. 69, no. 9, pp. 5761–5770, 2021, ISSN: 15582221. DOI: 10.1109/TAP.2021.3060920.

[35] C. Bourlier, "Low-grazing angle propagation and scattering by an object above a highly conducting rough sea surface in a ducting environment from an accelerated MoM," *Waves in Random and Complex Media*, vol. 28, no. 4, pp. 724–742, 2018, ISSN: 17455049. DOI: 10.1080/17455030.2017.1392647.

[36] N. Geng, A. Sullivan, L. Carin, "Multilevel fast-multipole algorithm for scattering from conducting targets above or embedded in a lossy half space," *IEEE Transactions on Geoscience and Remote Sensing*, vol. 38, no. 4 I, pp. 1561–1573, 2000, ISSN: 01962892. DOI: 10.1109/36.851956.

[37] R. W. Xu, L. X. Guo, H. J. He, W. Liu, "A Hybrid FEM/MoM Technique for 3-D Electromagnetic Scattering from a Dielectric Object above a Conductive Rough Surface," *IEEE Geoscience and Remote Sensing Letters*, vol. 13, no. 3, pp. 314–318, 2016, ISSN: 1545598X. DOI: 10.1109/LGRS.2015.2508500.

[38] G. Tian, C. Ming Tong, H. Liu, P. Peng, "An improved MoM-PO hybrid method for scattering from multiple 3-D objects above the 2-D random conducting rough surface," *Electromagnetics*, vol. 39, no. 5, pp. 375–392, 2019, ISSN: 1532527X. DOI: 10.1080/02726343.2019.1619231.

[39] J. Li, L. X. Guo, S. R. Chai, Y. C. Jiao, "Electromagnetic scattering from a PEC object above a dielectric rough sea surface by a hybrid PO-PO method," *Waves in Random and Complex Media*, vol. 25, no. 1, pp. 60–74, 2015, ISSN: 17455049. DOI: 10.1080/17455030.2014.961587.

[40] K. Li, L. Guo, J. Li, S. Chai, "A fast and efficient method for the composite scattering of a coated object above 3D random rough surfaces," *IEEE Access*, vol. 6, pp. 56 192–56 199, 2018, ISSN: 21693536. DOI: 10.1109/ACCESS.2018.2872791.

[41] C. Li, S. Y. He, G. Q. Zhu, Z. Zhang, F. S. Deng, B. X. Xiao, "A hybrid 3DMLUV-ACA method for scattering from a 3-D PEC object above a 2-D gaussian dielectric rough surface," *Applied Computational Electromagnetics Society Journal*, vol. 27, no. 12, pp. 956–963, 2012, ISSN: 10544887.

[42] J. Li, L. X. Guo, Q. He, "Hybrid FE-BI-KA method in analysing scattering from dielectric object above sea surface," *Electronics Letters*, vol. 47, no. 20, pp. 1147–1148, 2011, ISSN: 00135194. DOI: 10.1049/el.2011.1444.

[43] S. Bellez, C. Bourlier, G. Kubicke, "3-D Scattering from a PEC Target Buried Beneath a Dielectric Rough Surface: An Efficient PILE-ACA Algorithm for Solving a Hybrid KA-EFIE Formulation," *IEEE Transactions on Antennas and Propagation*, vol. 63, no. 11, pp. 5003–5014, 2015, ISSN: 0018926X. DOI: 10.1109/TAP.2015.2480123.

[44] J. Chen, M. Zhu, M. Wang, S. Li, X. Li, "A hybrid MoM-PO method combining ACA technique for electromagnetic scattering from target above a rough surface," *Applied Computational Electromagnetics Society Journal*, vol. 29, no. 4, pp. 301–306, 2014, ISSN: 10544887.

[45] J. W. Hao, X. Q. Sheng, "Accurate and Efficient Simulation Model for the Scattering from a Ship on a Sea-Like Surface," *IEEE Geoscience and Remote Sensing Letters*, vol. 14, no. 12, pp. 2375–2379, 2017, ISSN: 1545598X. DOI: 10.1109/LGRS.2017.2765342.

[46] Y. W. Wei, C. F. Wang, C. Y. Kee, T. T. Chia, "An Accurate Model for the Efficient Simulation of Electromagnetic Scattering from an Object above a Rough Surface with Infinite Extent," *IEEE Transactions on Antennas and Propagation*, vol. 69, no. 2, pp. 1040–1051, 2021, ISSN: 15582221. DOI: 10.1109/TAP.2020.3019338.

[47] S. M. Rao, C. C. Cha, D. L. Wilkes, R. L. Cravey, "Electromagnetic Scattering from Arbitrary Shaped Conducting Bodies Coated with Lossy Materials of Arbitrary Thickness," *IEEE Transactions on Antennas and Propagation*, vol. 39, no. 5, pp. 627–631, 1991, ISSN: 15582221. DOI: 10.1109/8.81490.

[48] H. T. Chen, G. Q. Zhu, "Model the electromagnetic scattering from three-dimensional PEC object buried under rough ground by MoM and modified PO hybrid method," *Progress in Electromagnetics Research*, vol. 77, pp. 15–27, 2007, ISSN: 15598985. DOI: 10.2528/PIER07072202.

[49] H. Bağci, A. E. Yilmaz, V. Lomakin, E. Michielssen, "Fast solution of mixed-potential time-domain integral equations for half-space environments," *IEEE Transactions on Geoscience and Remote Sensing*, vol. 43, no. 2, pp. 269–279, 2005, ISSN: 01962892. DOI: 10.1109/TGRS.2004.841489.

[50] M. Lucido, "Electromagnetic scattering by a perfectly conducting rectangular plate buried in a lossy half-space," *IEEE Transactions on Geoscience and Remote Sensing*, vol. 52, no. 10, pp. 6368–6378, 2014, ISSN: 01962892. DOI: 10.1109/TGRS.2013.2296353.

[51] B. Esen, I. Akkaya, A. Yapar, "Scattering of a plane wave from a perfectly conducting sphere buried in a conducting dielectric," *Electromagnetics*, vol. 24, no. 8, pp. 607–621, 2004, ISSN: 02726343. DOI: 10.1080/02726340490513338.

[52] T. Jun Cui, W. Cho Chew, "Fast Evaluation of Sommerfeld Integrals for EM Scattering and Radiation by Three-Dimensional Buried Objects," *Ieee Transactions on Geoscience and Remote Sensing*, vol. 37, no. 2, 1999.

[53] F. Frezza, F. Mangini, L. Pajewski, G. Schettini, N. Tedeschi, "Spectral domain method for the electromagnetic scattering by a buried sphere," *Journal of the Optical Society of America A*, vol. 30, no. 4, p. 783, 2013, ISSN: 1084-7529. DOI: 10.1364/josaa.30.000783.

[54] G. Videen, "Light scattering from a sphere behind a surface," *Journal of the Optical Society of America A*, vol. 10, no. 1, p. 110, 1993, ISSN: 1084-7529. DOI: 10.1364/josaa.10.000110.

[55] C. Ozzaim, "Plane Wave Scattering by a Conducting Cylinder Located Near an Interface between Two Dielectric Half-Spaces: A Perturbation Method," *IEEE Transactions on Antennas and Propagation*, vol. 65, no. 5, pp. 2754–2758, 2017, ISSN: 0018926X. DOI: 10.1109/TAP.2017.2669720.

[56] D. Wang, E. K. Yung, R. S. Chen, D. Z. Ding, W. C. Tang, "On evaluation of the green function for periodic structures in layered media," *IEEE Antennas and Wireless Propagation Letters*, vol. 3, no. 1, pp. 133–136, 2004, ISSN: 15361225. DOI: 10.1109/LAWP.2004.831076.

[57] F. Capolino, D. R. Wilton, W. A. Johnson, "Efficient computation of the 2-D Green's function for 1-D periodic structures using the Ewald method," *IEEE Transactions on Antennas and Propagation*, vol. 53, no. 9, pp. 2977–2984, 2005, ISSN: 0018926X. DOI: 10.1109/TAP.2005.854556.

[58] M. J. Park, B. Lee, "Efficient calculation of the Green's function for 2-D periodic line sources using Ewald method," *IEEE Antennas and Wireless Propagation Letters*, vol. 8, pp. 565–567, 2009, ISSN: 15361225. DOI: 10.1109/LAWP.2009.2022652.

[59] R. Lampe, P. Klock, P. Mayes, "Integral Transforms Useful for the Accelerated Summation of Periodic, Free-Space Green's Functions," *IEEE Transactions on Microwave Theory and Techniques*, vol. 33, no. 8, pp. 734–736, 1985, ISSN: 15579670. DOI: 10.1109/TMTT.1985.1133067.

[60] S. Singh, W. F. Richards, J. R. Zinecker, D. R. Wilton, "Communications: Accelerating the Convergence of Series Representing the Free Space Periodic Green's Function," *IEEE Transactions on Antennas and Propagation*, vol. 38, no. 12, pp. 1958–1962, 1990, ISSN: 15582221. DOI: 10.1109/8.60985.

[61] G. Valerio, P. Baccarelli, P. Burghignoli, A. Galli, "Comparative analysis of acceleration techniques for 2-D and 3-D Green's functions in periodic structures along one and two directions," *IEEE Transactions on Antennas and Propagation*, vol. 55, no. 6 I, pp. 1630–1643, 2007, ISSN: 0018926X. DOI: 10.1109/TAP.2007.897340.

[62] K. E. Jordan, G. R. Richter, P. Sheng, "An efficient numerical evaluation of the Green's function for the Helmholtz operator on periodic structures," *Journal of Computational Physics*, vol. 63, no. 1, pp. 222–235, 1986, ISSN: 10902716. DOI: 10.1016/0021-9991(86)90093-8.

[63] I. Stevanović, P. Crespo-Valero, K. Blagović, F. Bongard, J. R. Mosig, "Integral-equation analysis of 3-D metallic objects arranged in 2-D lattices using the ewald transformation," *IEEE Transactions on Microwave Theory and Techniques*, vol. 54, no. 10, pp. 3688–3697, 2006, ISSN: 00189480. DOI: 10.1109/TMTT.2006.882876.

[64] P. S. Simon, "Modified RWG basis functions for analysis of periodic structures," *IEEE MTT-S International Microwave Symposium Digest*, vol. 3, pp. 2029–2032, 2002, ISSN: 0149645X. DOI: 10.1109/mwsym.2002.1012266.

[65] F. G. Hu, J. Song, "Integral-equation analysis of scattering from doubly periodic array of 3-D conducting objects," *IEEE Transactions on Antennas and Propagation*, vol. 59, no. 12, pp. 4569–4578, 2011, ISSN: 0018926X. DOI: 10.1109/TAP.2011.2165466.

[66] A. Kizilay, E. J. Rothwell, "Efficient computation of transient TM scattering from a cylinder above an infinite periodic surface," *Journal of Electromagnetic Waves and Applications*, vol. 13, no. 7, pp. 943–961, 1999, ISSN: 15693937. DOI: 10.1163/156939399X00420.

[67] A. Kizilay, E. J. Rothwell, "Transient TE scattering from a cylinder above an infinite periodic surface using a decomposition method," *Journal of Electromagnetic Waves and Applications*, vol. 15, no. 3, pp. 293–314, 2001, ISSN: 15693937. DOI: 10.1163/156939301X00472.

[68] A. Kizilay, "A perturbation method for transient multipath analysis of electromagnetic scattering from targets above periodic surfaces," Ph.D. dissertation, Michigan State University, 2000.

[69] S. Makal, A. Kizilay, "A decomposition method for the electromagnetic scattering from a conductive object buried in a lossy medium," *Applied Computational Electromagnetics Society Journal*, vol. 26, no. 4, pp. 340–347, 2011, ISSN: 10544887.

[70] S. Makal Yucedag, "Computation of electromagnetic fields scattered by cylindrical targets buried in a medium with a periodic surface," Ph.D. dissertation, Yildiz Technical University, 2012.

[71] S. Makal, A. Kizilay, "Computation of the scattered fields from a dielectric object buried in a medium with a periodic surface by a decomposition method," *IET Microwaves, Antennas and Propagation*, vol. 5, no. 14, pp. 1703–1709, 2011, ISSN: 17518725. DOI: 10.1049/iet-map.2011.0137.

[72] U. Saynak, A. Kizilay, "Computation of the scattered fields from an overfilled cavity embedded in a perfectly conducting ground plane," *Journal of Electromagnetic Waves and Applications*, vol. 30, no. 9, pp. 1217–1226, 2016, ISSN: 15693937. DOI: 10.1080/09205071.2016.1191379.

[73] U. Saynak, A. Kizilay, "Scattering from a dielectric cylinder partially buried in a dielectric half space with a periodic height profile by a decomposition method," *Journal of Electromagnetic Waves and Applications*, vol. 33, no. 8, pp. 1014–1026, 2019, ISSN: 15693937. DOI: 10.1080/09205071.2019.1584589.

[74] U. Saynak, "Scattering from partially buried objects," Ph.D. dissertation, Yildiz Technical University, 2016.

[75] F. G. Hu, J. Song, "Integral-equation analysis of scattering from doubly periodic array of 3-D conducting objects," *IEEE Transactions on Antennas and Propagation*, vol. 59, no. 12, pp. 4569–4578, 2011, ISSN: 0018926X. DOI: 10.1109/TAP.2011.2165466.

[76] R. F. Millar, "The Rayleigh hypothesis and a related least-squares solution to scattering problems for periodic surfaces and other scatterers," *Radio Science*, vol. 8, no. 8-9, pp. 785–796, Aug. 1973, ISSN: 00486604. DOI: 10.1029/RS008i008p00785. [Online]. Available: http://doi.wiley.com/10.1029/RS008i008p00785.

[77] S. Rao, D. Wilton, A. Glisson, "Electromagnetic scattering by surfaces of arbitrary shape," *IEEE Transactions on Antennas and Propagation*, vol. 30, no. 3, pp. 409–418, May 1982, ISSN: 0096-1973. DOI: 10.1109/TAP.1982.1142818. [Online]. Available: http://ieeexplore.ieee.org/document/1142818/.

[78] W. C. Gibson, *The method of moments in electromagnetics*. 2007, pp. 1–273, ISBN: 9781420061468. DOI: 10.1201/b17119.

[79] D. A. Dunavant, "High degree efficient symmetrical Gaussian quadrature rules for the triangle," *International Journal for Numerical Methods in Engineering*, vol. 21, no. 6, pp. 1129–1148, Jun. 1985, ISSN: 0029-5981. DOI: 10.1002/nme.1620210612. [Online]. Available: https://onlinelibrary.wiley.com/doi/10.1002/nme.1620210612.

[80] J. L. Volakis, K. Sertel, *Integral equation methods for electromagnetics*. 2012, pp. 1–392, ISBN: 9781613531129. DOI: 10.1049/SBEW045E.

[81] R. Graglia, "On the numerical integration of the linear shape functions times the 3-D Green's function or its gradient on a plane triangle," *IEEE Transactions on Antennas and Propagation*, vol. 41, no. 10, pp. 1448–1455, 1993, ISSN: 0018926X. DOI: 10.1109/8.247786. [Online]. Available: http://ieeexplore.ieee.org/document/247786/.

[82] M. G. Duffy, "Quadrature Over a Pyramid or Cube of Integrands with a Singularity at a Vertex," *SIAM Journal on Numerical Analysis*, vol. 19, no. 6, pp. 1260–1262, Dec. 1982, ISSN: 0036-1429. DOI: 10.1137/0719090. [Online]. Available: http://epubs.siam.org/doi/10.1137/0719090.

[83] D. Wilton, S. Rao, A. Glisson, D. Schaubert, O. Al-Bundak, C. Butler, "Potential integrals for uniform and linear source distributions on polygonal and polyhedral domains," *IEEE Transactions on Antennas and Propagation*, vol. 32, no. 3, pp. 276–281, Mar. 1984, ISSN: 0096-1973. DOI: 10.1109/TAP.1984.1143304. [Online]. Available: http://ieeexplore.ieee.org/document/1143304/.

[84] T. Eibert, V. Hansen, "On the calculation of potential integrals for linear source distributions on triangular domains," *IEEE Transactions on Antennas and Propagation*, vol. 43, no. 12, pp. 1499–1502, 1995, ISSN: 0018926X. DOI: 10.1109/8.475946. [Online]. Available: http://ieeexplore.ieee.org/document/475946/.

[85] I. Stevanoviæ, J. R. Mosig, "Periodic Green's function for skewed 3-D lattices using the Ewald transformation," *Microwave and Optical Technology Letters*, vol. 49, no. 6, pp. 1353–1357, Jun. 2007, ISSN: 08952477. DOI: 10.1002/mop.22429. [Online]. Available: https://onlinelibrary.wiley.com/doi/10.1002/mop.22429.

[86] M. Khayat, D. Wilton, "Numerical evaluation of singular and near-singular potential Integrals," *IEEE Transactions on Antennas and Propagation*, vol. 53, no. 10, pp. 3180–3190, Oct. 2005, ISSN: 0018-926X. DOI: 10.1109/TAP.2005.856342. [Online]. Available: http://ieeexplore.ieee.org/document/1514571/.

[87] S. Adanir, L. Alatan, "Singularity Cancellation for Accurate MoM Analysis of Periodic Planar Structures in Layered Media," *IEEE Antennas and Wireless Propagation Letters*, vol. 19, no. 8, pp. 1301–1305, Aug. 2020, ISSN: 1536-1225. DOI: 10.1109/LAWP.2020.2997798. [Online]. Available: https://ieeexplore.ieee.org/document/9099907/.

[88] J. Van Tonder, U. Jakobus, "Infinite periodic boundary conditions in FEKO," *Applied Computational Electromagnetics Society Journal*, vol. 24, no. 6, pp. 584–591, 2009, ISSN: 10544887.

[89] C.-T. Tai, "Dyadic Green functions in electromagnetic theory," *IEEE Press*, 1994. [Online]. Available: http://www.getcited.org/pub/103091504.

A
DERIVATION OF FREE-SPACE GREEN'S FUNCTION FOR 2-D PERIODIC STRUCTURES

For a 2-D periodic source, the general form of the wave equation will be as follows

$$(\nabla^2 + k^2)\varphi(x,y,z) = -f(x',y',z') \tag{A.1}$$

Here, $\varphi(x,y,z)$ and $f(x',y',z')$ are both periodic in x and y directions. Also, L_x and L_y are the periodicities, and β_x and β_y are phases constant in free space for these directions, respectively.

If we utilize Floquet-Bloch's theorem, these periodic functions must satisfy these

$$\frac{\varphi(x+mL_x,y,z)}{\varphi(x+(m-1)L_x,y,z)} = \frac{f(x'+mL_x,y',z')}{f(x'+(m-1)L_x,y',z')} = e^{-j\beta_x L_x} = const \tag{A.2}$$

$$\frac{\varphi(x,y+nL_y,z)}{\varphi(x,y+(n-1)L_y,z)} = \frac{f(x',y'+nL_y,z')}{f(x'+,y'+(n-1)L_y,z')} = e^{-j\beta_y L_y} = const \tag{A.3}$$

then,

$$\frac{\varphi(x+mL_x,y+nL_y,z)}{\varphi(x+(m-1)L_x,y+(n-1)L_y,z)} = e^{-j(\beta_x L_x)}e^{-j(\beta_y L_y)} \tag{A.4}$$

therefore, for any m^{th} and n^{th} cell

$$\varphi(x+mL_x,y+nL_y) = e^{-j(\beta_x mL_X+\beta_y nL_y)}\varphi(x,y) \tag{A.5}$$

$$f(x'+mL_x,y'+nL_y) = e^{-j(\beta_x mL_X+\beta_y nL_y)}f(x',y') \tag{A.6}$$

and, if we can write a periodic function to satisfy that

$$W(x,y) = e^{j(\beta_x x+\beta_y y)}\varphi(x,y) \tag{A.7}$$

where, the function $W(x,y)$ is again periodic with L_x and L_y

$$\begin{aligned} W(x+L_x, y+L_y) &= e^{j[\beta_x(x+L_x)+\beta_y(y+L_y)]}\varphi(x+L_x, y+L_y) \\ &= e^{j(\beta_x x+\beta_y y)}e^{j(\beta_x L_x+\beta_y L_y)}e^{-j(\beta_x L_x+\beta_y L_y)}\varphi(x,y) \\ &= W(x,y) \end{aligned} \tag{A.8}$$

As a result, $\varphi(x,y)$ can be stated as follows

$$\varphi(x,y) = e^{-j(\beta_x x+\beta_y y)}W(x,y) \tag{A.9}$$

Here, $W(x,y)$ can be expanded in a Fourier series

$$W(x,y) = \sum_{m=-\infty}^{+\infty}\sum_{n=-\infty}^{+\infty} A_{mn}e^{-j2m\pi\frac{x}{L_x}}e^{-j2n\pi\frac{y}{L_y}} \tag{A.10}$$

and the coefficients A_{mn}

$$A_{mn} = \frac{1}{L_x L_y}\int_0^{L_x}\int_0^{L_y} W(x,y)e^{j2m\pi\frac{x}{L_x}}e^{j2n\pi\frac{y}{L_y}}dxdy \tag{A.11}$$

Consequently, employing (A.9) in (A.11)

$$\begin{aligned} \varphi(x,y) &= \sum_{m=-\infty}^{+\infty}\sum_{n=-\infty}^{+\infty} A_{mn}e^{-j(\beta_x+2m\pi\frac{x}{L_x})}e^{-j(\beta_y+2n\pi\frac{y}{L_y})} \\ &= \sum_{m=-\infty}^{+\infty}\sum_{n=-\infty}^{+\infty} A_{mn}e^{-j\beta_m x}e^{-j\beta_n y} \end{aligned} \tag{A.12}$$

This is the Floquet-mode representation of the wave function $\varphi(x,y)$, where A_{mn} are the Floquet-mode amplitudes, and the phase terms

$$\beta_m = \beta_x + \frac{2m\pi}{L_x} \tag{A.13}$$

$$\beta_n = \beta_y + \frac{2n\pi}{L_y} \tag{A.14}$$

is defined. If a scattering problem having periodic impulse point sources, as given in Figure A.1 is considered, the wave equation is

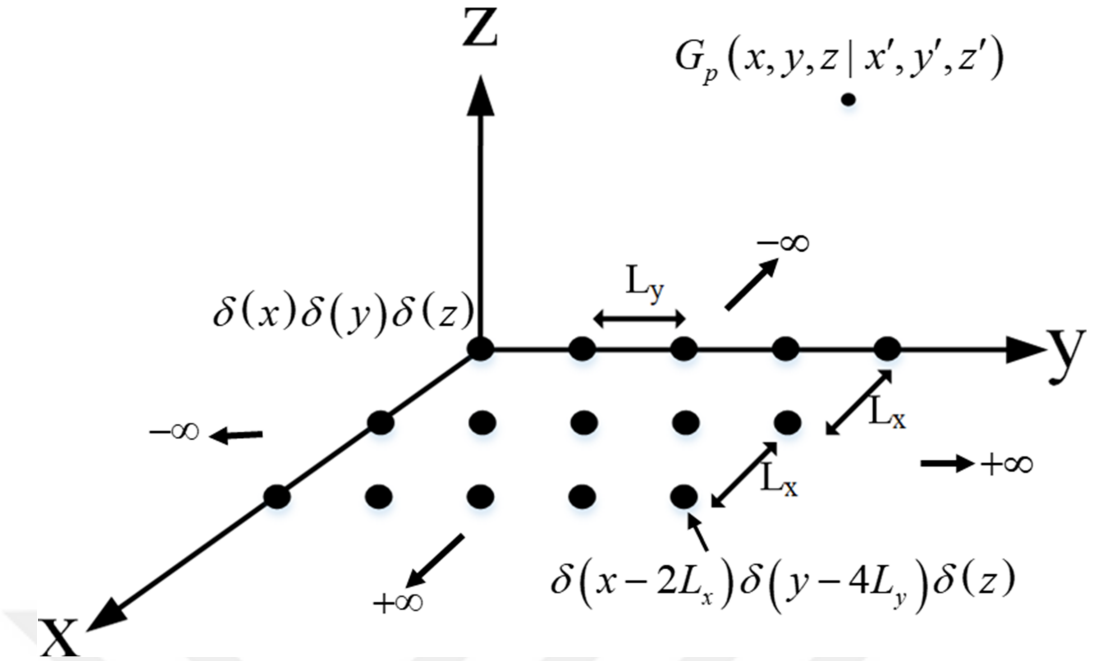

Figure A.1 Lattice representation of 2-D periodic impulse point sources

$$(\nabla^2 + k^2)G_p(x,y,z\,|\,x',y',z') = -\tilde{f}(x,y,z\,|\,x',y',z') \tag{A.15}$$

where

$$\tilde{f}(x,y,z\,|\,x',y',z') = \sum_{m=-\infty}^{+\infty}\sum_{n=-\infty}^{+\infty} e^{-j\beta_x mL_x}e^{-j\beta_y nL_y}\delta[x-(x'+mL_x)] \\ \delta[y-(y'+nL_y)]\delta(z-z') \tag{A.16}$$

is the periodic impulse point sources, and G_p must be the same as in (A.12)

$$G_p(x+mL_x, y+nL_y) = e^{-j\beta_x mL_x}e^{-j\beta_y nL_y}G_p(x,y) \tag{A.17}$$

Also, it can be stated by exploiting Floquet's theorem as follows

$$G_p(x,y,z\,|\,x',y',z') = \sum_{m=-\infty}^{+\infty}\sum_{n=-\infty}^{+\infty} g_{mn}(x',y',z\,|\,z')e^{-j\beta_m x}e^{-j\beta_n y} \tag{A.18}$$

Here, g_{mn} is the coefficients of the Floquet-mode amplitudes in obtaining the transfer function G_p, and it is sufficient to find the coefficients within the first period ($m = n = 0$, $0 \le x \le L_x$, $0 \le y \le L_y$). Therefore, G_p satisfy

$$(\nabla^2 + k^2)G_p(x,y,z \mid x',y',z') = -\delta(x-x')\delta(y-y')\delta(z-z') \tag{A.19}$$

then

$$\left(\frac{\partial^2}{\partial x^2} + \frac{\partial^2}{\partial y^2} + \frac{\partial^2}{\partial z^2} + k^2\right) \sum_{m=-\infty}^{+\infty} \sum_{n=-\infty}^{+\infty} g_{mn}(x',y',z \mid z') e^{-j\beta_m x} e^{-j\beta_n y} = -\delta(x-x')\delta(y-y')\delta(z-z') \tag{A.20}$$

as well as taking the partial derivatives for x and y

$$\sum_{m=-\infty}^{+\infty} \sum_{n=-\infty}^{+\infty} \left[\frac{\partial^2}{\partial z^2} + \left(k^2 - \beta_m^2 - \beta_n^2\right)\right] g_{mn}(x',y',z \mid z') e^{-j\beta_m x} e^{-j\beta_n y} = -\delta(x-x')\delta(y-y')\delta(z-z') \tag{A.21}$$

To put it more succinctly, h_{mn} can be defined by

$$h_{mn}(x',y',z \mid z') = g_{mn}(x',y',z \mid z')\left[\frac{\partial^2}{\partial z^2} + q_{mn}^2\right] \tag{A.22}$$

with the wavenumber q_{mn}

$$q_{mn}^2 = k^2 - \beta_m^2 - \beta_n^2 \tag{A.23}$$

Consequently, if we substitute it in (A.21)

$$\sum_{m=-\infty}^{+\infty} \sum_{n=-\infty}^{+\infty} h_{mn}(x',y',z \mid z') e^{-j\beta_m x} e^{-j\beta_n y} = -\delta(x-x')\delta(y-y')\delta(z-z') \tag{A.24}$$

is obtained. At this point, we utilize the orthogonality property of the Floquet modes

$$\int_0^{L_x} e^{-j\beta_m x} e^{-j\beta_k x} = \begin{cases} 0 & \cdots \quad \text{for } m \neq k \\ L_x & \cdots \quad \text{for } m = k \end{cases} = L_x \delta_{mk} \tag{A.25}$$

and

$$\int_0^{L_y} e^{-j\beta_n y} e^{-j\beta_l y} = \begin{cases} 0 & \cdots \quad \text{for } n \neq l \\ L_y & \cdots \quad \text{for } n = l \end{cases} \\ = L_y \delta_{nl} \tag{A.26}$$

Substituting these

$$\sum_{m=-\infty}^{+\infty} \sum_{n=-\infty}^{+\infty} h_{mn} L_x \delta_{mk} L_y \delta_{nl} = -\delta(z-z') \int_0^{L_x} \delta(x-x') e^{j\beta_k x} dx \int_0^{L_y} \delta(y-y') e^{j\beta_l y} dy \tag{A.27}$$

yields

$$h_{mn} = -\delta(z-z') \frac{e^{j\beta_m x'}}{L_x} \frac{e^{j\beta_n y'}}{L_y} \tag{A.28}$$

and, thus

$$\left[\frac{\partial^2}{\partial z^2} + q_{mn}^2 \right] g_{mn}(x', y', z \mid z') = -\delta(z-z') \frac{e^{j\beta_m x'}}{L_x} \frac{e^{j\beta_n y'}}{L_y} \tag{A.29}$$

is found. To solve this, the spectral form of g_{mn} can be exploited. Let

$$\tilde{g}_{mn}(x', y', s \mid z') = \int_{-\infty}^{+\infty} g_{mn}(x', y', z \mid z') e^{-jsz} dz \tag{A.30}$$

$$g_{mn}(x', y', z \mid z') = \frac{1}{2\pi} \int_{-\infty}^{+\infty} \tilde{g}_{mn}(x', y', s \mid z') e^{jsz} ds \tag{A.31}$$

i.e, $\mathscr{F}\{g_{mn}(x', y', z \mid z')\} = \tilde{g}_{mn}(x', y', s \mid z')$. Here, $\mathscr{F}$ implies Fourier transform, and using in (A.29) leads to

$$-(s^2-q_{mn}^2)\tilde{g}_{mn}=-e^{-jsz'}\frac{e^{j\beta_m x'}}{L_x}\frac{e^{j\beta_n y'}}{L_y} \tag{A.32}$$

$$\tilde{g}_{mn}=\frac{e^{-jsz'}}{(s^2-q_{mn}^2)}\frac{e^{j\beta_m x'}}{L_x}\frac{e^{j\beta_n y'}}{L_y} \tag{A.33}$$

Then, employing inverse transform $\mathscr{F}^{-1}\{g_{mn}(x',y',s\,|\,z')\}$ to solve $g_{mn}(x',y',z\,|\,z')$

$$g_{mn}(x',y',z\,|\,z')=\frac{e^{j\beta_m x'}e^{j\beta_n y'}}{L_x L_y}\frac{1}{2\pi}\int_{-\infty}^{+\infty}\frac{e^{js(z-z')}}{(s-q_{mn})(s+q_{mn})}ds \tag{A.34}$$

If we decompose the poles

$$e^{js(z-z')}=e^{-s_i(z-z')}+e^{js_r(z-z')} \tag{A.35}$$

As seen from (A.35), the poles in real axis is non-convergent. To insure the convergence of the poles, these two case must be provided:

Case #1: $z>z'\rightarrow s_i>0$

Let

$$s=\epsilon e^{j\psi}-q_{mn} \tag{A.36}$$

$$ds=j\epsilon e^{j\psi}d\psi \tag{A.37}$$

Here, q_{mn} as in (2.15), which is defined in the lower half space. For upper half clossure, Cauchy's thereom yields

$$q_{mn}(x',y',z\,|\,z')=\frac{e^{j\beta_m x'}e^{j\beta_n y'}}{2\pi L_x L_y}\int_{C_R^+}\frac{e^{js(z-z')}}{(s-q_{mn})(s+q_{mn})}ds \tag{A.38}$$

where C_R^+ is the infinitesimal integral circle. Therefore, this gives

$$
\begin{aligned}
F(z-z') &= \int_{C_R^+} \frac{e^{js(z-z')}}{(s-q_{mn})(s+q_{mn})} ds \\
&= \lim_{\epsilon\to 0} \int_{-\pi}^{+\pi} \frac{e^{j\epsilon(z-z')e^{j\psi}} e^{-jq_{mn}(z-z')}}{(\epsilon e^{j\psi}-2q_{mn})(\epsilon e^{j\psi})} j\epsilon e^{j\psi} d\psi = \frac{je^{-jq_{mn}(z-z')}}{-2q_{mn}} \int_{-\pi}^{+\pi} d\psi \\
&= -j2\pi \left(\frac{e^{-jq_{mn}(z-z')}}{2q_{mn}} \right)
\end{aligned}
\tag{A.39}
$$

substituting (A.39) in (A.38)

$$
g_{mn}(x', y', z \mid z') = -j \frac{e^{j\beta_m x'} e^{j\beta_n y'}}{2L_x L_y q_{mn}} e^{-jq_{mn}(z-z')} \tag{A.40}
$$

Case #2: $z < z' \rightarrow s_i < 0$

Similarly, let

$$
s = \epsilon e^{j\psi} + q_{mn} \tag{A.41}
$$

$$
ds = j\epsilon e^{j\psi} d\psi \tag{A.42}
$$

Using Cauchy's thereom in the lower half clossure for C_R^- the infinitesimal integral circle yields

$$
g_{mn}(x', y', z \mid z') = -j \frac{e^{j\beta_m x'} e^{j\beta_n y'}}{2L_x L_y q_{mn}} e^{-jq_{mn}(z'-z)} \tag{A.43}
$$

Consequently, a general expression can be formulated as

$$
g_{mn}(x', y', z \mid z') = -j \frac{e^{j\beta_m x'} e^{j\beta_n y'}}{2L_x L_y q_{mn}} e^{-jq_{mn}|z'-z|} \tag{A.44}
$$

and, the FS-PGF is finally derived as follows

$$
\begin{aligned}
G(x, y, z \mid x', y', z') &= \sum_{m=-\infty}^{+\infty} \sum_{n=-\infty}^{+\infty} g_{mn}(x', y', z \mid z') e^{-j\beta_m x} e^{-j\beta_n y} \\
&= \frac{-j}{2L_x L_y} \sum_{m=-\infty}^{+\infty} \sum_{n=-\infty}^{+\infty} \frac{e^{-j\beta_m (x-x')} e^{-j\beta_n (y-y')} e^{-jq_{mn}|z-z'|}}{q_{mn}}
\end{aligned}
\tag{A.45}
$$

B
DERIVATION OF IMAGE METHOD FORMULATIONS

In the filling the $\overline{\overline{Z}}$ matrix

$$Z_{\zeta\psi} = j\beta_0\eta_0 \left[\int_{T_\zeta^\pm} \vec{\mathbf{f}}_\zeta(\vec{\mathbf{r}}) \cdot \int_{T_\psi^\pm} \overline{\overline{\mathbf{G}}}_e \cdot \vec{\mathbf{f}}_\psi(\vec{\mathbf{r}}') dS'_{T_\psi^\pm} dS_{T_\zeta^\pm} \right] \tag{B.1}$$

and

$$Z_{\zeta\psi} = j\beta_0\eta_0 \left[\int_{T_\zeta^\pm} \vec{\mathbf{f}}_\zeta(\vec{\mathbf{r}}) \cdot \int_{T_\psi^\pm} \left\{ \left(\bar{\bar{\mathbf{I}}} - \frac{1}{\beta_0^2} \nabla\nabla' \right) \left[G_0(\vec{\mathbf{r}}|\vec{\mathbf{r}}') - G_0(\vec{\mathbf{r}}|\vec{\mathbf{r}}'_i) \right] + 2\hat{\mathbf{z}}\hat{\mathbf{z}} G_0(\vec{\mathbf{r}}|\vec{\mathbf{r}}'_i) \right\} \cdot \vec{\mathbf{f}}_\psi(\vec{\mathbf{r}}') dS'_{T_\psi^\pm} dS_{T_\zeta^\pm} \right] \tag{B.2}$$

finally

$$\begin{aligned} Z_{\zeta\psi} = & j\beta_0\eta_0 \left[\int_{T_\zeta^\pm} \vec{\mathbf{f}}_\zeta(\vec{\mathbf{r}}) \cdot \int_{T_\psi^\pm} \vec{\mathbf{f}}_\psi(\vec{\mathbf{r}}') \left[G_0(\vec{\mathbf{r}}|\vec{\mathbf{r}}') - G_0(\vec{\mathbf{r}}|\vec{\mathbf{r}}'_i) \right] dS'_{T_\psi^\pm} dS_{T_\zeta^\pm} \right. \\ & - \frac{1}{\beta_0^2} \int_{T_\zeta^\pm} \vec{\mathbf{f}}_\zeta(\vec{\mathbf{r}}) \cdot \left[\nabla \int_{T_\psi^\pm} \nabla' \left[G_0(\vec{\mathbf{r}}|\vec{\mathbf{r}}') - G_0(\vec{\mathbf{r}}|\vec{\mathbf{r}}'_i) \right] \cdot \vec{\mathbf{f}}_\psi(\vec{\mathbf{r}}') dS'_{T_\psi^\pm} \right] dS_{T_\zeta^\pm} \\ & \left. + 2 \int_{T_\zeta^\pm} \vec{\mathbf{f}}_\zeta(\vec{\mathbf{r}}) \cdot \int_{T_\psi^\pm} \hat{\mathbf{z}}\hat{\mathbf{z}} \cdot \vec{\mathbf{f}}_\psi(\vec{\mathbf{r}}') G_0(\vec{\mathbf{r}}|\vec{\mathbf{r}}'_i) dS'_{T_\psi^\pm} dS_{T_\zeta^\pm} \right] \end{aligned} \tag{B.3}$$

are derived. Then, in conjunction with the vector identities, in the arrangement of the second term on the right-hand side of (B.3), with $G(\vec{\mathbf{R}}) = \left[G_0(\vec{\mathbf{r}}|\vec{\mathbf{r}}') - G_0(\vec{\mathbf{r}}|\vec{\mathbf{r}}'_i) \right]$, if the following equation is considered

$$\vec{\mathbf{I}}_1(\vec{\mathbf{R}}) = -\nabla S(\vec{\mathbf{R}}) \tag{B.4}$$

where

$$S(\vec{\mathbf{R}}) = \int_{T_\psi^\pm} \nabla' G(\vec{\mathbf{R}}) \cdot \vec{\mathbf{f}}_\psi(\vec{\mathbf{r}}') dS'_{T_\psi^\pm} \tag{B.5}$$

Now, employing divergence theorem

$$\nabla' \cdot \left[G(\vec{\mathbf{R}}) \vec{\mathbf{f}}_\psi(\vec{\mathbf{r}}') \right] = \nabla' G(\vec{\mathbf{R}}) \cdot \vec{\mathbf{f}}_\psi(\vec{\mathbf{r}}') + G(\vec{\mathbf{R}}) \nabla' \cdot \vec{\mathbf{f}}_\psi(\vec{\mathbf{r}}') \tag{B.6}$$

thus

$$S(\vec{\mathbf{R}}) = \int_{T_\psi^\pm} \nabla' \cdot \left[G(\vec{\mathbf{R}}) \vec{\mathbf{f}}_\psi(\vec{\mathbf{r}}') \right] dS'_{T_\psi^\pm} - \int_{T_\psi^\pm} G(\vec{\mathbf{R}}) \nabla' \cdot \vec{\mathbf{f}}_\psi(\vec{\mathbf{r}}') dS'_{T_\psi^\pm} \tag{B.7}$$

is obtained. Here, the divergence theorem leads to a contour integral around triangle

$$\int_{T_\psi^\pm} \nabla' \cdot \left[G(\vec{\mathbf{R}}) \vec{\mathbf{f}}_\psi(\vec{\mathbf{r}}') \right] dS'_{T_\psi^\pm} = \oint_l G(\vec{\mathbf{R}}) \vec{\mathbf{f}}_\psi(\vec{\mathbf{r}}') \cdot d\vec{\mathbf{l}} \tag{B.8}$$

and, since $d\vec{\mathbf{l}}$ is perpendicular to the triangular surface

$$\vec{\mathbf{f}}_\psi(\vec{\mathbf{r}}') \cdot d\vec{\mathbf{l}} = 0 \tag{B.9}$$

Hence,

$$\vec{\mathbf{I}}_1(\vec{\mathbf{R}}) = \nabla \int_{T_\psi^\pm} G(\vec{\mathbf{R}}) \nabla' \cdot \vec{\mathbf{f}}_\psi(\vec{\mathbf{r}}') dS'_{T_\psi^\pm} \tag{B.10}$$

and substituting (B.10) in (B.3), we have

$$
\begin{aligned}
Z_{\zeta\psi} =& j\beta_0\eta_0 \Bigg[\int_{T_\zeta^\pm} \vec{\mathbf{f}}_\zeta(\vec{\mathbf{r}}) \cdot \int_{T_\psi^\pm} \vec{\mathbf{f}}_\psi(\vec{\mathbf{r}}') \left[G_0(\vec{\mathbf{r}}|\vec{\mathbf{r}}') - G_0(\vec{\mathbf{r}}|\vec{\mathbf{r}}_i') \right] dS'_{T_\psi^\pm} dS_{T_\zeta^\pm} \\
&+ \frac{1}{\beta_0^2} \int_{T_\zeta^\pm} \vec{\mathbf{f}}_\zeta(\vec{\mathbf{r}}) \cdot \left[\nabla \int_{T_\psi^\pm} \left[G_0(\vec{\mathbf{r}}|\vec{\mathbf{r}}') - G_0(\vec{\mathbf{r}}|\vec{\mathbf{r}}_i') \right] \nabla' \cdot \vec{\mathbf{f}}_\psi(\vec{\mathbf{r}}') dS'_{T_\psi^\pm} \right] dS_{T_\zeta^\pm} \\
&+ 2 \int_{T_\zeta^\pm} \vec{\mathbf{f}}_\zeta(\vec{\mathbf{r}}) \cdot \int_{T_\psi^\pm} \hat{\mathbf{z}}\hat{\mathbf{z}} \cdot \vec{\mathbf{f}}_\psi(\vec{\mathbf{r}}') G_0(\vec{\mathbf{r}}|\vec{\mathbf{r}}_i') dS'_{T_\psi^\pm} dS_{T_\zeta^\pm} \Bigg]
\end{aligned}
\tag{B.11}
$$

Here, again through the divergence theorem

$$
\vec{\mathbf{f}}_\zeta(\vec{\mathbf{r}}) \cdot P(\vec{\mathbf{R}}) = \nabla \cdot \left[P(\vec{\mathbf{R}}) \vec{\mathbf{f}}_\zeta(\vec{\mathbf{r}}) \right] - \nabla \cdot \vec{\mathbf{f}}_\zeta(\vec{\mathbf{r}}) P(\vec{\mathbf{R}})
\tag{B.12}
$$

Similarly in (B.8)

$$
\vec{\mathbf{f}}_\zeta(\vec{\mathbf{r}}) \cdot P(\vec{\mathbf{R}}) = -\nabla \cdot \vec{\mathbf{f}}_\zeta(\vec{\mathbf{r}}) P(\vec{\mathbf{R}})
\tag{B.13}
$$

Substituting this, eventually

$$
\begin{aligned}
Z_{\zeta\psi} =& j\beta_0\eta_0 \Bigg[\int_{T_\zeta^\pm} \int_{T_\psi^\pm} \vec{\mathbf{f}}_\zeta(\vec{\mathbf{r}}) \cdot \vec{\mathbf{f}}_\psi(\vec{\mathbf{r}}') \left[G_0(\vec{\mathbf{r}}|\vec{\mathbf{r}}') - G_0(\vec{\mathbf{r}}|\vec{\mathbf{r}}_i') \right] dS'_{T_\psi^\pm} dS_{T_\zeta^\pm} \\
&- \frac{1}{\beta_0^2} \int_{T_\zeta^\pm} \int_{T_\psi^\pm} \left[\nabla_s \cdot \vec{\mathbf{f}}_\zeta(\vec{\mathbf{r}}) \right] \left[\nabla'_s \cdot \vec{\mathbf{f}}_\psi(\vec{\mathbf{r}}') \right] \left[G_0(\vec{\mathbf{r}}|\vec{\mathbf{r}}') - G_0(\vec{\mathbf{r}}|\vec{\mathbf{r}}_i') \right] dS'_{T_\psi^\pm} dS_{T_\zeta^\pm} \\
&+ 2 \int_{T_\zeta^\pm} \int_{T_\psi^\pm} \left[\vec{\mathbf{f}}_\zeta(\vec{\mathbf{r}}) \cdot \hat{\mathbf{z}} \right] \left[\vec{\mathbf{f}}_\psi(\vec{\mathbf{r}}') \cdot \hat{\mathbf{z}} \right] G_0(\vec{\mathbf{r}}|\vec{\mathbf{r}}_i') dS'_{T_\psi^\pm} dS_{T_\zeta^\pm} \Bigg]
\end{aligned}
\tag{B.14}
$$

is found.

Moreover, if we are considered the fields in far-field region, an approximation for $\vec{\mathbf{R}}$ can be used in the amplitude and phase terms of GF

$$
r = \left\| \vec{\mathbf{R}} \right\| = \begin{cases} r - \vec{\mathbf{r}}' \cdot \hat{\mathbf{r}}, & \text{for phase} \\ r, & \text{for amplitude} \end{cases}
\tag{B.15}
$$

Therefore, in the far-field region, $G_0(\vec{\mathbf{r}}|\vec{\mathbf{r}}') - G_0(\vec{\mathbf{r}}|\vec{\mathbf{r}}_i')$ is

$$\frac{e^{-jk\left\|\vec{\mathbf{r}}-\vec{\mathbf{r}}'\right\|}}{4\pi\left\|\vec{\mathbf{r}}-\vec{\mathbf{r}}'\right\|}-\frac{e^{-jk\left\|\vec{\mathbf{r}}-\vec{\mathbf{r}}_i'\right\|}}{4\pi\left\|\vec{\mathbf{r}}-\vec{\mathbf{r}}_i'\right\|}=\frac{e^{-jkr}}{4\pi r}\left(e^{jk\vec{\mathbf{r}}'\cdot\hat{\mathbf{r}}}-e^{jk\vec{\mathbf{r}}_i'\cdot\hat{\mathbf{r}}}\right) \tag{B.16}$$

and the scattered E-field

$$\vec{\mathbf{E}}^s\left(\vec{\mathbf{J}}\right)=-j\omega\mu_0\int_{S'}\overline{\overline{\mathbf{G}}}_e(\vec{\mathbf{r}}|\vec{\mathbf{r}}')\cdot\vec{\mathbf{J}}\left(\vec{\mathbf{r}}'\right)dS' \tag{B.17}$$

$$\vec{\mathbf{E}}^s\left(\vec{\mathbf{J}}\right)=-j\omega\mu_0\int_{S'}\left\{\left(\bar{\bar{\mathbf{I}}}-\frac{1}{\beta_0^2}\nabla\nabla'\right)\left[G_0(\vec{\mathbf{r}}|\vec{\mathbf{r}}')-G_0(\vec{\mathbf{r}}|\vec{\mathbf{r}}_i')\right]+2\hat{\mathbf{z}}\hat{\mathbf{z}}G_0(\vec{\mathbf{r}}|\vec{\mathbf{r}}_i')\right\}\cdot\vec{\mathbf{J}}\left(\vec{\mathbf{r}}'\right)dS' \tag{B.18}$$

can be stated. After applied $\nabla\nabla'$ operator,

$$\begin{aligned}\vec{\mathbf{E}}^s\left(\vec{\mathbf{J}}\right)=-j\omega\mu_0\int_{S'}\frac{e^{-jkr}}{4\pi r}\left[e^{jk\vec{\mathbf{r}}'\cdot\hat{\mathbf{r}}}-e^{jk\vec{\mathbf{r}}_i'\cdot\hat{\mathbf{r}}}\right]\left[\vec{\mathbf{J}}\left(\vec{\mathbf{r}}'\right)-\hat{\mathbf{R}}\hat{\mathbf{R}}\cdot\vec{\mathbf{J}}\left(\vec{\mathbf{r}}'\right)\right]dS'\\ -j\omega\mu_0 2\hat{\mathbf{z}}\hat{\mathbf{z}}\int_{S'}\vec{\mathbf{J}}\left(\vec{\mathbf{r}}'\right)\frac{e^{-jkr}}{4\pi r}e^{jk\vec{\mathbf{r}}_i'\cdot\hat{\mathbf{r}}}dS'\end{aligned} \tag{B.19}$$

where

$$\hat{\mathbf{r}}\times\left[\hat{\mathbf{r}}\times\vec{\mathbf{J}}\left(\vec{\mathbf{r}}'\right)\right]=\hat{\mathbf{r}}J_r\left(\vec{\mathbf{r}}'\right)-\vec{\mathbf{J}}\left(\vec{\mathbf{r}}'\right)=-\vec{\mathbf{J}}\left(\vec{\mathbf{r}}'\right)_{\tan} \tag{B.20}$$

Thus, the scattered electric field

$$\begin{aligned}\vec{\mathbf{E}}^s\left(\vec{\mathbf{J}}\right)=j\omega\mu_0\int_{S'}\frac{e^{-jkr}}{4\pi r}\left[e^{jk\vec{\mathbf{r}}'\cdot\hat{\mathbf{r}}}-e^{jk\vec{\mathbf{r}}_i'\cdot\hat{\mathbf{r}}}\right]\hat{\mathbf{r}}\times\left[\hat{\mathbf{r}}\times\vec{\mathbf{J}}\left(\vec{\mathbf{r}}'\right)\right]dS'\\ -j\omega\mu_0 2\hat{\mathbf{z}}\hat{\mathbf{z}}\int_{S'}\vec{\mathbf{J}}\left(\vec{\mathbf{r}}'\right)\frac{e^{-jkr}}{4\pi r}e^{jk\vec{\mathbf{r}}_i'\cdot\hat{\mathbf{r}}}dS'\end{aligned} \tag{B.21}$$

can be written.

PUBLICATIONS FROM THE THESIS

Papers

1. Y. E. Yamac, A. Kizilay, "Scattering analyses of arbitrary roughness from 2-D perfectly conductive periodic surfaces with moments method", *Turkish Journal of Electrical Engineering and Computer Sciences*, vol. 30, no. 3, pp. 730-749, 2022. DOI: 10.55730/1300-0632.3808

2. Y. E. Yamac, A. Kizilay, "EFIE analyses of 3-D scattering from an object above arbitrarily rough periodic surfaces by current decomposition method", *Journal of Electromagnetic Waves and Applications*, vol. 36, no. 13, pp. 1882-1889, 2022. DOI:10.1080/09205071.2022.2046507

Projects

1. "Study and development of target imaging and recognition technologies for contact and forward-looking GPR systems", The Scientific and Technological Research Council of Turkey (TUBITAK), Project No: 119N196.